# Microwave Signal Processing for Foreign Object Identification

A thesis presented in partial fulfilment of the

requirements for the degree of

Doctor of Philosophy

in Technology

at Massey University,

Institute of Information and Mathematical Sciences

Albany Campus, New Zealand

G. G. Senaratne

August 2008

# Acknowledgements

This thesis builds upon the well-known solutions of the wave equation in different coordinate systems, in particular those of Helmholtz's equation. The original work presented in this thesis is the use of an inverse method of determining unknown properties (size, position and dielectric properties) of an embedded object in a host medium using the scattering of microwave signals. Using well-established solutions for the forward and backward electromagnetic fields and matching these with experimentally determined values of the reflection coefficients we verified the method worked for simple pre-determined shapes. Chapters 2, 3 and 4 use some of these solutions with appropriate references in order to proceed for developing the microwave application system. Chapters 6 and 7 are related to experimental work which was carried out at the premises of Keam Holdem Associates in Auckland, New Zealand.

I am very pleased to write this short note of appreciation with thanks to my supervisors Professor Graeme C. Wake, Dr. Winston L. Sweatman, Dr. Richard B. Keam and Dr. Ray Simpkin. I thoroughly appreciate your support and kind assistance given to me during this study. I am grateful to the staff in the Institute of Information and Mathematical Sciences including the IT support group who provided me an excellent service and support throughout this study. My special thank goes to Professor Robert McKibbin and my former fellow staff in Information Sciences and Computer Engineering groups in Massey University.

Next, my thanks go to Technology New Zealand and Keam Holdem Associates for providing a TIF fellowship for my studies.

I offer my sincere gratefulness with respect to my loving mother for her support and blessings. I thank my sons Keshawa and Thiwanka for supporting me to achieve this goal.

Finally, I offer my thanks to Peter Jaques, Ronald Begg and Amanda Elvin who supported me by proof reading the thesis. I am grateful to Freda Mickisch for her support given to me during this study. My fellow students including Qing Zhang, Dion O'Neale, Gang (John) Xie, Joanne Mann, Ratneesh Suri and Sharleen Harper

have always provided a very peaceful and supportive environment to achieve the expected goals in this project. I thank you all.

# Abstract

This thesis presents a novel approach for detecting an internal object using non-invasive surface measurements of the reflection coefficients. The low cost and safety of the low power microwave detection system may be practically suited to first level breast cancer screening with further development. The significant difference in the dielectric properties of a malignant tumour compared to healthy breast tissue makes it possible to estimate the size and position of a tumour using microwave frequencies.

Incident and backscattered electromagnetic waves are analysed using three coordinate systems. Starting from a plane wave reflection model, this approach advances to obtain mathematical solutions to the nonlinear scattering problems of cylindrically and spherically-shaped objects. The solution to the inverse problem for finding the position, size and electrical properties of the unknown microwave scatterer is determined using Newton's iterative method. Both of the forward and inverse algorithms are tested using simulations before proceedings to an experimental application.

# List of publications

1. G. G. Senaratne, R. B. Keam, W. L. Sweatman, G. C. Wake and R. Simpkin, *An inverse method for detection of a foreign object using microwave measurements*, IET Journal on Science, Measurements and Technology (in press), (2008).

2. G. G. Senaratne, R. B. Keam, W. L. Sweatman and G. C. Wake, *Solutions to the inverse problem with potential application for breast tumour detection using microwave measurements*, Journal on Computational and Mathematical Methods in Medicine, **8**, no. 4, 245-61, (2007).

3. —, *Solutions to the inverse problem in a two-dimensional model for microwave breast tumour detection*, Journal of Intelligent System Technologies and Applications, IJISTA, **3**, no. 1/2, 133-48, (2007).

4. —, *Solutions to the two-dimensional boundary value problem for microwave breast tumour detection*, IEEE Microwave and Wireless Component Letters, **16**, no. 10, 525-27, (2006).

5. —, *An investigation based on the electrical properties in normal and malignant human breast tissues for tumour detection*, proceedings of the IIMS PG Conference, Massey University, New Zealand, October, 74-79, (2006).

6. —, *Microwave scattering at malignant tissue boundaries: A new method for breast screening*, proceedings of the International Conference SICE-ICCAS, Bussan, Korea, TA 07, (2006).

7. G. G. Senaratne, R. B. Keam, W. L. Sweatman and G. C. Wake, *Solutions to the two-dimensional microwave scattering problem: A new approach for breast tumour detection*, proceedings of the IIMS PG Conference, Massey University, New Zealand, 156-164, (2005).

8. G. G. Senaratne, R. B. Keam, W. L. Sweatman and G. C. Wake, *A new approach to breast tumour detection using microwave frequencies: A two-dimensional model*, proceedings of the First International Conference on Sensing Technology, ICST, Massey University, New Zealand, 460-65, (2005).

9. —, *Inverse methods for the detection of internal objects using microwave technology: With potential for breast screening*, proceedings of the Fifth International Conference on Inverse Problems in Engineering: Theory and Practice, Cambridge University, UK, Leeds University Press, Leeds, UK, Vol III, Chapter **S01**, 1-10, (2005).

10. R. B. Keam, G. G. Senaratne and R. Pochin, *One-dimensional propagation difference between tumour and healthy breast tissue at 2 GHz*, proceedings of the New Zealand National Conference on Non Destructive Testing, 21-25, (2004).

11. G. Senaratne and S. C. Mukhopadhyay, *Investigation of the interaction of planar electromagnetic sensor with dielectric materials at radio frequencies*, proceedings of the Fifth ISEMA Conference on Wave Interaction with Water and Moisture Substances, New Zealand, 95-99, (2003).

12. S. C. Mukhopadhyay, J. D. Woolley, G. Senaratne, G. Sengupta and S.Yamada, *Experimental observation of the effect of dielectric materials on the transfer impedance of planar electromagnetic sensors*, proceedings of the ENDE conference, 21-23, (2003).

# Contents

# Chapter 1

# Introduction and background information

## 1.1 Introduction

This thesis presents a non-invasive method to detect a foreign object concealed within a largely homogeneous material. The object is illuminated by a microwave signal applied from the outside boundary of the host medium. Using the electromagnetic fields at the surface of the scattering object, the analytic expressions are derived for its scattered fields. The detailed characteristics of the scattered waves with respect to the different boundary conditions and the location of the internal object are considered. Three scattering problems are solved using one-dimensional, two-dimensional and three-dimensional coordinate systems. The back-scattered waves convey useful information about the scatterer and so the mathematical solutions we develop here can extract some parameters which may be useful for many engineering and medical applications.

The approach of this project has a potential, with further developments, for application to some in-vivo situations such as detecting a breast tumour in its early

stage. As microwave radiation is a form of non-ionising radiation and, as it can have low power, the use of microwave imaging in the medical field and everyday life poses fewer health risks than ionising radiation in forms such as X-rays.

A simple model is used to represent a physical system for detecting an internal object. Then, using physical theory, the results of microwave measurements are predicted. This problem of prediction is called the simulation problem or the forward problem in this thesis. When developing the solutions to the forward problems, some existing theories in electromagnetism are used with appropriate references. The novelty of the work presented in the thesis is the subsequent expansion of these results for the proposed application (section 1.6). The inverse problem first uses the simulated results and then uses the actual results of measurements to infer the necessary parameters which characterise the system (size, position and electrical properties).

The microwave application model represents the measurement system and the host material. In this set-up, the measurement system provides the microwave signal to the antenna system which radiates the radio signal into the host material. The backscattered signal from the internal structure of the host is received by the same antenna system and sent back to the measurement system for analysis. The measured data is then processed using an inverse algorithm.

A general introduction to microwave detection and the related information is given at the beginning of this chapter (sections 1.3 and 1.4). This study is multidisciplinary, spanning mathematics and engineering. Therefore, the discussions here are elementary at the beginning but more detailed situations are explained in subsequent chapters.

## 1.2 Electromagnetic radiation

In general, the electromagnetic (EM) radiation is a wave propagation in space with electric and magnetic components which oscillate in directions at right angles to each other. Electromagnetic radiation is classified in the electromagnetic spectrum according to the frequency of the wave. In order of increasing frequency, this spectrum consists of radio waves, microwaves, terahertz radiation, infrared radiation, visible light, ultraviolet radiation, X-rays and gamma rays. There are many different mechanisms which generate electromagnetic radiation and transfer energy to the outside world. The sun is a good example. It generates an enormous amount of electromagnetic radiation due to its nuclear reactions and transfers the energy to the earth. The behaviour of EM radiation depends on its wavelength which is the distance between two neighbouring points of the same phase in consecutive cycles of a wave.

Many technologies have been developed using microwave frequencies. Some of the applications are dielectric heating with microwave radiation, transmission of information for broadcasting and television, radar detection, telecommunication purposes such as microwave relay, satellite communication and mobile and wireless networks. Other major uses of microwaves are the quality control of food, foreign object detection and structural abnormalities and cavity detection in the engineering industry. Apart from these, there are many applications in medical fields such as tumour detection, inflammation and abnormality detection and treatments in the human body. More information on microwave applications can be found in references [1-6].

## 1.3 Electrical properties of materials

At high frequencies, measurements of the dielectric properties of materials provide a basis for developing methods to detect physical properties. The dielectric properties have frequency dependent characteristics. These properties differ from material to material. They have a high correlation with water content at microwave frequencies. Using this phenomenon, physical properties such as bulk density, moisture content and temperature can be determined.

Materials are classified using three basic properties: permittivity $\varepsilon$, permeability $\mu$ and electrical conductivity $\sigma$. The materials having large values of $\sigma$ are called conductors and those having small values of $\sigma$ are called insulators or dielectrics. Again, the conductors are characterised as perfect conductors when $\sigma$ is very large, considered infinite, and dielectrics are perfect dielectrics when $\sigma = 0$. Light is electromagnetic in nature and its velocity is denoted by $c$. In metric units, in a vacuum $c$ is approximately 299,792,500 metres per second (1,079,252,900 km/h), a value obtained from measurements. In free space,

$$c = \frac{1}{\sqrt{\mu_0 \epsilon_0}}, \tag{1.1}$$

where $\epsilon_0$ is the capacitivity or permittivity and $\mu_0$ is the inductivity or permeability of a vacuum. By definition, $\mu_0 = 4\pi \times 10^{-7}$ Henries per metre (H/m). The value for $\epsilon_0 = 8.854 \times 10^{-12}$ Farads per metre (F/m) which is obtained from equation (1.1). In other media, $\epsilon$ is always greater than that of a vacuum, $\epsilon_0$. The relative capacitivity or dielectric constant $\epsilon_r = \epsilon/\epsilon_0$ and similarly, the relative inductivity or relative permeability $\mu_r = \mu/\mu_0$.

Magnetic materials are classified relative to the permeability of free space, $\mu_0$. The materials for which $\mu$ is slightly less than $\mu_0$ are called diamagnetic, those where $\mu$ is slightly greater than $\mu_0$ are called paramagnetic and those where $\mu$ is much larger than $\mu_0$ are called ferromagnetic. The ferromagnetic metals are

extremely lossy materials and they also have a nonlinear characteristic with respect to complex permeability. Therefore these metals are not suitable for use with radio frequencies. In most linear matter (where properties are frequency non-dispersive), $\mu$ is approximately equal to $\mu_0$ and therefore $\mu_r = \mu/\mu_0$ is approximately equal to unity unless the material is ferromagnetic.

The complex permittivity $\hat{\epsilon}$ is a function of $\omega$, where $\omega = 2\pi f$ and $f$ is the frequency and, can be expressed in both rectangular and polar forms [8]:

$$\hat{\epsilon}(\omega) = \epsilon' - j\epsilon'' = |\hat{\epsilon}|e^{-j\delta}, \tag{1.2}$$

where $j = \sqrt{-1}$, $\epsilon'$, $\epsilon''$ and $\delta$ are real quantities and are called the a-c (alternating current) capacitivity, the dielectric loss factor and the dielectric loss angle, respectively. The real part ($\epsilon'$) contributes to the stored energy and the imaginary part ($\epsilon''$) contributes to energy loss in the material. Microwave materials are usually characterized by specific relative permittivity $\epsilon_r$ [7], $\epsilon' = \epsilon_r\epsilon_0$, and loss angle $\delta$ at a certain frequency which has been defined as

$$\delta = \tan^{-1}\frac{\epsilon''}{\epsilon'}. \tag{1.3}$$

In perfect dielectrics the dielectric loss is equal to zero ($\epsilon'' = 0$). The materials for which $\epsilon'$ is almost constant and $\epsilon''$ is very small at radio frequencies are called good dielectrics and the materials for which the values of $\epsilon'$ and $\epsilon''$ at radio frequencies are variable, with $\epsilon'' \neq 0$ are called "lossy dielectrics" [8]. We frequently use the terms "permittivity" or "relative permittivity" throughout this thesis to indicate the permittivity relative to that of free space, $\epsilon_0$. Thus, for example, the relative permittivity of water below the microwave range of frequencies is about 78 (relative permittivity has no units).

Similarly, the complex permeability $\hat{\mu}$ can be expressed as

$$\hat{\mu}(\omega) = \mu' - j\mu'' = |\hat{\mu}|e^{-j\delta_m}, \tag{1.4}$$

where $\mu'$, $\mu''$ and $\delta_m$ are real quantities and are the a-c inductivity, the magnetic loss factor and the magnetic loss angle, respectively. The real part ($\mu'$) relates to stored energy and the imaginary part ($\mu''$) relates to power dissipation in the material.

There are a number of uses of these properties in both engineering and medical applications. Experimental studies have shown that most materials differ in their material properties [9-11]. These property differences cause the individual materials to act differently when excited by microwave signals. Therefore, the information about hidden objects, disorder conditions and abnormalities of many materials can be detected using the differences in electrical properties.

There are three basic constitutive relationships for field vectors and this derivation is based on Maxwell's equations. For any material media having an electromagnetic field, the complex form of these relationships is

$$\mathbf{D} = \hat{\epsilon}(\omega)\mathbf{E}, \quad \mathbf{B} = \hat{\mu}(\omega)\mathbf{H}, \quad \mathbf{J} = \hat{\sigma}(\omega)\mathbf{E}, \tag{1.5}$$

where $\mathbf{E}$ (volts/m) is the complex electric intensity and $\mathbf{H}$ (amperes/m) is the complex magnetic intensity. From these relations, the complex values of $\mathbf{D}$ the electric flux density (coulombs/m$^2$), $\mathbf{B}$ the magnetic flux density (webers/m$^2$) and $\mathbf{J}$ the electric current density (amperes/m$^2$) are related to the complex values of the permittivity, permeability and conductivity, respectively. (Note that vectors are shown in bold font in this thesis.)

## 1.4 Wave functions of scattering problems

The physical basis for the microwave imaging is the contrast between the dielectric properties of the object being imaged and those of its surrounding host material. The incident microwave signal can be reflected, refracted or scattered from the boundaries where discontinuity occurs in any electrically inhomogeneous medium depending upon the size and the shape of its boundary. The amount of wave re-

flection and absorption changes with the electrical properties upon the two sides of the reflecting boundary between the media. The refraction of a microwave signal depends upon the refractive index of the refracting material and the incident angle of the wave [1, 12, 13]. In this study we are mostly focusing on microwave reflection and scattering at different object boundaries.

Microwave scattering mainly depends upon the dielectric property, as well as the shape, size and the position of the scattering object, with respect to the incident signal. In general, the solutions to the problems of microwave scattering at a plane boundary are solved in cartesian coordinatescoordinates and the subsequent waveforms are associated with rectangular wave functions more commonly referred to as plane waves [14, 15]. Similarly, the scattering problems of cylindrical boundaries are solved using cylindrical coordinate systems and their subsequent waveforms are associated with cylindrical wave functions.

The Bessel functions of the first and the second kinds form a basis of cylindrical wave functions. These are quasi-periodic functions with multiple zeros and are very similar to sine and cosine functions which represent standing waves. Linear combinations of Bessel functions of the two kinds are called the Hankel functions [16] and one of these functions ($H_n^{(2)}$) may be used to represent the outward-travelling waves as these waves vanish as $x \to \infty$ ($x$ is the distance from the boundary of the scattering object, see Appendix B for more details). Therefore, an appropriate selection of the wave functions with asymptotic conditions for large distances is very important for solving many scattering problems. In this study, the scattering problems of the cylindrically and spherically-shaped objects are solved using the infinite series of these wave functions and their modified functions in cylindrical and spherical coordinates, respectively. When the scattering problem is associated with a spherical object, it is necessary to use Legendre functions to solve the associated scattering problem (see Appendix D for details).

## 1.5 Literature review

In this section we discuss the information found in literature related to microwave imaging and the recent developments in imaging technology [4, 17-25]. Many of these studies are focused on breast cancer detection. The purpose of this review is to find suitable ideas and directions which may possibly support achieving the project goals. We first discuss the general microwave imaging methods and some existing imaging techniques and then consider their uses and drawbacks.

### 1.5.1 Microwave imaging

Microwave imaging can be divided into two categories: passive microwave imaging and active microwave imaging. Passive imaging is based on sensing the microwaves that are naturally occurring in the environment. A good example is microwave radiometric imaging which is used to monitor atmospheric conditions [26-29]. The other category is active microwave imaging which uses a generated microwave signal to interact with the target being imaged [30]. (These categories are further discussed in section 1.5.2.2.)

In general, the existing imaging techniques are categorized into two types: monostatic imaging and bistatic imaging. Monostatic imaging is based on the back reflection of the forward signal and the measurements are taken using the same antenna for transmission and reception. Bistatic imaging uses physically separate transmission and reception antennas and can provide information on waves transmitted through the object as well as backscattered waves [23, 31]. However, both of these categories are active microwave imaging techniques and these techniques are based on the wave interaction with the dielectric properties of materials. The measurements that are taken for active imaging are based on the signal propagation, reflection, diffraction and scattering of the incident wave which has been transmitted from the source. Our interest in this study is to develop a 'monostatic active microwave imaging

technique' to detect a foreign object inside a host material.

There are many detection methods available at present such as reflectometry, microwave tomography, and radar techniques. The reflectometry is used for cavity detection, localising damage and cable faults and many other similar types of application [1-3, 23, 32]. Microwave tomography is an imaging method based on contrast in dielectric properties of materials (more details are given in section 1.5.2.2). Image construction is achieved using a number of sensors but the quality of the image depends upon the spectral resolution of the receiving system. Most of the tomographic systems developed before the 1980s used ionising radiations from an isotope of an X-ray source and therefore these systems are bulky, expensive and have safety limitations [33]. The X-ray technique is used for obtaining tomographic images based on the density differences among the materials. In medical applications the important physical characteristics such as temperature, blood content and blood oxygenation cannot be differentiated by X-ray tomography. However, since microwave tomography is based on the dielectric properties and is often sensitive to such characteristics, this method can distinguish these conditions in biomedical applications [4, 30, 34, 35]. Long-term researches have been carried out in active microwave tomography systems operating in frequency-domain. When exposed to microwaves, the high water content of malignant breast tissues cause significant microwave scattering than normal tissues. More details are given in section 1.5.2.2.

### 1.5.2 Microwave application for breast imaging

Breast cancer begins in the breast tissue and forms a lump or mass called a tumour. Cancers are a group of diseases that cause cells in the body to change and grow out of control [41]. Breast cancer is considered a non-skin malignancy and is the most prevalent cause of female cancer mortality. According to the published data from cancer research in the UK, each year almost 44,100 cases of breast cancer are

diagnosed there of which 43,760 are female cases. This disease causes more than 12,500 deaths each year in the UK [36]. According to recent reports [37-39], breast cancer is the most common cancer in women in the US, accounting for nearly 1 in 3 cancers diagnosed. The World Health Organization says (in their 2006 report) [39] that there were a total of 58 million deaths worldwide in the year 2005 of which breast cancer accounts for 502,000 of these deaths. One in ten women in New Zealand will develop breast cancer in their lifetime. For 75 percent of these cases, the candidate will be over 50 years of age. Simple mathematics implies that 25 percent of cases still occur before the age of 50 [40].

There are a number of diagnosing methods for breast tumours at present. Among these existing technologies, X-ray mammography is the most usually available method and it is regarded as the 'gold standard' for breast cancer detection. However it suffers from a number of drawbacks [42-45]. According to the studies carried out by Christiansen *et al.* [46, 47], there were 6.5% false-positive mammograms found among 9747 screening mammograms of 2227 women, over a 10-year period. Depending upon the adjustments for the patient at the test, the characteristics of the radiologist and the testing method, the false-positive and false-negative rates vary. The accuracy of the test depends upon many factors including the breast compression when taking a mammogram, adjustments for the patient at the test, the characteristics of the radiologist or the doctor who make the decision and the testing method [11, 46]. In mammograms the breast is kept between the source and the receiver and compression is required to reduce the image blurring to obtain acceptable test results. Breast compression is uncomfortable and painful for the examinee whilst there is also a limit upon the number of exposures to the ionising radiation that may be safely undertaken.

To diagnose breast cancer a specimen is taken from the suspected lump (biopsy). Again a false diagnosis is possible: the final decision is usually taken by an experi-

enced doctor referring to other test results. These laboratory tests are not always accurate because it is very difficult to take an exact specimen if the lump is very small and hidden inside the breast tissue. However, given positive test results, a series of other follow-on tests may be conducted before proceeding to the subsequent treatment. There are some other approaches such as Digital Tomosynthesis, Sestamibi (Miraluma), Ductal Lavage, Positron Emission Tomography (PET) and Computerized Axial Tomography (CAT) scans [48, 49]. Some details of three electromagnetic breast imaging techniques with test results have been discussed in [50].

#### 1.5.2.1 The electrical properties of cancer cells

A precise knowledge of the dielectric properties of human breast tissue is important for many microwave imaging methods. Studies of the electrical properties of biological materials began more than 100 years ago. As a result, there is useful information in the literature which can be used to develop microwave detection methods for medical and biomedical applications [51-53]. Chaudhary *et al.* [54] have measured the dielectric properties using excised breast tissues obtained from 15 patients of different age groups and found that the relative dielectric constant of malignant tissue is strikingly higher than that of normal tissue. They have also found that the conductivity is considerably higher than that of normal tissue. Also both of these properties are frequency dependent.

According to their observations, the difference between the relative dielectric constant of normal and malignant tissue is much larger at frequencies below a few MHz. However, this difference remains almost constant up to frequencies of a few GHz and begins to reduce at frequencies higher than 2GHz. In this range (less than 2GHz) the relative dielectric constant of the malignant tissue is about 6-8 times higher than that of the normal tissue. According to this study [54], the conductivity of the malignant tissue maintains almost a constant difference with that of the

normal tissue (malignant tissue is about 6-7 times higher) up to a few GHz frequencies but the conductivity of the malignant tissue increases dramatically thereafter. The reports of the substantial contrast of the measured dielectric properties of normal and malignant breast tissues have promoted a great deal of interest in microwave techniques for breast cancer detection [55, 56].

The dielectric properties of breast carcinoma were measured by Andrzej *et al.* [53] using the specimens taken from seven different patients. The samples were taken from different locations of the breast using surgical procedures and dielectric properties have been determined using the reflection coefficients measured with a network analyser. They have used a range of frequencies from 20-100 MHz. A summary of their results is given in Table 1.1. (Here, the conductivity is given in milli Siemens per cm and the dielectric constant has no units.) There is a large spread of dielectric data for different specimens and these results have revealed significant differences in dielectric properties between the samples taken from different locations. Andrzej *et al.* [53] suggest that these differences can be associated with the cellular heterogeneity and structural differences of the tested samples. They have also suggested that the radio frequency impedance imaging can potentially be used as a diagnostic modality for the detection of human breast carcinoma.

The breast is filled with normal breast fat and fibrograndular tissue and is bounded by a skin layer of some thickness (a few millimetres). The malignant tumours have high protein hydration [6], therefore an increased dielectric permittivity inside the tumour can be expected. The fat density of the normal breast tissue is significantly higher and therefore the electrical properties of the normal tissue are significantly smaller compared to those of malignant breast tissue. The ex-vivo measurements which have been taken by Keam *et al.* [57] using the Keam Holdem VE2 analyzer show that a tumour has a significant difference in complex dielectric permittivity to that of healthy breast tissue. These measurements have

Table 1.1 Measured electrical properties of a breast tumour at low-frequency.

| Type of the measured property | Tumour tissue | Tissue surrounding the centre of the tumour | Normal breast tissue (2 cm from tumour) |
|---|---|---|---|
| Conductivity | 4-5 mS/cm (between 100 KHz and 100 MHz) | 5-7 mS/cm (between 100 KHz and 100 MHz) | < 1 mS/cm at 100 KHz |
| Dielectric constant | $2\times10^3$ - $6\times10^3$ (at 100 KHz) | $2.5\times10^3$ - $8\times10^3$ (at 100 KHz) | <500 at 100 KHz |

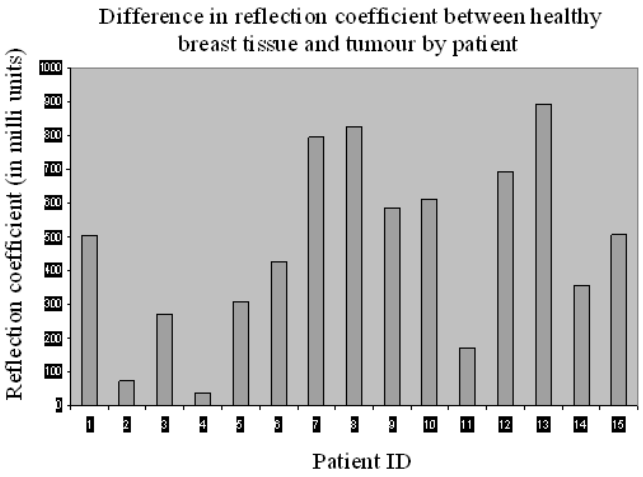


Figure 1.1: Measured reflection coefficients for breast tumours (shown in milli units; 1000mu=1) for 15 patients (Reproduced with permission from Keam Holdem Associates, New Zealand).

been highly influenced by the dielectric properties of the clinical samples of the tumour. The results of the measured reflection coefficients by patient are shown in Figure 1.1. The measured samples were categorised with the patient's age and the type of carcinoma. These results confirm that there is a significant difference in the microwave response at the tumour. In general, the tumour has a higher moisture content compared to that of normal tissue and therefore, the tumour's response at a given microwave frequency is significantly higher than that of the normal breast tissue. However, the difference in the reflection coefficient between healthy breast tissue and the tumour varies with the type of carcinoma and the patient's age.

#### 1.5.2.2 Microwave breast cancer detection

Breast cancer detection using microwaves relies on the dielectric property difference between the normal and malignant tissue in the breast. During the past few years, this area of research has made considerable progress and therefore there are hopes of successful clinical implementations to conventional mammography in the near future [11, 30, 51, 58-60]. There are three main approaches in microwave detection and these are called hybrid, passive and active breast imaging methods [61, 62].

**Hybrid methods**:

Thermo-acoustic tomography falls into the category of a hybrid method. In this method a microwave signal is used to heat the tumour and an image is constructed based on the ultrasound approach. Malignant tissue has high conductivity. Therefore, when the breast is illuminated by microwaves more energy is deposited in tumours resulting in selective heating of the lesions of the malignant tissue. Then, the tumour expands and generates pressure waves. These waves are detected by ultrasound transducers kept around the breast.

The basis of this approach depends on the change in the dielectric property of the tissue with temperature. Previous research has revealed that the dielectric property

of biological tissue varies with the temperature [63-65]. Therefore any imaging method which monitors the dielectric properties may also be able to determine a temperature distribution in biological tissue. In order to achieve this, inverse scattering methods have been introduced [66, 67]. Many of these approaches use Newton's iterative method for Hybrid Element (HE) image reconstruction and they require the derivation of inverse problem solutions.

Two methods for the reconstruction of the image have been proposed. In Computed Thermo-acoustic Tomography (CTT) [68-70], the breast is immersed in a water bath and illuminated at a given microwave frequency. Kruger *et al.* [68] used 434 MHz frequency. Tiny pulses of period 0.5 $\mu s$ are used to generate ultrasound waves. The ultrasound transducers are placed around a hemispherical bowl and record data as this bowl rotates through $360^0$. The reconstruction of the image is achieved using the filtered back-projection algorithm which was adopted from X-ray computed tomography. In Scanning Thermo-acoustic Tomography (STT), images are obtained using focused transducers to record the ultrasound waves [70, 71].

Microwave radiometry falls into the category of *passive microwave imaging* [21, 25, 69]. The imaging is based on the temperature increase of the tumour compared to that of the normal breast tissue. An example of passive microwave imaging is ONCOSCAN [2], a non-invasive test of thermal activity in the breast, where the microwave emission is measured by passive radiometry [22]. In this method the radiometric data is obtained from a transducer placed on the patient's abdomen. The scanning probe is placed in one position and held 15 seconds before going to the next position. For each patient, 20 position scans are performed for each breast. The clinical results obtained from each breast are compared. The ONCOSCAN has the potential to assist in the diagnosis of other methods such as mammograms.

**Active Microwave Imaging**:

Active microwave imaging techniques use several transmitters to illuminate the scat-

tering object and measure the scattered fields from the receivers kept at different locations. The shape and the location of the scattering object are found using the spectral distribution of the complex permittivity obtained from the information from the transmitted and received signals. In general, active microwave imaging can be categorized into two different techniques. One is the construction of breast images using near-field tomographic image reconstruction algorithms. The other technique is to collect the backscattered data using a short pulse transmitted towards the scattering object. This pulse is called an Ultra-Wide-Band (UWB) pulse because it has very small pulse-width, and therefore the transmitted signal requires a wider bandwidth [72-74].

**Microwave tomography**

Microwave tomography has been a major topic of breast image reconstruction for many years [11, 75]. Meaney *et al.* [76] have designed and constructed this type of prototype breast imaging interface which can be applied as a comfortable breast examination method, when compared to X-ray mammography. In this method the scanning object is immersed inside a water-coupled clinical interface and microwave measurements are taken using a number of receiving antennas. A fixed antenna array has been used to examine the breast from the nearest point to the chest wall up to the nipple. The examinations have been carried out without compression, while the patient lies in a prone position with the breast pendant in the coupling fluid. Generally, a tomographic method needs a large number of antennas to scan over planar or cylindrical surfaces. The microwave signals in the range from 300-1000 MHz in 100 MHz increments have been transmitted through the breast by 16 antennas and received by 16 antennas (altogether 32 channels) and both of these waves were measured to reconstruct the image of the breast. Each of the antennas operates in both transmit and receive modes. The reconstruction is made according to the dielectric distribution throughout the scanning area and this has been achieved by

matching the measured data with the computed data. Some iterative methods have been used for the reconstruction algorithm. The computed data have been obtained using the numerical methods based on a model with estimated material properties.

The tomographic methods use narrow band microwave signals and the forward and backward signals are analysed in the frequency domain. As the scattering waves have differences depending upon the properties and the boundary condition of the object, it is necessary to solve the scattering problem using suitable algorithms for the forward problem. Similarly, the subsequent inverse scattering problem is also required to be solved iteratively for successful image reconstruction. In general this is an ill-posed problem and needs suitable mathematical approaches in order to obtain meaningful solutions [76-78].

The microwave tomographic method presented by Bulyshev *et al.* in [78] uses a large number of transmit and receive antennas (in one, three or five rows of transmitters with 32 transmitters in each row and 32 rows of receivers with 32 receivers in each row) around a hemisphere of their dielectric breast model. The scalar Helmholtz equation is used to describe the electromagnetic waves and a point source has been considered as the incident field. Even if this solution is simple from a mathematical point of view, as the computations of the inverse method involve the data from a large number of receivers, an efficient inverse method such as Newton's iterative scheme is hardly applicable because the computations with this data are extremely time-consuming in the 3-D case. However, the approach presented in this thesis does not have such time consuming computations for Newton's method. The incident wave problems are solved using Helmholtz equations in cylindrical and spherical coordinates. Extracting unknown critical parameters of the object is achieved using the data obtained from a single antenna using several different frequencies. Also, Bulyshev *et al.* [78] use a coupling medium in the model on the outside of the breast and solve for the permittivity from the experimental data

whereas our method directly measures the reflection coefficient through the air and solves for a small number of unknowns.

**Radar-based approaches**

Recent research into a radar-based approach for breast cancer detection has made good progress. In this approach an ultra-wideband pulse (UWB) is transmitted and the backscattered data are collected from different receiving antennas. The data collected from the forward and backward waves are analysed in the time domain for image reconstruction. The time domain analysis of the scattering signal suffers from a number of drawbacks due to multiple scattering and the complex behaviour of the signal caused by the inhomogeneous structure of the breast.

The Confocal Microwave Imaging (CMI) method was first introduced by Hagness *et al.* [79, 80]. They also have used the dielectric permittivity difference between tumour and normal breast tissue for this analysis. The back-scattered energy from the tumour has been monitored using a short-pulse transmitted towards the tumour. They have presented the Finite Difference Time Domain (FDTD) [81] simulation results of both two-dimensional and three-dimensional modelling of the breast for detecting tumours to a depth of 5 cm. The back-scatter response levels tabulated in their three-dimensional study (based on simulations) have shown good results. (That is, in the worst case, the response is seen to be -115 dB relative to the source power [80].) The tumour response with respect to tumour depth shows linear decreases for all the tumour sizes, but in practical applications such a linear response could not be expected due to noise and interference within the system.

In the study of CMI for breast imaging by Fear *et al.* [82], the breast is modelled with planar and cylindrical configurations and methods are developed to detect and localise tumours in three dimensions. In this approach the FDTD method has been used to compute the back-scattered data. The practical application of this method is similar to the microwave tomographic breast scanner method [76] but most of those

techniques have very challenging computation and application difficulties. Fear *et al.* [82] have used an UWB signal for confocal microwave imaging of the breast. In the modelling of their study [83], they have assumed that the contrast between the malignant and the normal breast tissue is 5:1 in relative permittivity and 10:1 in conductivity. The scanning data from the breast have been obtained using a bow-tie antenna [80, 84]. In this method an UWB pulse is excited from each antenna position. This pulse is of the form [82]

$$V(t) = V_0\,(t - t_0)e^{-(t-t_0)^2/\tau^2}, \tag{1.6}$$

where $V_0(t - t_0)$ is the voltage adjustment of the pulse, $\tau$ is equal to 62.5 ps and $t_0 = 4\tau$. The width of this pulse is 0.17 ns. The current is recorded during and following the excitation in both the planar and cylindrical configurations. The image formation depends upon the time contents of the recorded pulse, mainly the reflection from the skin, tumour backscatter and the backscatter due to clutter. In this method a very robust signal processing algorithm is needed for the image reconstruction. However, the results vary with the number of antennas positioned in both planar and cylindrical models (testing has been conducted with 25, 41 and 45 antennas).

Li *et al.* [85] reviewed the status of Microwave Imaging Space-Time (MIST) beamforming for breast tumour detection. They have used two configurations; one is to assess the tumours adjacent to the chest wall (while the patient is in the supine position) and the other is to access the full volume of the breast while the patient is lying in the prone position. In this approach, a microwave signal is focused at one point and the position of this point is scanned throughout the breast by adjusting the beamformer for each new focal point. Similarly, a systematic procedure is used to scan the breast from point to point using the beamformer. The FDTD method was used to evaluate this MIST beamforming to detect small tumours in numerical breast models.

Li *et al.* have also simulated back-scattered signals obtained experimentally using physical breast phantoms. The UWB antenna sequentially scanned 49 different positions in the 1-11GHz frequency range to record the back-scattered data. In both analytical and experimental studies they have recovered the image from the tumour (using an analytical or synthetically designed object) which was kept in a fixed location among the breast tissue. Both the results very closely agree with the realisable energy distribution within the system considered.

Another set of methods of microwave imaging has been proposed by Xie *et al.* [86-87] for early breast cancer detection. These are the Multistatic Adaptive Microwave Imaging (MAMI) methods. In this application, a number of antennas transmit UWB pulses while all other antennas are used to receive the reflected signals. The pulses transmitted from different antennas are displaced so that the transmitted pulses are orthogonal to each other. The MAMI method can be considered as a special case of the Multi-Input Multi-Output (MIMO) method. The transmission and reception patterns of MAMI and MIMO antennas are different to each other. However, according to the interference coming from the breast skin, nipple and other scattering mechanisms, this method also needs robust data-adaptive algorithms to achieve high resolution.

In general, the UWB radar methods have more advantages for breast screening compared to conventional mammography and MRI methods, but there are still many challenges associated with UWB methods. Problems associated with the antenna array are common for this method as well as for the microwave imaging methods. As these approaches need a large number of antennas, to be kept in fixed positions or to be used by moving to different positions within the measuring environment, there exist focusing and location difficulties. Apart from the scattering from the tumour, there are other scattering mechanisms such as breast skin, chest wall, cell structures with high-density, etc. These would generate scattering responses apart

from the tumour response. Therefore in a practical application, apart from the signal processing requirement, more robust solutions are required for the practical problems such as positioning and focusing of the antennas to obtain better results. The management of aperture size and the scan time can play a major role in this imaging approach. Also, designing the antenna array is a challenging task as there are a large number of antennas in it.

In most of the time-domain applications [20, 21, 58, 74, 88, 89] an array of broadband antennas is placed surrounding the breast and an UWB microwave pulse is transmitted into the breast. As the pulse is very small, the transmitted signal must have a large bandwidth. When a higher frequency (eg. 10 GHz) is used for this, a large path-loss must be expected. The loss of the signal depends upon the distance between the antenna array and the target object and also on the characteristics of the propagation medium. Therefore, extracting the required information from a weak signal is a challenging task in practical applications. Again, the proposed method does not required such a high frequency. However, the signal's wavelength is important here as it must be long enough to cover the scanning range of the host material within which the target object is likely to found.

### 1.5.3 Other microwave applications

There are other applications based on microwave reflection from different dielectric materials. With the use of estimating the difference of forward and backward waves of such reflections, the sensing of grain and seed moisture, soil moisture and many other applications are performed in industry [9, 27, 90]. An experiment carried out by Keam *et al.* [91] for microwave salt and moisture measurement has given promising results. They have used their VE2 microwave analyser to measure the content of the moisture of butter in a production line. Figure 1.2 shows the in-line measurement results of butter moisture using one particular microwave frequency.

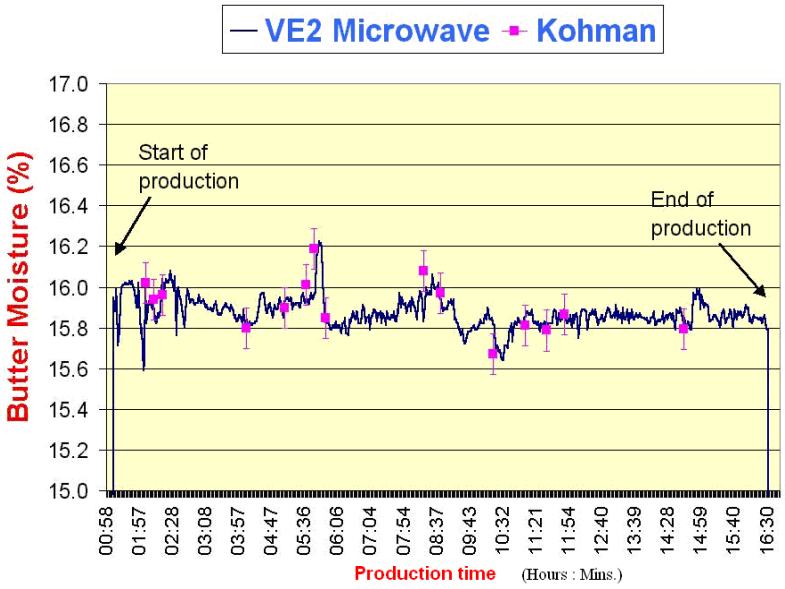


Figure 1.2: Microwave measurement of butter moisture (Reproduced with permission from Keam Holdem associates, New Zealand).

These results have a good association with the results of the traditional gravimetric oven method with a maximum least square error of less than 0.2% and mean least square error of less than 0.05%. The dielectric properties of the materials depends upon the amount of moisture and water content in their molecular structure. Microwave reflection from these materials have a very high correlation with their dielectric properties.

A similar experiment has been carried out by Senaratne and Mukhopadhyay [92] to investigate the microwave interaction with dielectric materials such as fats, protein, water and ice using a planar type electromagnetic sensor. The result of this experiment has confirmed that the proximity of any dielectric material has a significant effect on the field of the sensing coil which results in change to the transfer impedance of the sensor. The calculated transfer impedance of some materials having different relative permittivity values are given in Table 1.2.

The feasibility of the surface measurement of soil moisture using microwaves has

Table 1.2 Transfer impedance of a few cases

| Relative premittivity | Real part of transfer impedance (Ω) | Imaginary part of transfer impedance (Ω) |
|---|---|---|
| 1.0 | 461.11 | 3776.6 |
| 3.0 | 597.0 | 3961.0 |
| 15.0 | 369.0 | 3549.4 |
| 80.0 | 319.39 | 3379.0 |

been studied by Holdem *et al.* [93]. A soil moisture profile has been obtained to a depth of 1.5 cm by inverting, through function optimization, a simulation of the reflection coefficient from layered dielectric materials. This is a frequency-domain approach and the depth of penetration of radio waves into the soil is determined by the frequency. This method can have a low implementation complexity and therefore it is expected to be of interest to soil researchers and horticulturalists.

A model-based approach to improve the spatial solutions for imaging buried objects using microwave measurements has been proposed by James and Christian [94]. This is an example of another extension of active microwave imaging to the geophysical area for the detection and identification of buried inhomogeneities using electromagnetic waves. Nondestructive evaluation and nondestructive testing are some of the other fields in which microwaves can play a further increasing role [95]. In most of these applications, an improved inversion technique for electromagnetic evaluation and testing can play a significant role for the success of the method [96].

## 1.6 The proposed method: microwave object detection (MOD)

Most of the microwave imaging methods found in the literature consider the dielectric property differences between the internal object and its surrounding host material. When the waves are scattered from the object boundary, the resulting backward waves can have a nonlinear characteristic. That is, these waves have nonlinear magnitude variations with respect to the distance of the object from the wave source. The proposed method analyses the forward and backward wave functions in detail to study these effects using the mathematical solutions to these forward and inverse scattering problems.

### 1.6.1 Methodology

This method falls into the category of monostatic imaging and its application is based on the scattering of microwave signals applied to the surface of the host. The forward wave penetrates through the non-homogeneous internal structure of the host. The approach analyses the behaviour of both forward and backward signals and computes the size of the scattering object and its distance from the surface of the host material. The behaviour of the signal with different material properties has led to general equations which can be obtained from the well-known theory of electromagnetic wave propagation [14, 15]. Those equations contain information on the electrical properties of the internal structure and can be used to develop algorithms to compute the unknown parameters of the internal object. The front-end microwave measurements provide the required information which is needed to identify and then compute these parameters. Theoretical developments and associated analytical and experimental tests of this method are discussed in the following chapters in this thesis.

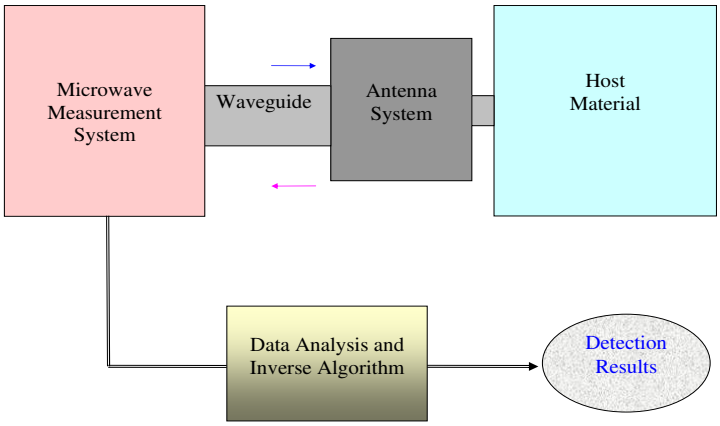


Figure 1.3: Experimental set-up for microwave measurements.

### 1.6.2 The microwave application system

The experimental set-up for the microwave application system is shown in Figure 1.3. The measurement system provides the microwave signal to the antenna system which sends the radio signal into the host material. The back-scattered signal from the internal structure of the host is received by the same antenna system which sends it back to the measurement system for analysis. Microwave measurements are obtained using a network analyser and the results are analysed in the frequency domain in this study.

The measured data is then processed using the reconstruction algorithms. In both the two-dimensional and three-dimensional situations, the phase and magnitude of the reflection coefficient is measured using this measurement system. In order to test the algorithms for these studies, analytical and experimental tests were conducted using a number of microwave signals with different frequencies. In these tests, the application system is almost identical except that the host is treated

differently according to the shape, size and the distance of the scattering mechanism of the internal object considered. The modelling of each approach and subsequent analytical and practical tests are discussed in separate chapters of this thesis.

## 1.7 Thesis summary

Three main cases are studied. One is to solve the forward and inverse problems of a one-dimensional multi-layered plane wave reflection model. The other two cases consider the internal object as cylindrically and spherically-shaped scatterers and solve the associated two-dimensional and three-dimensional forward problems in cylindrical and spherical coordinates, respectively. In each case, the subsequent inverse problems are solved to compute the unknowns.

In the second chapter, the one-dimensional approach is explained using a model for plane wave propagation. Simple canonical geometries are used initially in order to illustrate the general approach. The one-dimensional study is straightforward but helps the understanding of the practical difficulties with accuracy when working with plane wave measurements. This study is important because the computed results of the forward and inverse algorithms provide an insight into the subsequent two-dimensional and three-dimensional cases. Further, some of the equations developed in this chapter are required in the subsequent chapters. Newton's iterative method is used for computing the unknowns and this method is outlined in this chapter.

The third chapter solves the two-dimensional scattering problem of a cylindrically-shaped scatterer. This study is performed by modelling the host with an internal object in a cylindrical coordinate system. The forward problem of microwave scattering is solved using the Helmholtz equation and the field equations are obtained from the cylindrical wave functions. The forward equations are obtained for both plane and cylindrical waves and subsequently, these solutions are modified for the case of a non-conducting cylinder. Then, the inverse problem of finding the un-

knowns is discussed in detail using the calculated results of the forward equations. The simulated results in each case are presented in a separate section in this chapter.

A more realistic study is discussed in the fourth chapter using a spherical coordinate system. The host is modelled using a spherically-shaped object as a wave scatterer. Here, a three-dimensional coordinate system is used to develop a solution to this scattering problem. The solutions for both the forward and reflected waves are found using constructed solutions based on spherical wave functions. Firstly, the scattering problems of both plane and cylindrical waves are solved by considering the internal object to be a perfectly conducting sphere. Then, the same study is carried out using a dielectric sphere. Subsequently, an inverse method is developed to find the unknown shape and location of the scatterer. This algorithm is tested using a number of simulations.

In Chapter 5, the asymptotic conditions of the forward and inverse algorithms are studied for different situations. The field received at the measuring point is studied in detail with respect to the variables associated with the scattering object such as its radius and the distance of the object from the antenna. Using the data generated from the forward equations, the robustness of the inverse method with respect to the initial guess values is further studied. Also, using this data, the stability of calculating the unknowns in the presence of errors in the measured data is investigated. In order to use the algorithms for computing the unknowns, a scanning method is developed in this chapter. This is useful in practical applications as the information available for the unknown object is limited in many cases.

A laboratory experiment was conducted to test the mathematical solutions. In Chapter 6 this experiment and the results are discussed in detail. Here, the measured data is used to test for agreement with the data generated analytically from the corresponding forward equations. In this chapter, the effects of the other reflections when measuring the reflection coefficient of the scattering object are discussed.

These results and the subsequent analysis of the measured data for both the cylinder and the sphere are discussed in this chapter.

Chapter 7 presents the calculated results for the unknowns using the measured data. In order to construct the general equations, the previous solutions were incorporated with an experimental model to obtain the corresponding forward equations. Then, the calculated and measured data were compared. Finally, the inverse algorithm incorporated with the scanning method was used to find the unknowns using the measured data of the conducting cylinder and these results are compared with the actual values. The difference in the reflections from plane and cylindrical waves using both calculated and measured results are discussed.

Finally, the conclusions with an overall discussion including possible future work are given in Chapter 8 of this thesis.

# Chapter 2

# Plane wave reflection

A microwave reflection problem of a plane wave incident upon a number of plane boundaries is considered in this chapter. The purpose here is to illustrate the method in an idealised one-dimensional geometry. The forward problem is analysed using fundamental wave theory (see Harrington [8] and Ramo *et al.* [99]). The subsequent inverse problem is solved to calculate the unknown distances to the reflecting layers from the measurement plane and therefore to determine the thicknesses of the layers.

## 2.1 Reflection from plane boundaries

### 2.1.1 Wave solutions

In electromagnetic wave theory the time-varying field vectors can be mathematically analysed using complex-valued functions of the electric and magnetic wave components [97, 98, 14, 10]. As the fields are often considered to have sinusoidal time variations, a time variation of the form $e^{j\omega t}$ can be assumed. Then, in a source-free, linear, isotropic and homogeneous region the electric and magnetic field vectors ($\mathbf{E}$ and $\mathbf{H}$, respectively) can be expressed using Maxwell's equations which can be

written as

$$\begin{aligned} \nabla \times \mathbf{E} &= -\hat{z}(\omega)\mathbf{H}, \\ \nabla \times \mathbf{H} &= \hat{y}(\omega)\mathbf{E}, \end{aligned} \tag{2.1}$$

where $\hat{z}(\omega)$ and $\hat{y}(\omega)$ are complex valued functions which specify the electromagnetic characteristics of the medium. Specifically,

$$\begin{aligned} \hat{z} &= j\omega\hat{\mu}, \\ \hat{y} &= \sigma + j\omega\hat{\varepsilon}, \end{aligned} \tag{2.2}$$

where $j = \sqrt{-1}$, $\omega = 2\pi f$, $\sigma$ is the conductivity, $\hat{\varepsilon}$ is the complex permittivity and $\hat{\mu}$ is the complex permeability of the medium as explained in section 1.2. Here, the region is considered to be linear, that is $\hat{z}$ and $\hat{y}$ are independent of $|\mathbf{E}|$ and $|\mathbf{H}|$; homogeneous, that is $\hat{z}$ and $\hat{y}$ are independent of position; and isotropic, that is $\hat{z}$ and $\hat{y}$ are scalars.

The two equations in (2.1) determine the complex fields $\mathbf{E}$ and $\mathbf{H}$, where $\mathbf{E}$ is the complex electric field intensity (volts per metre) and $\mathbf{H}$ is the complex magnetic field intensity (amperes per metre). Using equation (2.1) the complex vectors $\mathbf{E}$ and $\mathbf{H}$ satisfy

$$\begin{aligned} \nabla \times (\nabla \times \mathbf{E}) - k^2\mathbf{E} &= \mathbf{0}, \\ \nabla \times (\nabla \times \mathbf{H}) - k^2\mathbf{H} &= \mathbf{0}, \end{aligned} \tag{2.3}$$

where $k$ is the wave number for the propagating medium and is defined using equation (2.2) as $k = \sqrt{-\hat{y}\,\hat{z}}$.

Using the vector identity $\nabla \times (\nabla \times \mathbf{A}) = \nabla(\nabla \cdot \mathbf{A}) - \nabla^2\mathbf{A}$ and the fact that $\mathbf{E}$ and $\mathbf{H}$ are both divergence-free, we obtain

$$\begin{aligned} \nabla^2\mathbf{E} + k^2\mathbf{E} &= \mathbf{0}, \\ \nabla^2\mathbf{H} + k^2\mathbf{H} &= \mathbf{0}\,. \end{aligned} \tag{2.4}$$

The rectangular components of $\mathbf{E}$ and $\mathbf{H}$ in equation (2.4) therefore satisfy the

Helmholtz equation

$$\nabla^2\psi + k^2\psi = 0\,. \tag{2.5}$$

Here, the symbol $\psi$ is used to denote the wave functions, that is solutions to equation (2.5), and $\nabla^2$ is the Laplacian operator. For a *perfect dielectric medium*, $\hat{y} = j\omega\epsilon$ and $\hat{z} = j\omega\mu$ (where $\mu$ and $\epsilon$ are real) and so

$$k = \omega\sqrt{\mu\varepsilon}. \tag{2.6}$$

If $\mathbf{E}$ only has an $x$-component independent of $x$ and $y$, so that $\mathbf{E} = (E_x(z), 0, 0)$, then the first equation of (2.4) reduces to

$$\frac{d^2E_x}{dz^2} + k^2E_x = 0\,. \tag{2.7}$$

From this equation, two independent solutions to the $x$-component of the electric field vector $\mathbf{E}$ can be found and

$$E_x(z) = E^+e^{-jkz} + E^-e^{jkz}, \tag{2.8}$$

where $E^+$ and $E^-$ are arbitrary constants. The first and second terms of the right hand side of equation (2.8) represent the electric fields of travelling waves in the positive and negative $z$ directions, respectively. Similarly, the $y$-component of the magnetic field vector $\mathbf{H} = (0, H_y(z), 0)$, can be found using the curl equation (2.1) and equation (2.8) as

$$H_y(z) = \frac{1}{\eta}[E^+e^{-jkz} - E^-e^{jkz}], \tag{2.9}$$

where $\eta$ is the wave impedance of the plane wave, and is defined as

$$\eta = \sqrt{\frac{\mu}{\varepsilon}}\ \cdot \tag{2.10}$$

For uniform plane waves, this impedance is also taken as the intrinsic impedance of the medium [7]. In free space, $\eta = 377\,\Omega$. The electric and magnetic vectors are orthogonal to each other and also orthogonal to $z$, the direction of propagation, and therefore this type of wave is called a transverse electromagnetic (TEM) wave.

For a lossy medium, the plane waves are affected by the conductivity of the medium and, therefore, with the wave number found using equation (2.2), the first equation of (2.4) can be written as

$$\nabla^2\mathbf{E} + \omega^2\mu\varepsilon(1 - \frac{j\sigma}{\omega\varepsilon})\mathbf{E} = 0\,. \tag{2.11}$$

Thus, for a lossy medium the $x$-component, when it is independent of $x$ and $y$, satisfies in this case

$$\frac{d^2E_x}{dz^2} - \gamma^2 E_x = 0\,, \tag{2.12}$$

where $\gamma$ is the propagation constant defined as

$$\gamma = \alpha + j\beta = j\omega\sqrt{\mu\varepsilon}\sqrt{1 - j\frac{\sigma}{\omega\varepsilon}}\,. \tag{2.13}$$

Here, $\alpha$ (the attenuation constant) and $\beta$ (the phase constant) determine the magnitude and phase changes of the travelling wave, respectively. From equation (2.13)

$$\alpha = \omega\sqrt{\left(\frac{\mu\varepsilon}{2}\right)\left[\sqrt{1 + \left(\frac{\sigma}{\omega\varepsilon}\right)^2} - 1\right]}, \quad \beta = \omega\sqrt{\left(\frac{\mu\varepsilon}{2}\right)\left[\sqrt{1 + \left(\frac{\sigma}{\omega\varepsilon}\right)^2} + 1\right]}. \tag{2.14}$$

Note that in the lossless case (the perfect dielectric case with $\sigma = 0$), $\gamma = j\beta = jk = j\omega\sqrt{\mu\epsilon}$.

With equation (2.13), the solution to equation (2.12) is found to be

$$E_x(z) = E^+e^{-\gamma z} + E^-e^{\gamma z}\,. \tag{2.15}$$

Equation (2.15) represents the $x$-component of $\mathbf{E}$ field to the $z$ direction. Similarly, using equation (2.9), the $y$-component of $\mathbf{H}$ field to the $z$ direction is found to be

$$H_y(z) = \frac{1}{\eta}(E^+e^{-\gamma z} - E^-e^{\gamma z})\,, \tag{2.16}$$

where

$$\eta = \sqrt{\frac{\mu}{\varepsilon}}\left(\frac{1}{\sqrt{1 - \frac{j\sigma}{\omega\varepsilon}}}\right)\,. \tag{2.17}$$

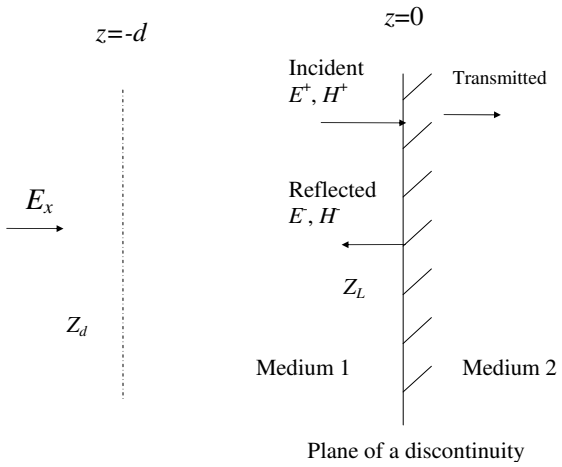


Figure 2.1: Reflection from a plane of discontinuity

The expression in (2.17) is the intrinsic impedance which is complex in the lossy medium. The first and second terms on the right hand side of equations (2.15) and (2.16) represent the electric and magnetic waves travelling in the positive and negative $z$ directions, respectively, within a lossy medium.

### 2.1.2 Plane of discontinuity

Figure 2.1 shows the reflection of a plane wave when it is normally incident upon a plane boundary. Assume the medium 1 to be homogeneous. Consider the origin of a coordinate system at $z$=0, on which there is a discontinuity of the field. Propagation of a plane wave, and its reflection from such a boundary of discontinuity in electrical properties, are analogous to voltage and current variation along a transmission line [99]. Therefore, the ratio of electric to magnetic fields in the wave analysis can be considered to be analogous to the ratio of voltage to current which is called the

impedance in transmission-line analysis.

Consider the electric field of the incident wave to be along the $x$ direction and the wave to be travelling in the $z$ direction. If this wave is incident upon a perfectly conducting plane boundary, it will be reflected fully from the boundary. Therefore there will be no transmitted wave in medium 2. Then the load impedance at the $z$ = 0 plane can be found using equations (2.15) and (2.16) as

$$Z_L = \frac{E_x(0)}{H_y(0)} = \frac{\eta\left(1+\frac{E^-}{E^+}\right)}{\left(1-\frac{E^-}{E^+}\right)}\,. \tag{2.18}$$

From equation (2.18),

$$\frac{E^-}{E^+} = \frac{Z_L-\eta}{Z_L+\eta}\,. \tag{2.19}$$

The ratio $\frac{E^-}{E^+}$ found in equation (2.19) is the reflection coefficient of the dielectric medium of intrinsic impedance $\eta$ when the wave is terminated at the load impedance $Z_L$. Now, a solution for the input impedance at a distance $d$ (for $z$=-$d$) from the $z = 0$ plane can be found using equations (2.15) and (2.16) as,

$$Z_i = \frac{E_x(-d)}{H_y(-d)} = \left.\frac{\eta(E^+e^{-\gamma z}+E^-e^{\gamma z})}{E^+e^{-\gamma z}-E^-e^{\gamma z}}\right|_{z=-d}\,. \tag{2.20}$$

By substituting the reflection coefficient found in equation (2.19) into equation (2.20) and further simplifying we obtain

$$Z_i = \frac{E_x(-d)}{H_y(-d)} = \frac{\eta\left(Z_L\cosh(\gamma d)+\eta\sinh(\gamma d)\right)}{\eta\cosh(\gamma d)+Z_L\sinh(\gamma d)} = \frac{\eta\left(Z_L+\eta\tanh(\gamma d)\right)}{\eta+Z_L\tanh(\gamma d)}\,. \tag{2.21}$$

For a loss-free medium, the attenuation constant in equation (2.13) can be assumed to be equal to zero and therefore,

$$\gamma = j\beta\,,\ \beta = \omega\sqrt{\mu\epsilon}. \tag{2.22}$$

Thus, the impedance of a loss-free medium at a distance $d$ from the reflecting boundary can be found using equations (2.21) and (2.22) as

$$Z_i = \frac{\eta\left(Z_L+j\eta\tan(\beta d)\right)}{\eta+jZ_L\tan(\beta d)}\,, \tag{2.23}$$

since $\tanh(j\theta) = j\tan\theta$.

The impedance $Z_L$ in equation (2.23) is the load impedance at $z$=0. When a wave travelling in medium 1 is normally incident upon a plane boundary with medium 2, which has different dielectric properties, the corresponding impedance at distance $d$ from the boundary can be found to be

$$Z_1 = \eta_1 \left( \frac{Z_2 + j\eta_1 \tan(\beta d)}{\eta_1 + jZ_2 \tan(\beta d)} \right), \tag{2.24}$$

where $Z_2$ is the impedance at the front face of the reflecting boundary in medium 2 and $\eta_1$ is the intrinsic impedance of medium 1.

## 2.2 Modelling for plane wave reflection

When the antenna, which is on the surface of the front layer, radiates the host with a microwave signal, the host will be filled with positively and negatively travelling waves. The behaviour of the field components of these waves can be analysed using the basic wave theory described in section 2.1. In a practical application, the reflection coefficients are calculated using the measured values of the forward and backward waves through the front-end antenna system. The reflection coefficient at the front surface of the model for any given profile may be found as

$$\Gamma(f) = \frac{Z_{in}(f) - Z_0}{Z_{in}(f) + Z_0}, \tag{2.25}$$

where $f$ represents the frequency of the microwave signal, $Z_{in}(f)$ is the complex electrical impedance into the surface of the host and $Z_0$ is the complex electrical impedance of the measurement system. In practice, the reflection coefficient $\Gamma(f)$ can be found by microwave measurements, whereas $Z_0$ can be found by a proper calibration method of the measurement system. This procedure has been explained in Keam *et al.* [91, 100].

The one-dimensional plane wave reflection model is shown in Figure 2.2. The internal structure of the host material is represented using a number of layers, each

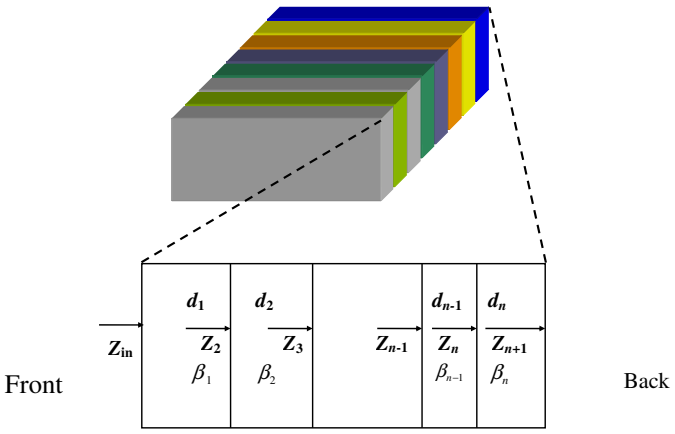


Figure 2.2: Plane wave reflection model. The host modelled with thin layers is shown at the top of the Figure. The detailed distribution of the layers is shown just below the host model.

of which is homogeneous. In particular, we assume that the electrical properties are constant throughout each of these layers. The layers inside the model are specified with individual material properties. These are the permittivity $\epsilon$, permeability $\mu$ and conductivity $\sigma$. In this study, the properties of the foreign object embedded in the host are assumed to be very different from those of the internal structure of the host.

The microwave signal applied from the front surface of the host penetrates through the layers and, if the properties of any two layers differ from each other, it reflects back from the boundary between them. In order to find the reflection from the surface of the host, it is necessary to perform a series of impedance transformations at the layer boundaries. The impedance transformation towards the front-end can be seen as a belt with $n$ cascaded strips, as shown in Figure 2.2.

The front-end impedances of the layers are indicated as $Z_{(.)}$ (looking from the

front) and the first and last layer impedances are taken as $Z_{in}$ and $Z_{n+1}$, respectively. Consider the host internal structure to be loss-free ($\sigma = 0$) for the electromagnetic waves. Therefore, from equation (2.13), the propagation constant $\gamma$ is purely imaginary. For simplicity, in the remainder of this discussion the magnetic permeability $\mu$ is assumed to be unity, but this is not a restriction for the application.

## 2.3 Forward problem for plane wave reflection

The forward problem is associated with the plane wave reflection from dielectric boundaries. The wave reflection depends upon the number of reflecting layers, layer thickness and their respective electrical properties. In practical applications, the impedance at the front-end $Z_{in}$ of the host may be known from the microwave measurements. Therefore this forward problem is solved by looking at the wave reflection from the impedance viewpoint considering changes of the impedance with respect to the dielectric properties through each of the reflecting layers in this model.

### 2.3.1 Layer impedance transformation

Consider any three layers with thickness of $d_{n-1}$, $d_n$ and $d_{n+1}$. The recursive equation to find the electrical impedance at the front of the $n^{th}$ layer of the model, that has a width of $d_n$, is found using equation (2.24)

$$Z_n(f) = \eta_n(f) \left( \frac{Z_{n+1}(f) + j\eta_n(f) \tan[\beta_n(f) d_n]}{\eta_n(f) + jZ_{n+1}(f) \tan[\beta_n(f) d_n]} \right) , \tag{2.26}$$

where $\eta_n(f)$ is the intrinsic impedance of the $n^{th}$ layer found using equation (2.10), with $\varepsilon = \varepsilon_r^{(n)} \varepsilon_0$ and $\mu = \mu_r \mu_0$,

$$\eta_n(f) = \frac{\eta_0}{\sqrt{\varepsilon_r^{(n)}}} . \tag{2.27}$$

where the constant $\eta_0 = \sqrt{\frac{\mu_0}{\epsilon_0}}$ is the intrinsic impedance of a vacuum (approximately equal to 377 Ohms), $\mu_0$ and $\epsilon_0$ are the permeability and permittivity of the free space

and $\varepsilon_r^{(n)}$ is the relative permittivity of the $n^{th}$ layer. We assume $\mu_r$, the relative permeability, is unity and $\sigma = 0$ for all layers. From equation (2.14) $\alpha = 0$ and $\beta_n(f)$, the phase constant of the $n^{th}$ layer, can be found from equation (2.13) as

$$\beta_n(f) = \frac{2\pi f\sqrt{\varepsilon_r^{(n)}(f)}}{c}\,. \tag{2.28}$$

Here, $c$ is the velocity of light (approximately $3 \times 10^8$ m/s) as given in equation (1.1) and $f$ is the frequency of the microwave signal. Equation (2.26) can be considered as the forward equation for the plane wave reflection. This can be used to solve the reflection problem of a multi-layered context.

Now consider the next layer, that is the layer to the front of the previous layer of the model. Similar to the $n^{th}$ layer, the front-impedance at the $(n-1)^{th}$ layer is

$$Z_{n-1}(f) = \eta_{n-1}(f)\left(\frac{Z_n(f) + j\eta_{n-1}(f)\tan[\beta_{n-1}(f)d_{n-1}]}{\eta_{n-1}(f) + jZ_n(f)\tan[\beta_{n-1}(f)d_{n-1}]}\right)\,. \tag{2.29}$$

The front-impedance of the $(n-1)^{th}$ layer can then be found by substituting $Z_n$ from equation (2.26) into equation (2.29). So, then

$$Z_{n-1}(f) =$$

$$\eta_{n-1}(f)\left(\frac{\begin{array}{c}(Z_{n+1}(f)\,[\eta_n(f) - \eta_{n-1}(f)\tan(\beta_n(f)d_n)\tan(\beta_{n-1}(f)d_{n-1})] \\ +\eta_n(f)j[\eta_n(f)\tan(\beta_n(f)d_n) + \eta_{n-1}(f)\tan(\beta_{n-1}(f)d_{n-1})])\end{array}}{\begin{array}{c}(Z_{n+1}(f)j[\eta_{n-1}(f)\tan(\beta_n(f)d_n) + \eta_n(f)\tan(\beta_{n-1}(f)d_{n-1})] \\ +\eta_n(f)[\eta_{n-1}(f) - \eta_n(f)\tan(\beta_n(f)d_n)\tan(\beta_{n-1}(f)d_{n-1})])\end{array}}\right). \tag{2.30}$$

Equation (2.30) calculates the front-impedance without explicitly finding the front-impedance $Z_n$ of the middle layer. Similarly, the front-impedance of the next layer in front (layer ($n$-2)) at frequency $f$ can be found using $Z_{n-1}$ in equation (2.30). This procedure can be continued up to the first layer to calculate the front-end impedance, $Z_{in}(f)$. The final equation using this process would be a large and complicated equation with a significant number of unknowns. However, it is possible

to obtain $i$ equations for $i$ different frequencies and these equations can be used to find $i$ unknowns.

## 2.4 Inverse algorithm for the plane wave reflection problem

The inverse algorithm is used to find unknowns related to the object inside the host with data from microwave measurements. When there is more than one unknown, it is not possible to obtain a solution using a single equation. This problem involves solving for multiple values of $d$ and $\beta$. Therefore, an algorithm based on Newton's iterative method [101] is used in view of its capability for fast convergence. Solving for more than one unknown is achieved by forming multiple equations using multiple frequencies. This section illustrates the procedure of this method by taking the thicknesses of two layers as the unknowns.

In order to find $n$ unknowns at least $n$ equations are needed. This is possible using equation (2.29) with $n$ frequencies. Since $\beta = 2\pi f\sqrt{\mu\epsilon}$, one can choose the correct $\beta$ for each frequency.

First, the general equation is formed using the solution to the forward problem and the front-impedance which is assumed to be available from the measurement results. This can be achieved by subtracting the right hand side of the forward equation (equation (2.30), when there are three layers) from the measured value of the front impedance. However, in the analytical study, the front-impedance values are calculated from the forward equation in order to test the inverse algorithm.

Newton's method is a standard procedure. The routine of finding the inverse solutions is shown in Figure 2.3. What follows are the main steps of the inverse algorithm for our problem. If only the widths of the layers are considered to be the unknowns, the set of equations for $n$ unknowns is

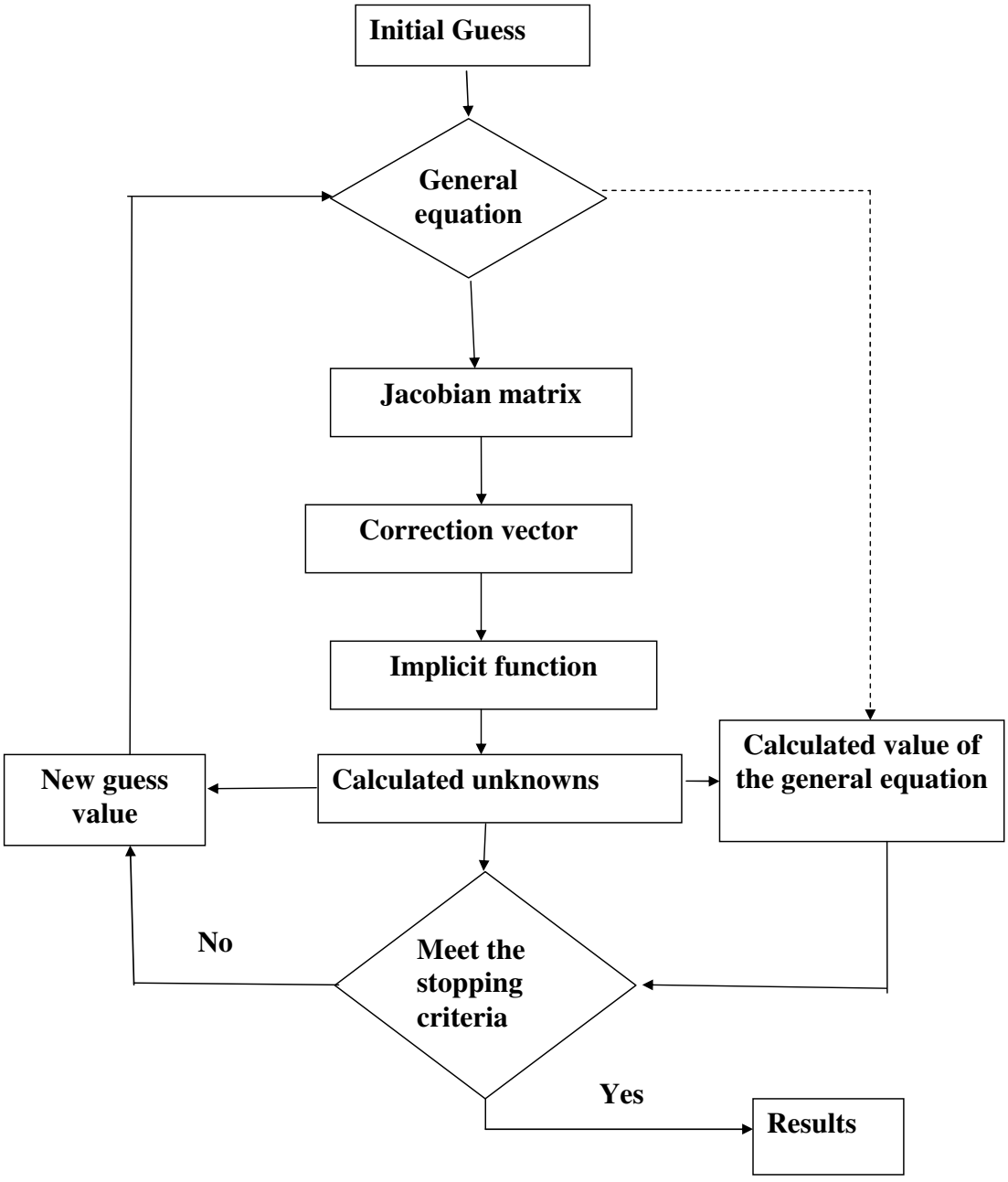


Figure 2.3: Inverse computing method for the calculation of unknowns.

$$\mathbf{F}(\mathbf{X}) = \begin{bmatrix} F_1(d_1, d_2, ...., d_n) \\ F_2(d_1, d_2, ...., d_n) \\ \vdots \\ F_n(d_1, d_2, ...., d_n) \end{bmatrix} = \begin{bmatrix} 0 \\ 0 \\ \vdots \\ 0 \end{bmatrix}, \quad \mathbf{X} = \begin{bmatrix} d_1 \\ . \\ . \\ d_n \end{bmatrix}. \tag{2.31}$$

The $n \times n$ Jacobian matrix of the above system of equations is

$$\mathbf{J} = [J_{k,l}], \tag{2.32}$$

where $J_{k,l} = \partial F_k / \partial d_l$ and $k$, $l = 1, 2, ...., n$. This is found explicitly by differentiating $\partial F_1/\partial d_1$, $\partial F_1/\partial d_2, ...\partial F_2/\partial d_1$, $\partial F_2/\partial d_2, ....\partial F_n/\partial d_n$, the values are shown later in Chapter 4.

The next iterate $\mathbf{X}^{(N+1)}$ is given by

$$\mathbf{X}^{(N+1)} = \mathbf{X}^{(N)} - \mathbf{J}(\mathbf{X}^{(N)})^{-1}\, \mathbf{F}(\mathbf{X}^{(N)}), \tag{2.33}$$

assuming $\mathbf{J}$ is non-singular [67, 101, 102].

A code written in MATLAB is used to run the iteration process for this algorithm. Using the initial guess for $\mathbf{X}^{(0)} = ({d_1}^0, {d_2}^0, ., {d_n}^0)^T$, we carry out the iterations to search for the solution to $\mathbf{F}(\mathbf{X}) = \mathbf{0}$. The solution of the above system often needs several iterations, the number of iterations is dependent mainly upon the number of unknowns and the value of the initial guess. The above procedure is repeated until the vector $\mathbf{X}^{(N)}$ satisfies some suitable stopping criterion, of $\mathbf{X}$ as a solution of $\mathbf{F}(\mathbf{X}) = \mathbf{0}$. A more detailed discussion on this method using a simple example is given below.

Consider the host to have three layers: the thicknesses $d_1, d_2$ are the unknowns. Take a simple case. Assume the front-impedance of the third layer is equal to zero, so that $Z_{n+1} = 0$ when $n = 2$ in this case. Then using equation (2.30), a general

equation is obtained as

$$j[\eta_1(f_i)]^2 \tan[\beta_1(f_i)d_1] + Z_1(f_i)\eta_2(f_i)\tan[\beta_1(f_i)d_1]\tan[\beta_2(f_i)d_2] \\ -Z_1(f_i)\eta_1(f_i) + j\eta_1(f_i)\eta_2(f_i)\tan[\beta_2(f_i)d_2] = 0\,, \tag{2.34}$$

where $f_i$ is the microwave frequency applied at each measurement, and $i$=1,2. The intrinsic impedance $\eta$ and phase constant $\beta$ of each layer at the measuring frequency can be found by knowing the properties of the layers. Assume the properties of the layers are known. Then, there are two unknowns, $d_1$ and $d_2$, in equation (2.34) and the corresponding two equations are of the form

$$\mathbf{F}(\mathbf{X}) = \begin{bmatrix} F_1(d_1, d_2) \\ F_2(d_1, d_2) \end{bmatrix} = \begin{bmatrix} 0 \\ 0 \end{bmatrix}. \tag{2.35}$$

Equation (2.35) in full with two general equations is,

$$\begin{bmatrix} F_1(d_1, d_2) \\ F_2(d_1, d_2) \end{bmatrix} =$$

$$\begin{bmatrix} j[\eta_1(f_1)]^2 \tan[\beta_1(f_1)d_1] + Z_1(f_1)\eta_2(f_1)\tan[\beta_1(f_1)d_1]tan[\beta_2(f_1)d_2] \\ -Z_1(f_1)\eta_1(f_1) + j\eta_1(f_1)\eta_2(f_1)\tan[\beta_2(f_1)d_2] \\ \\ j[\eta_1(f_2)]^2 \tan[\beta_1(f_2)d_1] + Z_1(f_2)\eta_2(f_2)\tan[\beta_1(f_2)d_1]tan[\beta_2(f_2)d_2] \\ -Z_1(f_2)\eta_1(f_2) + j\eta_1(f_2)\eta_2(f_2)\tan[\beta_2(f_2)d_2] \end{bmatrix} = \begin{bmatrix} 0 \\ \\ \\ 0 \end{bmatrix}. \tag{2.36}$$

There are in just four equations here if we considered the equations separately with their respective real and imaginary parts being zero. We do not take advantage of this possibility here and later, but acknowledge we could have done so. In practice we solve for complex values of $d_i, i = 1, 2$ but accept only values for which the imaginary part is very close to zero.

As before, the subscripts of $\eta$, $\beta$ and $Z$ represent the layer number. The algorithm starts with selecting the initial guess values $d_1^{(0)}, d_2^{(0)}$. These values are substituted

for $d_1$ and $d_2$ in equation(2.36). Next, the vector $\mathbf{X}^{(0)}$ is formed with the set of initial guess values,

$$\mathbf{X}^{(0)} = \begin{bmatrix} d_1^{(0)} \\ d_2^{(0)} \end{bmatrix}. \tag{2.37}$$

Then the Jacobian matrix is found with these guess values according to

$$\mathbf{J}(\mathbf{X}^{(0)}) = \begin{bmatrix} \frac{\partial F_1(d_1^{(0)}, d_2^{(0)})}{\partial d_1\,(0)} & \frac{\partial F_1(d_1^{(0)}, d_2^{(0)})}{\partial d_2^{(0)}} \\ \frac{\partial F_2(d_1^{(0)}, d_2^{(0)})}{\partial d_1^{(0)}} & \frac{\partial F_2(d_1^{(0)}, d_2^{(0)})}{\partial d_2^{(0)}} \end{bmatrix}. \tag{2.38}$$

$$\mathbf{J}^{-1}\mathbf{F}(\mathbf{X}) = \mathbf{J}^{-1} \begin{bmatrix} j[\eta_1(f_1)]^2 \tan[\beta_1(f_1)d_1] + Z_1(f_1)\eta_2(f_1)\tan[\beta_1(f_1)d_1]tan[\beta_2(f_1)d_2] \\ -Z_1(f_1)\eta_1(f_1) + j\eta_1(f_1)\eta_2(f_1)\tan[\beta_2(f_1)d_2] \\ \\ j[\eta_1(f_2)]^2 \tan[\beta_1(f_2)d_1] + Z_1(f_2)\eta_2(f_2)\tan[\beta_1(f_2)d_1]tan[\beta_2(f_2)d_2] \\ -Z_1(f_2)\eta_1(f_2) + j\eta_1(f_2)\eta_2(f_2)\tan[\beta_2(f_2)d_2] \end{bmatrix}. \tag{2.39}$$

This calculates the new values for $d_1$ and $d_2$ in the vector $\mathbf{X}^{(1)} = \mathbf{X}^{(0)} - \mathbf{J}^{-1}(\mathbf{X}^{(0)})\mathbf{F}(\mathbf{X}^{(0)})$. Next, these calculated values are used as the new guess values and we repeat the same procedure. This process is continued until a suitable stopping criterion is met (such as, when the successive iteration values are sufficiently close). It is required that $\mathbf{F(X)}$ tends to zero, as well as the calculated values of the unknowns remain real and positive for a satisfactory result.

The selection of the guess values to form the initial vector $\mathbf{X}^{(0)}$ has to be made carefully as these values make a significant impact on the acceptable results of the process. A further analysis of this effect is carried out using the calculated values of the forward equation and these details are discussed in Chapter 5.

## 2.5 Results and discussion

There are two main results in this study: the calculated front impedance of the model using the forward equation and the calculated unknowns using the inverse algorithm. Computations to obtain these results have been performed using computer programs written in MATLAB.

### 2.5.1 Front-impedance

In order to find the effect of the front-impedance with respect to the electrical properties of the internal structure of the host, a simple test was carried out with the results in section 2.3.1. Using equation (2.26), the front-impedances of 10 layers were calculated recursively. Starting with the last layer $n = 10$, the calculations were carried out from layer to layer up to the first layer $Z_1 = Z_{in}$. The results of the calculations are shown in Figure 2.4. Two plots are shown: (1) the layers have identical properties (2) the last layer has different properties to all other layers (which remain identical to each other). At the end of the iterative process, the results show that there is a significant difference in the calculated value of front-impedance when the permittivity of the last layer is 50 rather than 10 as in the other layers. For simplicity, the scenario where only the permittivity differs significantly between the host and the foreign object is considered. However, using equation (2.13), the permittivity and permeability could both be included in the forward equation.

The high contrast observed in the front-impedance calculation provides promising results for microwave object detection. When the host contains a foreign object with a higher permittivity, a large value for the front-impedance in the microwave measurement can be expected compared to the value obtained from the host with no object inside.

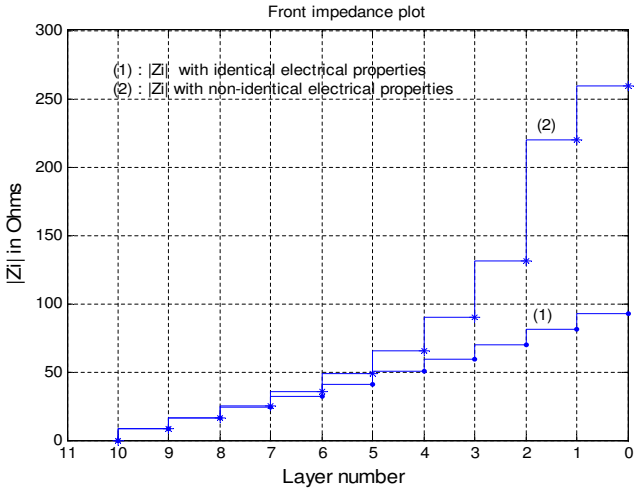


Figure 2.4: Plot of the layers' front-impedances.

### 2.5.2 Distance calculation

The thicknesses of two layers ($n$=2) within the reflection model have been calculated using the inverse method as discussed in section 2.4. In this analytical study, the front-impedances of the first layer were calculated using equation (2.26) for two different frequencies. The thickness of the second layer and of the first layer are taken to be 0.002 and 0.004 metres, respectively. Thus, from the values of $Z_1(f_i)$ at the two different frequencies, the values of $d_1$ and $d_2$ may be estimated. In a practical application, the $Z$'s are obtained by measurements and so the distance can be found without prior knowledge. Starting with a set of initial values ($d_1$=0.009 and $d_2$=0.01m), the estimation process was carried out to find the unknowns. The simulation results obtained using MATLAB are plotted in Figure 2.5. The two graphs show that the approximations to $d_1$ and $d_2$ in $F_1$ and $F_2$ rapidly approach the exact values of $d_1$=0.002 metres and $d_2$=0.004 metres.

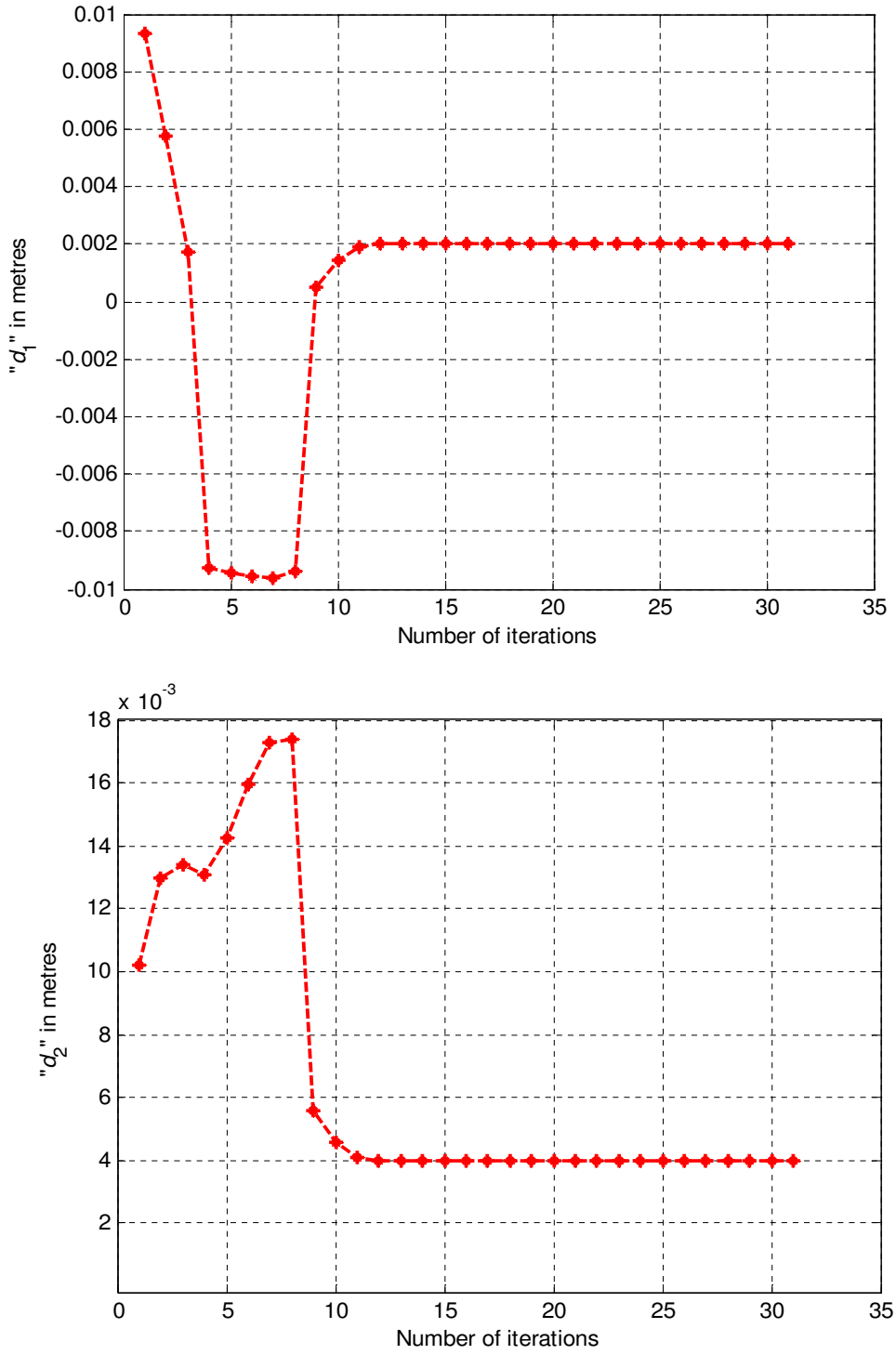


Figure 2.5: Computed results of layer thickness, $d_1$ and $d_2$ (which have imaginary part zero). Each plot shows the values of the calculated layer thicknesses of 32 iteration cycles.

When there are more layers in the host, the equation for the layer thickness calculation is more complicated. Once the forward equation is formed, calculating the individual thicknesses of the layers is only a matter of running a few iteration cycles using the inverse method. The test conducted using the inverse method has calculated only two unknowns but there is no restriction for finding other unknowns (such as permittivity of the layers) using the front-impedance. Again, this will need more general equations and these equations can be formed using a large range of frequencies.

The results achieved in this chapter provide useful insight before developing more complicated methods in the following chapters. In addition, the equations presented in this chapter will be used throughout the subsequent discussions in the chapters to come.

# Chapter 3

# The two-dimensional scattering problem

A microwave scattering problem of a cylindrically-shaped object is discussed in this chapter. The host is modelled with a foreign object through it, assumed to be a long circular cylinder, whose length is sufficiently large that it can be treated as infinite in the model. The microwaves scattered from the boundary of the cylinder consist of both electric and magnetic fields. These fields vary in both magnitude and phase with respect to the distances through which the waves propagate.

The application system is similar to that shown in Figure 1.3. There are two main cases:

(1). Firstly, the object inside the host is assumed to be a conducting circular cylinder to formulate and analyse the associated forward problem.

(2). Then, a non-conducting cylinder is considered so as to analyse the problem for a more realistic situation.

Both of these cases are solved for the scattering of plane waves as well as cylindrical waves. For the detection process, an inverse method is developed. We tested this method using data generated analytically and the results are discussed in this

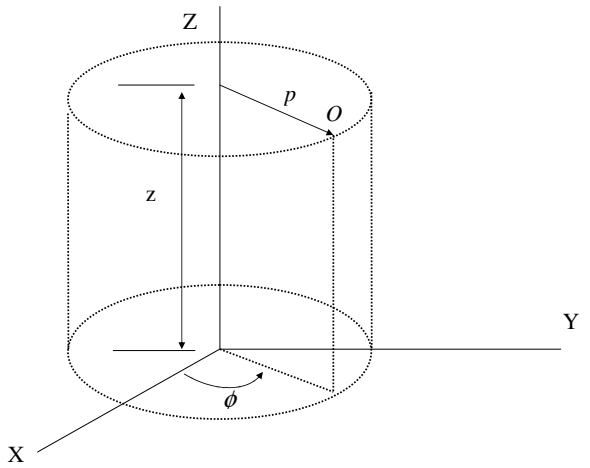


Figure 3.1: The circular cylindrical coordinate system.

chapter.

## 3.1 Wave functions at cylindrical boundaries

The field distribution in regions with boundaries having cylindrical surfaces can be mathematically expressed using a cylindrical coordinate system. In the literature, many solutions to this kind of scattering problems have been obtained using the scalar Helmholtz equation.

Figure 3.1 shows the coordinate system of a circular cylindrical object of radius $p$. Consider a point $O$ on the surface of the cylinder so that the line joining the origin to its projection on the plane z=0 has an angle $\phi$ with the $x$ axis. Equation (2.5) for this geometry can be written with the Laplacian expressed in cylindrical

coordinates and it is of the form [99]

$$\frac{1}{p}\frac{\partial}{\partial p}\left(p\frac{\partial \psi}{\partial p}\right)+\frac{1}{p^2}\frac{\partial^2 \psi}{\partial \phi^2}+\frac{\partial^2 \psi}{\partial z^2}+k^2\psi=0. \tag{3.1}$$

This equation is called the scalar Helmholtz equation in cylindrical coordinates. In order to solve equation (3.1) a method of "separation of variables" can be used similar to Harrington [8]. The solutions are assumed to be of the form,

$$\psi\left(p,\phi,z\right)=P(p)\Phi(\phi)Z(z). \tag{3.2}$$

Then equation (3.1) separates into three ordinary differential equations:

$$p\frac{d}{dp}\left(p\frac{dP}{dp}\right)+\left[(k_p p)^2-n^2\right]P=0 \tag{3.3}$$

$$\frac{d^2\Phi}{d\phi^2}+n^2\Phi=0 \tag{3.4}$$

$$\frac{d^2Z}{dz^2}+k_z^2 Z=0 \tag{3.5}$$

where $k_p$ is defined by

$$k_p^2=k^2-k_z^2 \tag{3.6}$$

and $k_z$ is a constant and $n$ is an integer. Equation (3.3) is Bessel's equation of order $n$ and equations (3.4) and (3.5) are harmonic equations. The solutions to these equations can be found as

$$P(p)=B_n(k_p p)\ ,\ \Phi(\phi)=e^{\pm jn\phi},\ \ Z(z)=e^{\pm jk_z z}. \tag{3.7}$$

The solutions in equation (3.7) are three elementary wave functions. The term $B_n(k_p p)$ is a solution to Bessel's equation of order $n$ ($n$ is an integer since $\Phi$ must be periodic in $\phi$ with period $2\pi$). This may take the forms: $J_n(k_p p)$ the Bessel function of first kind and $Y_n(k_p p)$ the Bessel function of second kind or $H_n^{(1)}(k_p p)$ the Hankel function of the first kind and $H_n^{(2)}(k_p p)$ the Hankel function of the second kind. More details on the Bessel functions are given in Appendix B. The other terms $e^{\pm jn\phi}$ and $e^{\pm jk_z z}$ are harmonic functions.

Now, a complete solution to Helmholtz's equation can be formed using equation (3.2). As the field has to be finite at $p = 0$ (see Figure 3.1), the wave solution is a linear combination of solutions of the form

$$\psi(p, \phi, z) = J_n(k_p p) e^{jn\phi} e^{jk_z z}. \tag{3.8}$$

Here, the function $J_n(k_p p)$ is selected because this is the only function which is finite at $p = 0$ (for positive, zero and negative integers $n$).

## 3.2 Plane wave scattering from a conducting cylinder

A block diagram of the application system is shown in Figure 3.2. The host is modelled with a circular conducting cylinder to represent the unknown internal object (see Figure 3.3). In this discussion, the wave incident upon the conducting cylinder is assumed to be a plane wave. The antenna is connected to the measuring system (see Figure 3.2) where the reflection coefficient is calculated using the forward and backward signals at the antenna. In practical applications, in order to find the location of the object, there should be a number of antenna positions in the array. This study is carried out with only one antenna in an idealised situation, that is, the antenna is assumed to be perfectly aligned with the object inside the host material. In a practical application the distances to the centre of the object from each individual antenna may be calculated with the data obtained from the microwave measurements. Then, using the geometry of the situation, the exact location of the object can be found. However, when obtaining microwave measurements, each antenna must be properly aligned with the target object, that is, at the position where the maximum response from the scattering object is received at the measuring instrument. This is a requirement of this model and a limitation of the

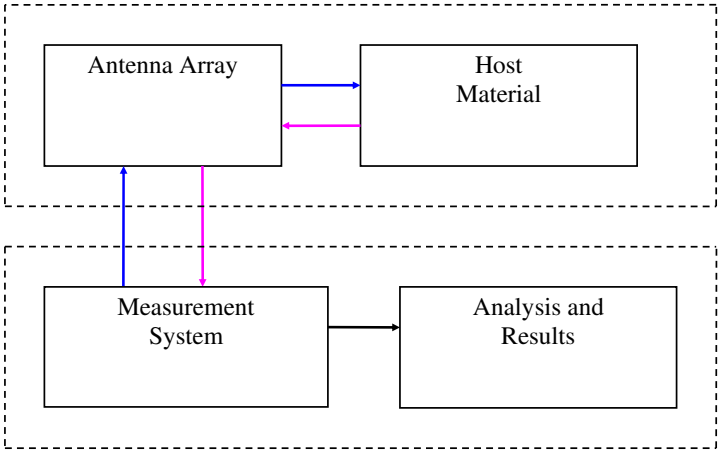


Figure 3.2: Block diagram of the application system.

approach taken here. The scattered fields are calculated for the study in this section but the measured results are used in subsequent investigations and these details are discussed in Chapters 7 and 8.

### 3.2.1 Forward problem of plane wave scattering

The cylindrical coordinate system of the two-dimensional model is shown in Figure 3.3. The circle inside the model is the conducting cylinder ($C$ is the centre) representing the unknown object. The $z$-axis of the cylindrical coordinate system is not shown but it is perpendicular to the $xy$-plane out of the page. The coordinate orientation is similar to that in Figure 3.1 but here, the point $O$ is outside the cylinder. The wall shown in the model represents a reflecting plane behind the object. The effect of the backreflection from this plane is considered later in this thesis.

Consider a uniform plane wave incident upon the conducting cylinder: assume

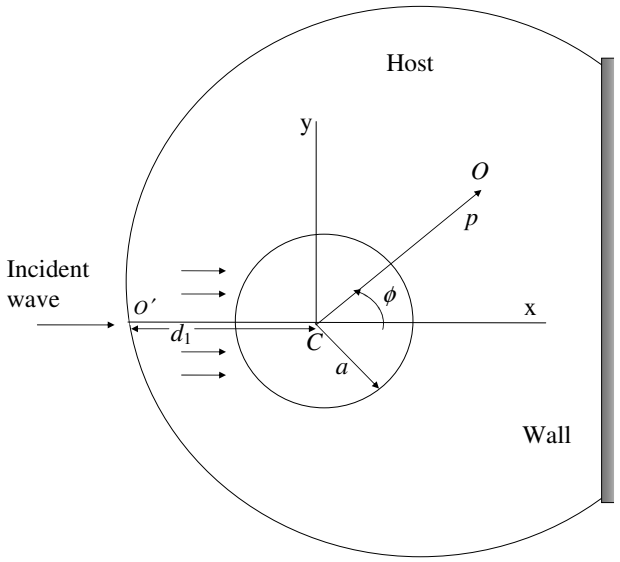


Figure 3.3: Plane wave reflection model with the cylindrical coordinate system.

the wave to be $z$-polarized so that the electric fields are parallel to the $z$-axis and travelling in the $x$-direction towards the cylinder. This means $\mathbf{E} = (0, 0, E_z(x, y))$ is independent of $z$ and $k_p = k$. Then, using equation (2.8), for the incident plane wave of frequency $f_1$,

$$E^i_{1,z}(p, \phi) = E_0 e^{-jk_1 x} = E_0 e^{-jk_1 p \cos\phi}, \tag{3.9}$$

where $k = k_1$ is the wave number of the medium outside the cylinder given by

$$k_1 = 2\pi f_1 \sqrt{\mu_1 \varepsilon_1}\,, \tag{3.10}$$

where $\varepsilon_1$ and $\mu_1$ are the permittivity and permeability of the medium.

Consider the coordinate system in Figure 3.3. This wave has a finite value $E_0$ at $C$, the centre of the cylinder, and it is periodic in $\phi$ with period $2\pi$. As the wave is incident upon a cylindrical boundary, we first express this in terms of a wave function in cylindrical coordinates [8]. This can be obtained using the elementary

wave functions as given in equation (3.7). Consider the singularity condition of the wave at the point $C$. That is for the wave to be finite at $C$, the $B_n(k_p p)$ in equation (3.7) should be $J_n(k_p p)$ (only these functions are finite at $p = 0$). Therefore, the solution for the field of the incident wave at the point $O$ can be expressed using the infinite series of the elementary wave functions of the form

$$E_0 e^{-jk_1 p\cos\phi} = E_0 \sum_{n=-\infty}^{\infty} u_n J_n(k_1 p) e^{jn\phi}\,, \tag{3.11}$$

where the $u_n$ are constants and can be evaluated as

$$u_n = j^{-n}\,. \tag{3.12}$$

(See Appendix C for details.) Thus, for the incident field

$$E^i_{1,z}(p,\phi) = E_0 \sum_{n=-\infty}^{\infty} j^{-n} J_n(k_1 p) e^{jn\phi}. \tag{3.13}$$

The wave which is incident upon the perfectly conducting cylinder will be completely scattered away from its boundary. Thus, the scattered wave field must be composed of the $H^{(2)}_n(k_1 p)$ as these are the only Hankel functions which tend to zero at infinity (see Appendix B). Therefore, the field of the outward travelling wave due to the scattering at the cylinder boundary is

$$E^s_{1,z}(p,\phi) = E_0 \sum_{n=-\infty}^{\infty} j^{-n} a_n H^{(2)}_n(k_1 p)\, e^{jn\phi}\,, \tag{3.14}$$

where the $a_n$'s are constant. The total field at point $O$ is the sum of the incident and scattered field, that is

$$E_{1,z} = E^i_{1,z} + E^s_{1,z}\ . \tag{3.15}$$

Using equations (3.13) and (3.14), equation (3.15) can be written as

$$E_{1,z}(p,\phi) = E_0 \sum_{n=-\infty}^{\infty} j^{-n} \left[J_n(k_1 p) + a_n H^{(2)}_n(k_1 p)\right] e^{jn\phi}\ . \tag{3.16}$$

The constants $a_n$ can be found by considering the boundary conditions on the scattering object. On the boundary of the conducting cylinder the resultant field

should equal zero, that is, $E_{1,z} = 0$ at $p = a$. Therefore, from equation (3.16), the constants $a_n$ can be found as

$$a_n = -\frac{J_n(k_1 a)}{H_n^{(2)}(k_1 a)} \,. \tag{3.17}$$

Using equation (3.17) the total field at point $O$ is therefore

$$E_{1,z}(p,\phi) = E_0 \sum_{n=-\infty}^{\infty} j^{-n} \left[ J_n(k_1 p) - \frac{J_n(k_1 a)}{H_n^{(2)}(k_1 a)} H_n^{(2)}(k_1 p) \right] e^{jn\phi} \,. \tag{3.18}$$

Suppose the point $O$ is rotated to $O'$ so that $\phi = \pi$. Then it will lie along the $x$-axis. As discussed earlier, this is the ideal situation such that the antenna is properly aligned with the scattering object (to receive the maximum response from the scattering object). Accordingly, the distance $p$ becomes $d_1$ which is the distance to the centre of the cylinder from the antenna point. (From here onward, $d_1$ is used to represent the distance between the centre of the cylinder and the antenna.) The new equation is

$$E_{1,z}(d_1,\pi) = E_0 \sum_{n=-\infty}^{\infty} j^{n} \left[ J_n(k_1 d_1) - \frac{J_n(k_1 a)}{H_n^{(2)}(k_1 a)} H_n^{(2)}(k_1 d_1) \right] . \tag{3.19}$$

This solution is applicable when a single antenna is used for both transmission and receiving the microwave signal. However, equation (3.18) gives a more general solution which can be used when the received field is measured from a different location using a separate antenna.

The computational cost can be reduced by combining terms with positive and negative values of $n$. Using the identities of the Bessel function of first kind and the Bessel function of second kind (Appendix B);

$$J_{-n}(z) = (-1)^n J_n(z) \,,\; Y_{-n}(z) = (-1)^n Y_n(z) \,,\; H_n^{(2)}(z) = J_n(z) - jY_n(z) \,, \tag{3.20}$$

equation (3.19) can be written as

$$E_{1,z}(d_1,\pi) =$$

$$E_0 \left[ J_0(k_1 d_1) - \tfrac{J_0(k_1 a)}{H_0^{(2)}(k_1 a)} H_0^{(2)}(k_1 d_1) \right] + E_0 \sum_{n=1}^{\infty} \left[ J_n(k_1 d_1) - \tfrac{J_n(k_1 a)}{H_n^{(2)}(k_1 a)} H_n^{(2)}(k_1 d_1) \right] 2j^n \,. \tag{3.21}$$

Equation (3.21) is the field equation for the antenna position one with frequency $f_1$ and this can be used to find the unknowns using the inverse algorithm. In the forward problem, if $a$, $d_1$ and the properties of the medium are known, the field components $E_{i,z}$ for different frequencies $f_i$ can be numerically calculated using equation (3.21). In a practical application, $E_{i,z}$ can be found using the reflection coefficient measurements. The procedure for obtaining microwave measurements is explained in section 6.2.

### 3.2.2 Inverse problem of plane wave scattering

The inverse problem is to find unknowns using the information embedded in the data obtained from microwave measurement. A method for constructing a suitable algorithm to solve this inverse problem is discussed in this section.

#### 3.2.2.1 The general equation

The general equation may be formed from the difference of the field vectors obtained by subtracting the calculated field component from the measured electrical fields. Figure 3.4 shows the procedure for forming the general equation. For simplicity, the electrical properties of the host are assumed to be known in this study. There is no restriction to prevent taking these properties as unknowns although the subsequent construction is complicated and requires more data obtained with additional frequencies. In this study we aim to find the two unknowns, the cylinder radius $a$ and its distance $d_1$ from the surface of the host (measured towards the centre of the cylinder). As discussed in section 2.4, at least two frequencies are needed to find these two unknowns. For antenna position 1, the general equation is of the form

$$\mathbf{F} = \Delta\mathbf{E} = \begin{bmatrix} \Delta E_{1,z}(a, d_1) \\ \\ \Delta E_{2,z}(a, d_1) \end{bmatrix} = \begin{bmatrix} 0 \\ \\ 0 \end{bmatrix}, \tag{3.22}$$

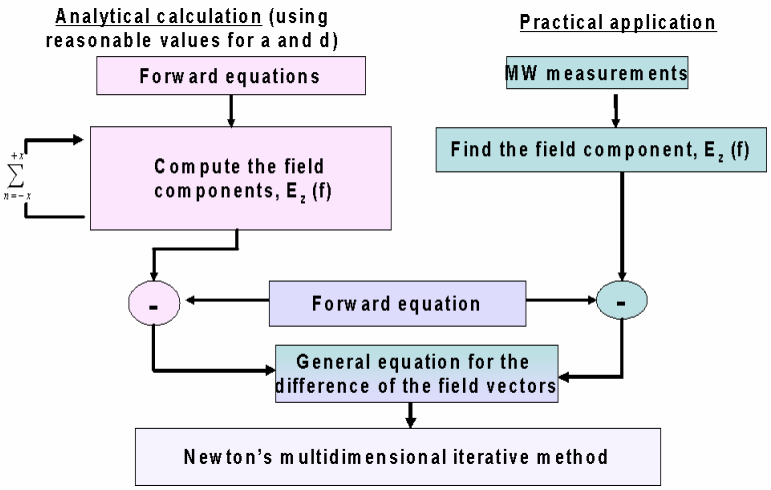


Figure 3.4: Procedure for both analytical study and practical application.

where we now use the subscripts 1 and 2 of $E_z$ to indicate the two different frequencies. Using equation (3.21), for antenna one position the general equation to find the two unknowns $a$ and $d_1$ is

$$\begin{bmatrix} E_1 - E_0 \sum_{n=1}^{\infty} \left[ J_n(k_{1,1}d_1) - \frac{J_n(k_{1,1}\,a)}{H_n^{(2)}(k_{1,1}\,a)} H_n^{(2)}(k_{1,1}d_1) \right] 2j^n \\ \qquad -E_0 \left[ J_0(k_{1,1}d_1) - \frac{J_0(k_{1,1}\,a)}{H_0^{(2)}(k_{1,1}a)} H_0^{(2)}(k_{1,1}d_1) \right] \\ E_2 - E_0 \sum_{n=1}^{\infty} \left[ J_n(k_{1,2}d_1) - \frac{J_n(k_{1,2}a)}{H_n^{(2)}(k_{1,2}\,a)} H_n^{(2)}(k_{1,2}d_1) \right] 2j^n \\ \qquad -E_0 \left[ J_0(k_{1,2}d_1) - \frac{J_0(k_{1,2}\,a)}{H_0^{(2)}(k_{1,2}\,a)} H_0^{(2)}(k_{1,2}d_1) \right] \end{bmatrix} = \begin{bmatrix} 0 \\ \\ \\ \\ 0 \end{bmatrix} \tag{3.23}$$

where $E_1$ and $E_2$, for frequency $f_1$ and $f_2$, respectively, are either measured values or calculated field components and $k_{1,1}$ and $k_{1,2}$ are the wave numbers at the two different frequencies which can be found as

$$k_{1,1} = 2\pi f_1 \sqrt{\mu_1 \varepsilon_1}\,, \quad k_{1,2} = 2\pi f_2 \sqrt{\mu_1 \varepsilon_1}\,. \tag{3.24}$$

#### 3.2.2.2 Solutions to the inverse problem

Finding solutions for the unknowns in equation (3.23) is possible using several frequencies. At every antenna point it is necessary to record a sufficient number of amplitude and phase measurements for each frequency. By using this data in the inverse algorithm a successful reconstruction of the internal object may be achieved.

This procedure is very similar to the method in section 2.4. We start from an initial approximation to our unknowns, $\mathbf{X}^{(0)} = (a_0, d_{1,0})^T$. The subsequent improvements to this approximation $\mathbf{X}^{(N)} = (a_N, d_{1,N})^T$, $N$=1,2,..., are obtained as indicated in Figure 2.3. In this inverse method, the values for $a$ and $d_1$ are updated iteratively starting from the initial approximation $a_0, d_{1,0}$, and then successively $a_1, d_{1,1}$, then $a_2, d_{1,2}$ and so on. The complete routine of finding unknowns is summarized as follows:

(1). Using equation (3.15), compute the field components $E_{1,z}$ based on the sum of the incident $E_{1,z}^{incident}$ and the scattered $E_{1,2}^{scattered}$ fields. The circular boundary of the cylinder is the potential cause of the scattering and the angle $\phi$ determines the receiver location for the measuring system. The wave number $k$ is frequency dependent and there exists a different vector field for each frequency.

(2). Form the difference of the field vectors by subtracting the calculated field components from the measured electric fields.

(3). Construct the $n \times n$ Jacobian matrix (equation (2.32)). Use $n$=2 in this case.

(4). Obtain the updated vector by Newton's method (equation (2.33)). (This procedure is explained in section 2.4.)

(5). Repeat steps 1-4 until the vector $\mathbf{X}^{(N)}$ satisfies some suitable stopping criterion (this will be further discussed later in this chapter and also in Chapter 5).

The final results of this computation depend upon the initial guess values. In order to test the convergence we ran the inverse algorithm using different guess

values. The algorithm followed the above procedure and it is similar to the example explained in section 2.4. The results are expected when $|\Delta E_{1,z}(a, d_1)|$ and $|\Delta E_{2,z}(a, d_1)|$ are sufficiently small. The results are presented in section 3.6.1.2.

## 3.3 Plane wave scattering from a non-conducting cylinder

In this section, a more realistic approach for a microwave application is considered using the dielectric property difference between the scattering object and the host material. The circular object inside the model is assumed to be a non-conducting cylinder with internal properties similar to that of a foreign object.

### 3.3.1 Forward problem of the non-conducting cylinder

In order to construct a solution for the wave reflection from the non-conducting cylinder, its boundary condition with respect to the two sets of properties inside and outside the cylinder is considered. Here, the same coordinate system as in Figure 3.3 is used but the object inside the model is assumed to be a non-conducting cylinder. In order to find a solution for the scattered waves from the boundary in this situation, the wave impedances on both the sides of the non-conducting cylinder are found using a single term (the $n$-term) of the series for the incident and scattered waves (we call this the *modal impedance*). The procedure is as follows:

Assume the two regions, region 1 (outside the cylinder) and region 2 (inside the cylinder) are source-free and homogeneous. Consider the wave to be $z$-polarised and travelling in the $x$ direction. For transverse magnetic (TM) incident plane waves, the modal impedance (for the $n^{th}$ mode) outside the cylinder is

$$Z_{1,n} = \frac{E_{z,1}}{H_{\phi,1}} = \frac{E_{z,1}^{incident} + E_{z,1}^{scattered}}{H_{\phi,1}^{incident} + H_{\phi,1}^{scattered}}, \tag{3.25}$$

where $E_{z,1}$ and $H_{\phi,1}$ are the non-zero electric and magnetic field components in region 1, respectively. For the inward-travelling wave, the modal impedance inside the cylinder is

$$Z_{2,n} = \frac{E_{z,2}}{H_{\phi,2}}, \tag{3.26}$$

where $E_{z,2}$ and $H_{\phi,2}$ are the non-zero electric and magnetic field quantities in region 2, respectively.

The **E** and **H** fields can be represented in terms of the wave function $\psi$. Consider a field with $H_z = 0$ so that it is TM to the $z$ direction. Let the electric vector potential be $\mathbf{F} = 0$ and the magnetic vector potential be $\mathbf{A} = \mathbf{u}_z\psi$ where $\mathbf{u}_z$ is a unit vector in the $z$ direction. Then **E** and **H** fields can be represented in terms of **A** (equation (A.23) in Appendix A) as

$$\begin{aligned} \mathbf{E} &= -\hat{z}\mathbf{A} + \tfrac{\mathbf{1}}{\hat{y}}\nabla\left(\nabla\cdot\mathbf{A}\right), \\ \mathbf{H} &= \nabla\times\mathbf{A}, \end{aligned} \tag{3.27}$$

where $\hat{z} = j\omega\mu$, $\hat{y} = j\omega\varepsilon$ are the characteristics of the perfect dielectric media (section 2.1.1). By expanding equation (3.27) in Cartesian coordinates for the TM plane wave incident at the non-conducting cylinder, for the cylindrical coordinate system in Figure 3.3, we obtain (see also equation (A.24) in Appendix A)

$$\begin{aligned} E_z &= \tfrac{1}{\hat{y}}\left(\tfrac{\partial^2}{\partial z^2} + k^2\right)\psi, \\ H_\phi &= -\tfrac{\partial\psi}{\partial p}, \end{aligned} \tag{3.28}$$

where $\hat{y}_1 = j2\pi f_1\epsilon$, $\epsilon = \epsilon_1$ or $\epsilon_2$, and $k$ is the wave number. A set of linearly independent solutions for $\psi$ has been obtained in equation (3.8). Now, taking $\psi = \psi(p,\phi) = E_0 j^{-n}[J_n(k_1p) + C_nH_n^{(2)}(k_1p)]e^{jn\phi}$, the fields are found using equations (3.28) and, using equation (3.25), the wave modal impedance on the outside of the cylinder at $p = a$ is found as

$$Z_{1,n} = -\frac{k_1(J_n(k_1a) + C_nH_n^{(2)}(k_1a))}{\hat{y}_1(J_n'(k_1a) + C_nH_n^{(2)\prime}(k_1a))}, \tag{3.29}$$

where $k_1$ is the wave number of the host material and $C_n$ is the modal coefficient of the scattered wave ($n^{th}$ mode of the series is taken here). Similarly, taking $\psi = \psi(p,\phi) = E_0 j^{-n} J_n(k_2 p) e^{jn\phi}$ in equation (3.28) we obtain the wave modal impedance on the inside of the cylinder at $p = a$ as

$$Z_{2,n} = -\frac{k_1^2 J_n(k_2 a)}{\hat{y}_1 k_2 J'_n(k_2 a)}. \tag{3.30}$$

The terms $J'_n(.)$ and $H_n^{(2)\prime}(.)$ denote the derivatives of $J_n(.)$ and $H_n^{(2)}(.)$, respectively. Using the identities of the Bessel functions and Hankel functions [8, 16], as given in Appendix B, the above derivatives can be found as

$$J'_n(k_i a) = \frac{1}{2}\left(J_{n-1}(k_i a) - J_{n+1}(k_i a)\right), \tag{3.31}$$

$$H_n^{(2)\prime}(k_i a) = \frac{1}{2}\left(H_{n-1}^{(2)}(k_i a) - H_{n+1}^{(2)}(k_i a)\right), \tag{3.32}$$

where $i = 1, 2$.

The boundary conditions on the cylinder surface $p = a$ require that the tangential components of electric and magnetic fields are continuous and so, $Z_{1,n} = Z_{2,n}$ and, using equations (3.29) and (3.30), the modal coefficient $C_n$ is found as

$$C_n = \frac{-J_n(k_1 a)}{H_n^{(2)}(k_1 a)} \left[ \frac{\frac{\varepsilon_2 J'_n(k_2 a)}{\varepsilon_1 k_2 J_n(k_2 a)} - \frac{J'_n(k_1 a)}{k_1 J_n(k_1 a)}}{\frac{\varepsilon_2 J'_n(k_2 a)}{\varepsilon_1 k_2 J_n(k_2 a)} - \frac{H_n^{(2)\prime}(k_1 a)}{k_1 H_n^{(2)}(k_1 a)}} \right], \tag{3.33}$$

$$C_n = a_n \, R_{c,n}, \tag{3.34}$$

where

$$R_{c,n} = \frac{\left(\varepsilon_2 k_1 J_n(k_1 a) J'_n(k_2 a) - \varepsilon_1 k_2 J_n(k_2 a) J'_n(k_1 a)\right) H_n^{(2)}(k_1 a)}{\left(\varepsilon_2 k_1 H_n^{(2)}(k_1 a) J'_n(k_2 a) - \varepsilon_1 k_2 J_n(k_2 a) H_n^{(2)\prime}(k_1 a)\right) J_n(k_1 a)} \tag{3.35}$$

and $a_n = \frac{-J_n(k_1 a)}{H_n^{(2)}(k_1 a)}$, as found in equation (3.17). This modifies equation (3.14) and so, for the outward-travelling wave, the scattered field of the non-conducting cylinder is

$$E_{1,z}^s(p,\phi) = E_0 \sum_{n=-\infty}^{\infty} j^{-n} a_n R_{c,n} H_n^{(2)}(k_1 p) \, e^{jn\phi}, \tag{3.36}$$

where $R_{c,n}$ and $a_n$ are given by equations (3.35) and (3.17), respectively. From equation (3.19), the new equation for the total field at distance $d_1$ along the $x$ axis with frequency $f_1$ is

$$E_{1,z}(d_1,\pi) = E_0 \sum_{n=-\infty}^{\infty} j^n \left[ J_n(k_1 d_1) + a_n R_{c,n} H_n^{(2)}(k_1 d_1) \right]. \tag{3.37}$$

For this case, the wave numbers $k_1$ and $k_2$ are given for frequency $f_1$ by

$$k_1 = 2\pi f_1 \sqrt{\mu_1 \varepsilon_1}\,, \quad k_2 = 2\pi f_1 \sqrt{\mu_2 \varepsilon_2}\,, \tag{3.38}$$

where $\varepsilon_1$, $\mu_1$ are the permittivity and permeability outside the non-conducting cylinder and $\varepsilon_2$, $\mu_2$ are the permittivity and permeability inside the non-conducting cylinder.

Equation (3.37) is the solution for the forward problem of the non-conducting cylinder. In a practical application, the properties outside the cylinder are assumed to be the same as those of the host material and the properties inside the cylinder are assumed to be the same as those of the target object. From equation (3.35), one can see that equation (3.37) approaches the case of a conducting cylinder when $\varepsilon_2$, the permittivity inside the cylinder boundary, is large (when $\epsilon_2 \to \infty, R_{c,n} \to 1$). Computation of the unknowns using this solution is described in section 3.6.2.

### 3.3.2 Inverse problem of plane wave scattering from the non-conducting cylinder

The inverse problem for the case of a non-conducting cylinder is similar to that of the conducting cylinder. However, compared to the previous case, the inverse solution associated with this forward equation needs more iterations to converge to a reasonable solution.

#### 3.3.2.1 The general equation

We recall that the form of general equation is:

$$\Delta E_z = \begin{bmatrix} \Delta E_{1,z}(a, d_1) \\ \Delta E_{2,z}(a, d_1) \end{bmatrix} = \begin{bmatrix} 0 \\ 0 \end{bmatrix}, \tag{3.39}$$

Using equation (3.37), the general equation to find the two unknowns $a$ and $d_1$ are

$$\begin{bmatrix} E_{1,z} - E_0 \sum_{n=-\infty}^{\infty} j^n \left[ J_n(k_1 d_1) + a_n R_{c,n,1} H_n^{(2)}(k_1 d_1) \right] \\ E_{2,z} - E_0 \sum_{n=-\infty}^{\infty} j^n \left[ J_n(k_3 d_1) + a_n R_{c,n,2} H_n^{(2)}(k_3 d_1) \right] \end{bmatrix} = \begin{bmatrix} 0 \\ 0 \end{bmatrix}. \tag{3.40}$$

The field components $E_{1,z}$ and $E_{2,z}$ are either measured values or are calculated. Here, $k_1$ and $k_3$ are the wave numbers of the medium outside the non-conducting cylinder at frequency $f_1$ and frequency $f_2$, respectively. The modal coefficients $R_{c,n,1}$ and $R_{c,n,2}$ at frequency $f_1$ and frequency $f_2$ are found as

$$R_{c,n,1} = \frac{(\varepsilon_2 k_1 J_n(k_1 a) J'_n(k_2 a) - \varepsilon_1 k_2 J_n(k_2 a) J'_n(k_1 a))\, H_n^{(2)}(k_1 a)}{\left(\varepsilon_2 k_1 H_n^{(2)}(k_1 a) J'_n(k_2 a) - \varepsilon_1 k_2 J_n(k_2 a) H_n^{(2)\prime}(k_1 a)\right) J_n(k_1 a)} \tag{3.41}$$

and

$$R_{c,n,2} = \frac{(\varepsilon_2 k_3 J_n(k_3 a) J'_n(k_4 a) - \varepsilon_1 k_4 J_n(k_4 a) J'_n(k_3 a))\, H_n^{(2)}(k_3 a)}{\left(\varepsilon_2 k_3 H_n^{(2)}(k_3 a) J'_n(k_4 a) - \varepsilon_1 k_4 J_n(k_4 a) H_n^{(2)\prime}(k_3 a)\right) J_n(k_3 a)}. \tag{3.42}$$

When the frequency $f_1$ is used, $k_1$ and $k_2$ are the wave numbers of the medium one outside the cylinder and medium two inside the cylinder, respectively, and can be found in equation (3.38). Similarly when the frequency $f_2$ is used, $k_3$ and $k_4$ are the wave numbers of the medium one outside the cylinder and medium two inside the cylinder, respectively, and can be found as

$$k_3 = 2\pi f_2 \sqrt{\mu_1 \varepsilon_1}\,, \qquad k_4 = 2\pi f_2 \sqrt{\mu_2 \varepsilon_2}\,. \tag{3.43}$$

With the two frequencies, the derivatives of Bessel and Hankel functions in equation (3.42) can be found from equations (3.31) and (3.32) with $i = 3, 4$.

$$J'_n(k_3a) = \frac{1}{2}\left(J_{n-1}(k_3a) - J_{n+1}(k_3a)\right), \quad J'_n(k_4a) = \frac{1}{2}\left(J_{n-1}(k_4a) - J_{n+1}(k_4a)\right) \tag{3.44}$$

$$H_n^{(2)\prime}(k_3a) = \frac{1}{2}\left(H_{n-1}^{(2)}(k_3a) - H_{n+1}^{(2)}(k_3a)\right), \; H_n^{(2)\prime}(k_4a) = \frac{1}{2}\left(H_{n-1}^{(2)}(k_4a) - H_{n+1}^{(2)}(k_4a)\right). \tag{3.45}$$

#### 3.3.2.2 Solutions to the inverse problem

The procedure of solving the inverse problem is similar to the previous approaches. Again, for simplicity, only $a$ and $d_1$ are considered as unknowns assuming that the electrical properties of the regions in both the sides of the cylinder are known. However, there is no restriction against including these properties as unknowns in the inverse algorithm. The Jacobian matrix is constructed and it is of the form

$$\mathbf{J} = \begin{bmatrix} A_1(a, d_1) & A_2(a, d_1) \\ \\ A_3(a, d_1) & A_4(a, d_1) \end{bmatrix}, \tag{3.46}$$

where

$$A_1(a, d_1) = \frac{\partial}{\partial a}\left(E_1 - E_0 \sum_{n=-\infty}^{\infty} j^n \left[J_n(k_1d_1) + a_n R_{c,n,1} H_n^{(2)}(k_1d_1)\right]\right), \tag{3.47}$$

$$A_2(a, d_1) = \frac{\partial}{\partial d_1}\left(E_1 - E_0 \sum_{n=-\infty}^{\infty} j^n \left[J_n(k_1d_1) + a_n R_{c,n,1} H_n^{(2)}(k_1d_1)\right]\right), \tag{3.48}$$

$$A_3(a, d_1) = \frac{\partial}{\partial a}\left(E_2 - E_0 \sum_{n=-\infty}^{\infty} j^n \left[J_n(k_2d_1) + a_n R_{c,n,2} H_n^{(2)}(k_2d_1)\right]\right), \tag{3.49}$$

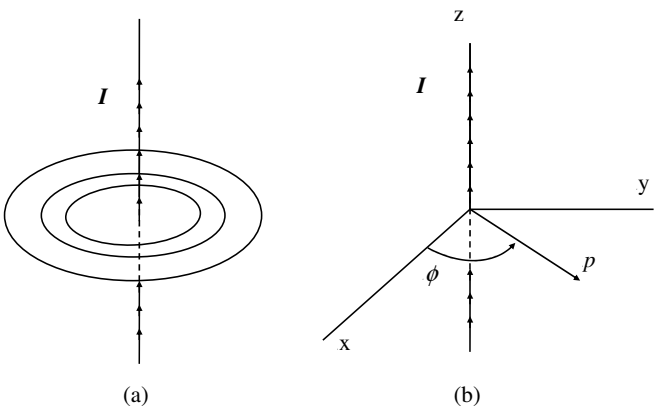


Figure 3.5: The source generating the cylindrical waves (a) Current filament (b) Coordinate system.

$$A_4(a, d_1) = \frac{\partial}{\partial d_1}\left(E_2 - E_0 \sum_{n=-\infty}^{\infty} j^n \left[J_n(k_2 d_1) + a_n R_{c,n,2} H_n^{(2)}(k_2 d_1)\right]\right). \qquad (3.50)$$

Note the $R_{c,n,i}(i = 1, 2)$ is a function of $a$ as given in equations (3.41) and (3.42). Once the Jacobian matrix is formed from (3.40) the rest of the inverse method is similar to that of the conducting cylinder.

## 3.4 Cylindrical wave scattering from a conducting cylinder

A wave having its phase constant over cylindrical surfaces is called a cylindrical wave. A source independent of the $z$-coordinate can generate cylindrical waves.

When a microwave signal is excited from a current source, the waves in the nearby region are cylindrical waves. Therefore, if the object is placed closer to the source, the scattering from its boundary would be caused by cylindrical waves rather than plane waves. However, when the object is further away from the source, one can consider that the scattering has resulted from plane waves.

In this section, the scattering problem of a cylindrical wave is discussed. Again a conducting cylinder is chosen as the object inside the host (Figure 3.3). An infinitely long current filament placed parallel to the cylinder is taken as the source which generates the cylindrical waves. This is similar to the method used by Harrington in [8]. The source and its coordinate system are shown in Figure 3.5.

### 3.4.1 Forward problem of cylindrical wave scattering

The field generated from the source is expected to be TM to the $z$-direction (so the field has $H_z = 0$) and can be expressed in terms of a magnetic vector potential having only a $z$-component. The wave function is also symmetric and independent of $\phi$ and $z$ (see Figure 3.5) and so $A_z = \psi(p)$. The wave function for the outward travelling wave can be written using equation (3.8) as

$$\psi(p) = GH_0^{(2)}(kp), \tag{3.51}$$

where $k$ is the wave number of the medium and $G$ is a constant which can be found by considering the current $I$ of the source filament.

The electromagnetic field component $E_z$ can be expressed in terms of wave functions $\psi$ associated with cylindrical coordinates as

$$E_z = \frac{1}{\hat{y}} \left( \frac{\partial^2}{\partial z^2} + k^2 \right) \psi. \tag{3.52}$$

(see the Appendix A1). Consider a perfect dielectric medium with $\sigma = 0$. Then, using equations (2.2) and (3.51), and by simplifying the equation (3.52) we obtain

$$E_z(p) = EH_0^{(2)}(kp), \tag{3.53}$$

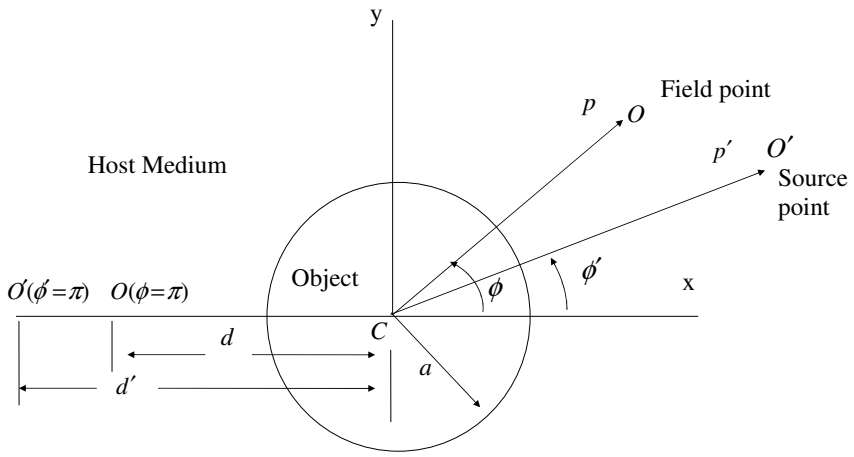


Figure 3.6: Cylindrical coordinate system for cylindrical wave functions.

where

$$E = \frac{k^2 G}{j\omega\varepsilon}. \tag{3.54}$$

Equation (3.53) gives the field component $E_z$ at a point which has a distance $p$ from the source. Now we shall use this wave to illuminate the cylindrical object inside the host. The source and the cylindrical coordinate system are shown in Figure 3.6. Here, the $z$ axis is not shown but it is perpendicular to the $xy$-plane and lies out of the page with $C$ as the origin.

Consider the source filament to be placed not along the $z$ axis but at a point $O'$ and parallel to the $z$ axis. Our aim is to find a field solution at the point $O$ (shown in Figure 3.6) due to the field excited from the source at $O'$. Therefore equation (3.53) can be used by replacing $p$ with the distance from $O$ to $O'$. We specify the field point at $O$ and the source point at $O'$ using the radius vector notation as $\mathbf{r} = \mathbf{u}_x x + \mathbf{u}_y y$ and $\mathbf{r}' = \mathbf{u}_x x' + \mathbf{u}_y y'$, respectively. The distance from source point

$O'$ to field point $O$ is

$$|\mathbf{r}-\mathbf{r}\,'| = \sqrt{(x-x\,')^2+(y-y\,')^2} = \sqrt{p^2+p\,'^2-2pp\,'\cos(\phi-\phi\,')}, \tag{3.55}$$

where $p$ and $p\,'$ are the distances form $O$ to $C$ and $O\,'$ to $C$, as indicated in Figure 3.6. Equation (3.53) can be written for the incident field at point $O$ due to the source at $O'$ as

$$E_z^i = E\,H_0^{(2)}(k\,|\mathbf{r}-\mathbf{r}\,'|). \tag{3.56}$$

Then, for $p < p\,'$, from the addition theorem [8, 16],

$$E_z^i\,(p,p\,',\phi,\phi\,') = E\sum_{n=-\infty}^{\infty} H_n^{(2)}(kp\,')J_n(kp)e^{jn(\phi-\phi\,')}. \tag{3.57}$$

The field component $E_z^i$ in equation (3.57) is for the incident wave at the field point $O$ due to the wave source at point $O\,'$.

Now we use the asymptotic condition in the field equation: as $x \to \infty$,

$$H_n^{(2)}(x) \approx \sqrt{\frac{2j}{\pi x}}j^n e^{-jx}\,. \tag{3.58}$$

Therefore, as $p\,' \to \infty$ for $\phi\,' = 0$, equation (3.57) becomes

$$E_z^i \approx E\sqrt{\frac{2j}{\pi kp\,'}}e^{-jkp\,'}\sum_{n=-\infty}^{\infty} j^n J_n(kp)e^{jn\phi}. \tag{3.59}$$

In equation (3.59) we can see that $E_z^i$ has become the field of a plane wave. This result is to be expected when the source that generates the cylindrical waves is far away from the field point.

The scattered field at point $O$ can be found by replacing $J_n(.)$ in equation (3.57) with $H_n^{(2)}(.)$ and the result is

$$E_z^s\,(p,p\,',\phi,\phi\,') = E\sum_{n=-\infty}^{\infty} a_n H_n^{(2)}(kp\,')H_n^{(2)}(kp)e^{jn(\phi-\phi\,')}, \tag{3.60}$$

where the $a_n$ are constants. Using equations (3.57) and (3.60), the total field at point $O$ is found to be

$$\begin{aligned} &E_z\,(p,p\,',\phi,\phi\,') = E_z^i\,(p,p\,',\phi,\phi\,') + E_z^s\,(p,p\,',\phi,\phi\,') = \\ &E\sum_{n=-\infty}^{\infty}\left[H_n^{(2)}(kp\,')J_n(kp) + a_n H_n^{(2)}(kp\,')H_n^{(2)}(kp)\right]e^{jn(\phi-\phi\,')}\,. \end{aligned} \tag{3.61}$$

which is valid for $p < p'$. Again the constants $a_n$ can be found by considering the boundary condition of a perfectly conducting cylinder: $a_n = -\frac{J_n(k_1 a)}{H_n^{(2)}(k_1 a)}$. Equation (3.61) is the forward equation for the scattering of cylindrical waves from a conducting cylinder. This gives total field component $E_z$ which can be measured from the field point.

The forward problem of wave scattering from cylindrical waves has now been solved. Knowing the distance $p$ and the angle $\phi$, this result can be used to find the field component at any point. Similarly, the source point can also have any location with $p' > p$. As an example, suppose the points $O$ and $O'$ are rotated through angles $\pi - \phi$ and $\pi - \phi'$, respectively. Then these points lie along the $x$ axis. These new positions and the distances from the centre of the cylinder are shown in Figure 3.6 (see also Figure 7.5 (ii) in section 7.2.2). The solution for the field point at a distance $d$ along the $x$ axis is

$$E_z\left(d, d'\right) = E \sum_{n=-\infty}^{\infty} \left[ H_n^{(2)}(kd') J_n(kd) + a_n H_n^{(2)}(kd') H_n^{(2)}(kd) \right], \tag{3.62}$$

where $d'$ is the distance to the source point from the centre of the object (Figure 3.6). Equation (3.62) can be used only if the source and the field points are collinear with the centre of the object. In practice this may be hard to achieve but we presume that it is possible to do this by aligning the antenna for the purpose of this modal.

The result in equation (3.61) may be used to find unknowns using data obtained from field measurements. In order to find the angles $\phi$ and $\phi'$, it is necessary to record the source and the receiver locations very accurately in the measurement plane. A detailed practical development is beyond the task of this study. However, these solutions have been tested with the data obtained from both analytical calculations and experimental measurements. The results are discussed later in this thesis (sections 3.7 and 7.4).

## 3.5 Cylindrical waves with a non-conducting cylinder

Here, a non-conducting cylinder is used as the scattering object inside the model. Again, in this case we consider the boundary condition with respect to the two sets of properties inside and outside the non-conducting cylinder.

Similar to the method used in section 3.3, the field components at point $O$ can be found using a frequency $f_1$. Then the equation for the total field that can be measured from antenna one is

$$\begin{aligned} &E_{z,1}(p_1, {d_1}', \phi_1, {\phi_1}') = \\ &E \sum_{n=-\infty}^{\infty} \left[ H_n^{(2)}(k_1 {d_1}') J_n(k_1 p_1) + a_n R_{c,n,1} H_n^{(2)}(k_1 {d_1}') H_n^{(2)}(k_1 p_1) \right] e^{jn(\phi_1 - {\phi_1}')}, \end{aligned} \tag{3.63}$$

where $a_n$ are the constants given in equation (3.17), $R_{c,n,1}$ is the coefficient at frequency $f_1$ which can be found in equation (3.41), $p_1$ is the distance to the field point and $d_1'$ is the distance to the source point. These distances are measured from the centre of the cylinder. The constants $k_1$ and $k_2$ are the wave numbers for frequency $f_1$ which can be found using equation (3.38). Similarly, the forward equation with frequency $f_2$ is

$$\begin{aligned} &E_{z,2}(p_1, {d_1}', \phi_1, {\phi_1}') = \\ &E \sum_{n=-\infty}^{\infty} \left[ H_n^{(2)}(k_3 {d_1}') J_n(k_3 p_1) + a_n R_{c,n,2} H_n^{(2)}(k_3 {d_1}') H_n^{(2)}(k_3 p_1) \right] e^{jn(\phi_1 - {\phi_1}')}, \end{aligned} \tag{3.64}$$

where $R_{c,n,2}$ (which depends on $k_3, k_4$) is the coefficient at frequency $f_2$ which can be found in equation (3.42) and $k_3$ and $k_4$ are the wave numbers of the media outside and inside of the non-conducting cylinder, respectively, for frequency $f_2$ as found in equation (3.43).

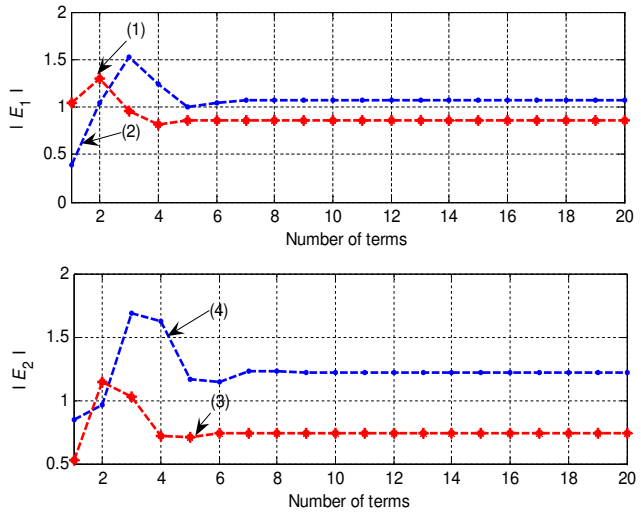


Figure 3.7: Plot of the calculated E fields using the forward equations of the conducting cylinder. (1): $|E_1|$ for $a = 0.002$m, $d_1$ =0.06m. (2): $|E_1|$ for $a = 0.002$m, $d_1$ =0.04m. (3): $|E_2|$ for $a = 0.002$m, $d_1$ =0.06m. (4):$|E_2|$ for $a = 0.002$m, $d_1$ =0.04m.

## 3.6 Results and discussion: plane wave scattering

### 3.6.1 Results with a conducting cylinder

The solutions to the forward and inverse scattering problems of a conducting cylinder have been obtained in section 3.2. This section presents the results of calculations to test these solutions.

#### 3.6.1.1 Calculation of field vectors

The field equations for the two frequencies $f_1$ and $f_2$ are obtained from equation (3.23). We use two sets of reasonable values for $a$ and $d_1$ ($a = 0.002$ m, $d_1 = 0.04$ m and $a = 0.002$ m, $d_1$=0.06 m) and calculate the two corresponding values each of $E_1$ and $E_2$ with $f_1 = 2.0$ GHz and $f_2 = 2.2$ GHz frequencies. Also, we assume that $\mu_r = 1$ and $\epsilon_r = 10$ in the medium of the wave propagation. The solutions to the

system of equations (3.23) have been computed using the infinite series indexed by $n$ until they converge towards a constant value (from $n = 1$ to $n = 20$ terms in the series). These calculations were performed by using code written in MATLAB and the results are shown in Figure 3.7. ($E_1$ and $E_2$ are normalised with $E_0 = 1$ volts $m^{-1}$.) This illustrates that $|E_1|$ and $|E_2|$ can be determined to sufficient accuracy by truncation of the series after 10 terms. In the study, these values, instead of measured results, are used to test the inverse algorithm.

#### 3.6.1.2 Calculation of the unknowns

The inverse algorithm developed in section 3.2.2 was tested by calculating the cylinder radius $a$ and the distance $d_1$ to antenna one from the centre of the cylinder. A computer program written in MATLAB was used for this calculation. The iteration process follows the sequence given in Figure 2.3. First, a set of guess values was chosen for $a$ and $d_1$. Then these values were substituted into the algorithm to run the whole process. According to the general equations in (3.23), at the end of the iteration cycle we seek solutions to $a$ and $d_1$ as the residual tends to zero. If the solutions are not acceptable, another set of guess values can be chosen to run the same process. We have used several values for $a$ and $d_1$ in the neighbourhood of the true values and found that there are limits on those guess values for which we can expect a reasonable solution for the unknowns. Figure 3.8 illustrates the results of the iteration process using two different sets of guess values. These plots show the two unknowns $a$ and $d_1$ converging towards their exact values ($a$=0.002 and $d_1$=0.04 m). The two sets of graphs in Figure 3.9 show the plots of $|\Delta E_1|$ (residual of $(3.23)_1$) and $|\Delta E_2|$ (residual of $(3.23)_2$) versus the number of iterations. Both $|\Delta E_1|$ and $|\Delta E_2|$ converge towards zero as $a$ and $d_1$ approach 0.002m and 0.04m, respectively, after approximately 15 iterations.

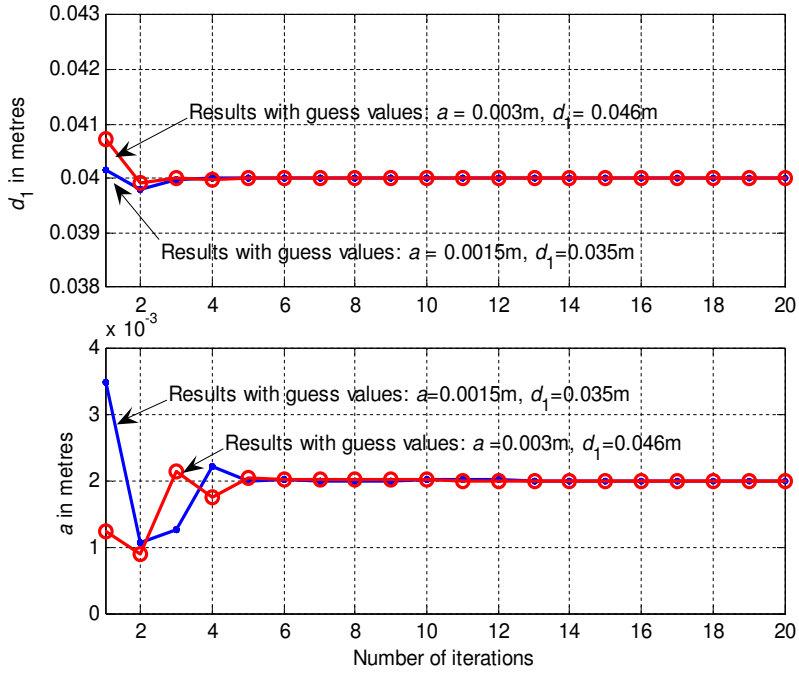


Figure 3.8: Calculated values of $a$ and $d_1$ of the conducting cylinder. Results with two sets of guess values.

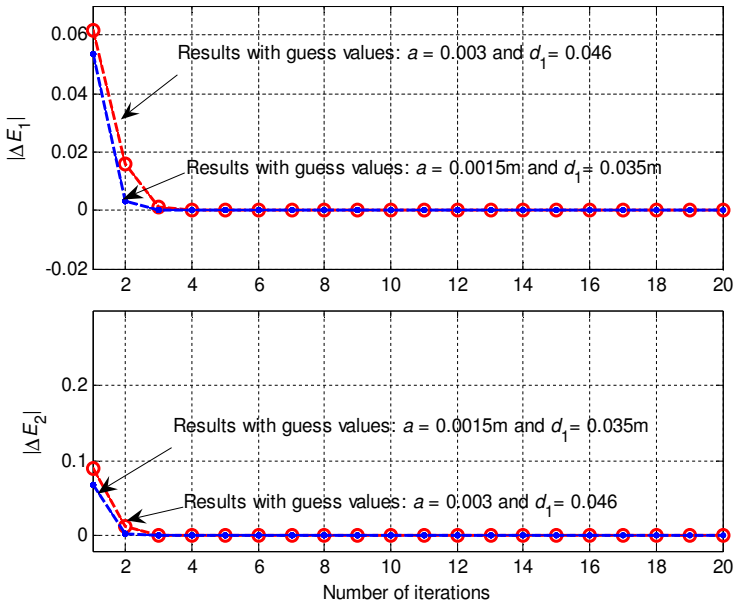


Figure 3.9: Calculated values of $|\Delta E_1|$ and $|\Delta E_2|$ of the conducting cylinder.

### 3.6.2 Results with a non-conducting cylinder

First, we calculated $R_{c,n,1}$, the modal coefficient for frequency $f_1$, and $R_{c,n,2}$, the modal coefficient for frequency $f_2$, for different values of $\epsilon_1$, the permittivity outside the cylinder and $\epsilon_2$, the permittivity inside the cylinder. Equations (3.41) and (3.42) were used for these calculations with $a$= 0.01 m and $d_1$=0.16m. The results are summarised as follows.

(1). Both $R_{c,n,1}$ and $R_{c,n,2}$ increase when the permittivity of the medium inside the cylinder increases.

(2). $R_{c,n,1} = R_{c,n,2} = 0$ when $\varepsilon_1$, the permittivity outside the cylinder, and $\varepsilon_2$, the permittivity inside the cylinder, are the same.

(3). The magnitudes of $R_{c,n,1}$, $R_{c,n,2} \to 1$ when permittivity inside the cylinder is very large (when $\varepsilon_2 \to \infty$).

These results also agree with equation (2.19). When the electrical properties on both the sides of the reflecting boundary are the same one can expect a zero reflection as in (2) above. Similarly when the dielectric property of the reflecting medium is very large, assuming the permittivity makes the main contribution, a full reflection can be expected as in (3) above.

#### 3.6.2.1 Calculations of the field vectors

The solution to the scattering problem of a non-conducting cylinder which has been obtained in section 3.3.1, was used to calculate the field components. Using equation (3.37), the field components for the two different frequencies are

$$E_1 = E_0 \sum_{n=-\infty}^{\infty} j^n \left[ J_n(k_1 d_1) + a_n R_{c,n,1} H_n^{(2)}(k_1 d_1) \right]$$
$$E_2 = E_0 \sum_{n=-\infty}^{\infty} j^n \left[ J_n(k_2 d_1) + a_n R_{c,n,2} H_n^{(2)}(k_2 d_1) \right], \tag{3.65}$$

where $R_{c,n,1}$ and $R_{c,n,2}$ are the modal coefficients for frequency $f_1$ and frequency $f_2$ as given in equations (3.41) and (3.42), respectively. The calculated $E_1$ and $E_2$ for

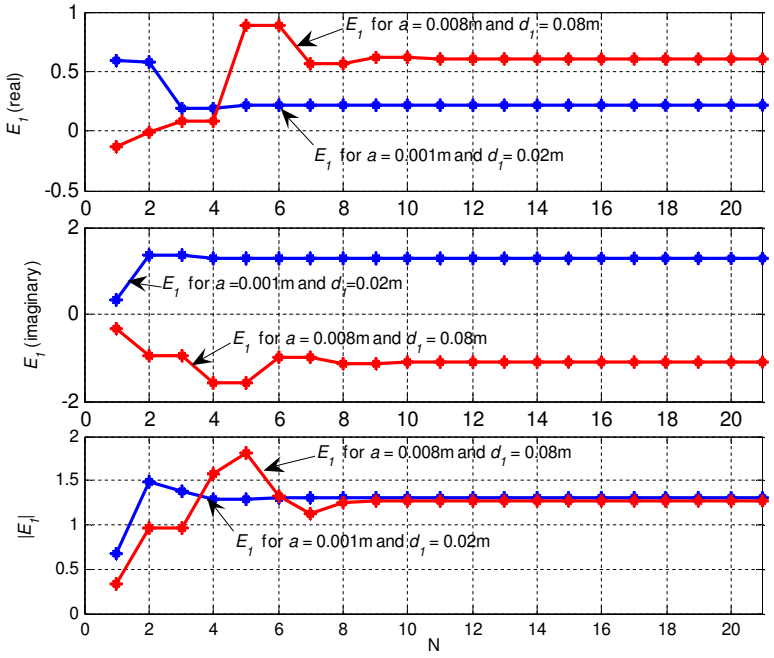


Figure 3.10: Calculated field components $E_1$ for the non-conducting cylinder.

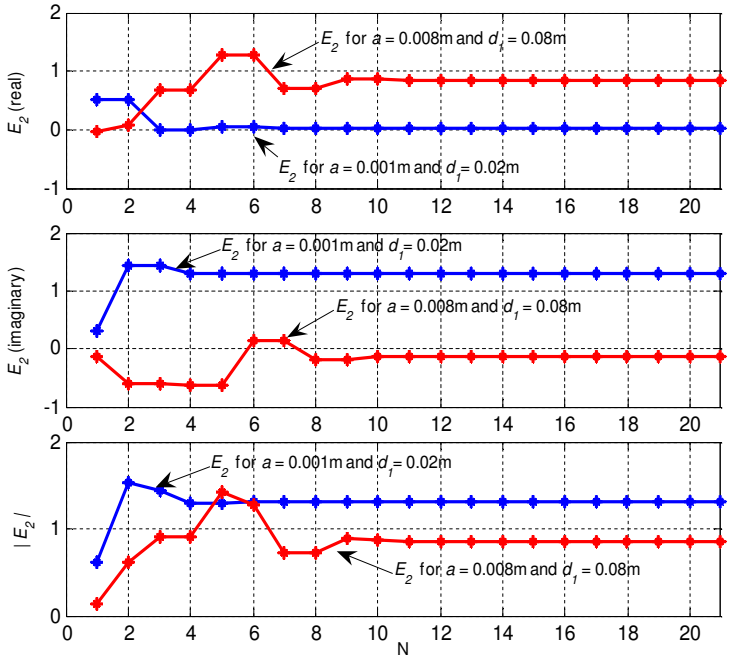


Figure 3.11: Calculated field components $E_2$ for the non-conducting cylinder.

two sets of $a$ and $d_1$ values are plotted in Figures 3.10 and 3.11, respectively ($E_1$ and $E_2$ are normalised with $E_0 = 1$ volts m$^{-1}$).

Taking the partial series from $n$ = -N to N, the expressions (3.65) for $E_1$ and $E_2$ need approximately N = 15 to converge to a constant value. As the computer code has more variables, these simulations needed more computing time compared to those with the conducting cylinder. However, these results may be more appropriate for a realistic application in detecting a foreign object.

#### 3.6.2.2 Calculation of unknowns

In order to calculate unknowns, we used the inverse algorithm developed in section 3.3.2. The general equations obtained in equation (3.40) need field components $E_1$ and $E_2$ given by (3.65) for the subsequent iteration process of the inverse method. In a practical application these components would be measured. In order to test the inverse method, these field components were calculated using the field equations in (3.65). Again, the inverse method we used is similar to the method explained in sections 2.4 and 3.2.2. However, the Jacobian matrix and the subsequent explicit function are rather complicated compared to those used in the inverse algorithms of the conducting cylinder. We tested with two sets of guess values for $a$ and $d_1$ in the neighbourhood of their true values.

Figure 3.12 shows the calculated results of the two unknowns. With guess values $a = 0.0015$ m, $d_1 = 0.035$ m and $a$ =0.003 m, $d_1$ =0.046 m as initial guesses both $|\Delta E_1|$ (residual of $(3.40)_1$) and $|\Delta E_2|$ (residual of $(3.40)_2$) converge towards zero as $a$ and $d_1$ approach 0.002m and 0.04 m, respectively ($a = 0.002m$ and $d_1 = 0.04m$ are the true values). Figure 3.13 shows the plots of $|\Delta E_1|$ and $|\Delta E_2|$ versus number of iterations for these two sets of guess values.

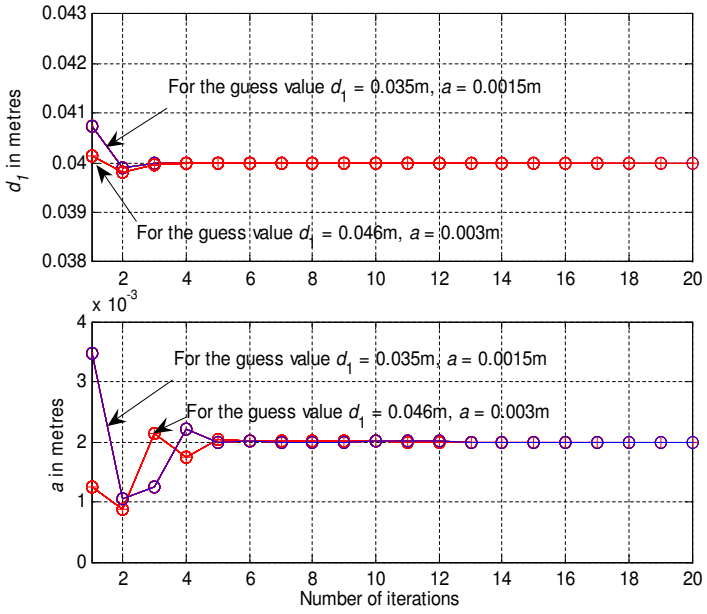


Figure 3.12: Calculated values of $a$ and $d_1$ using inverse algorithm for the non-conducting cylinder. Results are shown for two different sets of guess values.

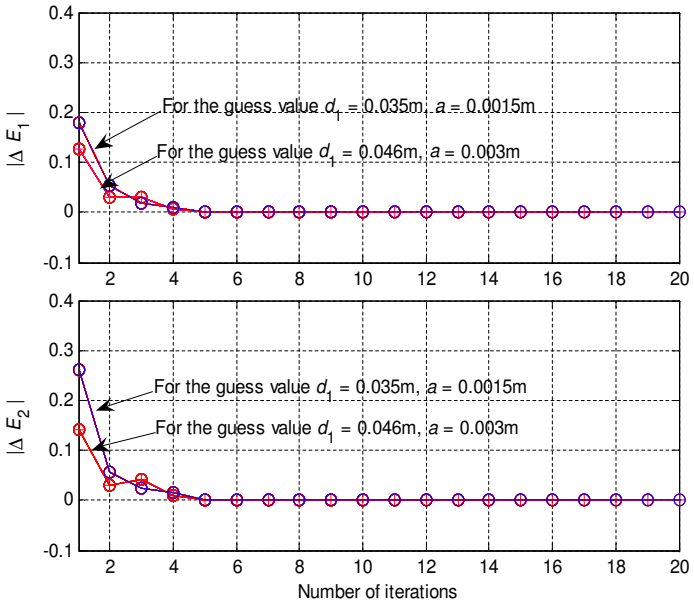


Figure 3.13: Plots of $|\Delta E_1|$ and $|\Delta E_2|$ when tested with two different sets of guess values.

## 3.7 Results and discussion: cylindrical wave scattering

The forward equation developed for the cylindrical wave scattering from a conducting cylinder is given in equation (3.61). Unlike the case with the plane waves, the solution for the forward problem has three basic variables. These are $a$ the radius of the cylinder, $p$ the distance to the centre of the cylinder from the measuring point and $p'$ the distance to the source point from the centre of the cylinder. The magnitude values of the field component which can be measured at the measuring point can be changed with $\phi$ , the angle that the field point makes with the axis of the source point (see Figure 3.6). Therefore, apart from calculating the field components with different frequencies, we also determined the field components at different positions of the field point. The value of the field components vary with respect to frequency of the wave, position of the field point and the position of the source point.

### 3.7.1 Calculation of field components of the cylindrical waves

Consider the field point $O$ and the source point $O'$ to be rotated by angles $\pi$ and $\pi - \phi'$, respectively (Figure 3.14). Then the source point lies along the $x$ axis and the field point $O$ makes an angle $-(\phi - \phi')$ with the direction of the source point. Then the two field components for frequency $f_1$ and frequency $f_2$ can be obtained using equation (3.61) as

$$E_1\left(p, d', \phi'\right) = E \sum_{n=-\infty}^{\infty} \Big[ H_n^{(2)}(k_1 d') J_n(k_1 p) - \frac{J_n(k_1 a)}{H_n^{(2)}(k_1 a)} H_n^{(2)}(k_1 d') H_n^{(2)}(k_1 p) \Big] \, e^{-jn(\phi - \phi')}, \tag{3.66}$$

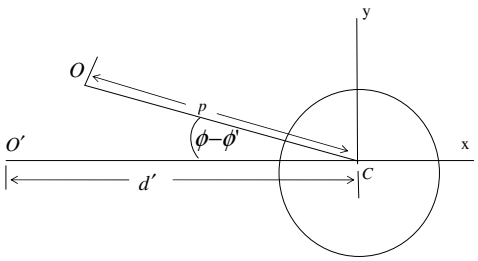


Figure 3.14: Scattering with cylindrical waves: The field point and the source point are shown after rotation.

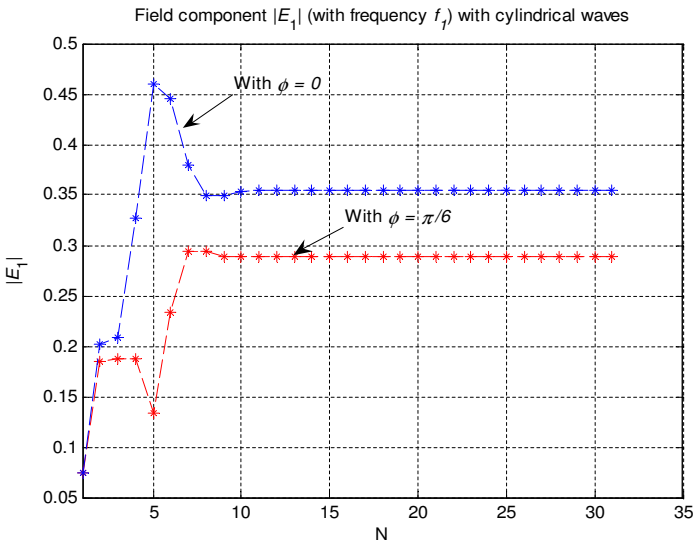


Figure 3.15: Calculated $|E_1|$ with a frequency of $f_1$= 2.0 GHz for cylindrical wave scattering from a conducting cylinder.

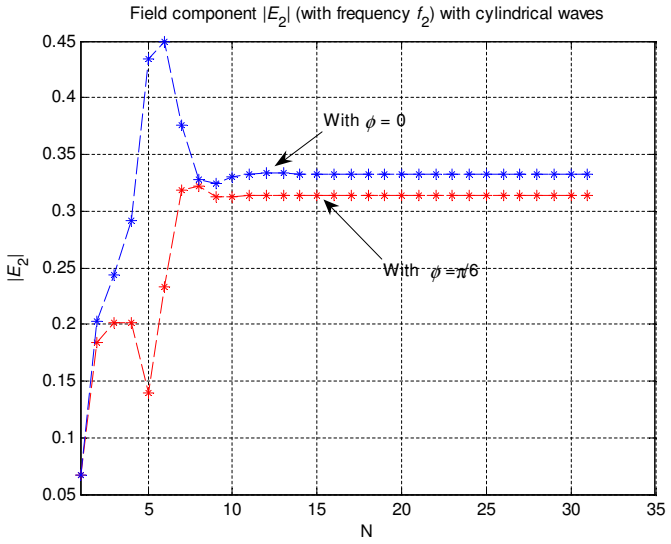


Figure 3.16: Calculated $|E_2|$ with a frequency of $f_2$= 2.2 GHz for cylindrical wave scattering from a conducting cylinder.

$$E_2\left(p, d', \phi'\right) = E \sum_{n=-\infty}^{\infty} \Big[ H_n^{(2)}(k_2 d') J_n(k_2 p) - \frac{J_n(k_2 a)}{H_n^{(2)}(k_2 a)} H_n^{(2)}(k_2 d') H_n^{(2)}(k_2 p) \Big] e^{-jn(\phi - \phi')}, \tag{3.67}$$

where $k_1$ and $k_2$ are the wave numbers for frequency $f_1$ and frequency $f_2$ , respectively. For these calculations, we used a set of reasonable values: the cylinder radius $a$ = 0.0065 m and the distance to the field point from the centre of the cylinder $p$= 0.04 m. We calculated the two corresponding values of $|E_1|$ and $|E_2|$ with $f_1$ = 2.0 GHz and $f_2$ = 2.2 GHz frequencies and these results, as a functions of the number of terms in the series expansions (3.66) and (3.67) have been plotted in Figures 3.15 and 3.16, respectively.

### 3.7.2 Summary of the simulation results of the cylindrical waves

The convergence of these field components of the cylindrical waves is similar to the results we obtained with plane waves but the values of the calculated field components now depend, not only on $k$, $a$ and $p$ but also on the angle $\phi$ and the position of the source point $O'$ which has a distance $d'$ from the centre of the cylinder. A number of simulations have been carried out using the field equations in order to observe the changes in fields with respect to the positions of the field point and the source point. Here, we have not produced all the simulated results but some of the observations can be summarised as follows:

(1). When $p < d'$ , both $|E_1|$ and $|E_2|$ converge to constant values after a reasonable number of iterations.

(2). The number of iterations in (1) above is minimum when $\phi = 0$. As $\phi$ increases in magnitude $|E_1|$ and $|E_2|$ need more iterations.

(3). As $\phi$ increases in magnitude the corresponding computed values of $|E_1|$ and $|E_2|$ decrease. (Plots are marked with the angle $\phi$. See Figures 3.15 and 3.16.)

(4). When $d' \leq p$, there are no results. (This is not valid according to the forward equation.)

(5). As $\phi \to 0$, the magnitude values of $|E_1|$ and $|E_2|$ are maximised.

We observed that the magnitude and phase values of $E_1$ and $E_2$ depend upon the position of $O$ and $O'$. These changes have been studied in detail to investigate the scattering difference between plane waves and cylindrical waves. This will be further discussed in Chapter 7.

# Chapter 4

# Three-dimensional scattering problem

A three-dimensional scattering problem of a spherically-shaped object is considered in this chapter. A simple host model was used. Similar problems to this have been solved previously and the results are available in literature [7, 8, 14, 15]. We used some of those results to obtain a solution to the forward scattering problem of a uniform sphere inside our model. The application system is similar to that used in the cylindrical case (Figure 3.2). The object is illuminated by a microwave signal which is applied from the surface of the host.

The forward and inverse solutions provide the necessary base for a possible practical application. First, the object is assumed to be a conducting sphere and the associated forward problem is solved. Then the result is modified for a more realistic situation using a non-conducting sphere. The inverse scattering problems in both cases are then solved to compute the unknown size and the location of the object. At the beginning of this chapter, some equations in wave theory found in Harrington [8] are used. The full derivations are given for completeness.

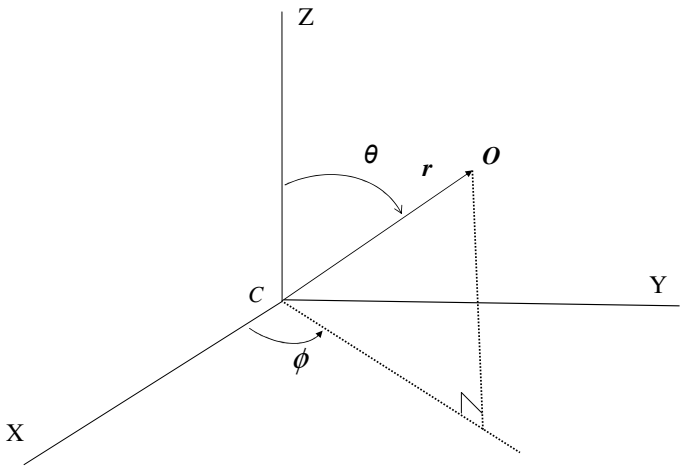


Figure 4.1: The spherical coordinate system.

## 4.1 Wave functions at spherical boundaries

The spherical coordinate system $(r, \theta, \phi)$ corresponds to the spherical wave functions and is shown in Figure 4.1. Consider a point $O$ with a distance $r$ from $C$ the centre of the coordinate system. The Helmholtz equation in spherical coordinates which can be obtained using the Laplacian of $\psi$, is of the form

$$\frac{1}{r^2}\frac{\partial}{\partial r}\left(r^2\frac{\partial \psi}{\partial r}\right) + \frac{1}{r^2\sin\theta}\frac{\partial}{\partial \theta}\left(\sin\theta\frac{\partial \psi}{\partial \theta}\right) + \frac{1}{r^2\sin^2\theta}\frac{\partial^2 \psi}{\partial \phi^2} + k^2\psi = 0. \tag{4.1}$$

In order to solve equation (4.1) we use the method of separation of variables. It is assumed that the solution is a product of three functions of the form,

$$\psi\left(r, \theta, \phi\right) = R(r)\Theta(\theta)\Phi(\phi). \tag{4.2}$$

Using equations (4.1) and (4.2), three separated equations can be found

$$\frac{d}{dr}\left(r^2\frac{dR}{dr}\right) + \left[(kr)^2 - n(n+1)\right]R = 0, \tag{4.3}$$

$$\frac{1}{\sin\theta}\frac{d}{d\theta}\left(\sin\theta\frac{d\Theta}{d\theta}\right)+\left[n(n+1)-\frac{m^2}{\sin^2\theta}\right]\Theta=0, \tag{4.4}$$

$$\frac{d^2\Phi}{d\phi^2}+m^2\Phi=0, \tag{4.5}$$

where $m$ and $n$ are constants. The above three equations have solutions which are each functions of one variable: $r$, $\theta$ and $\phi$, respectively. Equations (4.3) and (4.4) are related to Bessel's equation and Legendre's equation [8, 103], respectively. Equation (4.5) is the harmonic equation which has a solution of the form

$$\Phi(\phi)=\Phi_m(\phi)=e^{jm\phi}, \tag{4.6}$$

where $m$ is an integer. This ensures the solution is periodic with a period of $2\pi$ as it clearly should be since $\Phi(\phi+2\pi)=\Phi(\phi)$.

The solutions to the Bessel's equation are called spherical Bessel functions, denoted by $b_n(kr)$, and $n$ is a positive integer, since the functions in the solutions for $\Theta$ are not finite at $\theta=0,\pi$ unless this is so (this will be discussed in section 4.2.1). The spherical Bessel functions are related to the ordinary Bessel functions $B_{n+1/2}$ by [103]

$$b_n(kr)=\sqrt{\frac{\pi}{2kr}}B_{n+1/2}(kr). \tag{4.7}$$

The solutions to Legendre's equation (4.4) are called the associated Legendre functions and, in general, these are denoted by $L_n^m(\cos\theta)$. There are two linearly independent families of solutions for Legendre's equation:

- $P_n^m(\cos\theta)$ which are the associated Legendre functions of the first kind,
- $Q_n^m(\cos\theta)$ which are the associated Legendre functions of the second kind.

Now, the solutions to the Helmholtz equation can be found using the product in equation (4.2) as

$$\psi\left(r,\theta,\phi\right)=b_n(kr)L_n^m(\cos\theta)e^{jm\phi}. \tag{4.8}$$

The appropriate function for $L_n^m(\cos\theta)$ is selected from the two solutions $P_n^m(\cos\theta)$ and $Q_n^m(\cos\theta)$ by considering the singularities in their domains. The solutions to Legendre's equation have singularities when $\theta = 0$ or $\theta = \pi$ except $P_n^m(\cos\theta)$ with $n$ as an integer (see Appendix D). We seek solutions for $\psi$ to be finite in the range from $\theta = 0$ to $\theta = \pi$ (this problem will be discussed in the next section). Therefore, $L_n^m(\cos\theta)$ must be $P_n^m(\cos\theta)$ and not the $Q_n^m(\cos\theta)$ as this is not finite at $\theta = 0$ and $\theta = \pi$ (see [8,16]). A general solution can be formed using a linear combination of all possible wave functions over $n$ and $m$ as

$$\psi(r,\theta,\phi) = \sum_{n=0}^{\infty} \sum_{m=-\infty}^{\infty} Z_{n,m} b_n(kr) P_n^m(\cos\theta) e^{jm\phi}, \tag{4.9}$$

where $Z_{n,m}$ are constants. Equation (4.9) represents a linear combination of all the possible elementary wave functions. According to equation (4.9), there are three different wave functions (of one variable) associated with the spherical coordinate system.

## 4.2 Forward equation: scattering from plane waves

The model for the host and the internal object with a spherical coordinate system is shown in Figure 4.2. The internal object is considered to be a conducting sphere with radius $a$ ($C$ is the centre) illuminated by an incident plane wave. This sphere represents the unknown object whose size and location are determined using a set of microwave measurements obtained from the surface of the host. This study is carried out with a single antenna. In a practical application, a number of antennas could be used and the location of the object found using the geometry of the situation.

The spherical coordinate system for the scattering sphere inside the host is shown in Figure 4.3. Consider the wave to be $x$-polarized and travelling in the $z$ direction toward the conducting sphere. Then the incident plane wave of $E$ and $H$ fields are

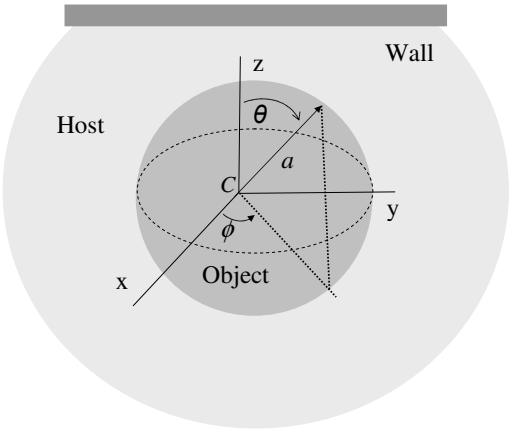


Figure 4.2: Three-dimensional modelling for the scattering from the spherical object.

given by scalar parameters:

$$E_x^i = E_0 e^{-jkz} = E_0 e^{-jkr\cos\theta}, \tag{4.10}$$

$$H_y^i = \frac{E_0}{\eta} e^{-jkz} = \frac{E_0}{\eta} e^{-jkr\cos\theta}, \tag{4.11}$$

where $\eta = \sqrt{\frac{\mu}{\epsilon}}$ and $k = \omega\sqrt{\mu\epsilon}$ are the intrinsic impedance and the wave number of the medium outside the sphere, respectively. The subscripts $x$ on $E$ and $y$ on $H$ represent their polarized directions, respectively.

Figure 4.3 shows a conducting sphere illuminated by an incident plane wave. From the coordinate system, the $r$-component of the incident electric field along OC can be written as

$$E_r^i(r,\theta,\phi) = E_x^i \cos\phi \sin\theta. \tag{4.12}$$

Using equations (4.10) and (4.12),

$$E_r^i(r,\theta,\phi) = \frac{E_0}{jkr}\cos\phi \frac{\partial}{\partial\theta}\left(e^{-jkr\cos\theta}\right). \tag{4.13}$$

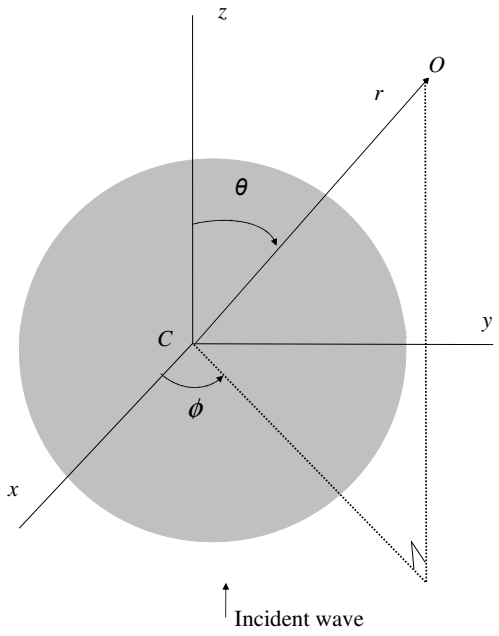


Figure 4.3: Incident wave in spherical coordinate system.

Consider the plane wave incident upon the boundary of the sphere. Then, similar to the method used for the cylindrical coordinate system in section 3.2.1, this wave can be expressed in terms of spherical wave functions. As this wave is travelling in the $z$ direction, it is independent of $\phi$ and therefore, $m = 0$ and equation (4.4) becomes the form of the ordinary Legendre's equation. Then, $P_n^m(\cos\theta)$ becomes $P_n(\cos\theta)$, the Legendre polynomials of the first kind [8, 16] and, since all $P_n^m(\cos\theta)$ $= 0$ for $m > n$, the integer $n$ must be a positive number.

The spherical Bessel function can be of the form of either an inward or an outward-travelling wave. As the wave is taken to be finite at $r = 0$, we select the spherical Bessel function $j_n(kr)$ for $b_n(kr)$ to represent the possible field inside the sphere. Thus,

$$e^{-jkz} = e^{-jkr\cos\theta} = \sum_{n=0}^{\infty} g_n j_n(kr) P_n(\cos\theta), \tag{4.14}$$

where $j_n(kr)$ are spherical Bessel functions (these are the only spherical Bessel

functions finite at $r = 0$ [8]) and $g_n$ are constants which can be evaluated (Appendix C) as

$$g_n = j^{-n}(2n + 1). \tag{4.15}$$

Therefore, from equations (4.14) and (4.15), the plane waves can be expressed in terms of spherical wave functions as

$$e^{-jkz} = e^{-jkr\cos\theta} = \sum_{n=0}^{\infty} j^{-n}(2n + 1)j_n(kr)P_n(\cos\theta). \tag{4.16}$$

The incident field $E_r^i$ can be obtained by substituting equation (4.16) in equation (4.13), and this yields

$$E_r^i(r, \theta, \phi) = \frac{E_0}{jkr}\cos\phi \sum_{n=0}^{\infty} j^{-n}(2n + 1)j_n(kr)\frac{d}{d\theta}P_n(\cos\theta). \tag{4.17}$$

As $\frac{\partial}{\partial\theta}P_0(\cos\theta) = 0$, the term at $n = 0$ within the summation vanishes to give

$$E_r^i(r, \theta, \phi) = \frac{E_0}{jkr}\cos\phi \sum_{n=1}^{\infty} j^{-n}(2n + 1)j_n(kr)\frac{d}{d\theta}P_n(\cos\theta). \tag{4.18}$$

### 4.2.1 Radial components of the field

The field components generated by the scattering of waves from the sphere are associated with spherical boundary conditions. Therefore, the field at any point in the neighbourhood of $C$ depends upon the values of $r$, $\theta$ and $\phi$. In order to represent electromagnetic fields in terms of wave functions $\psi$, we let $\psi$ be a rectangular component of magnetic vector potential $\mathbf{A}$ or electric vector potential $\mathbf{F}$ and then the field is constructed as a superposition of two parts (this will be discussed further in this section). For this, we choose $\mathbf{A} = A_r\mathbf{u}_r$ and $\mathbf{F} = F_r\mathbf{u}_r$ where $\mathbf{u}_r$ is a unit vector in the radial direction. When $A_\theta$, $A_\phi = 0$, $A_r \neq 0$ and $F_r = 0$, the field is transverse magnetic (TM ) to $r$. Similarly, when $A_\theta = A_\phi = 0$, $F_r \neq 0$ and $A_r = 0$, the field is transverse electric (TE) to $r$ (see Appendix A for more details on TM and TE fields).

Now consider point $O$ in Figure 4.3 which has a radial distance $r$ from $C$, the centre of the sphere. In order to find the electromagnetic fields in the $r$-direction, it is convenient to construct solutions in terms of the magnetic vector potential $\mathbf{A}$ and the electric vector potential $\mathbf{F}$. This type of construction is fundamental electromagnetic theory and some of the relevant formulae are given in Appendix A. Here, some of these fundamental equations are used, similar to Harrington [8], to obtain field equations which represent $\mathbf{E}$ and $\mathbf{H}$ in terms of the vector potentials $\mathbf{A}$ and $\mathbf{F}$.

If the wave function $\psi$ is considered to be a rectangular component of a vector potential $\mathbf{A}$ or $\mathbf{F}$, there will be fields either TM to the $z$ direction or TE to the $z$ direction, respectively. However, we need the radial component of the electromagnetic field in order to construct a solution for the scattering problem in this coordinate system. Therefore it is convenient to consider a possible field in the $r$ direction as a result of a superposition of fields TM to $r$ and TE to $r$. Consider the two general equations for these vector potentials (equation (A.17) in Appendix A),

$$\nabla \times (\nabla \times \mathbf{A}) - k^2 \mathbf{A} = -\hat{y} \nabla \Phi^a, \tag{4.19}$$

$$\nabla \times (\nabla \times \mathbf{F}) - k^2 \mathbf{F} = -\hat{z} \nabla \Phi^f, \tag{4.20}$$

where $k = \omega\sqrt{\mu\varepsilon}$, $\Phi^a$ and $\Phi^f$ are arbitrary scalar functions. The electromagnetic fields of $\mathbf{E}$ and $\mathbf{H}$ can be obtained in terms of vector potentials $\mathbf{A}$ and $\mathbf{F}$ (equations (A.19) and (A.20)) as

$$\mathbf{E} = -\nabla \times \mathbf{F} + \frac{1}{\hat{y}} \nabla \times (\nabla \times \mathbf{A}), \tag{4.21}$$

$$\mathbf{H} = \nabla \times \mathbf{A} + \frac{1}{\hat{z}} \nabla \times (\nabla \times \mathbf{F}). \tag{4.22}$$

Letting $\mathbf{A} = A_{\mathrm{r}} \mathbf{u}_r$, that is, $\mathbf{A}$ is a vector potential for a spherical wave and expanding equation (4.19), we obtain

$$\frac{\partial^2 A_r}{\partial r \partial \theta} = -\hat{y} \frac{\partial \Phi^a}{\partial \theta}, \tag{4.23}$$

$$\frac{\partial^2 A_r}{\partial r \partial \phi} = -\hat{y}\frac{\partial \Phi^a}{\partial \phi}. \tag{4.24}$$

We can see that $\Phi^a$ satisfies both equations (4.23) and (4.24) if

$$\Phi^a = -\frac{1}{\hat{y}}\frac{\partial A_r}{\partial r}. \tag{4.25}$$

Using the vector identity $\nabla^2\mathbf{A} = \nabla(\nabla\cdot\mathbf{A}) - \nabla\times(\nabla\times\mathbf{A})$ , equation (4.19) can be expanded as

$$\nabla(\nabla\cdot\mathbf{A}) - \nabla^2\mathbf{A} - k^2\mathbf{A} = -\hat{y}\nabla\Phi^a. \tag{4.26}$$

As $(\nabla^2\mathbf{A})_r \neq \nabla^2 A_r$, we use the component of $\nabla\times(\nabla\times\mathbf{A})$ in the radial direction which in spherical coordinates is

$$\nabla\times(\nabla\times\mathbf{A})|_r = \frac{1}{r^2\sin\theta}\frac{\partial}{\partial\theta}\left(\sin\theta\frac{\partial A_r}{\partial\theta}\right) + \frac{1}{r^2\sin^2\theta}\frac{\partial^2 A_r}{\partial\phi^2}. \tag{4.27}$$

Now, using this result in equation (4.19) and substituting for $\Phi^a$ from equation (4.25), the resultant equation simplifies to

$$\frac{\partial^2 A_r}{\partial r^2} + \frac{1}{r^2\sin\theta}\frac{\partial}{\partial\theta}\left(\sin\theta\frac{\partial A_r}{\partial\theta}\right) + \frac{1}{r^2\sin^2\theta}\frac{\partial^2 A_r}{\partial\phi^2} + k^2 A_r = 0. \tag{4.28}$$

In spherical coordinates, the Laplacian of $A_r/r$ can be written as

$$\nabla^2(A_r/r) = \frac{1}{r^2}\frac{\partial}{\partial r}\left(r^2\frac{\partial(A_r/r)}{\partial r}\right) + \frac{1}{r^2\sin\theta}\frac{\partial}{\partial\theta}\left(\sin\theta\frac{\partial(A_r/r)}{\partial\theta}\right) + \frac{1}{r^2\sin^2\theta}\frac{\partial^2(A_r/r)}{\partial\phi^2}. \tag{4.29}$$

Equation (4.29) is simplified to

$$\nabla^2(A_r/r) = \frac{1}{r}\left(\frac{\partial^2 A_r}{\partial r^2} + \frac{1}{r^2\sin\theta}\frac{\partial}{\partial\theta}\left(\sin\theta\frac{\partial A_r}{\partial\theta}\right) + \frac{1}{r^2\sin^2\theta}\frac{\partial^2 A_r}{\partial\phi^2}\right). \tag{4.30}$$

Using the results in equation (4.30), equation (4.28) can be written as

$$\left(\nabla^2 + k^2\right)\frac{A_r}{r} = 0. \tag{4.31}$$

According to equation (4.31), $\frac{A_r}{r}$ is a solution to the scalar Helmholtz equation. Similarly, using the dual relationship, the radial component for $\mathbf{F} = \mathbf{u}_r F_r$ satisfies the equation

$$\left(\nabla^2 + k^2\right)\frac{F_r}{r} = 0, \tag{4.32}$$

and $\frac{F_r}{r}$ is a solution to the scalar Helmholtz equation. Accordingly, the field solutions to the scalar Helmholtz equation should be $\psi^a = \frac{A_r}{r}$ and $\psi^f = \frac{F_r}{r}$. Thus, the solutions to **E** and **H** fields can be formed by choosing the field vectors $\mathbf{A} = \mathbf{r}\psi^a$ and $\mathbf{F} = \mathbf{r}\psi^f$ where $\mathbf{r} = r\mathbf{u}_r$ is the radius vector from the origin. Therefore, with these field solutions, the field equations for **E** and **H** are found from (4.21) and (4.22), respectively, as

$$\mathbf{E} = -\nabla \times (\mathbf{r}\psi^f) + \frac{1}{\hat{y}}\nabla \times (\nabla \times (\mathbf{r}\psi^a)), \tag{4.33}$$

$$\mathbf{H} = \nabla \times (\mathbf{r}\psi^a) + \frac{1}{\hat{z}}\nabla \times (\nabla \times (\mathbf{r}\psi^f)), \tag{4.34}$$

where $\psi^a$ and $\psi^f$ are the wave functions of **A** and **F**, respectively.

From equations (4.33) and (4.34) we can see that the field $\psi$ in both **E** and **H** equations is always multiplied by $\mathbf{r} = r\mathbf{u}_r$. Therefore, there is another kind of *alternative spherical Bessel function* which has been defined by Schelkunoff [97] and later used by Harrington [8]. The spherical Bessel functions relate to the alternative spherical Bessel functions $\hat{B}_n(kr)$ as

$$\hat{B}_n(kr) = krb_n(kr). \tag{4.35}$$

Here for convenience, $\hat{B}_n(.)$ is used to distinguish this alternative spherical Bessel function from the ordinary Bessel function $B_n(.)$. Recall that the spherical Bessel functions relate to the ordinary Bessel functions [16] (see Appendix B) as

$$b_n(kr) = \sqrt{\frac{\pi}{2kr}}B_{n+1/2}(kr). \tag{4.36}$$

Therefore, from equations (4.35) and (4.36) the alternative spherical Bessel functions are related to the ordinary Bessel functions as

$$\hat{B}_n(kr) = \sqrt{\frac{\pi kr}{2}}B_{n+1/2}(kr). \tag{4.37}$$

The alternative form of differential equation (4.3) can be obtained by substituting $b_n$ using equation (4.35) into the Bessel equation:

$$\frac{d}{dr}\left(r^2\frac{d\left(\frac{\hat{B}_n}{kr}\right)}{dr}\right) + \left[(kr)^2 - n\left(n+1\right)\right]\frac{\hat{B}_n}{kr} = 0. \tag{4.38}$$

Then, the general form for $A_r$ and $F_r$ in terms of spherical Bessel function in equation (4.37) is $\sum_{n=0}^{\infty} g_n \hat{B}_n(kr) P_n(cos\theta)$. Multiplying equation (4.38) by $k/r$ and further simplifying we obtain

$$\left[\frac{d^2}{dr^2} + k^2 - \frac{n(n+1)}{r^2}\right] \hat{B}_n = 0. \tag{4.39}$$

Equation (4.39) is the differential equation that the spherical Bessel functions defined in equation (4.37) satisfy. Therefore $j_n(kr)$ in equation (4.18) should be replaced with $\hat{J}_n(kr)$ that can be found from equation (4.35), with $\hat{B}_n(kr)$ replaced with $\hat{J}_n(kr)$, as

$$\hat{J}_n(kr) = krj_n(kr). \tag{4.40}$$

Thus, the field which satisfies the wave function relationship in equation (4.18) is

$$E_r^i(r,\theta,\phi) = \frac{-jE_0}{(kr)^2}\cos\phi \sum_{n=1}^{\infty} j^{-n}(2n+1)\hat{J}_n(kr)\frac{d}{d\theta}P_n(\cos\theta), \tag{4.41}$$

where $\hat{J}_n(kr)$ is the alternative spherical Bessel functions of first kind, as defined in equation (4.40). The function $\hat{J}_n(.)$ was selected because the field must be finite at $r = 0$. The function $P_n(.)$ was selected because the field must be finite at $\theta = 0$ and $\pi$. The function $e^{-jkz}$ was selected because the input field is in the form of a wave that is $x$-polarized and travelling in the $z$ direction.

The point is described by spherical coordinates and so we need to find the electromagnetic field at $O$ in terms of the wave functions $\psi$ found in equation (4.9). By taking $\psi$ as a rectangular component of $\mathbf{A}$ or $\mathbf{F}$, the field components can be constructed. The explicit formulas for some field components in terms of $A_r$ and $F_r$ can now be found by expanding equations (4.21) and (4.22) with $\mathbf{A} = A_{\mathrm{r}}\mathbf{u}_r$ and $\mathbf{F} = F_{\mathrm{r}}\mathbf{u}_r$. The solutions for the incident vector potentials are,

1. in terms of the TM mode with $F_r = 0$:

$$E_r = \frac{1}{\hat{y}}\left(\frac{\partial^2}{\partial r^2} + k^2\right) A_r, \tag{4.42}$$

2. in terms of TE mode with $A_r = 0$:

$$H_r = \frac{1}{\hat{z}}\left(\frac{\partial^2}{\partial r^2} + k^2\right) F_r, \tag{4.43}$$

and,

3. with both $A_r$ and $F_r \neq 0$:

$$E_\theta = -\frac{1}{r\sin\theta}\frac{\partial F_r}{\partial \phi} + \frac{1}{\hat{y}r}\frac{\partial^2 A_r}{\partial r \partial \theta}, \qquad H_\theta = \frac{1}{r\sin\theta}\frac{\partial A_r}{\partial \phi} + \frac{1}{\hat{z}r}\frac{\partial^2 F_r}{\partial r \partial \theta}, \tag{4.44}$$

$$E_\phi = \frac{1}{r}\frac{\partial F_r}{\partial \theta} + \frac{1}{\hat{y}r\,\sin\theta}\frac{\partial^2 A_r}{\partial r \partial \phi}, \qquad H_\phi = -\frac{1}{r}\frac{\partial A_r}{\partial \theta} + \frac{1}{\hat{z}r\,\sin\theta}\frac{\partial^2 F_r}{\partial r \partial \phi}, \tag{4.45}$$

where $\hat{y}$ and $\hat{z}$ represent the characteristics of the medium as defined in equation (2.2). Equation (4.42) can be written as

$$E_r = \frac{1}{\hat{y}}\left(\frac{\partial^2}{\partial r^2} + k^2 - \frac{n(n+1)}{r^2}\right) A_r + \frac{n(n+1)}{\hat{y}r^2} A_r. \tag{4.46}$$

According to equation (4.39), the first term of $A_r$ on the right hand side of equation (4.46) vanishes to yield, for the incident wave,

$$E_r^i = \frac{n(n+1)}{\hat{y}r^2} A_r^i. \tag{4.47}$$

Then, by substituting for $E_r^i$ from equation (4.41)

$$A_r^i\,(r,\theta,\phi) = \frac{E_0\cos\phi}{\omega\mu}\sum_{n=1}^{\infty} c_n \hat{J}_n(kr)\frac{d}{d\theta}P_n(\cos\theta\,), \tag{4.48}$$

where

$$c_n = \frac{j^{-n}(2n+1)}{n(n+1)}. \tag{4.49}$$

Equation (4.48) gives the $r$-component of the magnetic vector potential of the incident wave in terms of the TM mode. Using a similar procedure with the magnetic field $H_r^i$, the $r$-component of the electric vector potential of the incident wave can be found as

$$F_r^i\,(r,\theta,\phi) = \frac{E_0\sin\phi}{k}\sum_{n=1}^{\infty} c_n \hat{J}_n(kr)\frac{d}{d\theta}P_n(\cos\theta\,), \tag{4.50}$$

where the constant term $c_n$ is the same as given in equation (4.49). This is the solution for the vector potential of the incident wave in terms of the TE mode. The $r$-component of the vector potentials of the scattered field in terms of both the TM and TE modes, can be found as

$$A_r^s(r,\theta,\phi) = \frac{E_0\cos\phi}{\omega\mu}\sum_{n=1}^{\infty} s_n \hat{H}_n^{(2)}(kr)\frac{d}{d\theta}P_n(\cos\theta), \tag{4.51}$$

$$F_r^s(r,\theta,\phi) = \frac{E_0\sin\phi}{k}\sum_{n=1}^{\infty} e_n \hat{H}_n^{(2)}(kr)\frac{d}{d\theta}P_n(\cos\theta), \tag{4.52}$$

where $s_n$ and $e_n$ are constants and $\hat{H}_n^{(2)}$ is the Hankel function of second kind associated with equation (4.37) which are chosen since $\hat{H}_n^{(2)}(kr) \to 0$ as $r \to \infty$. The total $r$-components of the vector potentials are found from equation (4.48), (4.50), (4.51) and (4.52) as

$$A_r(r,\theta,\phi) = \frac{E_0\cos\phi}{\omega\mu}\sum_{n=1}^{\infty}\left[c_n\hat{J}_n(kr) + s_n\hat{H}_n^{(2)}(kr)\right]\frac{d}{d\theta}P_n(\cos\theta), \tag{4.53}$$

$$F_r(r,\theta,\phi) = \frac{E_0\sin\phi}{k}\sum_{n=1}^{\infty}\left[c_n\hat{J}_n(kr) + e_n\hat{H}_n^{(2)}(kr)\right]\frac{d}{d\theta}P_n(\cos\theta). \tag{4.54}$$

Now we use the boundary conditions on the conducting sphere, with $r = a$, to find the constants $s_n$ and $e_n$. At the boundary (at $r = a$ where $a$ is the radius of the sphere), $E_\phi = E_\theta = 0$. We have found the relationship of $A_r$ and $F_r$ with the field components $E_\theta$ and $E_\phi$ in equations (4.44) and (4.45), respectively. Accordingly, by using these boundary conditions in equations (4.53) and (4.54), the two constants are found as

$$s_n = -c_n\frac{\hat{J}_n'(ka)}{\hat{H}_n^{(2)\prime}(ka)}, \tag{4.55}$$

$$e_n = -c_n\frac{\hat{J}_n(ka)}{\hat{H}_n^{(2)}(ka)}. \tag{4.56}$$

Using the solution in equation (4.37), the functions $\hat{J}_n(kr)$ and $\hat{H}_n^{(2)}(kr)$ can be written in terms of ordinary Bessel functions as

$$\hat{J}_n(kr) = \sqrt{\frac{\pi kr}{2}}J_{n+1/2}(kr), \tag{4.57}$$

$$\hat{H}_n^{(2)}(kr) = \sqrt{\frac{\pi kr}{2}} H^{(2)}_{n+1/2}(kr). \tag{4.58}$$

Now we substitute these formulas for $\hat{J}_n(kr)$ and $\hat{H}_n^{(2)}(kr)$ in equations (4.53) and (4.54) to obtain equations for $A_r$ and $F_r$ in terms of ordinary Bessel functions. Thus,

$$A_r(r,\theta,\phi) = -\frac{E_0 \cos\phi \sin\theta}{\omega\mu}\sqrt{\frac{\pi kr}{2}} \sum_{n=1}^{\infty} \left[c_n J_{n+1/2}(kr) + s_n H^{(2)}_{n+1/2}(kr)\right] P_n'(\cos\theta), \tag{4.59}$$

$$F_r(r,\theta,\phi) = -\frac{E_0 \sin\phi \sin\theta}{k}\sqrt{\frac{\pi kr}{2}} \sum_{n=1}^{\infty} \left[c_n J_{n+1/2}(kr) + e_n H^{(2)}_{n+1/2}(kr)\right] P_n'(\cos\theta), \tag{4.60}$$

since

$$\frac{d}{d\theta} P_n(\cos\theta) = -\sin\theta P_n'(\cos\theta). \tag{4.61}$$

### 4.2.2 Field components

In order to find the field component of $E_r$, we substitute for $A_r$ from equation (4.59) in equation (4.42), then simplify further to yield

$$\begin{aligned} E_r(r,\theta,\phi) = {} & \tfrac{1}{\hat{y}} \tfrac{E_0 \cos\phi \sin\theta}{4r\omega\mu}\sqrt{\tfrac{\pi k}{2r}} \Bigg( \sum_{n=1}^{\infty} \left[c_n J_{n+1/2}(kr) + s_n H^{(2)}_{n+1/2}(kr)\right] P_n'(\cos\theta) \\ & -k \sum_{n=1}^{\infty} \left[c_n J'_{n+1/2}(kr) + s_n H^{(2)}_{n+1/2}{}'(kr)\right] P_n'(\cos\theta) \\ & - k^2\sqrt{r} \sum_{n=1}^{\infty} \left[c_n J''_{n+1/2}(kr) + s_n H^{(2)}_{n+1/2}{}''(kr)\right] P_n'(\cos\theta)\Bigg) \\ & -\tfrac{1}{\hat{y}} \tfrac{k^2 E_0}{\omega\mu}\sqrt{\tfrac{\pi kr}{2}} \cos\phi \sin\theta \sum_{n=1}^{\infty} \left[c_n J_{n+1/2}(kr) + s_n H^{(2)}_{n+1/2}(kr)\right] P_n'(\cos\theta) \end{aligned} \tag{4.62}$$

where

$$
\begin{aligned}
J'_{n+1/2}(kr) &= \tfrac{J_{n-1/2}(kr)-J_{n+3/2}(kr)}{2}, \\
J''_{n+1/2}(kr) &= \tfrac{J_{n-3/2}(kr)-2J_{n+1/2}(kr)+J_{n+5/2}(kr)}{4}, \\
H^{(2)}_{n+1/2}{}'(kr) &= \tfrac{H^{(2)}_{n-1/2}(kr)-H^{(2)}_{n+3/2}(kr)}{2}, \\
H^{(2)}_{n+1/2}{}''(kr) &= \tfrac{H^{(2)}_{n-3/2}(kr)-2H^{(2)}_{n+1/2}(kr)+H^{(2)}_{n+5/2}(kr)}{4} \quad .
\end{aligned}
\tag{4.63}
$$

Similarly, the field component $E_\theta$ is found by substituting for $A_r$ and $F_r$ from equations (4.59) and (4.60), respectively, in equation (4.44) and further simplifying to yield

$$
\begin{aligned}
E_\theta\,(r,\theta,\phi) &= \tfrac{E_0}{kr}\cos\phi\sqrt{\tfrac{\pi kr}{2}}\sum_{n=1}^{\infty}\Big[c_nJ_{n+1/2}(kr)+e_nH^{(2)}_{n+1/2}(kr)\Big]P'_n(\cos\theta) \\
&-\tfrac{E_0}{\hat{y}r\omega\mu}\cos\phi\cos\theta\,\tfrac{1}{2}\sqrt{\tfrac{\pi k}{2r}}\sum_{n=1}^{\infty}\Big[c_nJ_{n+1/2}(kr)+s_nH^{(2)}_{n+1/2}(kr)\Big]P'_n(\cos\theta) \\
&-\tfrac{E_0}{\hat{y}r\omega\mu}\cos\phi\cos\theta\sqrt{\tfrac{\pi kr}{2}}k\sum_{n=1}^{\infty}\Big[c_nJ'_{n+1/2}(kr)+s_nH^{(2)}_{n+1/2}{}'(kr)\Big]P'_n(\cos\theta) \\
&+\tfrac{E_0}{\hat{y}r\omega\mu}\cos\phi\sin^2\theta\,\tfrac{1}{2}\sqrt{\tfrac{\pi k}{2r}}\sum_{n=1}^{\infty}\Big[c_nJ_{n+1/2}(kr)+e_nH^{(2)}_{n+1/2}(kr)\Big]P''_n(\cos\theta) \\
&+\tfrac{E_0}{\hat{y}r\omega\mu}\cos\phi\sin^2\theta\sqrt{\tfrac{\pi kr}{2}}k\sum_{n=1}^{\infty}\Big[c_nJ'_{n+1/2}(kr)+e_nH^{(2)}_{n+1/2}{}'(kr)\Big]P''_n(\cos\theta) \quad .
\end{aligned}
\tag{4.64}
$$

In order to find $E_\phi$, we substitute for $A_r$ and $F_r$ from equations (4.59) and (4.60), respectively, in equation (4.45). The resulting equation found for $E_\phi$ is

$$E_\phi(r,\theta,\phi) = -\tfrac{E_0}{kr}\sin\phi\cos\theta\sqrt{\tfrac{\pi kr}{2}}\sum_{n=1}^{\infty}\Big[c_n J_{n+1/2}(kr) + e_n H^{(2)}_{n+1/2}(kr)\Big]P'_n(\cos\theta)$$

$$+\tfrac{E_0}{kr}\sin\phi\sin^2\theta\sqrt{\tfrac{\pi kr}{2}}\sum_{n=1}^{\infty}\Big[c_n J_{n+1/2}(kr) + e_n H^{(2)}_{n+1/2}(kr)\Big]P''_n(\cos\theta)$$

$$+\tfrac{E_0}{2\hat{y}r\omega\mu}\sin\phi\sqrt{\tfrac{\pi k}{2r}}\sum_{n=1}^{\infty}\Big[c_n J_{n+1/2}(kr) + s_n H^{(2)}_{n+1/2}(kr)\Big]P'_n(\cos\theta)$$

$$+\tfrac{E_0}{\hat{y}r\omega\mu}\sin\phi\sqrt{\tfrac{\pi kr}{2}}k\sum_{n=1}^{\infty}\Big[c_n J'_{n+1/2}(kr) + s_n H^{(2)}{}'_{n+1/2}(kr)\Big]P'_n(\cos\theta) \quad . \tag{4.65}$$

### 4.2.3 Final solution for the total field

The field components $E_r$, $E_\theta$ and $E_\phi$ are the possible fields at point $O$ in this coordinate system. The total field depends upon the position of the point $O$ concerned. In other words, these field components can be changed in both magnitude and phase, depending upon the distance $r$ and the angles $\theta$ and $\phi$. Therefore, the total field $\mathbf{E}$ at the point $O$ is

$$\mathbf{E} = \mathbf{u}_r E_r + \mathbf{u}_\theta E_\theta + \mathbf{u}_\phi E_\phi, \tag{4.66}$$

where $E_r$, $E_\theta$ and $E_\phi$ are the field components found in equations (4.62), (4.64) and (4.65) and $\mathbf{u}_r$, $\mathbf{u}_\theta$ and $\mathbf{u}_\phi$ are the unit vectors to $r$, $\theta$ and $\phi$-directions, respectively.

Using an approach similar to the method used in the scattering problem of a cylindrical object, we now find a solution for the scattering field of the sphere at the measuring point. According to the set-up of the measuring system, the field is measured at the same antenna point from which the microwave signal is transmitted. Again, the need for an accurate alignment of the antenna applies here. As described in the two-dimensional approach, this result applies appropriately if the system is properly aligned to receive the maximum scattering response from the internal object. Suppose point $O$ is rotated to $O'$, (i.e. $\theta$ changes by an angle $\pi - \theta$)

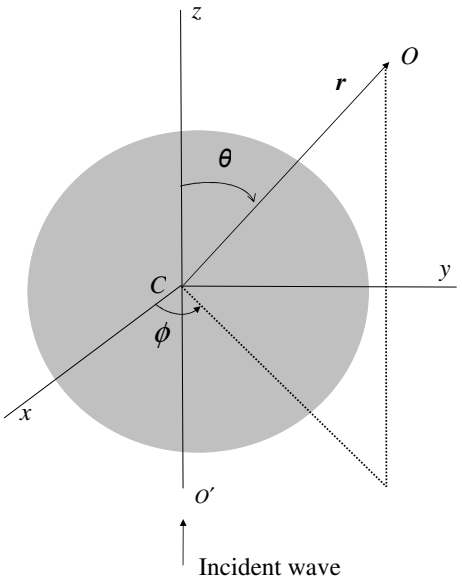


Figure 4.4: The spherical coordinate system with the field point $O$ rotated to measuring point.

then this point will lie along the $z$ axis and the distance $r$ becomes $d_1$, the distance to the centre of the sphere from the antenna point one. The spherical coordinate system after the rotation is shown in Figure 4.4. The new equation for the total field $\mathbf{E}$ at point $O'$ is

$$\mathbf{E} = [\mathbf{u}_r E_r + \mathbf{u}_\theta E_\theta + \mathbf{u}_\phi E_\phi] \underset{r=d_1}{\overset{\theta=\pi}{}} \tag{4.67}$$

where $E_r$, $E_\theta$ and $E_\phi$ are the field components at $O'$ which can be found using equations (4.62), (4.64) and (4.65), respectively, with $\phi = 0, \theta = \pi$, and $r = d_1$. Therefore, $\mathbf{E} = (0, E_\theta, 0)$. Thus, the total field at $O'$ is

$$E_\theta = E_0 \sqrt{\tfrac{\pi}{2kd_1}} \sum_{n=1}^{\infty} \left( c_n \left(1 - \tfrac{j}{2kd_1}\right) J_{n+1/2}(kd_1) \right.$$

$$\left. + \left(e_n - \tfrac{j\, s_n}{2kd_1}\right) H^{(2)}_{n+1/2}(kd_1) - j \left(c_n J'_{n+1/2}(kd_1) + s_n H^{(2)\,\prime}_{n+1/2}(kd_1)\right) \right) P'_n(-1) \quad . \tag{4.68}$$

In order to find the constants $s_n$, we substitute for $c_n$ from equation (4.49) in equation (4.55) and, by replacing $\hat{J}'_n(ka)$ and $\hat{H}_n^{(2)\prime}(ka)$ with $J'_n(ka)$ and $H_n^{(2)\prime}(ka)$, respectively using equation (4.37), and with further simplification we obtain

$$s_n = -\frac{j^{-n}(2n+1)}{n(n+1)} \frac{\left(J'_{n+1/2}(ka) + \frac{1}{2ka} J_{n+1/2}(ka)\right)}{\left(H_{n+1/2}^{(2)\prime}(ka) + \frac{1}{2ka} H_{n+1/2}^{(2)}(ka)\right)}. \tag{4.69}$$

Similarly the constants $e_n$ are found using equations (4.49), (4.56) and (4.37), and further simplifying to yield

$$e_n = -\frac{j^{-n}(2n+1)}{n(n+1)} \frac{J_{n+1/2}(ka)}{H_{n+1/2}^{(2)}(ka)}. \tag{4.70}$$

Now we substitute for the constants $c_n$, $s_n$ and $e_n$, from equations (4.49), (4.69) and(4.70), respectively, in equation (4.68), and obtain

$$E_\theta = E_0 \sqrt{\tfrac{\pi}{2kd_1}} \sum_{n=1}^{\infty} j^{-n} \tfrac{(2n+1)P'_n(-1)}{2} \left( \left(1 - \tfrac{j}{2kd_1}\right) J_{n+1/2}(kd_1) - H_{n+1/2}^{(2)}(kd_1) \tfrac{J_{n+1/2}(ka)}{H_{n+1/2}^{(2)}(ka)} \right.$$

$$\left. + \left( \tfrac{2kaJ'_{n+1/2}(ka) + J_{n+1/2}(ka)}{2kaH_{n+1/2}^{(2)\prime}(ka) + H_{n+1/2}^{(2)}(ka)} \right) \left( \tfrac{j}{2kd_1} H_{n+1/2}^{(2)}(kd_1) + jH_{n+1/2}^{(2)\prime}(kd_1) \right) - jJ'_{n+1/2}(kd_1) \right). \tag{4.71}$$

Equation (4.71) gives the solution for the scattering problem of the sphere inside the host when the field point is at the new position $O'$. This result is now appropriate for the use of a single antenna for both the transmit and receive signals. This is further explained in Chapter 6. However, using equation (4.66), this method can be generalised to obtain a solution for the forward problem at any point in the scattering field around the neighbourhood of the centre of the sphere (it is $C$ in this model). If we apply this model for internal object detection, then $a$ and $d_1$ in equation (4.71) represent the radius of the object and its distance from the surface of the host (the subscript "1" in $d_1$ is for antenna one). Similar to the two-dimensional wave problem, the forward equation found for the spherical waves also has an infinite series of wave functions. A reasonable solution can be obtained by computing partial sums of the series in equation (4.71) until they approach a constant value.

## 4.3 Inverse scattering problem of the conducting sphere

The inverse problem associated with the scattering from a sphere has to deal with the solutions obtained for forward problems in previous sections. There are field components in three different directions $r$, $\theta$ and $\phi$. When obtaining measurements in a location apart from the position of the antenna of transmission (when two antennas are used: one for transmission and one for receiving), then the angles $\phi$ and $\theta$ depend upon the position of the receiving antenna. With these data, the inverse method can compute the radius of the object and its distance from the measuring point. Again, the antenna alignment is very important here. It should be noted that the solution to the forward problems we obtained are for an ideal situation and therefore, in order to achieve good results, the microwave measurements must be obtained only after aligning the antenna to receive the maximum response from the foreign object.

The solutions to this inverse problem are found using the same iterative procedure explained previously in the one-dimensional and two-dimensional cases. However, the development of the inverse algorithm and computation of the unknowns are much harder compared to the previous cases as the forward equations need more terms in order to converge to sufficient accuracy. Again, for simplicity, we take the case with just two unknowns.

### 4.3.1 The general equation

Using the solutions to the forward problem obtained in equation (4.71), we form two general equations with two frequencies of the form

$$\Delta\mathbf{E} = \begin{bmatrix} M_1 - E_1 \\ M_2 - E_2 \end{bmatrix} = \begin{bmatrix} 0 \\ 0 \end{bmatrix}, \tag{4.72}$$

where $E_1$ and $E_2$ are found from equation (4.71) with $k = k_i$ (where $k_i$ are the wave numbers which can be found from equation (3.24) with frequencies $f_i$ for $i = 1, 2$) and $M_i$ for $i = 1, 2$ are the measured field components with these two frequencies. Equations for $E_1$ and $E_2$ in (4.72) are

$$E_i = -E_0\sqrt{\tfrac{\pi}{2k_id_1}}\sum_{n=1}^{\infty} j^{-n}\tfrac{(2n+1)P_n'(-1)}{2}\left(\left(1+\tfrac{j}{2k_id_1}\right)J_{n+1/2}(k_id_1)\right.$$

$$-\tfrac{H^{(2)}_{n+1/2}(k_id_1)\,J_{n+1/2}(k_ia)}{H^{(2)}_{n+1/2}(k_ia)} - \left(\tfrac{2k_iaJ'_{n+1/2}(k_ia)+J_{n+1/2}(k_ia)}{2k_iaH^{(2)\,\prime}_{n+1/2}(k_ia)+H^{(2)}_{n+1/2}(k_ia)}\right)\times \tag{4.73}$$

$$\left.\left(\tfrac{j}{2k_id_1}H^{(2)}_{n+1/2}(k_id_1) - jH^{(2)\,\prime}_{n+1/2}(k_id_1)\right) + jJ'_{n+1/2}(k_id_1)\,\right),$$

where $i = 1, 2$.

### 4.3.2 Jacobian matrix and the iterative procedure

The procedure of calculating the unknowns is very similar to that we used in the previous chapters and therefore the explanation here is limited. Consider

$$\begin{aligned} F_1 &= \Delta E_1 = M_1 - E_1, \\ F_2 &= \Delta E_2 = M_2 - E_2. \end{aligned} \tag{4.74}$$

We construct the Jacobian matrix of the form

$$\mathbf{J}(a, d_1) = \begin{bmatrix} J_{1,1}(a, d_1) & J_{1,2}(a, d_1) \\ J_{2,1}(a, d_1) & J_{2,2}(a, d_1) \end{bmatrix}, \tag{4.75}$$

where

$$J_{1,1}(a, d_1) = \frac{\partial E_1}{\partial a},\;\; J_{1,2}(a, d_1) = \frac{\partial E_1}{\partial d_1},\;\; J_{2,1}(a, d_1) = \frac{\partial E_2}{\partial a},\;\; J_{2,2}(a, d_1) = \frac{\partial E_2}{\partial d_1}, \tag{4.76}$$

in which we use the expression for the fields $E_1$ and $E_2$ (these are for two frequencies)

given by equation (4.73). (For convenience, we use only two variables to demonstrate the procedure of solving for unknowns.) The derivatives are explicitily

$$\mathbf{J}_{1,1}(a,d_1) =$$

$$E_0\sqrt{\tfrac{\pi}{2k_1d_1}}\sum_{n=1}^{\infty}\tfrac{j^{-n}(2n+1)}{2}P_n'(-1)\left(\frac{H_{n+1/2}^{(2)}(k_1d_1)}{\left(H_{n+1/2}^{(2)}(k_1a)\right)^2}\left(H_{n+1/2}^{(2)}(k_1a)k_1J_{n+1/2}'(k_1a)-\right.\right.$$

$$\left.J_{n+1/2}(k_1a)k_1H_{n+1/2}^{(2)\prime}(k_1a)\right) \;+\; \frac{j\left(\frac{H_{n+1/2}^{(2)}(k_1d_1)}{2k_1d_1}-H_{n+1/2}^{(2)\prime}(k_1d_1)\right)}{\left(H_{n+1/2}^{(2)\prime}(k_1a)+\frac{1}{2k_1a}H_{n+1/2}^{(2)}(k_1a)\right)^2}\times$$

$$\left(H_{n+1/2}^{(2)\prime}(k_1a)+\tfrac{1}{2k_1a}H_{n+1/2}^{(2)}(k_1a)\right)\left(k_1J_{n+1/2}''(k_1a)+\tfrac{1}{2a}J_{n+1/2}'(k_1a)-\right.$$

$$\left.J_{n+1/2}(k_1a)\tfrac{1}{2k_1a^2}\right)-\left(J_{n+1/2}'(k_1a)+\tfrac{1}{2k_1a}J_{n+1/2}(k_1a)\right)\times$$

$$\left.\left(k_1H_{n+1/2}^{(2)\prime\prime}(k_1a)+\tfrac{1}{2a}H_{n+1/2}^{(2)\prime}(k_1a)-H_{n+1/2}^{(2)}(k_1a)\tfrac{1}{2k_1a^2}\right)\right), \tag{4.77}$$

$$J_{1,2}(a,d_1) =$$

$$E_0\sqrt{\tfrac{\pi}{2k_1d_1}}\sum_{n=1}^{\infty}\tfrac{j^{-n}(2n+1)P_n'(-1)}{2}\left(-k_1J_{n+1/2}'(k_1d_1)\left(1+\tfrac{j}{2k_1d_1}\right)+J_{n+1/2}(k_1d_1)\tfrac{j}{2k_1d_1^2}+\right.$$

$$k_1H_{n+1/2}^{(2)}{}'(k_1d_1)\tfrac{J_{n+1/2}(k_1a)}{H_{n+1/2}^{(2)}(k_1a)}+j\left(\tfrac{J_{n+1/2}'(k_1a)+\frac{1}{2k_1a}J_{n+1/2}(k_1a)}{H_{n+1/2}^{(2)}{}'(k_1a)+\frac{1}{2k_1a}H_{n+1/2}^{(2)}(k_1a)}\right)\times$$

$$\left.\left(\tfrac{H_{n+1/2}^{(2)}{}'(k_1d_1)}{2d_1}-\tfrac{H_{n+1/2}^{(2)}(k_1d_1)}{2k_1d_1^2}-k_1H_{n+1/2}^{(2)}{}''(k_1d_1)\right)-jk_1J_{n+1/2}''(k_1d_1)\right)$$

$$-E_0\sqrt{\tfrac{\pi}{2k_1d_1^3}}\sum_{n=1}^{\infty}\tfrac{j^{-n}(2n+1)P_n'(-1)}{2}\left(-J_{n+1/2}(k_1d_1)\left(1+\tfrac{j}{2k_1d_1}\right)+\tfrac{H_{n+1/2}^{(2)}(k_1d_1)J_{n+1/2}(k_1a)}{H_{n+1/2}^{(2)}(k_1a)}+\right.$$

$$\left.j\left(\tfrac{J_{n+1/2}'(k_1a)+\frac{1}{2k_1a}J_{n+1/2}(k_1a)}{H_{n+1/2}^{(2)}{}'(k_1a)+\frac{1}{2k_1a}H_{n+1/2}^{(2)}(k_1a)}\right)\left(\tfrac{H_{n+1/2}^{(2)}(k_1d_1)}{2k_1d_1}-H_{n+1/2}^{(2)}{}'(k_1d_1)\right)-jJ_{n+1/2}'(k_1d_1)\right), \tag{4.78}$$

$$J_{2,1}(a,d_1) =$$

$$E_0\sqrt{\tfrac{\pi}{2k_2d_1}}\sum_{n=1}^{\infty}\tfrac{j^{-n}(2n+1)}{2}P_n'(-1)\left(\tfrac{H_{n+1/2}^{(2)}(k_2d_1)}{\left(H_{n+1/2}^{(2)}(k_2a)\right)^2}\left(H_{n+1/2}^{(2)}(k_2a)k_2J_{n+1/2}'(k_2a)-\right.\right.$$

$$\left.J_{n+1/2}(k_2a)k_2H_{n+1/2}^{(2)}{}'(k_2a)\right)+\frac{j\left(\frac{H_{n+1/2}^{(2)}(k_2d_1)}{2k_2d_1}-H_{n+1/2}^{(2)}{}'(k_2d_1)\right)}{\left(H_{n+1/2}^{(2)}{}'(k_2a)+\frac{1}{2k_2a}H_{n+1/2}^{(2)}(k_2a)\right)^2}\times$$

$$\left(H_{n+1/2}^{(2)}{}'(k_2a)+\tfrac{1}{2k_2a}H_{n+1/2}^{(2)}(k_2a)\right)\left(k_2J_{n+1/2}''(k_2a)+\tfrac{1}{2a}J_{n+1/2}'(k_2a)-\right.$$

$$\left.J_{n+1/2}(k_2a)\tfrac{1}{2k_2a^2}\right)-\left(J_{n+1/2}'(k_2a)+\tfrac{1}{2k_2a}J_{n+1/2}(k_2a)\right)\times$$

$$\left.\left(k_2H_{n+1/2}^{(2)}{}''(k_2a)+\tfrac{1}{2a}H_{n+1/2}^{(2)}{}'(k_2a)-H_{n+1/2}^{(2)}(k_2a)\tfrac{1}{2k_2a^2}\right)\right), \tag{4.79}$$

$$
\begin{aligned}
&J_{2,2}(a,d_1) = \\
&E_0\sqrt{\tfrac{\pi}{2k_2d_1}}\sum_{n=1}^{\infty}\tfrac{j^{-n}(2n+1)P_n'(-1)}{2}\left(-k_2J'_{n+1/2}(k_2d_1)\left(1+\tfrac{j}{2k_2d_1}\right)+J_{n+1/2}(k_2d_1)\tfrac{j}{2k_2d_1^2}+\right. \\
&k_2{H^{(2)}_{n+1/2}}'(k_2d_1)\tfrac{J_{n+1/2}(k_2a)}{H^{(2)}_{n+1/2}(k_2a)}+j\left(\tfrac{J'_{n+1/2}(k_2a)+\frac{1}{2k_2a}J_{n+1/2}(k_2a)}{{H^{(2)}_{n+1/2}}'(k_2a)+\frac{1}{2k_2a}H^{(2)}_{n+1/2}(k_2a)}\right)\times \\
&\left.\left(\tfrac{{H^{(2)}_{n+1/2}}'(k_2d_1)}{2d_1}-\tfrac{H^{(2)}_{n+1/2}(k_2d_1)}{2k_2d_1^2}-k_1{H^{(2)}_{n+1/2}}''(k_2d_1)\right)-jk_2J''_{n+1/2}(k_2d_1)\right) \\
&-E_0\sqrt{\tfrac{\pi}{2k_2d_1^3}}\sum_{n=1}^{\infty}\tfrac{j^{-n}(2n+1)P_n'(-1)}{2}\left(-J_{n+1/2}(k_2d_1)\left(1+\tfrac{j}{2k_2d_1}\right)+\tfrac{H^{(2)}_{n+1/2}(k_2d_1)J_{n+1/2}(k_2a)}{H^{(2)}_{n+1/2}(k_2a)}+\right. \\
&\left.j\left(\tfrac{J'_{n+1/2}(k_2a)+\frac{1}{2k_2a}J_{n+1/2}(k_2a)}{{H^{(2)}_{n+1/2}}'(k_2a)+\frac{1}{2k_2a}H^{(2)}_{n+1/2}(k_2a)}\right)\left(\tfrac{H^{(2)}_{n+1/2}(k_2d_1)}{2k_2d_1}-{H^{(2)}_{n+1/2}}'(k_2d_1)\right)-jJ'_{n+1/2}(k_2d_1)\right).
\end{aligned}
\tag{4.80}
$$

Each derivative consists of an infinite series indexed by $n$. Also, the Bessel functions and Hankel functions have first and second order derivatives given by

$$
{J'}_{n+1/2}(k_ia) = \frac{1}{2}\left(J_{n-1/2}(k_ia)-J_{n+3/2}(k_ia)\right), \tag{4.81}
$$

$$
{H^{(2)}_{n+1/2}}'(k_ia) = \frac{1}{2}\left(H^{(2)}_{n-1/2}(k_ia)-H^{(2)}_{n+3/2}(k_ia)\right), \tag{4.82}
$$

$$
{J''}_{n+1/2}(k_ia) = \frac{1}{4}\left(J_{n-3/2}(k_ia)-2J_{n+1/2}(k_ia)+J_{n+5/2}(k_ia)\right), \tag{4.83}
$$

$$
{H^{(2)}_{n+1/2}}''(k_ia) = \frac{1}{4}\left(H^{(2)}_{n-3/2}(k_ia)-2H^{(2)}_{n+1/2}(k_ia)+H^{(2)}_{n+5/2}(k_ia)\right), \tag{4.84}
$$

where $i = 1, 2$. A code was written in MATLAB for the above system. Each infinite series needs to be truncated at a point at which the truncation error is negligible. Once the Jacobian matrix is formed, the rest of the procedure is very similar to the method used in sections 2.4 and 3.2.2.

Again, this system needs a set of guess values for computing the unknowns. Starting from the initial guess values, the program runs for a number of iterations until the stopping criterion is satisfied. Here we use the minimum values of the difference of the field components, $|\Delta E_1|$ and $|\Delta E_2|$, for the stopping criterion. We have developed a scanning method for calculating unknowns and this will be discussed in Chapter 5.

## 4.4 Plane wave scattering from a non-conducting sphere

Here, we consider the object to be a non-conducting sphere. Similar to the approach for the non-conducting cylinder, we solve for the boundary condition of the object. The host model and its coordinate system are the same as in Figure 4.2 except that the circular object inside the model is assumed to be a non-conducting sphere.

### 4.4.1 Forward problem

The electrical properties inside and outside the non-conducting sphere are assumed to be same as those of the object and the host, respectively. The corresponding coordinate system is the same as in Figure 4.3. Here, the modal coefficients are found using the incident and scattered waves. Again, this approach is similar to the procedure used for the dielectric cylinder in section 3.3.1.

In equations (4.44) and (4.45), the solutions to $E_\theta$ and $H_\phi$ (with both $A_r, F_r \neq 0$) have been obtained by expanding equations (4.21) and (4.22). For the transverse magnetic (TM) mode, $F_r = 0$ and therefore, by substituting for $A_r$ from equation (4.48) in equations (4.44) and (4.45) and further simplifying, the impedance for the $n^{th}$ mode of the radially directed inward and outward-travelling waves at $r = a$

outside the sphere is obtained as

$$Z_{1,n} = -\frac{E_\theta}{H_\phi} = \frac{\frac{k_1}{\varepsilon_1} k_1 \hat{J}'_n(k_1 a) + \frac{k_1}{\varepsilon_1} C^{TM}_{s,n} \hat{H}^{(2)'}_n(k_1 a)}{\hat{J}_n(k_1 a) + C^{TM}_{s,n} \hat{H}^{(2)}_n(k_1 a)}, \tag{4.85}$$

where $\varepsilon_1$ and $k_1$ are the permittivity and the wave number of medium one (the host) outside the sphere, respectively, and $C^{TM}_{s,n}$ is the modal coefficient of the scattered wave for TM mode. Here, the media are assumed to be perfect and also $\mu = 1$. Similarly, the modal impedance for a radially directed wave inside the sphere, at $r = a$ is

$$Z_{2,n} = -\frac{E_\theta}{H_\phi} = \frac{\frac{k_2}{\varepsilon_2} \hat{J}'_n(k_2 a)}{\hat{J}_n(k_2 a)}, \tag{4.86}$$

where $\varepsilon_2$ and $k_2$ are the permittivity and the wave number of the medium inside the dielectric sphere (the object), respectively. The boundary conditions of the surface of the sphere $r = a$ require the tangential component of the electric and magnetic fields to be continuous and so, $Z_{1,n} = Z_{2,n}$ and, using equations (4.85) and (4.86), the modal coefficient $C^{TM}_{s,n}$ is found as

$$C^{TM}_{s,n} = -\frac{\hat{J}'_n(k_1 a)}{\hat{H}^{(2)'}_n(k_1 a)} \left[ \frac{\frac{\varepsilon_2 \hat{J}_n(k_2 a)}{\varepsilon_1 k_2 \hat{J}'_n(k_2 a)} - \frac{\hat{J}_n(k_1 a)}{k_1 \hat{J}'_n(k_1 a)}}{\frac{\varepsilon_2 \hat{J}_n(k_2 a)}{\varepsilon_1 k_2 \hat{J}'_n(k_2 a)} - \frac{\hat{H}^{(2)}_n(k_1 a)}{k_1 \hat{H}^{(2)'}_n(k_1 a)}} \right]. \tag{4.87}$$

Equation (4.87) is simplified to yield

$$C^{TM}_{s,n} = q_n R^{TM}_{s,n}. \tag{4.88}$$

where $q_n = \frac{-\hat{J}'_n(k_1 a)}{\hat{H}^{(2)'}_n(k_1 a)}$ and

$$R^{TM}_{s,n} = \frac{(\varepsilon_2 k_1 \hat{J}_n(k_2 a)\hat{J}'_n(k_1 a) - \varepsilon_1 k_2 \hat{J}_n(k_1 a)\hat{J}'_n(k_2 a))H^{(2)\prime}_n(k_1 a)}{(\varepsilon_2 k_1 \hat{J}_n(k_2 a)\hat{H}^{(2)\prime}_n(k_1 a) - \varepsilon_1 k_2 \hat{J}'_n(k_2 a)\hat{H}^{(2)}_n(k_1 a))\hat{J}'_n(k_1 a)}. \tag{4.89}$$

Similarly, for the transverse electric (TE) mode, $A_r = 0$ and therefore, by substituting for $F_r$ from equation (4.50) in equations (4.44) and (4.45) and further simplifying, the modal impedances outside and inside the sphere for the $n^{th}$ mode of the radially directed inward and outward-travelling waves at $r = a$ are found and

subsequently the modal coefficient for the TE mode is found as

$$C_{s,n}^{TE} = -\frac{\hat{J}_n(k_1 a)}{\hat{H}_n^{(2)}(k_1 a)} \left[ \frac{\frac{\sqrt{\varepsilon_2}\hat{J}'_n(k_2 a)}{\sqrt{\varepsilon_1}\hat{J}_n(k_2 a)} - \frac{\hat{J}'_n(k_1 a)}{\hat{J}_n(k_1 a)}}{\frac{\sqrt{\varepsilon_2}\hat{J}'_n(k_2 a)}{\sqrt{\varepsilon_1}\hat{J}_n(k_2 a)} - \frac{\hat{H}_n^{(2)\prime}(k_1 a)}{\hat{H}_n^{(2)}(k_1 a)}} \right]. \tag{4.90}$$

$$C_{s,n}^{TE} = a_n R_{s,n}^{TE}, \tag{4.91}$$

where $a_n = \frac{-\hat{J}_n(k_1 a)}{\hat{H}_n^{(2)}(k_1 a)}$ and

$$R_{s,n}^{TE} = \frac{(\sqrt{\varepsilon_2}\hat{J}'_n(k_2 a)\hat{J}_n(k_1 a) - \sqrt{\varepsilon_1}\hat{J}'_n(k_1 a)\hat{J}_n(k_2 a))H_n^{(2)}(k_1 a)}{(\sqrt{\varepsilon_2}\hat{J}'_n(k_2 a)\hat{H}_n^{(2)}(k_1 a) - \sqrt{\varepsilon_1}\hat{H}_n^{(2)\prime}(k_1 a)\hat{J}_n(k_2 a))\hat{J}_n(k_1 a)} \ . \tag{4.92}$$

Now, the scattered fields for the dielectric sphere are found using the modal coefficients in equations (4.88) and (4.91) with constants $s_n$ and $e_n$ in equations (4.55) and (4.56), respectively. That is,

$$c_n\, C_{s,n}^{TM} = c_n\, q_n\, R_{s,n}^{TM} = s_n\, R_{s,n}^{TM}\ ,$$

$$c_n\, C_{s,n}^{TE} = c_n\, a_n\, R_{s,n}^{TE} = e_n\, R_{s,n}^{TE}\ .$$

Thus, the new equations for the total vector components $A_r$ and $F_r$ analogous to equations (4.59) and (4.60) are

$$A_r(r,\theta,\phi) = \frac{E_0 \cos\phi}{\omega\mu} \sum_{n=1}^{\infty} \left[ c_n \hat{J}_n(kr) + s_n R_{s,n}^{TM} \hat{H}_n^{(2)}(kr) \right] \frac{d}{d\theta} P_n(\cos\theta\,), \tag{4.93}$$

$$F_r(r,\theta,\phi) = \frac{E_0 \sin\phi}{k} \sum_{n=1}^{\infty} \left[ c_n \hat{J}_n(kr) + e_n R_{s,n}^{TE} \hat{H}_n^{(2)}(kr) \right] \frac{d}{d\theta} P_n(\cos\theta\,), \tag{4.94}$$

where the constants $s_n$ and $e_n$ have been replaced with $s_n R_{s,n}^{TM}$ and $e_n R_{s,n}^{TE}$, respectively. The constants $R_{s,n}^{TM}$ and $R_{s,n}^{TE}$ modify equations (4.53) and (4.54) so that the parameters for the properties of both regions, inside and outside the sphere, appear inside the equations. The functions $\hat{J}_n(.)$, $\hat{H}_n^{(2)}(.)$ and their derivatives are given in equations (4.57), (4.58) and (4.63), respectively. Once these modified equations are obtained, the rest of the procedure for finding equations for the total field at the measuring point is similar to the procedure for the conducting sphere discussed in section 4.2.2.

Again, as in the case of the non-conducting cylinder, one can see that, when the permittivity inside the sphere is large, that is when $\epsilon_2$ in equations (4.87) and (4.90) is large, the coefficients $R_{s,n}^{TM}$ and $R_{s,n}^{TE}$ tend to unity and therefore equations (4.93) and (4.94) become similar to equations (4.53) and(4.54) which have been obtained for the case of a conducting sphere.

## 4.5 Inverse problem of the non-conducting sphere

The solutions to the inverse problem of the non-conducting sphere are found using the same iterative method we used previously. The two general equations are found from equation (4.72) with the new forward equations. These equations can be found by using the vector components found in equations (4.93) and (4.94) and following the same procedure discussed in sections 4.2.2 and 4.2.3. Thus, equation (4.68) is modified to obtain the field components at $O'$ for frequency $f_1$ and frequency $f_2$ as

$$\begin{aligned} E_{\theta,1} &= E_0\sqrt{\tfrac{\pi}{2k_1d_1}}\sum_{n=1}^{\infty}\Big(c_n\left(1-\tfrac{j}{2k_1d_1}\right)J_{n+1/2}(k_1d_1)+ \\ &+\left(e_nR_{s,n,1}^{TE}-\tfrac{js_nR_{s,n,1}^{TM}}{2k_1d_1}\right)H_{n+1/2}^{(2)}(k_1d_1)-j\Big(c_nJ'_{n+1/2}(k_1d_1)+ \\ &s_nR_{s,n,1}^{TM}H_{n+1/2}^{(2)\prime}(k_1d_1))\Big)P'_n(-1))\,, \end{aligned} \tag{4.95}$$

$$\begin{aligned} E_{\theta,2} &= E_0\sqrt{\tfrac{\pi}{2k_3d_1}}\sum_{n=1}^{\infty}\Big(c_n\left(1-\tfrac{j}{2k_3d_1}\right)J_{n+1/2}(k_3d_1)+ \\ &+\left(e_nR_{s,n,2}^{TE}-\tfrac{js_nR_{s,n,2}^{TM}}{2k_3d_1}\right)H_{n+1/2}^{(2)}(k_3d_1)-j\Big(c_nJ'_{n+1/2}\,(k_3d_1)+ \\ &s_nR_{s,n,1}^{TM}H_{n+1/2}^{(2)\prime}(k_3d_1))\Big)P'_n(-1))\,, \end{aligned} \tag{4.96}$$

where $R_{s,n,1}^{TM}$ and $R_{s,n,1}^{TE}$ are the coefficients for frequency $f_1$ which can be found from

equations (4.89) and (4.92) and $R^{TM}_{s,n,2}$ and $R^{TE}_{s,n,2}$ are the coefficients for frequency $f_2$ which can be obtained with $k_1$ replaced with $k_3$ and $k_2$ replaced with $k_4$, respectively. Equations for $R^{TM}_{s,n,2}$ and $R^{TE}_{s,n,2}$ are

$$R^{TM}_{s,n,2} = \frac{(\varepsilon_2 k_3 \hat{J}_n(k_4a)\hat{J}'_n(k_3a) - \varepsilon_1 k_4 \hat{J}_n(k_3a)\hat{J}'_n(k_4a))H_n^{(2)\prime}(k_3a)}{(\varepsilon_2 k_3 \hat{J}_n(k_4a)\hat{H}_n^{(2)\prime}(k_3a) - \varepsilon_1 k_4 \hat{J}'_n(k_4a)\hat{H}_n^{(2)}(k_3a))\hat{J}'_n(k_3a)} ,$$

$$R^{TE}_{s,n,2} = \frac{(\sqrt{\varepsilon_2}\hat{J}'_n(k_4a)\hat{J}_n(k_3a) - \sqrt{\varepsilon_1}\hat{J}'_n(k_3a)\hat{J}_n(k_4a))H_n^{(2)}(k_3a)}{(\sqrt{\varepsilon_2}\hat{J}'_n(k_4a)\hat{H}_n^{(2)}(k_3a) - \sqrt{\varepsilon_1}\hat{H}_n^{(2)\prime}(k_3a)\hat{J}_n(k_4a))\hat{J}_n(k_3a)} . \quad (4.97)$$

The constants $c_n, s_n$ and $e_n$ in equations (4.95) and (4.96) can be found from equations (4.49), (4.55) and (4.56), respectively. Wave numbers $k_1$ and $k_2$ for frequency $f_1$ and $k_3$ and $k_4$ for frequency $f_2$ can be found from equations (3.24) and (3.43), respectively. The rest of the procedure to find solutions for the inverse problem with the non-conducting sphere is similar to the method we explained in sections 3.3.2 and 4.3.

## 4.6 Results and discussion: spherical wave scattering

The forward equations of the conducting and non-conducting spheres obtained in the previous sections, were tested using MATLAB programs and the results are discussed in this section. A set of data which have been calculated using simulations was used to test the inverse algorithms.

### 4.6.1 Calculation of the field components

The two forward equations of the conducting sphere for frequency $f_1$ and frequency $f_2$ are found from equation (4.73). Using this result, the real and imaginary values of the field components of $E_1$ and $E_2$ were calculated for two sets of $a$ and $d_1$ values ($a$ and $d_1$ are the radius of the sphere and the distance to the measuring point from

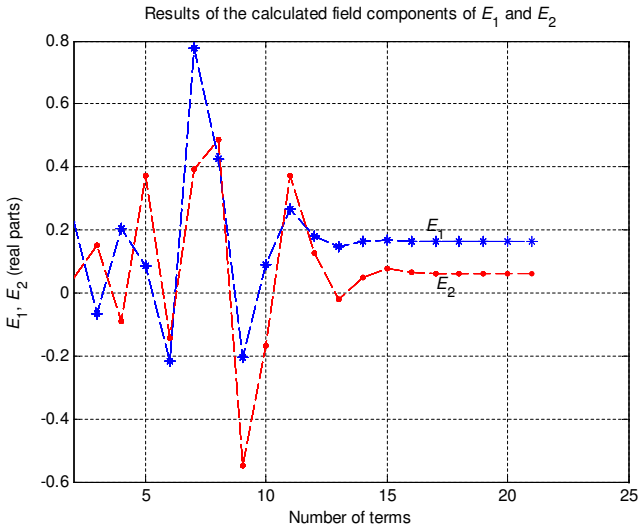


Figure 4.5: Plots of the real parts of $E_1$, $E_2$ calculated using the forward equation for a spherically-shaped object, with two different frequencies $f_1$ and $f_2$.

the centre of the sphere, respectively) and the results are plotted in Figures 4.5 and 4.6, respectively. ($E_1$ and $E_2$ are normalised with $E_0 = 1$ volts m$^{-1}$.) Note: convergence here is subjective - it is the level of accuracy to which we are looking (the level of convergence depends upon the number of terms used). We can see that the field components have converged after approximately sixteen terms. These results are acceptable.

### 4.6.2 Calculation of unknowns

Figures 4.7 and 4.8 show the plots of the calculated values of $a$, the radius of the sphere, and $d_1$, the distance to the centre of the sphere from the measuring point, respectively. Similar to the previous results for the calculation of unknowns, the corresponding values of $|\Delta E_1|$ and $|\Delta E_2|$ for frequencies $f_1$ and $f_2$, respectively, approach zero as can be seen in Figure 4.9. The inverse algorithm discussed in section 4.3 was used to obtain these results. For this test, two sets of guess values were

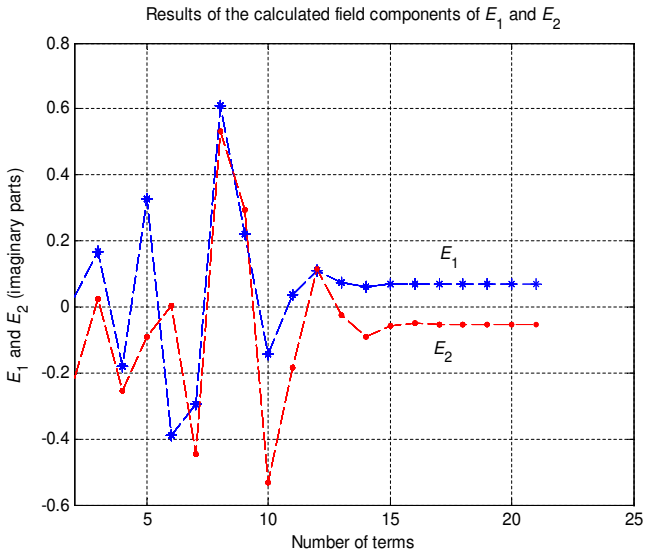


Figure 4.6: Plots of the imaginary parts of $E_1$, $E_2$ calculated using the forward equation for a spherically-shaped object, with two different frequencies $f_1$ and $f_2$.

used: $a$=0.0035 m, $d_1$=0.045 m and $a$=0.0025 m, $d_1$=0.035 m and, in the Figures 4.7, 4.8 and 4.9, the corresponding results are marked as (a) and (b), respectively. With each set of these guess values, the simulation process ran for 31 iterations.

In both of these simulation cycles, the algorithm has converged to the exact values $a$ and $d_1$ ($a$=0.003 m and $d_1$ =0.04 m) to machine accuracy. Also at the same time the corresponding values of $|\Delta E_1|$ and $|\Delta E_2|$ have reached zero (Figure 4.9). In practical applications, the measured data can have errors due to noise. Here we investigate the effect of this noise for the calculation of unknowns using the inverse method. With $a$ = 0.002 m and $d_1$ = 0.04 m, we calculated $E_{\theta,1}$ and $E_{\theta,2}$ from equations (4.95) and (4.96), respectively. Then errors were added into these calculated values and the unknowns were found using the inverse method of the sphere. The guess values were taken as $a$ =0.0022 m and $d_1$ =0.044 m while the real values of $a$ and $d_1$ are: $a$ =0.002 m and $d_1$ =0.04 m. The unknowns were calculated with 7, 3 and 0 percent errors added into the calculated values of $E_{\theta,1}$ and $E_{\theta,2}$.

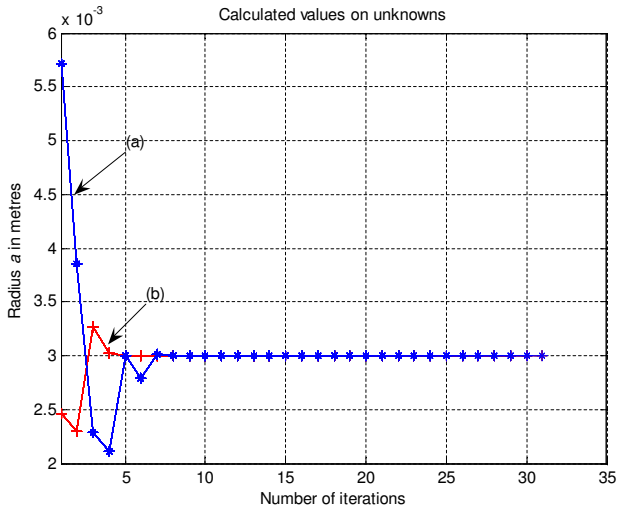


Figure 4.7: Plot of the calculated values of radius $a$ of the sphere using the inverse method. Plot (a) with guess values $a$=0.0035 m, $d_1$=0.045 m and (b) with $a$=0.0025 m, $d_1$=0.035 m (shown from the first iteration).

The errors were added into the real and imaginary values of the calculated $E_{\theta,1}$ and $E_{\theta,2}$ as a percentage. It was found that the results still converges to values $a$ and $d_1$ close to the original exact values but with some errors. The results are plotted in Figures 4.10 and 4.11. The calculated value of $a$ is more sensitive to noise compared to that of $d_1$. One should realise that the size of $a$ we used here is equal to 1/20 of the size of $d_1$ in metres. This effect is further investigated using the results of the cylindrical object and will be discussed in the next chapter.

We have calculated $a$ and $d_1$ with different sets of guess values. From these results we observed that the accuracy of the calculated values depends upon the guess values. If they are very far from the actual values one needs more iterations for the same accuracy. These limitations in the convergence process need to be further investigated and are discussed in the next chapter.

Solutions to the scattering problem of a non-conducting sphere discussed in

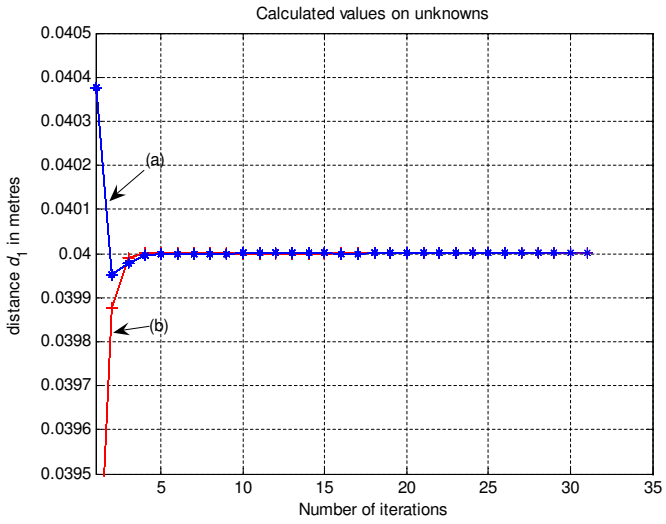


Figure 4.8: Plot of the calculated distance $d_1$ of the sphere using the inverse method. Plot (a) with guess values $a$=0.0035 m, $d_1$=0.045 m and (b) with $a$=0.0025 m, $d_1$=0.035 m (the initial guess and first iterations are outside of the scale used).

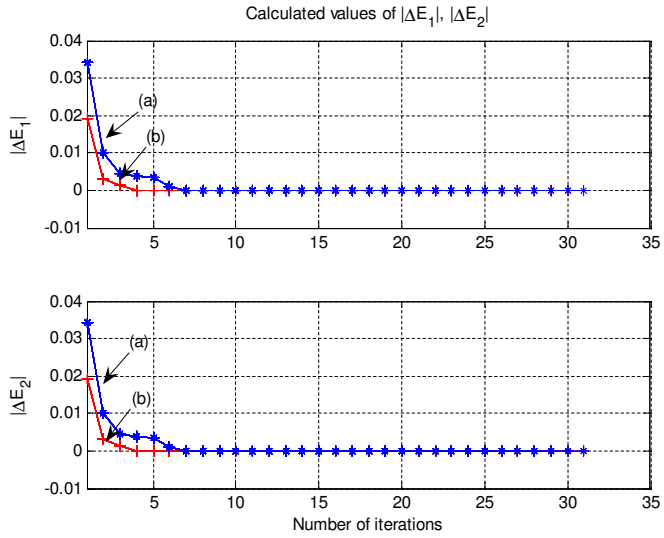


Figure 4.9: Values of $|\Delta E_1|$ and $|\Delta E_2|$ for each iteration within the inverse method.

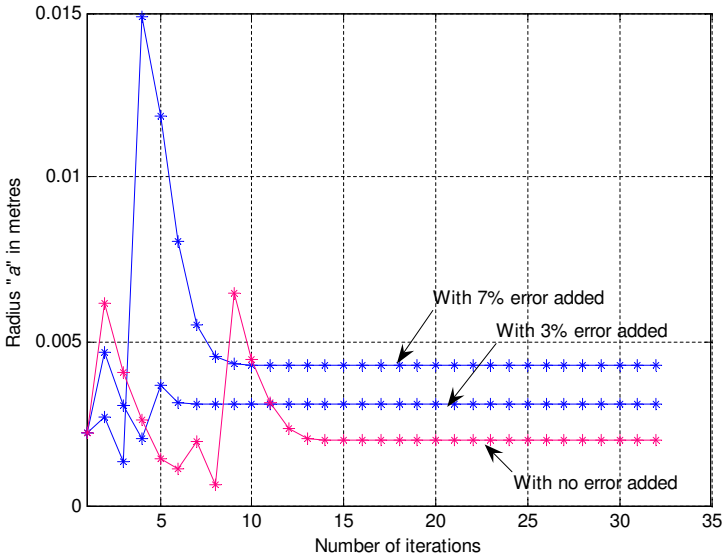


Figure 4.10: Calculated sphere radius $a$ with errors added into the field components.

this chapter may be appropriate for a more realistic situation. Even though the unknowns calculated here are only the radius of the sphere and its distance from the measuring point, we can also, in principle, find some other unknowns (such as electrical properties) using several frequencies. If the permittivities inside and outside the object are also included as unknowns, then there would be four unknowns and the algorithm could have a $4 \times 4$ Jacobian matrix constructed from four general equations by using four different frequencies.

The derivatives of the Jacobian matrix have many terms that include series of Bessel functions, Hankel functions and Legendre functions and therefore the iteration process is more complicated. On the other hand, if the guess values are closer to the exact values of the unknowns, then the results can easily (with a lesser number of terms) converge to constant values. This is not the case when the guess values are far away from the exact values of unknowns. In practical situations there may be only limited information available for the unknowns. Therefore, in the next

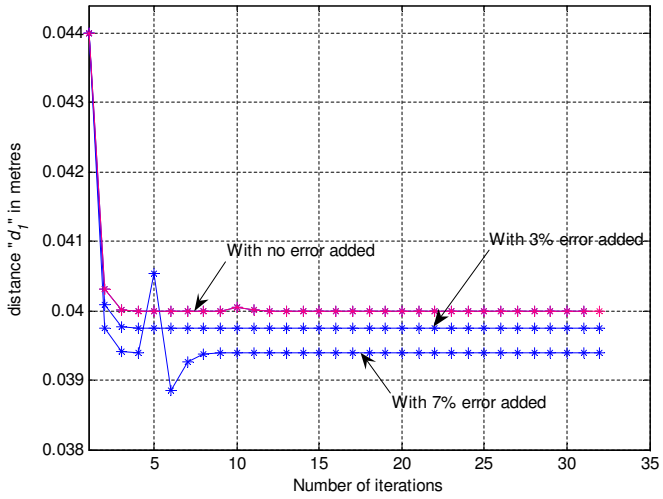


Figure 4.11: Calculated sphere distance $d_1$ with errors added into the field components.

chapter we develop a method to support the computation of the unknowns. This process scans for possible unknowns over certain ranges within which the values of the unknowns can be expected.

# Chapter 5

# Scattering response and computational stability

In previous chapters, both the forward and inverse problems of two-dimensional and three-dimensional scattering have been discussed. Here we further investigate the behaviour of the incident and backscattered field components with respect to variables such as the size of the object, the distance of the object from the measuring point and the dielectric properties of both the host and the scattering object. Also, an analysis is carried out for the inverse method to investigate the computational robustness with respect to the selection of guess values. In experimental or practical situations the data obtained with microwave measurements can have errors due to noise. Therefore the stability of the inverse method is further investigated with respect to errors added into phase and magnitude values of the field components. Overall, the motivation for these studies is to refine the forward and inverse methods for use in experimental and practical applications. We will use a two-dimensional case of a cylinder for illustration purposes.

## 5.1 Investigation on scattering response

According to the forward equations obtained in the previous chapters, both field components, $E_1$ and $E_2$ (for frequency $f_1$ and frequency$f_2$, respectively), can vary with the dielectric properties inside and outside the object as well as with the values of $a$ and $d_1$. In practice the size and the location of the object is not known but some information for the possible ranges within which these unknowns are expected may be available. When using the inverse method for computing unknowns, having this prior knowledge of the behaviour of the field components with respect to different values of the unknowns may be useful. In this section the response of the fields $E_1$ and $E_2$ is investigated when the scattering object takes different sizes, as well as different distances from the measuring point. Both the case of the object being a conducting cylinder and the subsequent modification of this to a non-conducting cylinder are considered. The latter case is tested by calculating $R_{c,n}$ for the asymptotic values when $\varepsilon_2$, the relative permittivity inside the cylinder, is large.

### 5.1.1 Field effect from the scattering object

The field components $E_1$ and $E_2$ were calculated using the forward equation (3.21) with frequency $f_1 = 2.0$ GHz and $f_2 = 2.2$ GHz of the of the conducting cylinder with different values of $a$ and $d_1$. For six pairs of $a$ and $d_1$ the corresponding field components were calculated using two different frequencies. For each pair of $a$ and $d_1$ the calculation process used sixteen terms after which $E_1$ and $E_2$ had converged to sufficient accuracy. The calculated results for the magnitudes of $E_1$ and $E_2$ are plotted in Figure 5.1 ($E_1$ and $E_2$ are normalised with $E_0 = 1$ volt m$^{-1}$).

The first three subplots show three sets of magnitudes for $E_1$ calculated with two sets of $a$ and $d_1$ values (set (1): $a = 0.004$ m and $d_1 = 0.02$ m, $a = 0.004$ m and $d_1 = 0.025$ m, and $a = 0.004$ m and $d_1 = 0.03$ m; set (2): $a = 0.002$ m and $d_1 = 0.025$ m, $a = 0.002$ m and $d_1 = 0.025$ m, and $a = 0.002$ m and $d_1 = 0.03$ m).

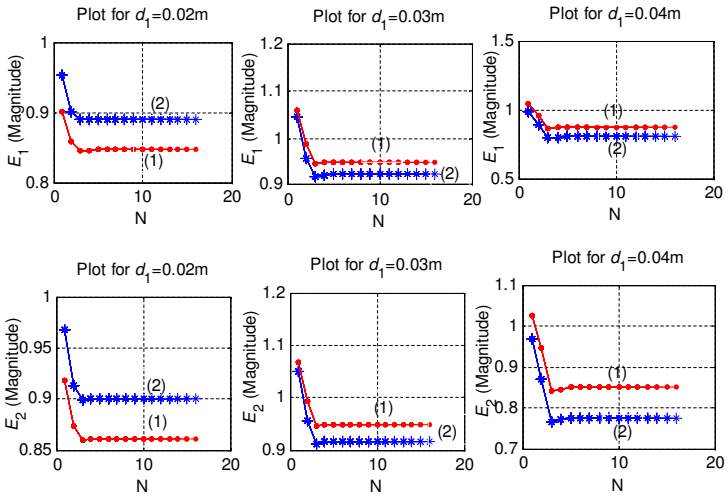


Figure 5.1: The calculated results of $E_1$ and $E_2$ (Magnitude) for different values of $a$ and $d_1$ (Plot (1) for $a$=0.004 m, Plot(2) for $a$=0.002 m).

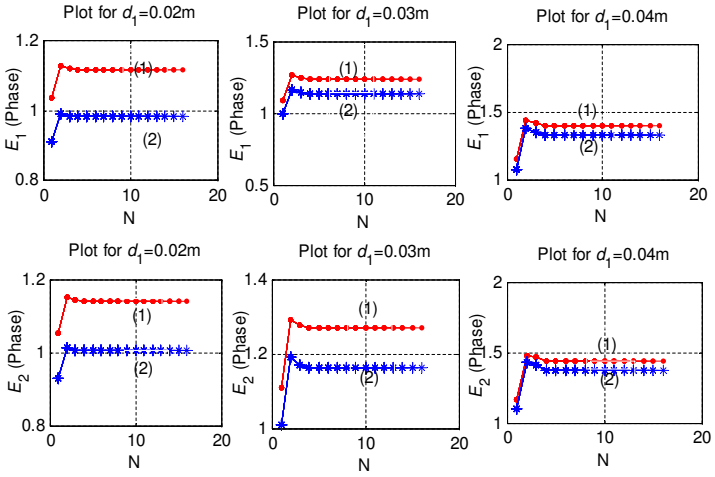


Figure 5.2: The calculated results of $E_1$ and $E_2$ (Phase) for different values of $a$ and $d_1$ (Plot (1) for $a$=0.004 m, Plot(2) for $a$=0.002 m).

Similarly, the second three subplots show three sets of calculated magnitudes of $E_2$ with the same two sets of $a$ and $d_1$ values. In each plot the $x$-axis shows N, the number of terms in the calculation process. Similarly, the phase values of the field components $E_1$ and $E_2$ were calculated and the results are plotted in Figure 5.2.

In order to study the variations of $E_1$ and $E_2$ further, we solved the forward equation using a large range of $a$ and $d_1$. The results are plotted in Figures 5.3 and 5.4. The magnitude values of $E_1$ and $E_2$ oscillate trending downwards with respect to the distance $d_1$. The phase values of $E_1$ and $E_2$ increase steadily with the distance of the object from the antenna. For convenience, we have plotted the phase values in a range between $\pm\pi$ (one can see that the phase values have sudden jumps of $2\pi$ and this is purely because we have presented the results modulo $2\pi$).

The oscillations observed in magnitude and also the rate of change of the phase are related to the frequency of the signal used in the equations of $E_1$ and $E_2$. The magnitude oscillation repeats at a distance of one half of the wavelength of the microwave frequency, while the phase changes from $-\pi$ to $+\pi$ at a distance equal to the wavelength of the microwave frequency. (The wavelengths of $E_1$ and $E_2$ are approximately 15 cm and 13.6 cm, respectively.)

### 5.1.2 Field effect from dielectric properties

In this section the response of the scattered field with respect to the dielectric properties of the object inside the host is investigated. The modifications made to the forward equations using a non-conducting cylinder in Chapter 3 have been taken into consideration for this analysis. The values of $R_{c,n,1}$ and $R_{c,n,2}$ in equations (3.41) and (3.42) were calculated with different values of permittivities inside and outside the non-conducting cylinder. The simulation process needs a similar approach to that used in the previous calculations as there are terms containing Bessel and Hankel functions in these equations. We found that at least 30 terms were needed

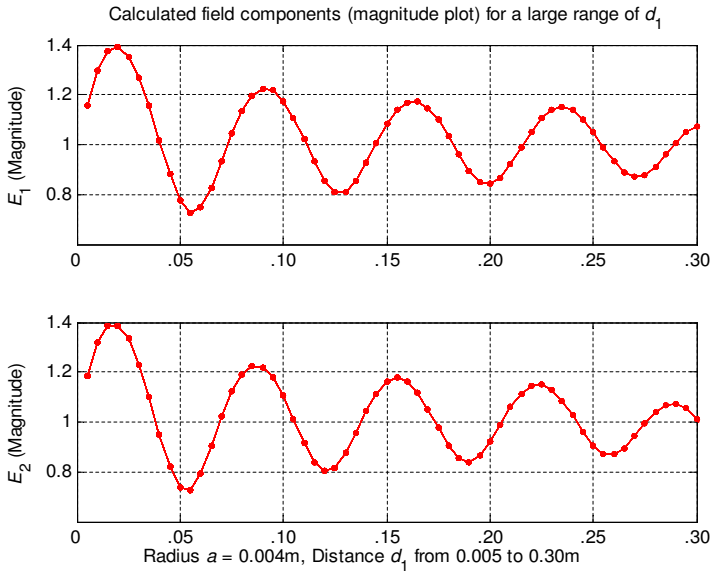


Figure 5.3: Calculated values (magnitude) of $E_1$ for 2.0 GHz and $E_2$ for 2.2 GHz as functions of $d_1$.

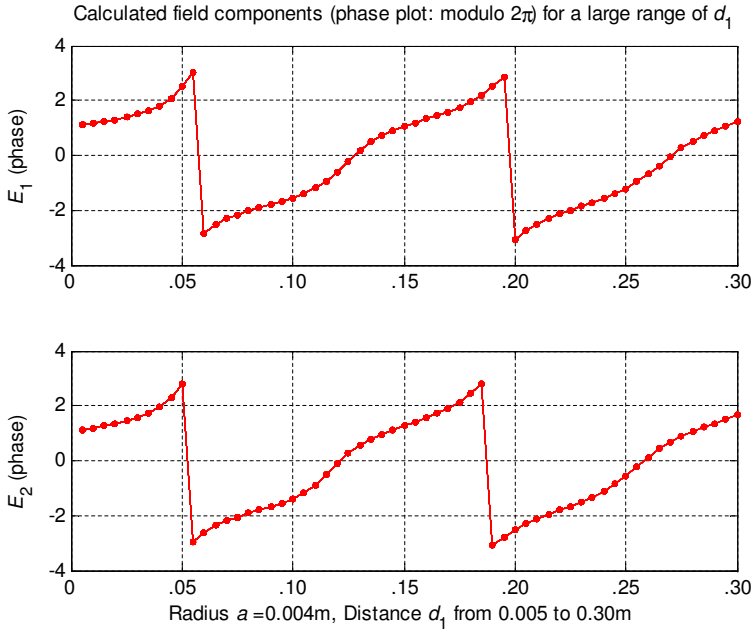


Figure 5.4: Calculated values of $E_1$ and $E_2$ (Phase) as functions of $d_1$.

for the series to converge to sufficient accuracy.

We used two frequencies and a set of reasonable values of $a$ and $d_1$ for these calculations. The relative permittivity outside the object ($\varepsilon_1$) was kept constant at 10 while the relative permittivity inside the object ($\varepsilon_2$) was changed logarithmically up to a very large value (from 10 to $10^{15}$ in 14 steps). The results obtained using equation (3.35) are plotted in Figure 5.5 ($R_{c,n,1}$ and $R_{c,n,2}$ have no units.). This figure illustrates some of the features of the magnitude of the coefficient $R_{c,n}$:

1. The magnitudes of $R_{c,n,1}$ and $R_{c,n,2}$ increase as the relative permittivity $\varepsilon_2$ increases.

2. When $\varepsilon_1 = \varepsilon_2,\ R_{c,n,1} = R_{c,n,2} = 0$.

3. As $\varepsilon_2 \to \infty$, magnitudes of $R_{c,n,1},\ R_{c,n,2} \to 1$.

With large values of $\varepsilon_2$, the calculated values of field components $E_1$ and $E_2$ are approximately equal to those calculated with a conducting cylinder.

## 5.2 Limitations of the inverse method

When calculating the unknowns using the inverse method, we encounter a number of limitations. Here we analyse those factors in order to develop a robust system for the detection process. Consider the initial guess values of $a$ and $d_1$. These have a large influence on the convergence to the solution. In section 3.6.1.2, Figure 3.8 illustrates the calculation of unknown $a$ and $d_1$ values using two different sets of initial guess values. The results are acceptable as both sets of iterations converge to the actual values of $a$ and $d_1$. However, for guess values further from the actual values this method does not converge.

Using the inverse method, we have computed a set of unknowns from different guess values. A set of known values ($a = 0.01$ m and $d_1 = 0.16$ m) was taken for

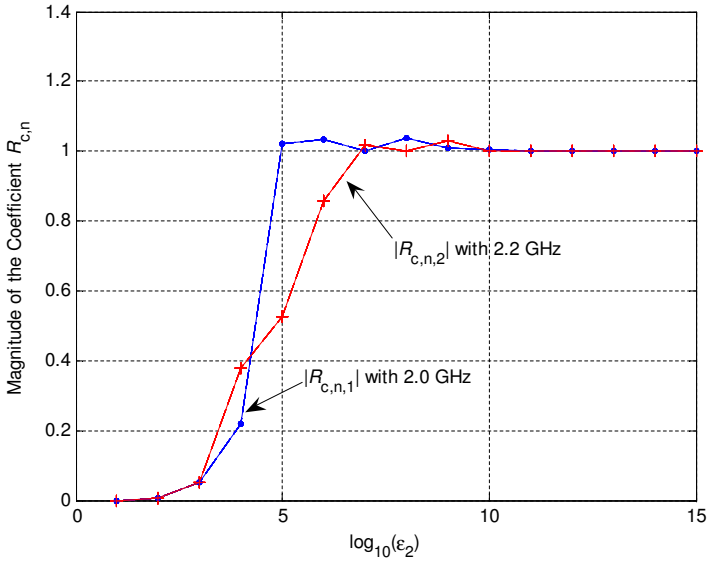


Figure 5.5: Calculated values of $R_{c,n}$ with different values of permittivity inside the object. (Note: the values have exceeded unity because of numerical error.)

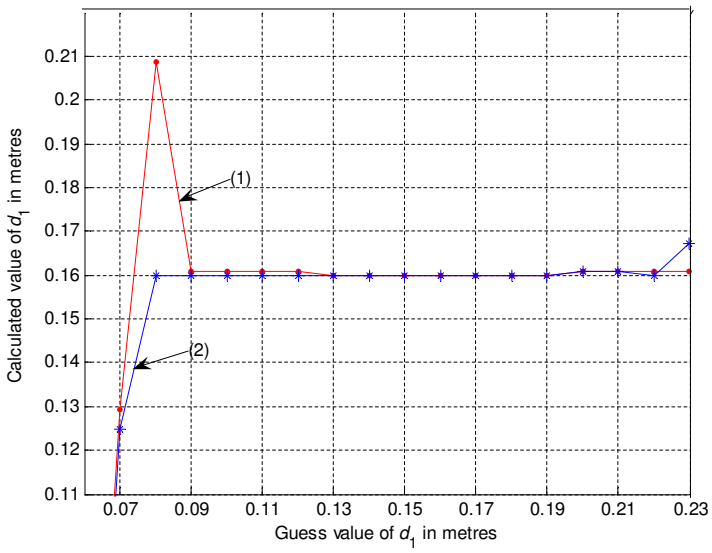


Figure 5.6: Calculated values of the distance $d_1$ for a range of guess values. (The exact value of $d_1$ is 0.16m.)

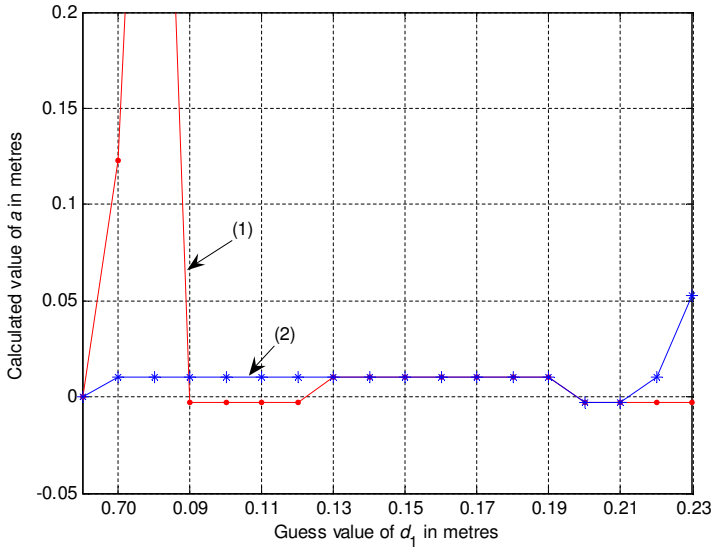


Figure 5.7: Calculated values of the radius $a$ for a range of guess values.(The exact value of $a$ is 0.01m.)

this computation. Each pair of guess values is iterated 30 times to compute $a$ and $d_1$. The total simulation process was then run for all pairs of guess values within a range. Final results of this simulation are plotted in Figures 5.6 and 5.7. Plot (1) was obtained with the guess values of $a = 0.006$ m and $d_1$ from 0.06 to 0.23 m in steps of 0.01 m, and plot (2) was obtained with the guess values of $a = 0.013$ m and $d_1$ from 0.06 to 0.23 m in steps of 0.01 m. These figures indicate that the calculated values of $a$ and $d_1$ are correct only within a certain range of guess values. Both calculated values of $a$ and $d_1$ are equal to their exact values only when the selected guess values of $d_1$ are within 0.13 to 0.19 m.

For each set of exact values of $a$ and $d_1$, there is a specific range of initial guess values within which the algorithm can calculate acceptable values for unknowns. We call this the *safe range*. The safe range for two specific examples is presented in table 5.1. However, the range of initial guess values of these unknowns can

Table 5.1 Range of guess values for convergence

| Exact values of $a$ and $d_1$ in metres. | | The range of guess values that converge to the exact values (safe range). | |
|---|---|---|---|
| $d_1$ | $a$ | $d_{1,G}$ | $a_G$ |
| 0.16 | 0.01 | 0.13 - 0.19 | 0.007 - 0.04 |
| 0.04 | 0.001 | 0.009 - 0.09 | 0.0002 - 0.002 |

be further extended at the expense of some acceptable errors in calculated results. Further to these results, the number of iterations needed for convergence varies with the selected guess values. The effects of these upon the computational performance will be discussed in the next section.

## 5.3 Stability analysis

This section demonstrates the results of an analysis carried out to test the performance of the inverse algorithm. First, the performance of the convergence process for calculating unknowns was tested using a large number of guess values. Secondly, the accuracy of the calculated results in the presence of noise in the measurement result is investigated.

We carried out a number of simulations to test our inverse algorithm for convergence. First, using the forward method for the conducting cylinder (equation (3.21)), the values of $E_1$ and $E_2$ were calculated for the values of $a$ and $d_1$ equal

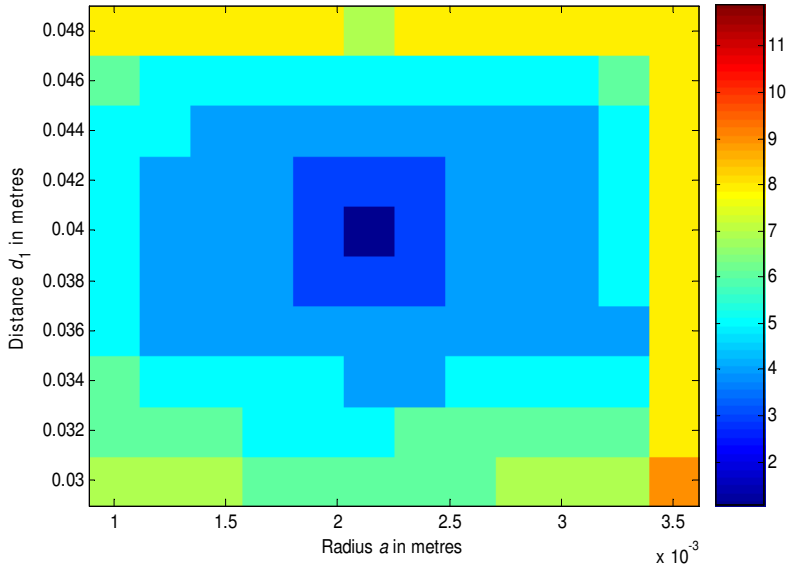


Figure 5.8: Number of iterations required for convergence of the simulations with different initial guess values of $a$ and $d_1$.

to 0.002 m and 0.04 m, respectively. Then, the inverse algorithm (section 3.2.2) was tested for convergence using a range of initial (guess) values of $a$ and $d_1$. The selected range starts from $a$ = 0.001 m and $d_1$= 0.03 m with steps of 0.0002 and 0.002 m, respectively, to $a$ = 0.0035 m and $d_1$= 0.048 m. Every pair of initial values was tested separately to determine the number of iterations, N, required for convergence. In Figure 5.8, the number of iterations is shown for each pair of initial (guess) values of $a$ and $d_1$. (See key at right-hand corner of the chart.)

When the guess values are closer to the exact values the system requires only a few iterations (blue colour regions in the chart). On the other hand, when the initial values are far away from the true values we require a large number of iterations and furthermore there exists a range beyond which we cannot expect any accuracy in the convergence. In our test, with less than 9 iterations, $a$ and $d_1$ can vary up to $\pm$50% and $\pm$25% from their actual values, respectively. For our example we found

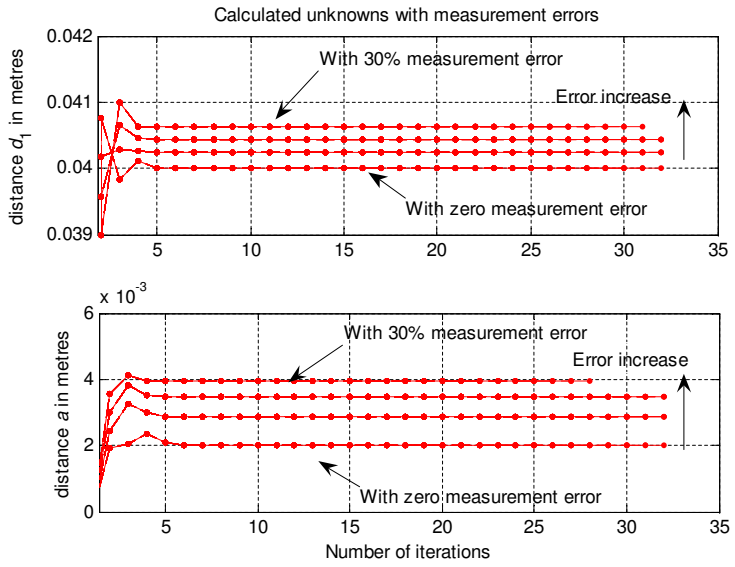


Figure 5.9: Inverse solutions for $a$ and $d_1$ from the field components with added measurement errors.

$a = 0.001$ to $0.003$ m and $d_1 = 0.03$ to $0.48$ m are the safe ranges for convergence to exact values of $a = 0.002$ m and $d_1 = 0.04$ m. We suggest that in general 20 iterations are used in order to determine whether the process is within a safe range before restarting the iteration process with alternative starting values for $a$ and $d_1$. It is important to display the result with double precision in order to obtain the exact solutions so that more realistic answers for the unknowns can be identified.

## 5.4 Error analysis

In a practical situation, there will be errors in the measurement process due to a number of factors such as inaccuracy in the calibration, antenna alignment, focusing, etc. Finding approximate solutions to the inverse problem, even with some errors in the measurement data (in an acceptable range), is then required.

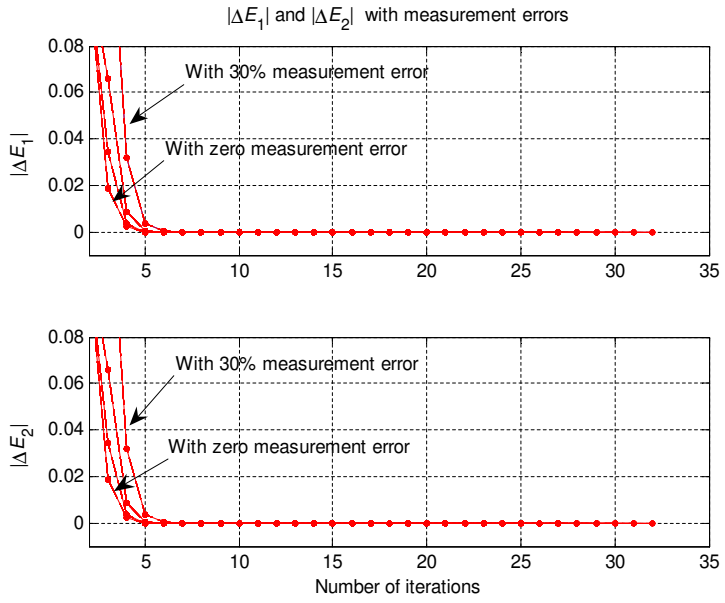


Figure 5.10: Calculated $\Delta E_1$ and $\Delta E_2$ from the field components with added measurement errors. (Initial guess and first iterations are out of the scale used.)

In section 4.6.2, we added errors into the field components to investigate the subsequent errors in the calculated unknowns. Further to this, here in this section, we carry out a series of tests to find the stability of the inverse method against the errors in the field components.

By adding errors to the results of the calculated values of the forward equation, that is $E_1$ and $E_2$ in equation (3.23), we simulated to find the corresponding errors in $a$ and $d_1$. With one set of guess values within the acceptable safe range, the values of $a$ and $d_1$ were computed using the inverse algorithm. We added 10%, 20% and 30% errors into the calculated field components in the general equation (3.23) to simulate the inverse algorithm for convergence. The results of the calculated unknowns $a$ and $d_1$, and $|\Delta E_1|$ and $|\Delta E_2|$ are shown in Figures 5.9 and 5.10, respectively. $|\Delta E_1|$ and $|\Delta E_2|$ have converged towards zero. When the error added into $E_1$ and $E_2$ is small the corresponding errors in the calculated values of $a$ and $d_1$ are relatively small.

Apart from this, we have carried out separate simulations to investigate the behaviour of the inverse algorithm at the presence of errors in the field components. The errors in the measurement values and the corresponding errors found in the real values of $a$ and $d_1$ are presented in Table 5.2 (this investigation is different to the test results discussed above).

Table 5.2 Result of the error analysis.

| Measurement error | Error in $a$ | Error in $d_1$ |
|---|---|---|
| 1% | 2.1% | 0.005% |
| 2% | 5.1% | 0.125% |
| 3% | 10.5% | 0.16% |
| 5% | 18.5% | 0.31% |
| 7.5% | 29.5% | 0.41% |
| 10% | 41.5% | 0.54% |

The percentage error in $a$ is quite large with large measurement errors (percentage error is defined as the percentage of the absolute difference of the calculated values and the exact values of the unknowns). We should note that our original value of $a$ is small compared to $d_1$ ($d_1$ is twenty times larger than $a$). However, in general, $d_1$ is less sensitive to measurement errors than $a$. In the application the value of $d_1$ which is the distance to the location of the object is more important. In practice some form of calibration could be performed to reduce the influence of the measurement error.

## 5.5 Scanning method

To obtain acceptable solutions using microwave measurement data in practical applications, the inverse method has to deal with two major situations. One is the noise which can be included in the measurement data (section 5.4). The other is the lack of information about the unknowns. When finding solutions to the inverse problem in simulations, we have information about the exact values of the unknowns, but in practical applications the information is more limited. For example, in breast tumour detection, it is known that a tumour must be within a possible range of 0 to 6 cm within the breast. Therefore, we develop an approach capable of finding suitable solutions within an appropriate range, depending upon the type of application.

### 5.5.1 Safe range

The final result of the inverse method depends upon the following factors:

1. Selection of the guess values.
2. Number of terms required for the forward equations to converge.
3. Stopping criteria of the simulation process.
4. Number of iterations required for the calculation process.
5. The values of the residuals at convergence (to converge to zero).
6. The values of the calculated unknowns.

In practical applications, in order to find the unknowns using the measured data, we need to know the possible safe regions that can be used in the inverse algorithm. The safe region is the limit of the guess values of unknowns ($a$ and $d_1$) where the general equation safely converges to a feasible value (real, positive and of the right

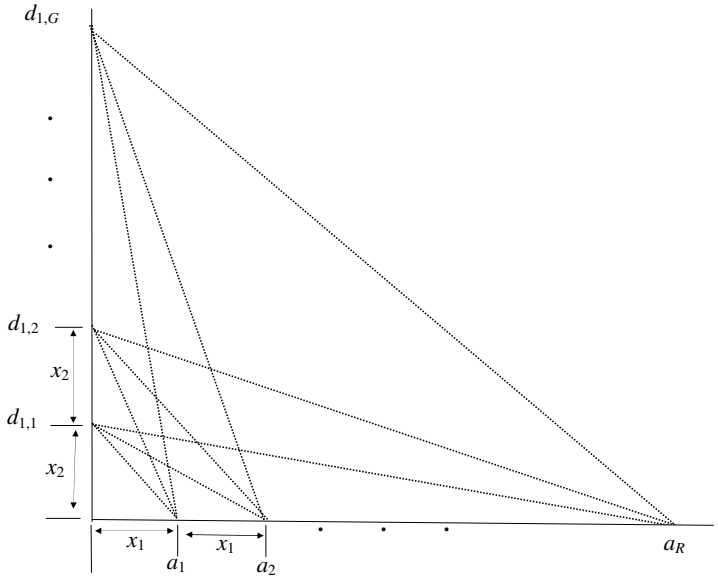


Figure 5.11: Distribution of the chosen grid points: Convergence test for the safe region.

magnitude). This can be found by using several guess values (section 5.3). That is, using a number of guess values, $a_g$, $d_{1,g}$ the safe regions for $a$ and $d_1$, respectively, are found such that within these regions the system converges safely to the exact known values of $a$ and $d_1$. Then, by using these estimates with step- size of $x_1$ and $x_2$, a complete test for finding the unknowns can be performed. Here, the ranges within which the unknown values of $a$ and $d$ can be expected are divided equally are called the safe ranges. This is described in the following paragraph and illustrated in Figure 5.11.

### 5.5.2 Test for convergence

In order to find the exact solution for the unknown radius of the object and its position, the scanning method requires a series of tests. The distribution of the grid points chosen for the convergence test is shown in Figure 5.11. The procedure is

as follows: Take $a_r, r = 1, \ldots, R$ where $a_r$ denotes the $r^{th}$ candidate object radius from a set of radii ranging from $a_1$ in steps of $x_1$ to $a_R$ where $x_1$ is the smallest safe range for the radius $a$. Similarly for the antenna one, $d_{1,g}, g = 1, \ldots, G,$ where $d_{1,g}$ denotes the $g^{th}$ candidate object distance from a set of distances ranging from $d_{1,1}$, in steps of $x_2$ to $d_{1,G}$ where $x_2$ is the smallest safe range for the distance $d_1$. Then, we use a set of $G \times R$ tests where the initial hypothesis is that either no object is present at distance $d_{1,g}$ or the object radius $a_r$ is incorrect. An alternative candidate is selected sequentially for the next test from the set of candidate identities;

$$\left\{ \begin{bmatrix} a_1 \\ d_{1,1} \end{bmatrix}, \begin{bmatrix} a_1 + x_1 \\ d_{1,1} \end{bmatrix}, \begin{bmatrix} a_1 + 2x_1 \\ d_{1,1} \end{bmatrix}, \ldots \right.$$
$$\left. \ldots, \begin{bmatrix} a_R \\ d_{1,1} \end{bmatrix}, \begin{bmatrix} a_1 \\ d_{1,1} + x_2 \end{bmatrix}, \begin{bmatrix} a_1 + x_1 \\ d_{1,1} + x_2 \end{bmatrix}, \ldots, \begin{bmatrix} a_R \\ d_{1,1} + x_2 \end{bmatrix}, \ldots, \begin{bmatrix} a_R \\ d_{1,G} \end{bmatrix} \right\}. \tag{5.1}$$

The validity of the initial hypothesis is decided using criteria which depend upon certain conditions (for example, that the distances are feasible and positive real). Results of each simulation (that is real and imaginary values of $\Delta E$, object radius $a$ and distance $d_1$) are compared at the end of each test according to:

- the initial hypothesis is selected if the results do not exactly match the criteria,
- otherwise, the alternative hypothesis is selected to stop the testing process and to provide estimates for the unknowns.

The criteria for accepting the solutions as correct are decided by considering the final value of $|\Delta E|$ and the calculated values of $a$ and $d_1$. Further investigation on this has been carried out with an experimental situation so as to confirm the accuracy and the results are discussed in Chapter 7.

In the simulation test, we calculated unknowns when $|\Delta E| \leq 1 \times 10^{-8}$ and $a$ and $d_1$ are purely positive and real. We set the total scanning range $a$ from 0.0005 to

0.004 m and $d_1$ from 0.005 to 0.06 m to test for some known pairs of $a$ and $d_1$ values using the inverse method. Using a 3.2 GHz, P4 processor our program took less than a minute to find $a$ and $d_1$ even if their exact values are in the extreme positions of this scanning range (exact values of $a$ and $d_1$ are 0.004 and 0.06 m, respectively). This procedure can be used to compute the radius of the object and its distance from other antenna positions using respective phase and magnitude values of the field components. Then it is a matter of geometry to find the location of the object within the host.

## 5.6 Chest-wall effect

In this section the effect of the chest wall on the signal scattered from the tumour is discussed. According to the biological structure, it is hard to distinguish the effect of the signal reflected from the chest wall completely but, it may be possible to minimise the prediction error of the values of the calculated unknowns by considering the backscattering effect in the proximity of chest muscle. We are analysing the signal in the frequency domain. Therefore, the influence of various sources of clutter that can obscure the tumour detection do not severely affect the results when compared to the noise and dispersion effects in time-domain microwave breast imaging methods [81, 104].

In practical applications, the field at the antenna point is found using microwave measurements. Then the values for the unknown tumour radius and its distance from the breast surface may be calculated using the inverse method. However, as well as the reflection from the tumour, the reflection from the chest wall can have a significant effect on the measurements. Therefore, using the same model we shall now discuss the effect of the chest wall which we assume to be just behind the (presumed to be) conducting cylinder.

When the signal is sent from the antenna front-end, we would expect that a large

amount of its energy would be dissipated through the chest wall while only a small amount of the signal is reflected back to the antenna. From equations (3.14) and (3.36), the new equation for the resultant field at the antenna due to the reflection of both the tumour and the chest wall may be found as

$$E_{1,z}^{s,t}(d_1, f_1) = E_0 \sum_{n=-\infty}^{\infty} j^{-n} \left[ - \frac{J_n(k_1 a)}{H_n^{(2)}(k_1 a)} R_{c,n} H_n^{(2)}(k_1 d_1) \right] e^{jn\phi} + E_{1,z}^{s,w}(d_1, f_1), \quad (5.2)$$

where $E_{1,z}^{s,w}(d_1, f_1)$ is the reflected signal from the chest wall. If the magnitude of the reflection coefficient of the chest wall is $R_w$ then

$$E_{1,z}^{s,w}(d_1, f_1) = E_0 R_w e^{j(k_1 d_1 + 2k_1(y - d_1) + \theta_w)}, \quad (5.3)$$

where $y$ is the distance to the chest wall from the antenna point and $\theta_w$ is the phase shift of the reflected signal at the wall boundary. Here, the total field is considered as approximately equal to the superposition of the scattered field from the tumour and the scattered field from the chest wall. We show this using a similar situation in the experimental study which is explained in Chapter 6.

Now, equation (3.37) can be modified (this is the forward equation of the two-dimensional scattering problem of the dielectric cylinder after $\phi$ is rotated by an angle $\pi - \phi$) to include the chest-wall effect. The resultant field at the antenna due to the reflection of both the cylinder and the chest wall is

$$E_{1,z}^{t}(d_1, f_1) = E_0 \sum_{n=-\infty}^{\infty} j^{n} \left[ J_n(k_1 d_1) - \frac{J_n(k_1 a)}{H_n^{(2)}(k_1 a)} R_{c,n} H_n^{(2)}(k_1 d_1) \right] + E_{1,z}^{s,w}(d_1, f_1). \quad (5.4)$$

where $E_{1,z}^{s,w}(d_1, f_1)$, the reflected signal from the chest-wall at the receiving point in the absence of an object which would of course present practical difficulties for in-vivo breast tumour detection, is replaced with equation (5.3) (here, we assume that there no effect due to multiple scattering). Once the total field is measured at the antenna point, the same procedure of the inverse method is used to find more accurate values for the unknown tumour radius and location.

## 5.7 Frequency selection

When a microwave signal is propagating in a lossy medium the wave is attenuated in the direction of travel. Equation (3.10) which was used for a loss-less medium can now be modified for a lossy medium and the wave number at frequency $f_1$ can be written as

$$k_1^l = \frac{\omega_1}{c}\sqrt{(\varepsilon' - j\varepsilon'') - \frac{j\,\sigma}{\omega_1 \varepsilon_0}}\ , \tag{5.5}$$

where $\sigma$ is the conductivity, $\varepsilon'$ is the relative permittivity, $\varepsilon''$ is the relative dielectric loss factor and $\varepsilon_0$ is the permittivity of free space given by $8.854 \times 10^{-12}$ F/m. Here we assume the relative permeability does not make a significant contribution to the loss of the signal and therefore equate it to 1.

The measured data for the above properties of both the breast tissue and the tumour are available in the literature [104, 54]. By selecting reasonable values for the properties of the tumour and the breast tissue, we can find the wave number for the breast tissue using equation (5.5). Then, equation (3.10) can be replaced with equation (5.5) when used in practical applications. According to the results of the practical measurements [54, 57], the permittivity and conductivity of a tumour are significantly different to normal breast tissue. The effect of conductivity on the wave propagation can be considered as having a smaller contribution at high frequencies (this can be seen from equation (5.5)) compared to that of the permittivity.

The breast tissue in which the microwave signal travels is frequency dispersive. This can be clarified when looking at the experimentally determined results in [104, 105]. The relative dielectric constant of a tumour is significantly higher at low frequencies of the order of few MHz, but it is highly frequency dispersive at low frequencies. Therefore, it is very important to select a range of frequencies in which there exists a minimal variation in the electrical properties of both the breast tissue and the tumour.

Apart from this, the scan-depth can vary with the wavelength of the signal. Accordingly, a frequency range of 1-3 GHz can be used for this application.

# Chapter 6

# Laboratory experiment for microwave detection

The solutions obtained for the two-dimensional and three-dimensional scattering problems are tested experimentally in this chapter. First, the experimental set-up and the measurement procedure are described. Then the measurement results are analysed for the purpose of detecting a foreign object using microwave measurements. The experimental results have a good agreement with the analytically calculated results.

## 6.1 Measurement system

The experimental set-up for microwave detection is shown in Figure 6.1. This arrangement is similar to the microwave application system shown in Figure 1.3. In this experiment, the backscattered field measured at a single antenna is studied in detail. The arrangement is as follows: The Network Analyser (NA) sends the microwave signal to the antenna through the waveguide. The scattering object, which is kept in front of the antenna, is illuminated by the microwave signal radiated from its aperture. In this experiment, the air represents the host in the model which was

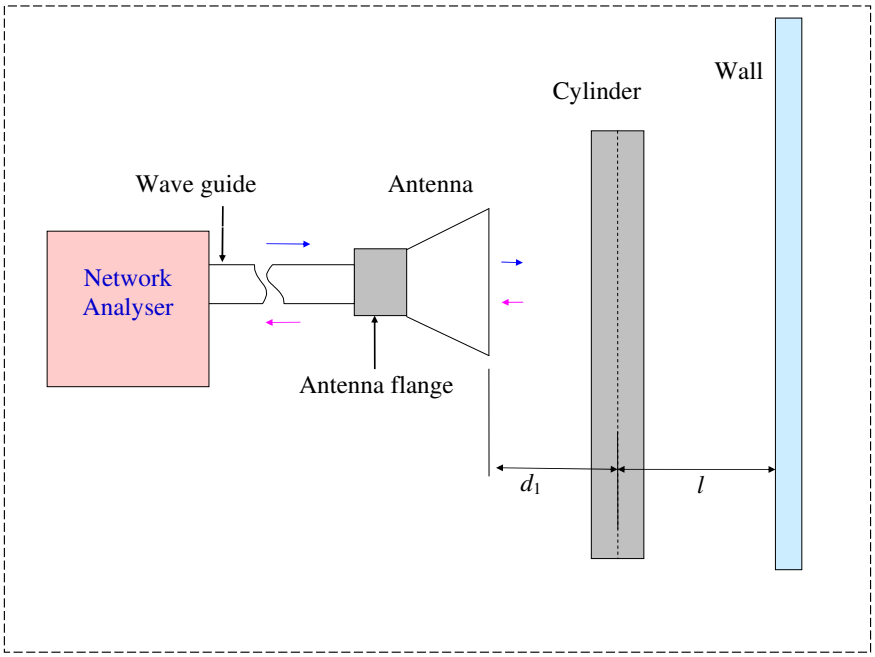


Figure 6.1: Experimental set up for microwave measurements.

used in the analytical study (see Figure 3.3). Similarly the concrete wall behind the object represents the wall in the model. The backscattered signal is received by the same antenna and is sent back to the analyser for measurements. A long copper cylinder was taken as the object for this experiment.

A Vector Network Analyser (VNA) was used for this experiment to obtain accurate measurements of the reflection coefficient. (Network analysers are used to measure microwave signals and analyse both the amplitude and phase properties [2, 35].) The specification of the instrument is as follows: The product is Agilent Technologies 8714ES Radio Frequency Network Analyser (S-parameter), 300kHz to 3GHz. More details are available in the user's guide [106]. The NA generates the microwave signal. The RF coaxial type wave guide carries forward and backward signals between the analyser and the antenna. The RF loss in the wave guide and the connectors are assumed to be very minimal and therefore can be neglected in

this analysis. One end of the wave guide is connected to the NA while the other end is connected to the antenna flange. The design parameters of the flange are given in the next section. More details on wave guides and microwave transmission are available in the references [10, 97].

### 6.1.1 Antenna and design parameters

An electromagnetic horn antenna is used to match the waves from the guiding system to a large radiating aperture. Figure 6.2 shows an isometric view of the antenna through which the signals are transmitted and received in this experiment. The design parameters of the antenna flange follow the basic concepts of wave guide theory [7, 14, 107]. Its physical size, $U$ and $V$ in Figure 6.2, determines the mode of propagation. It is considered that this system fulfils the following requirements:

1. The waves (transmitted and received) can be propagated between the NA and the antenna aperture with minimal loss of signal.

2. The rectangular wave guide (flange) is able to propagate the dominant mode, $TE_{01}$, in a loss-free dielectric medium.

3. It is possible to operate well above the cut-off frequency.

The actual antenna dimensions are $A = 0.235$ m, $B = 0.308$ m (these are vertical and horizontal lengths, respectively), $V = 0.10$ m, $U = 0.05$ m with an antenna horn angle of 17.5 degrees.

In this antenna system, microwave propagation takes place only when the width of the wave guide ($V$ in the diagram) is greater than one half of the wavelength [14, 8]. Accordingly, $\lambda_c$, the cut-off wavelength, is 20 cm for $TE_{01}$ mode ($V/U$=2 to have a 2:1 frequency range of single-mode operation [14]) and therefore the cut-off frequency is found according to the fundamental relationship

$$f_c = \frac{c}{\lambda_c}, \tag{6.1}$$

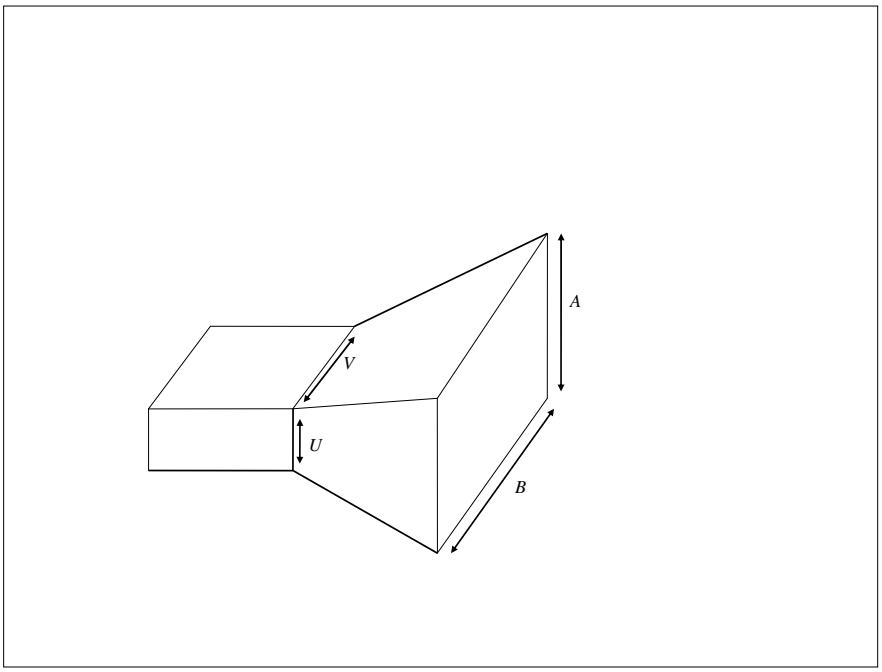


Figure 6.2: Antenna with the wave guide flange.

where $c$ is the velocity of light. In this experiment the size of the waveguide feed has been chosen so that the desired operating frequency of 2-3 GHz lies within the frequency range for which only the transverse electric ($TE_{01}$) mode propagates. When frequencies of 2-3 GHz are used, this system operates well above the cut-off.

### 6.1.2 Measuring environment

When the microwave field measurements were obtained, the antenna was directed at a blank concrete wall. A copper circular cylinder which represents the *object* in this experiment was placed in front of the antenna parallel to its front face as shown in Figure 6.1. The NA, waveguide and the antenna were placed on a wooden bench so that this whole system can be moved forward and backward. Similarly, the cylinder was fixed in a separate stand to make it possible to change the distance to the cylinder from the aperture of the antenna. The experimental set-up was not

isolated from external microwave sources and so, in principle, it was possible for noise to affect the measuring environment.

### 6.1.3 Instrumental calibration for measurements

The microwave network consists of the wave guide and its connectors, the antenna system and the host which is electrically coupled with the antenna aperture (we take air as the medium of the host in this experiment).

The NA is adjusted before connecting to the circuit for measurements. The frequency, power, magnitude, phase and other parameters were set using the keypad of the analyser. The details of the settings and the instrument calibration procedure are available in the guidelines of the user's manual of the NA [106].

#### 6.1.3.1 Normalising at the antenna aperture

When the wave propagates to the antenna from the instrument, its amplitude and phase can change due to the characteristic impedance of the microwave circuit. In order to deal with this situation, the signal at the front-face (aperture) of the antenna was normalised before obtaining the measurements.

There is a simple procedure to normalise the signal to the antenna aperture. First, the signal frequency and its power have to be adjusted at the NA to the desired values. Then, the front-face of the horn antenna has to be closed properly using a conducting plate to make a perfect short circuit at the antenna aperture. Then, the instrument is set to the normalising mode. Now, the instrument itself adjusts the transmitted signal so that the signal which has been set in the instrument keypad would be available at the aperture when the short circuit is removed. According to our settings, the antenna aperture radiates a signal of unit amplitude with zero degrees for the phase angle.

#### 6.1.3.2 Measurement procedure

Microwave measurements are taken from the analyser in several situations as required for our investigation. The copper cylinder was illuminated with a microwave signal radiated from the antenna to measure the reflection coefficient. The NA was connected to a computer to record the measurement data using a data transport network. Some of the important steps followed for obtaining microwave measurements with the cylinder are:

1. Ensure all the connections of the experimental set-up are in order.
2. Set the NA for reflection coefficient measurements and adjust to the required frequency (for more details on NA settings, see [106]).
3. Normalise the signal at the antenna front-end.
4. Obtain measurements with the antenna directed towards the wall. Also measure the distance from the antenna to the wall (the length $d_1 + l$ in Figure 6.1).
5. Obtain measurements with the scattering object placed in front of the antenna along its bore sight axis (the cylinder must be kept parallel to the aperture plane of the antenna).
6. Repeat step 5 with the object placed at different positions along the bore sight axis in front of the antenna. At every measurement, when moving the object, the distance to the centre of the cylinder from the antenna aperture is measured (the length $d_1$ in Figure 6.1).
7. Change the frequency and repeat 3-6.

Apart from the measurements with the cylinder, we conducted a similar experiment with a sphere. The procedure for obtaining measurements with the sphere is much the same as the above steps. More details are given later in this chapter.

## 6.2 Experimental data record

The measuring instrument was adjusted to display the amplitude and phase values of the reflection coefficients. It is not possible to measure the reflection coefficient of the cylinder directly. Instead it is computed from two sets of measured data with and without the cylinder. In the first part of the experiment, the antenna is kept fixed and the cylinder is moved away from the antenna towards the wall in 5 mm steps to obtain measurements. (Note that the antenna was kept closer to the front wall in order to minimise the effect from neighbouring walls.) For each position of the cylinder, the measurements are repeated twenty times at the selected frequencies. The results at each frequency are averaged. All distances are measured in metres.

In the second part of the experiment, measurements were obtained without the cylinder and with only the wall. The antenna was moved towards the wall and, after each step, the length between the aperture and the wall ($l + d_1$ in Figure 6.1) and the reflection coefficients were measured. The output power of the signal is 1 mW.

**Details of the recorded items:**

1. $U$(s/c) and $\theta$(s/c) - Magnitude and phase of the reflection coefficient with short circuit (s/c) antenna. These measurements are related to the antenna normalization discussed in section 6.1.3.1. It is important to make a good short circuit at the aperture so that the values of $U$(s/c) and $\theta$(s/c) are equal to one and zero radians, respectively.

2. $U$(o/c) and $\theta$(o/c) - Magnitude and phase of the reflection coefficient with open circuit (o/c) antenna, that is, the short circuit of the antenna aperture is removed and the reflection from the wall is measured (without the cylinder).

3. $U_{c+w}$ and $\theta_{c+w}$ - Magnitude and phase of the reflection coefficient with the

cylinder and the wall. For this case, the cylinder is placed between the antenna and the wall and then the reflection coefficient is measured.

4. $a$ and $d_1$ - Radius of the cylinder and the distance of its centre from the antenna. For each measurement, the distance to the centre of the cylinder from the aperture plane was recorded (distance $d_1$ in Figure 6.1).

5. The room in which the measurements were made is approximately 8 m $\times$ 6 m $\times$ 3 m in size. The distance between the aperture plane and the wall ($l + d_1$ in Figure 6.1) is equal to 83.5 cm. The walls are made of concrete materials but we are not aware of their electrical properties. Further investigation on the surrounding materials and their effect on microwave frequencies is beyond the scope of the project at this stage.

## 6.3 Measurement results

The data collected from the measurements with a cylinder of diameter 1.3 cm have been plotted in Figure 6.3. The magnitude of the reflection coefficient oscillates in a pattern with respect to the distance $d_1$. The repetition of the maxima and the minima is found to be approximately equal to one half of the wavelength of the signal that is used to obtain these measurements ($\lambda/2 = 6.25$ cm at 2.4 GHz). The phase of the reflection coefficient oscillates in a similar way to the magnitude (see Figure 6.4). These variations are discussed further in section 6.4.

### 6.3.1 Calculation of the cylinder reflections from measured results

Once the signal is excited from the antenna aperture, it propagates towards the cylinder and the wall (we assume the medium inside the room is loss-free). Two

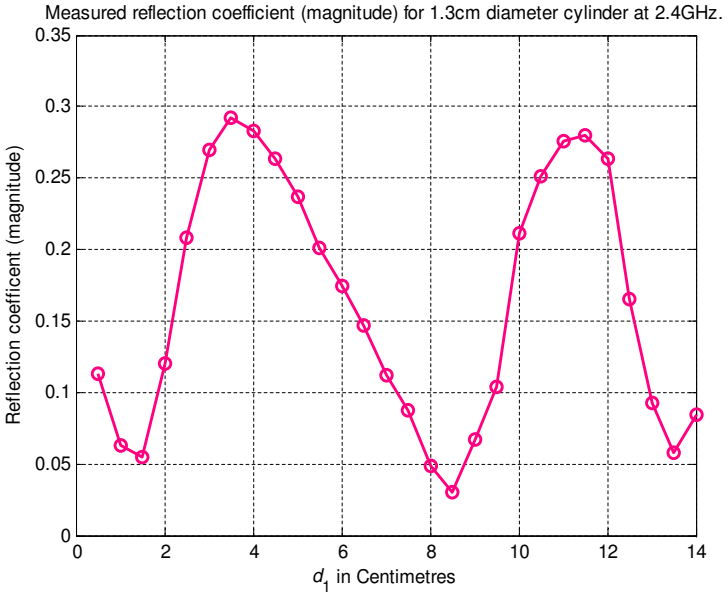


Figure 6.3: Reflection coefficient measured with the wall and the cylinder at 2.4 GHz frequency: magnitude versus distance.

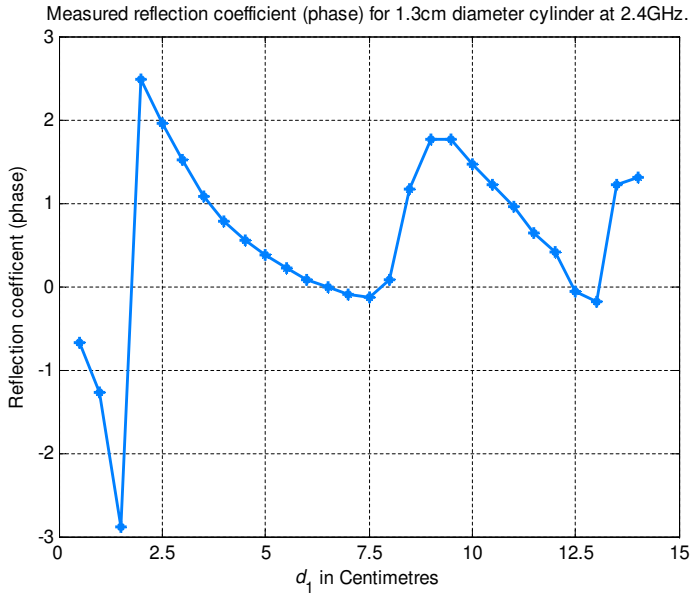


Figure 6.4: Reflection coefficient measured with the wall and the cylinder at 2.4 GHz frequency: phase (modulo $2\pi$) versus distance.

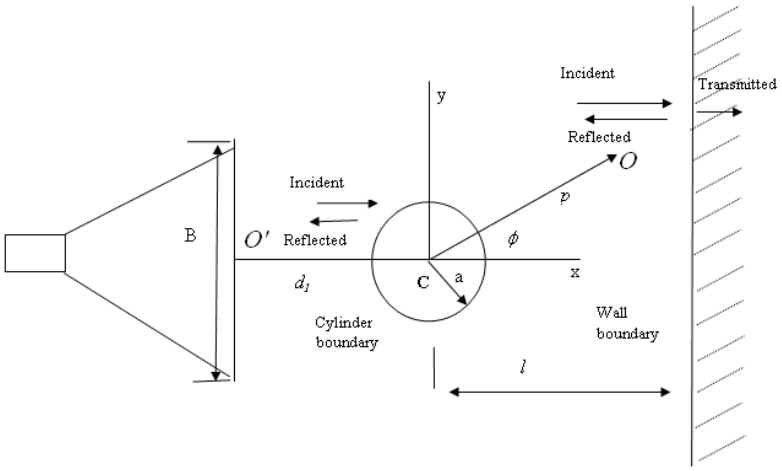


Figure 6.5: Wave reflection and transmission at the boundaries of the propagation medium.

major backward waves can be expected. When the wave is incident upon the boundary of the wall, a part of this wave may be reflected back from the boundary while the rest is being transmitted through the surface into the wall. This is illustrated in Figure 6.5. The waves which hit the conducting cylinder are completely scattered away from its boundary. Accordingly, two backscattered waves can be expected: one which is from the cylinder and another from the wall. These scattered waves are captured when they reach the aperture of the antenna. Figure 6.5 shows the wave transmission and reflection from the boundaries of the wall and the conducting cylinder. It also illustrates the cylindrical coordinate system associated with the conducting cylinder. The length B, as marked along the front-face of the antenna, and other details of the microwave network are given in section 6.1.1 (see under antenna dimensions). The bore sight axis of the antenna is perpendicular to the wall. The wave excited from the antenna is $z$-polarized and travelling in the

$x$-direction towards the wall in the $xy$-plane. The complex reflection coefficient of the wall looking at $O'$, that is from a distance $d_1 + l$ from the boundary of the wall, can be written as

$$U_w e^{j\theta_w} = \Gamma_w e^{-j(2k_1(d_1+l)+\xi)}, \tag{6.2}$$

where $\Gamma_w$ and $\xi$ are the magnitude and phase of the reflection coefficient of the wall at its boundary, respectively, and $k_1$ is the wave number of the medium at frequency $f_1$. The complex reflection coefficient of the conducting cylinder at $O'$, which is at a distance $d_1$ from the centre of the cylinder is given by,

$$U_c e^{j\theta_c} = \Gamma_c(0) e^{-2jk_1 d_1}, \tag{6.3}$$

where $\Gamma_c(0)$ is the magnitude of the complex valued reflection coefficient of the cylinder at its boundary. In equations (6.2) and (6.3) it is considered that the magnitudes of the reflection coefficients remain unchanged ($U_w = \Gamma_w$ and $U_c = \Gamma_c(0)$) while their phase angles are changed with respect to the distance to the antenna from the scattering object.

Consider an error box (a two port network) and let $\Gamma_L$ be the reflection coefficient of the wall and the cylinder. We need to find the reflection of the cylinder. The error box represents the error due to the reflection from the wall. This situation can be interpreted using a two port network and

$$\Gamma = \frac{a + b\Gamma_L}{c + d\Gamma_L}, \tag{6.4}$$

where $a, b, c$ and $d$ are parameters of the error box and these can be found by connecting successively three known terminations to the measuring port (see more details in [108]). Thus, considering the separate measurements that can be obtained with only the wall present, from the above bilinear transformation [108]

$$U_c e^{j\,\theta_c} = \frac{g\,U_{c+w} e^{j\,\theta_{c+w}} + h}{q\,U_{c+w} e^{j\,\theta_{c+w}} + 1}, \tag{6.5}$$

where $U_{c+w}$ is the magnitude of the complex reflection coefficient measured at $O'$ with both the wall and the cylinder present and $\theta_{c+w}$ is the corresponding phase angle. In the experiment, we measured $U_{c+w}$, $\theta_{c+w}$, $U_w$ and $\theta_w$ with several frequencies. We used these data in equation (6.5) to find $U_c$ and $\theta_c$. Good approximate results are observed by setting $g = 1, q = 0,\ h = -U_w \mathrm{e}^{j\,\theta w}$ ($q = 0$ is the best match without multiple reflection) and so the complex reflection coefficient of the cylinder can be found as

$$U_c e^{j\,\theta_c} \approx U_{c+w} e^{j\,\theta_{c+w}} - U_w e^{j\,\theta_w}\,. \tag{6.6}$$

### 6.3.2 Reflection from the wall and the cylinder

The reason for the variations of the reflection coefficient with respect to the distance $d_1$ can be identified by considering the received waves at the antenna aperture. Assume the medium inside the room is loss-free and the antenna receives only the waves scattered directly from the wall and the cylinder. The reflection coefficient is defined as the ratio of the amplitude of the reflected wave to the amplitude of the incident wave at the load (this is considered as the discontinuity in transmission line [7]). This can be generalised to any point along the line that the wave travels. Thus, the reflection coefficient of the conducting cylinder referred to the antenna aperture (point $O'$ in Figure 6.5) can be found according to equation (2.8) as

$$\Gamma_c(-d_1) = \frac{E^- e^{-jk_1 d_1}}{E^+ e^{jk_1 d_1}} = \Gamma_c(0) e^{-2jk_1 d_1}, \tag{6.7}$$

where $\Gamma_c(0) = \frac{E^-}{E^+}$ is the magnitude of the reflection coefficient of the conducting cylinder at its boundary and $E^+$ and $E^-$ are the magnitudes of the electric field intensities of the forward and backward waves, respectively. From the antenna normalization, it is known that the antenna transmits a wave with unit magnitude and a zero phase angle from its aperture. Therefore, the reflected wave from the

cylinder received at the antenna aperture plane is

$$E_c^r = \Gamma_c(0) E_0 e^{-2jk_1 d_1}, \tag{6.8}$$

where $E_0$ is the magnitude of the field of the transmitted wave, $E_0 = |E^+|$. Similarly, the reflected wave from the wall received at the antenna aperture plane is

$$E_w^r = \Gamma_w E_0 e^{-j(2k_1(d_1+l)+\xi)}, \tag{6.9}$$

where $\Gamma_w$ and $\xi$ are the magnitude and phase of the reflection coefficient of the wall at its boundary. The resultant field received at the antenna aperture plane can be considered as a superposition of the two reflected waves. Therefore using equations (6.8) and (6.9), the total field received at the antenna is

$$E_{c+w}^r = \Gamma_c(0) E_0 e^{-2jk_1 d_1} + \Gamma_w E_0 e^{-j(2k_1(d_1+l)+\xi)} = |E_{c+w}^r|\, e^{j\theta_{c+w}}. \tag{6.10}$$

The field in equation (6.10) can be expressed in terms of amplitude and phase. The root mean square amplitude of this resultant field is

$$\left|E_{c+w}^r\right| = E_0 \sqrt{(\Gamma_c(0))^2 \; + \; (\Gamma_w)^2 \; + 2\Gamma_c(0)\Gamma_w \cos(2k_1 l + \xi)} \;, \tag{6.11}$$

and the phase of the resultant field is

$$\theta_{c+w} = -\tan^{-1}\left(\frac{\Gamma_c(0)\sin(2k_1 d_1) + \Gamma_w \sin(2k_1(d_1+l)+\xi)}{\Gamma_c(0)\cos(2k_1 d_1) + \Gamma_w \cos(2k_1(d_1+l)+\xi)}\right). \tag{6.12}$$

The root mean square amplitude of the reflected field in equation (6.11) varies with respect to the argument of the cosine term. The NA displays the reflection coefficient which was calculated as the ratio of the received to transmitted signals at its aperture. Therefore, we can expect a variation of the magnitude of the measured reflection coefficient with respect to the distance between the cylinder and the wall according to the argument of the cosine function in (6.11). Note that the incident and reflected fields considered here are only for understanding the variations of the measured results with respect to the distance from the antenna. A complete solution

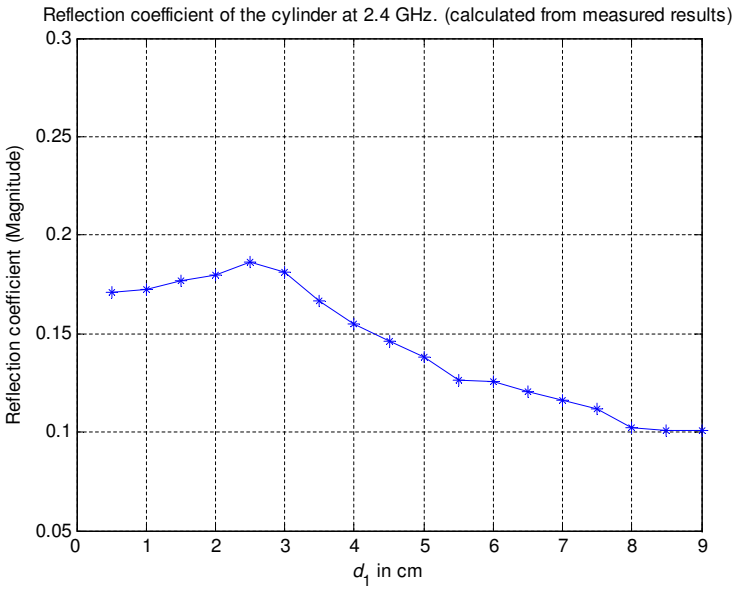


Figure 6.6: Reflection coefficient of the cylinder at 2.4 GHz frequency, calculated from the measured data (Magnitude versus distance $d_1$).

for the incident and scattered fields in the experimental situation is given in section 7.1.

Even if the wave number $k_1$ is constant, the length $l$, the gap between the centre of the cylinder and the wall, varies with $d_1$ ($l$ decreases as the cylinder is moved away from the antenna towards the wall). Therefore, in this experiment, a significant change in the magnitude of the total reflected field relative to the position of the cylinder can be expected. Similarly, according to equation (6.12), the phase of the total field also changes between $-\pi$ and $+\pi$ depending upon the position of the cylinder. These variations can be seen in Figure 6.4. Further discussion on this appears later in this chapter.

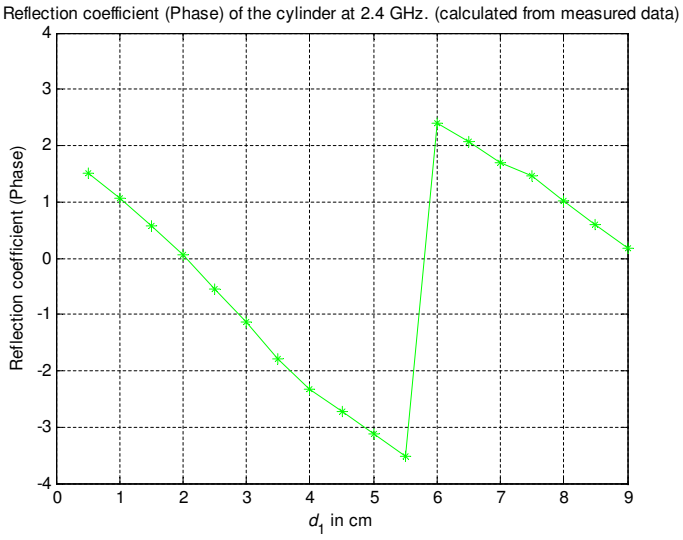


Figure 6.7: Reflection coefficient of the cylinder at 2.4 GHz frequency, calculated from the measured data (Phase (modulo $2\pi$) versus distance $d_1$).

### 6.3.3 Cylinder reflection

Equation (6.6) is used to calculate the reflection coefficient of the cylinder from the experiments. The calculated magnitude and phase of the reflection coefficients were plotted against $d_1$, the distance of the cylinder from the measuring point, and the results are shown in Figures 6.6 and 6.7, respectively.

The new results show significant changes when compared to the results plotted in Figures 6.3 and 6.4. Once the effect of the wall reflection has been removed from the reflection coefficients measured with the wall and the cylinder, the oscillations in magnitude with respect to $d_1$ are significantly reduced. The new results give us the reflection coefficient of the cylinder as measured at the aperture of the antenna. Even though the oscillations have been removed, there is still a reduction in the magnitude of the reflection coefficient with respect to $d_1$ in general. This may be because the reflection has taken place from a cylindrically-shaped boundary (see the forward equation of the cylinder: equation (3.21) has evidence for this behaviour

and there is further explanation in section 3.2.1).

There may be other factors involved due to the antenna near field effect and noise due to other reflections, multiple scattering, interferences from other sources, etc. Apart from these, there may be experimental errors when moving the cylinder and measuring the distance between the aperture of the antenna and the centre of the cylinder. All of these effects should be minimised to achieve better results.

## 6.4 Analysis of the measurement results

### 6.4.1 Polar display of the measured data

It is convenient to analyse the measured data using a polar display and comparing it with the Smith chart. The Smith chart is plotted on the complex reflection coefficient plane in two dimensions and is scaled with normalised impedance. In many transmission line problems, the Smith chart is used to find how impedances are transformed along the line or to find how the impedance relates to the reflection coefficient. This chart consists of loci of constant resistance and reactance plotted on a polar diagram.

The Smith chart has circumferential scaling in wavelengths and degrees. The wavelengths scale represents the distance measured along the transmission line (considered as the line connected between the generator or source and the load) to the point under consideration. The degrees scale represents the phase angle of the reflection coefficient at that point. Use of the Smith chart and the interpretation of the results obtained using it require a good understanding of AC circuit theory and transmission line theory. The method of finding impedance and reflection coefficients using the Smith chart is available at [99, 106, 109].

The behaviour of the complex reflection coefficient was monitored using the Smith chart display of the NA and it was observed that its locus always moves

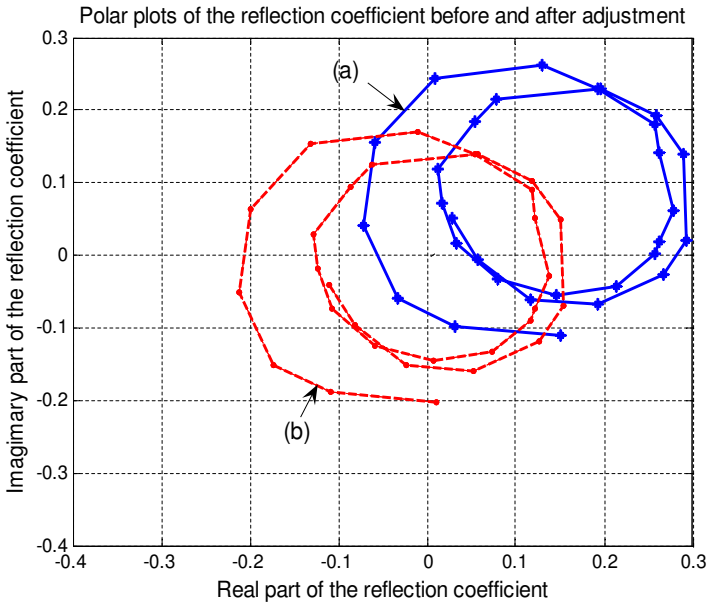


Figure 6.8: Polar plot of the reflection coefficient at 2.4 GHz frequency measured with both the wall and the cylinder. (a) Before adjustment. (b) After adjustment.

towards the generator (the source) when the cylinder moves towards the wall. The cylinder is moved in steps of 0.5 cm over a distance of 15 cm (which gives us 30 steps in total). At a frequency of 2.0 GHz, the cylinder's movement in one step (0.5 cm) is equivalent to $1/30^{th}$ of the wavelength $\lambda$ ($\lambda = 15$ cm at this frequency) and this corresponds to a movement of $1/15^{th}$ of the full circle of the Smith chart. Increasing the distance from the load corresponds to moving towards the generator and this corresponds to a clockwise motion about the complex plane of the Smith chart. Also, we observe that, throughout the whole movement, the absolute magnitude of the reflection coefficient slowly decreases with an increase in $d_1$.

Figure 6.8 (line (a)) shows a polar plot of the measured reflection coefficients with both the wall and the cylinder. In this graph, the locus of the magnitude of the reflection coefficient rotates in a clockwise circular path but its centre does not coincide with the zero point of the real and imaginary axis, the centre of the

Smith chart, see [99]. In order to find the correct path of the locus in our polar plot, through trial and error we aligned its centre by eye to coincide with the zero point of the real and imaginary axes and estimated the amount of off-set in magnitude and phase of the measured results. The corrected results are plotted in Figure 6.8 (line (b)). As expected, the amount of off-set in magnitude and phase is almost identical to the measured wall reflection at the same distance. This shift of the centre point of the locus of the measured reflection coefficient reveals how the wall reflection has interacted with the cylinder's reflection causing an off-set in the measured results.

### 6.4.2 Study of the wall effect

The combined reflection with both the wall and the cylinder was studied by using measurements of the reflection coefficient without the cylinder, again for various distances between the antenna and the wall. In order to perform this operation, the whole measurement system was moved together with the antenna in 0.5 cm steps and the amplitude and phase of the reflection coefficient were measured. These results are plotted in Figure 6.9. This plot has a pattern similar to that of the plot of the measurement results with the cylinder and wall in Figure 6.3. The maxima and minima also repeat with a period equal to one half of the wavelength of the signal used. A frequency of 2.4 GHz was used and therefore the wave length is 12.5 cm. The period of oscillation of the reflection coefficient plotted in Figure 6.3 is also approximately equal to 6.25 cm. When the two plots in Figures 6.3 and 6.9 are compared, it can be seen that the magnitude values of the reflection coefficient measured with the wall are in general smaller than those with the wall and the cylinder as would be expected.

Apart from the above conclusions, the measurement results of the wall reveal information about the proportion of the signal energy that is received back at the antenna from the signal transmitted. From the measured reflection coefficients

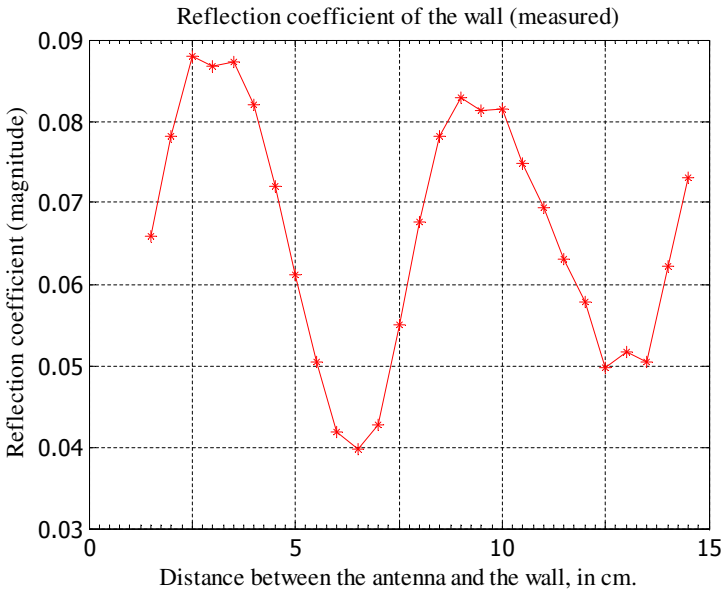


Figure 6.9: The magnitude of the measured reflection coefficient due to the wall, without the cylinder present, for various positions of the antenna.

(magnitude), we can see that only a very small amount of signal is received back at the antenna compared to that transmitted. We must realise that not all of the reflected field components from the wall would travel back to the antenna. Also, not all the incident field components at the wall would be reflected from its boundary as some of the waves penetrate through the wall (Figure 6.5). From the results it can be seen that the total loss of the signal is approximately 94% of the total field excited from the antenna. In other words, in this experiment, the energy received back at the antenna is about 6% of the total microwave energy that has been transmitted from the antenna .

## 6.5 Experimental test with the sphere

Microwave scattering from a sphere was examined using the same experimental application system. In this case a conducting sphere was illuminated by a microwave signal which was radiated from the antenna aperture. The procedure for obtaining measurements is very similar to that we used with the conducting cylinder. These experiments have been conducted for just one frequency of 2.6 GHz (wavelength is approximately 11.5 cm) and illustrate the results of the measured reflection coefficient but the inverse method was not used on these data.

### 6.5.1 Scattering object

A number of spheres with different diameters were used to observe the reflection using the NA. In order to receive a reasonable signal at the NA, it is important to have a fairly large sphere (even though it is a conducting sphere) compared to the aperture area of the antenna. The spheres which were used to obtain the measurements are shown in Figure 6.10. The diameters of the spheres (from the right) in Figure 6.10 are 1.5 cm, 2.0 cm, 2.5 cm and 8.5 cm, respectively. The reflection coefficients with all of these spheres were measured but, as the sizes of the first three spheres are very small compared to the area of the antenna aperture, the microwave responses from these ones were very small at the instrument. Therefore, the sphere having 8.5 cm diameter was selected for obtaining microwave measurements. The ratio of the effective area of this sphere to the effective area of the aperture is approximately equal to 0.1.

### 6.5.2 Experimental procedure

Figure 6.11 shows the experimental apparatus arranged for microwave measurements. The sphere is aligned along the bore sight axis of the antenna (hanging in

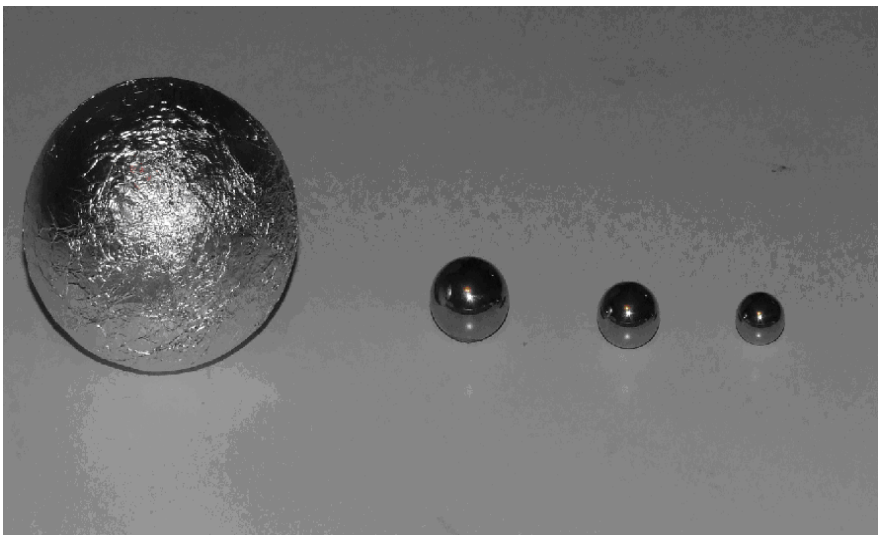

Figure 6.10: Spheres used in experimental observations for microwave detection.

front in the picture) using wrapping materials which have no considerable effect on the microwave signal. The antenna is directed towards a wall which is perpendicular to the bore sight axis (this is not visible in Figure 6.11) such that its aperture can capture the backward waves scattered from the boundaries of both the sphere and the wall. Each time when taking measurements, the distance to the centre of the sphere is measured from the centre of the aperture of the antenna. The experimental procedure is similar to that we followed when obtaining measurements with the conducting cylinder. The reflection coefficients were measured with the sphere moving with 0.5 cm steps towards the wall with the antenna and wall fixed at 90 cm apart. Also, the reflection coefficients without the sphere were measured. Similar to the case with the cylinder, when both the sphere and the wall are present, the reflected wave from the wall can be added on that from the sphere. Therefore, using equation (6.5), the reflection coefficient of the sphere was calculated using these two

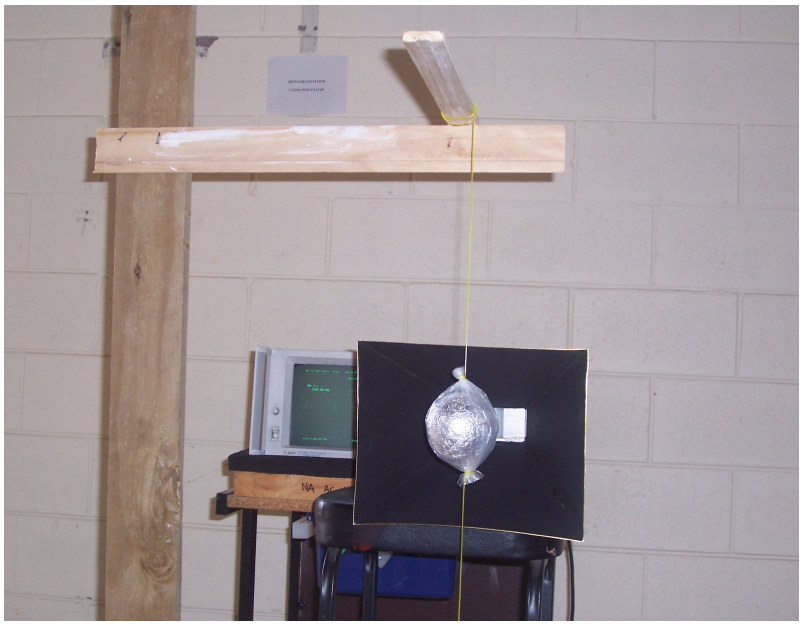

Figure 6.11: The experimental apparatus for the microwave measurements with the sphere.

measured data sets.

### 6.5.3 Measured results and discussion

The measured data obtained by moving the sphere are plotted with respect to $d_1$ and shown in Figure 6.12. The magnitude of the reflection coefficient oscillates with a period equal to one half of the wavelength of the microwave signal which was used for these measurements (approximately 11.5 cm).

Similar to the case with the cylinder, it is not possible to obtain direct measurements from the sphere. Therefore, using the two sets of the separate measurements, with the wall by itself and with the wall and the sphere together, the magnitude of the reflection coefficient of the sphere was calculated using equation (6.5) and the results are plotted in Figure 6.13. These plots have significant differences in the behaviour of the magnitude of the reflection coefficient when compared to those

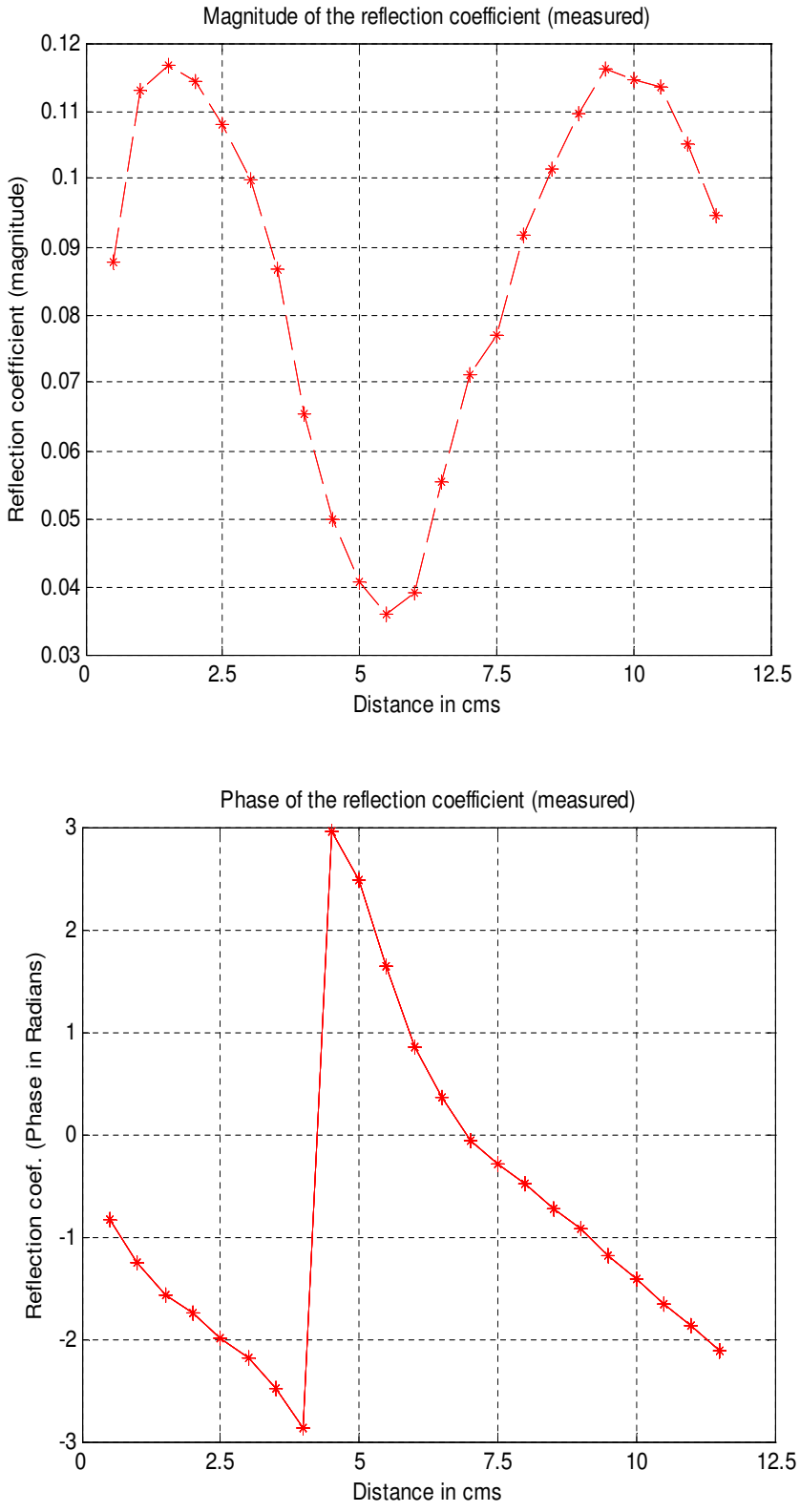


Figure 6.12: Measured reflection coeff. (mag. and phase (modulo $2\pi$)) of the wall and the sphere together plotted with respect to the distances $d_1$ in cm at 2.6 GHz.

obtained with the wall and the sphere together in Figure 6.12. As with the cylinder experiment, the oscillations have been largely removed. Note that, there may be other effects from interfering noise from the surroundings (section 6.3.3) and further corrections might provide more accurate results.

From the phase plot in Figure 6.12, we can see that the phase of the reflection coefficient varies with respect to distance $d_1$ (here, we have plotted modulo $2\pi$ ). The calculated results using equation (6.5) are plotted in Figure 6.13 and this shows a little improvement compared to the previous plot (now the change in phase is approximately linear with respect to the distance of the object from the antenna as expected). The calculated phase angles of the reflection coefficient of the sphere from the measured data have a significant change with respect to the distance of the sphere from the measuring point.

Figure 6.14 shows the polar plots of the reflection coefficients we obtained in this experiment. Each point in a plot corresponds to a particular distance $d_1$. In this case, we have plotted the real and imaginary values of the reflection coefficient with respect to $d_1$ (which varies from 0.5 to 12.5 cm with 0.5 cm steps, increasing in the clockwise direction). In the plot obtained with the measured data with the sphere and the wall (line marked as "measured"), the locus of the magnitude of the reflection coefficient is a circular path with respect to $d_1$ but its centre does not coincide with the origin of the real and imaginary axis. The data obtained after removing the wall effect is also plotted in Figure 6.14 (the line marked as "calculated from measured data") and now we can see that the centre of the locus has been moved much closer to the zero point of the real and imaginary axes. We have verified with the measured result and found that the amount of off-set of the centre of the reflection coefficient in both magnitude and phase is very similar to those values obtained by measuring the reflection coefficient only with the wall (as was also true for the cylinder as explained in section 6.4.1). In these two experiments the

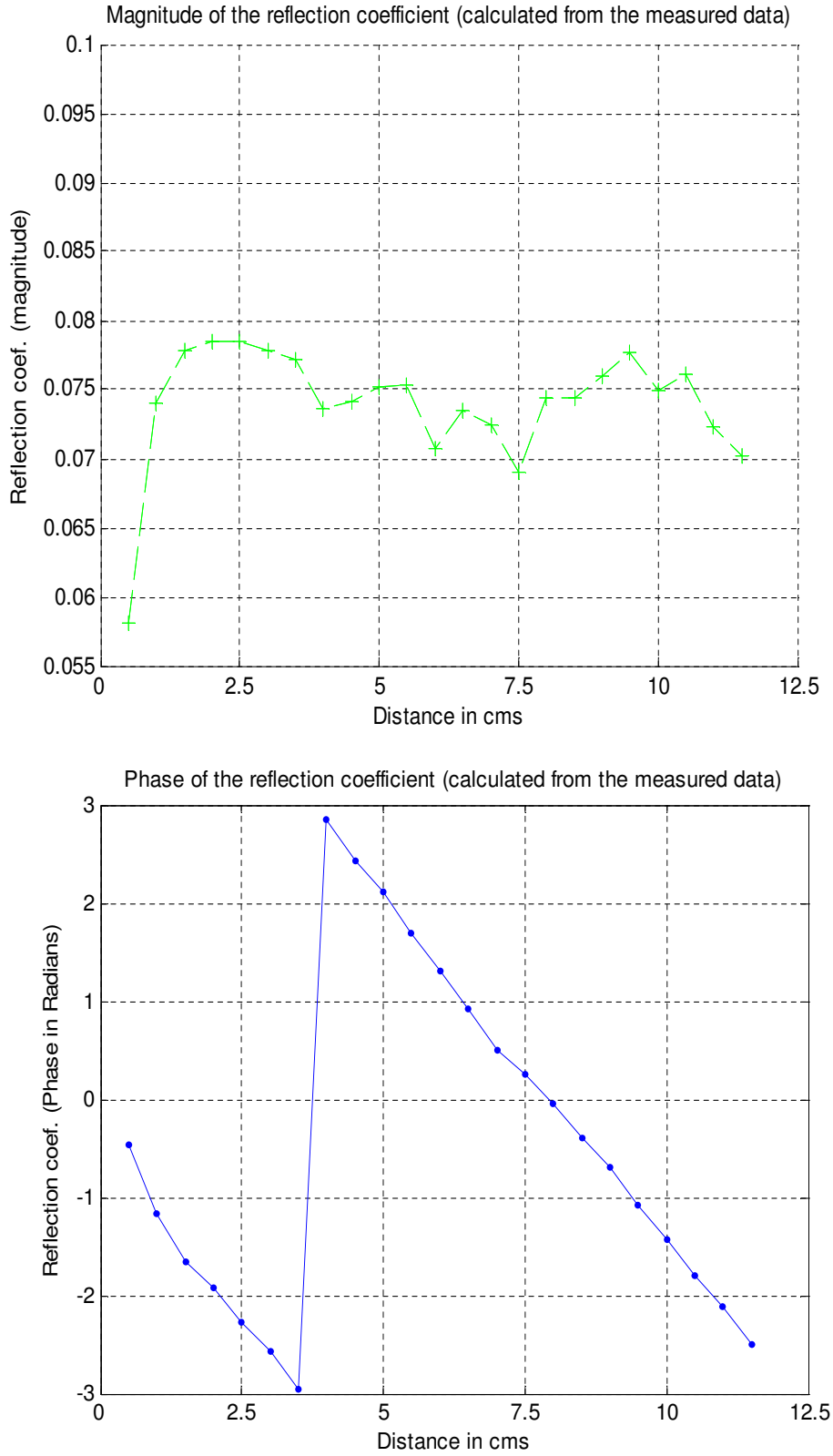


Figure 6.13: Reflection coefficients (magnitude and phase (modulo $2\pi$)) of the sphere calculated from the measured data are plotted with respect to distances $d_1$ in cm.

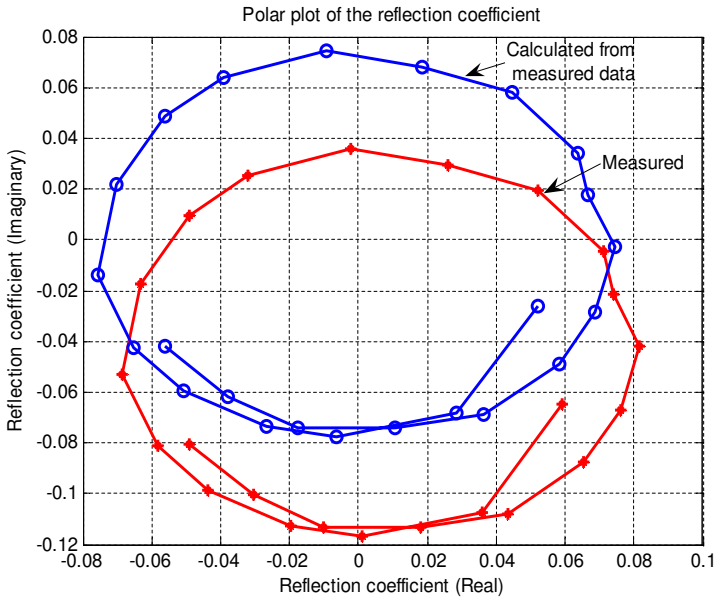


Figure 6.14: Polar plot of the reflection coefficient of the sphere at 2.6 GHz. These plots were obtained using data from the experiment with the sphere.

Smith chart off set with the cylinder is different to the off set with the sphere. This can be expected as the effective scattering area of the sphere is smaller compared to that of the cylinder.

As discussed in the experiment with the cylindrical object, the polar plots and subsequent corrections are equally applicable for the sphere. It would be necessary to obtain further measurements with different frequencies to use the inverse method for calculating unknowns.

# Chapter 7

# Object detection using measurement results

The experiments (for cylindrical and spherical objects) conducted in the previous chapter have shown that these objects can make a significant difference to the measured reflection coefficient data. We obtained the numerical results in Chapters 3 and 4, by modelling the host with the internal object and simulating to test the associated forward problem. In the experiments, the source is an antenna which radiates a beam of waves towards the scattering object. In this chapter, we modify the forward equations for the experimental geometry to calculate the fields and then solve the subsequent inverse problems. Finally, the calculated unknowns using the measured data and those calculated from the numerical data are compared.

In the experiment, the object was moved to a reasonable distance from the antenna aperture. The object moves from near-zone fields to far-zone fields. It is unclear if the waves involved in the scattering can be entirely treated as planar or whether cylindrical waves would be more appropriate. We consider both of these cases separately and then discuss the differences in scattering due to the experimental situation.

## 7.1 Consideration of the experimental geometry

In this section, we use our forward solutions of the theoretical model in the experimental application. We have the measured data, the magnitude and the phase values of the reflection coefficients. In order to compute the unknowns using these data, we first obtain the forward equation for the experimental arrangement.

### 7.1.1 Forward equation in the experimental application

Now the forward equations are obtained in terms of the reflection coefficient which is appropriate for the experimental set-up. Figure 7.1 (a) shows the two-dimensional model which is similar to the analytical model shown in Figure 3.3. This model also includes the wall (behind the object). Three antennas are shown in the xy-plane, each of which transmits and receives microwave signals at the surface of the host. Figure 7.1(b) shows the two-dimensional coordinate system and the geometry of the experimental apparatus which represent the host model with a single antenna (antenna $A_1$).

The wave excited from the antenna is $z$-polarized and travelling in the $x$ direction towards the wall. It is assumed that the scattering from both the wall and the cylinder takes place due to plane waves incident upon their boundaries. Two situations are considered here: one is the scattering from both the wall and the cylinder and the other is the scattering from the wall by itself. Assume the wave to be finite at the point $C$ (at the centre of the cylinder) and periodic with a period $2\pi$ in the polar angle. The reflected wave at the point $O$ due to the reflection from the cylinder is found from equations (3.14) and (3.17) as

$$E^s_{z,c}(p,\phi;f_i) = E_0 \sum_{n=-\infty}^{\infty} j^{-n} \left[ -\frac{J_n(k_i a)}{H^{(2)}_n(k_i a)} H^{(2)}_n(k_i p) \right] e^{jn\phi}, \tag{7.1}$$

where $f_i$ is the frequency of the transmitted signal, $a$ is the radius of the cylinder and $p$ is the distance to $O$ from the centre of the cylinder. Here, $j = \sqrt{-1}$ and $k_i$ is

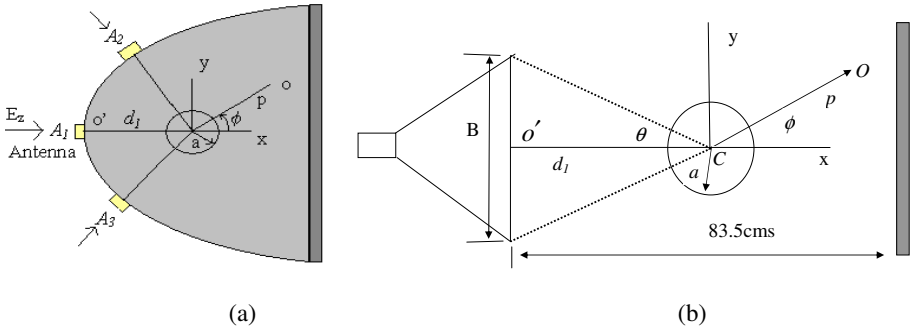


Figure 7.1: Experimental implementation for microwave measurement. (a) The two-dimensional host model. (b) Geometry of the experimental set-up.

the wave number of the medium given as $k_i = 2\pi f_i\sqrt{\mu\varepsilon}$, and a time dependence $e^{j\omega t}$ is assumed, where $\omega = 2\pi f_i$. Also, $\mu$ and $\varepsilon$ are the permeability and permittivity of the medium, respectively. The subscript $i$ relates to the frequency $f_i$ of the signal used. This experiment was carried out in air and therefore $\sigma$ the conductivity of the medium is assumed to be equal to zero. The reflected wave received at the antenna is captured by its aperture and sent back to the measuring instrument (explained in the previous chapter). In this xy-plane, the scattering about the circular boundary of the cylinder is not uniform but rather it depends upon the incident angle.

As in section 3.2.1, suppose we rotate the point $O$ through an angle $\pi - \phi$ so that it lies along the $x$ axis. The distance $p$ is chosen to be $d_1$ which is the distance to the centre of the cylinder from the centre point of the antenna (corresponding

to antenna $A_1$ in Figure 7.1(a)). Now, using equation (7.1), the scattered field at point $O'$ can be found as

$$E^s_{z,c}(d_1, \pi; f_i) = E_0 \sum_{n=-\infty}^{\infty} j^n \left[ -\frac{J_n(k_i a)}{H^{(2)}_n(k_i a)} H^{(2)}_n(k_i d_1) \right]. \tag{7.2}$$

### 7.1.2 Scattered field captured by the antenna aperture

The total field at the antenna plane is the sum of all the field components being captured by the antenna aperture (see Figure 7.1 (b)) and can be found by adding together the entire field values across the antenna and normalising (averaging) over the aperture of angular width $2\theta$, as

$$E^s_{z,c}(f_i) = 2E_0 \sum_{n=-\infty}^{\infty} j^{-n} \left[ -\frac{J_n(k_i a)}{2\theta H^{(2)}_n(k_i a)} \right] \int_{\pi-\theta}^{\pi} H^{(2)}_n \left( \frac{-k_i d_1}{\cos(\phi)} \right) e^{jn\phi} d\phi, \tag{7.3}$$

where $\theta$=$\tan^{-1}(B/2d_1)$ is the angle that $CO$ makes with the $x$ axis when $O$ is moved to lie at either end of the antenna aperture (Figure 7.1 (b)). The numerical value of the argument of the Hankel function in equation (7.3) varies with the position of the object: the distance to the centre of the cylinder to the xy-plane of the antenna aperture is the only variable in the argument. This distance varies from $d_1$ to $d_1 \sec\theta$ within the aperture plane. Therefore, in order to find a reasonable solution for the length $p = d_1 \sec\phi$ we replace the argument of the Hankel function in equation (7.3) with $k_i d_1/\cos(\theta/2)$ by taking the average value of $\phi$ over the interval $(\pi-\theta,\ \pi)$. The reflected wave is expressed in cylindrical coordinates but the parameter $d_1$ needs to be modified to become $d_1^* = d_1 + \Delta$, where $\Delta$ is a parameter with units of length which accounts for the curvature of the wave-fronts in the aperture of the horn antenna (see Appendix E for more details). This is incorporated in the detailed computations carried out later. Then, we have

$$E^s_{z,c}(f_i) = 2E_0 \sum_{n=-\infty}^{\infty} j^{-n} \left[ -\frac{J_n(k_i a)}{2\theta\, H^{(2)}_n(k_i a)} H^{(2)}_n \left( \frac{k_i d_1^*}{\cos(\theta/2)} \right) \right] \quad \int_{\pi-\theta}^{\pi} e^{jn\phi} d\phi \ . \tag{7.4}$$

When the wave is radiating from large apertures and the distance to the object is comparatively large, one can consider $\theta$ to be very small so that $\cos(\theta/2)$ may

be equated to unity (the paraxial approximation in far-field zones [99]). For this experimental application, we have values of $d_1$ somewhere between the near-field and the far-field zones of the antenna radiation.

The negative, positive and zero terms of equation (7.4) are separated to obtain

$$\begin{aligned} E^s_{z,c}(f_i) = 2E_0 \sum_{n=-\infty}^{-1} j^{-n} \left[ -\frac{J_n(k_i a)}{2\theta\, H_n^{(2)}(k_i a)} H_n^{(2)}\left(\frac{k_i d_1^*}{\cos(\theta/2)}\right)\right] \int_{\pi-\theta}^{\pi} e^{jn\phi} d\phi \\ +2E_0 \sum_{n=1}^{\infty} j^{-n} \left[ -\frac{J_n(k_i a)}{2\theta\, H_n^{(2)}(k_i a)} H_n^{(2)}\left(\frac{k_i d_1^*}{\cos(\theta/2)}\right)\right] \int_{\pi-\theta}^{\pi} e^{jn\phi} d\phi \\ +2E_0 \left[ -\frac{J_0(k_i a)}{2\theta\, H_0^{(2)}(k_i a)} H_0^{(2)}\left(\frac{k_i d_1^*}{\cos(\theta/2)}\right)\right] \int_{\pi-\theta}^{\pi} e^{j0} d\phi \ . \end{aligned} \tag{7.5}$$

Equation (7.5) is simplified to yield

$$\begin{aligned} E^s_{z,c}(f_i) = 2E_0 \sum_{n=-\infty}^{-1} j^{n} \left[ -\frac{J_n(k_i a)}{2\theta\, H_n^{(2)}(k_i a)} H_n^{(2)}\left(\frac{k_i d_1^*}{\cos(\theta/2)}\right)\right] \left(\frac{1-e^{-jn\theta}}{jn}\right) \\ +2E_0 \sum_{n=1}^{\infty} j^{n} \left[ -\frac{J_n(k_i a)}{2\theta\, H_n^{(2)}(k_i a)} H_n^{(2)}\left(\frac{k_i d_1^*}{\cos(\theta/2)}\right)\right] \left(\frac{1-e^{-jn\theta}}{jn}\right) \\ +E_0 \left[ -\frac{J_0(k_i a)}{H_0^{(2)}(k_i a)} H_0^{(2)}\left(\frac{k_i d_1^*}{\cos(\theta/2)}\right)\right] \ . \end{aligned} \tag{7.6}$$

From the Bessel function relationships we have

$$J_{-n}(z) = (-1)^n J_n(z)\,, \quad Y_{-n}(z) = (-1)^n Y_n(z), \quad H_n^{(2)}(z) = J_n(z) - jY_n(z), \tag{7.7}$$

and we simplify the first term of equation (7.6) to obtain

$$\begin{aligned} 2E_0 \sum_{n=-\infty}^{-1} j^{n} \left[ -\frac{J_n(k_i a)}{2\theta\, H_n^{(2)}(k_i a)} H_n^{(2)}\left(\frac{k_i d_1^*}{\cos(\theta/2)}\right)\right] \left(\frac{1-e^{-jn\theta}}{jn}\right) \ = \\ 2E_0 \sum_{n=1}^{\infty} j^{n} \left[ \frac{J_n(k_i a)}{2\theta\, H_n^{(2)}(k_i a)} H_n^{(2)}\left(\frac{k_i d_1^*}{\cos(\theta/2)}\right)\right] \left(\frac{(1-e^{jn\theta})}{jn}\right) \ . \end{aligned} \tag{7.8}$$

Then the solution to the reflected wave in equation (7.6) is

$$\begin{aligned} E^s_{z,c}(f_i) = E_0 \left[ -\frac{J_0(k_i a)}{H_0^{(2)}(k_i a)} H_0^{(2)}\left(\frac{k_i d_1^*}{\cos(\theta/2)}\right)\right] \\ +2E_0 \sum_{n=1}^{\infty} \left[ -\frac{J_n(k_i a)}{H_n^{(2)}(k_i a)} H_n^{(2)}\left(\frac{k_i d_1^*}{\cos(\theta/2)}\right)\right] \frac{j^n \sin(n\theta)}{n\theta} \ . \end{aligned} \tag{7.9}$$

The expression in (7.9) is, however, not quite the final result. There is an additional scale factor that needs to be applied to account for the fact that the electric field distribution in the antenna aperture is not uniform due to the $TE_{01}$ mode propagating in the waveguide. The aperture field has the following form:

$$E_z(y,z) = E_{0z} \cos(\frac{\pi y}{B}), \tag{7.10}$$

where $E_{0z}$ is the maximum field strength in the aperture. It should be noted that for the case we have here, when the cylinder diameter is much smaller than the aperture dimension $B$, and with the cylinder axis located at $y$ =0, the incident field on the cylinder has an amplitude approximately equal to the maximum field strength in the aperture (= $E_{0z}$). It is therefore virtually unaffected by the non-uniformity of the aperture field. In receive mode, however, the non-uniform aperture field must be accounted for in some way.

The procedure now is to introduce an equivalent uniform field distribution spanning the entire antenna aperture. The field amplitude of this equivalent distribution is the average aperture field $\bar{E}_z$, which is evaluated as follows:

$$\bar{E}_z = \frac{E_{0z} \int_{-B/2}^{+B/2} \cos(\frac{\pi y}{B}) dy}{\int_{-B/2}^{+B/2} dy} = \frac{2E_{0z}}{\pi}. \tag{7.11}$$

Now, the average field amplitude in equation (7.11) can be seen to be a factor $2/\pi$ times the maximum field amplitude. The average sensitivity of the antenna to incoming radiation from the cylinder is therefore reduced by the factor $2/\pi$ compared to the case of a uniform field distribution in the aperture. This gives the final result for the average scattered field as

$$\bar{E}_{scat}(\bar{r}) = \frac{2E_0}{\pi} \left[ -\frac{J_0(k_i a)}{H_0^{(2)}(k_i a)} H_0^{(2)}(k_i \bar{r}) - 2 \sum_{n=1}^{\infty} j^n \frac{J_n(k_i a)}{H_n^{(2)}(k_i a)} H_n^{(2)}(k\bar{r}) \frac{\sin(n\theta)}{n\theta} \right]. \tag{7.12}$$

where the variable $\bar{r}$ in equation (7.12) is the approximate average arc length to the aperture plane from the centre of the cylinder, that is,

$$\bar{r} = \frac{d_1^*}{\cos(\theta/2)}. \tag{7.13}$$

Consider now the transmitted wave from the antenna. In this experiment, the microwave network was normalized to zero decibels (1 mW ) power and zero phase at the antenna front face (see section 6.1.3.1). Since the cylinder is small compared

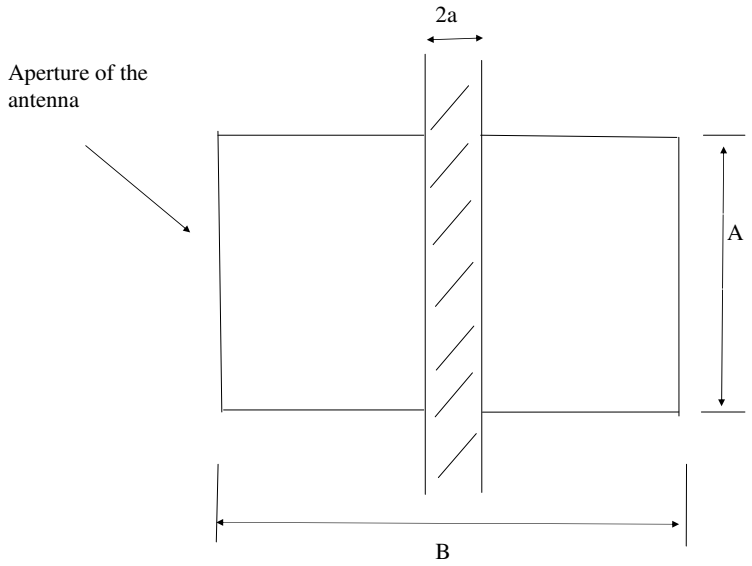


Figure 7.2: The yz-plane. This shows the cylinder and the aperture of the antenna.

to the aperture width of the antenna (Figure 7.2), the transmitted field can be written as

$$E^t_{z,c}(f_i) = E_0 e^{jk_i d_1}. \tag{7.14}$$

The reflection coefficient is defined as the ratio of the reflected signal to the incident signal [99, 8]. Therefore the reflection coefficient of the cylinder measured at the antenna front face relative to the centre of the cylinder is

$$\begin{gathered}\Gamma_i = -\frac{\bar{E}_{scat}(\bar{r})}{E_0 e^{jk_i d_1}} = \\ \frac{2}{\pi} e^{-jk_i d_1} \left[ \frac{J_0(k_i a)}{H_0^{(2)}(k_i a)} H_0^{(2)}(k_i \bar{r}) + 2 \sum_{n=1}^{\infty} j^n \frac{J_n(k_i a)}{H_n^{(2)}(k_i a)} H_n^{(2)}(k_i \bar{r}) \frac{sin(n\theta)}{n\theta} \right].\end{gathered} \tag{7.15}$$

In equation (7.15), the minus sign in the definition of $\Gamma$ stems from the normalisation to a short circuit at the aperture plane.

## 7.2 Comparison of experimental results with theoretical results

In this section, measured results are compared with computed results using the forward equations. We first calculate the reflection coefficient using equation (7.15) obtained by considering the scattering due to a plane wave incident upon the conducting cylinder. Then, this result is compared with the experimental results we have in section 6.3.

### 7.2.1 Measurement results together with the theoretical results

The reflection coefficients were calculated for different values of $d_1$ using equation (7.15). The values of $a$, A and B are known for the experiment (see section 6.1.1) and, as the experiment is performed in the air, $\varepsilon$ the relative permittivity and $\mu$ the relative permeability are both taken as one and $\sigma$ the conductivity as zero in these calculations.

The computation needs several terms to converge to a constant value. These computations were carried out in MATLAB and the results are plotted in Figures 7.3 and 7.4. The experimental data obtained from microwave measurements (using equation (6.5)) have been plotted on Figure 7.3 for easy comparison. These results are presented in Senaratne *et al.* [113, 114]. In general, the calculated and measured data are very similar.

### 7.2.2 Agreements and disagreements

In Figure 7.3, the behaviour of the two sets of graphs, for the measured and calculated values, is very similar as expected. General comments on the results can be made as follows:

(i)

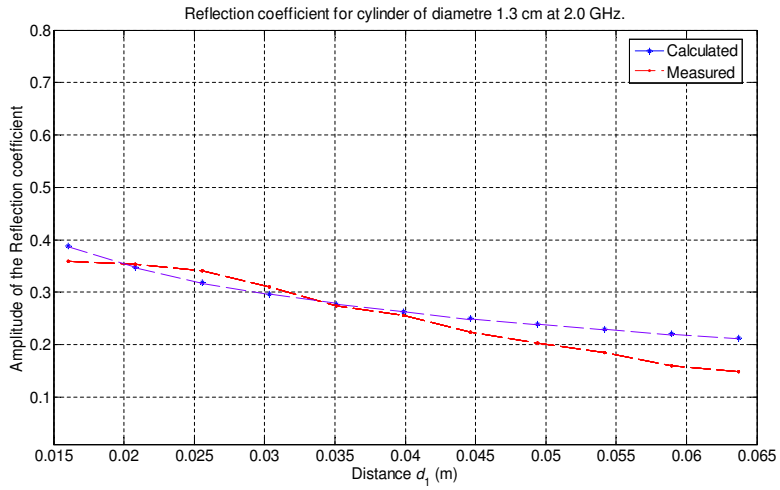


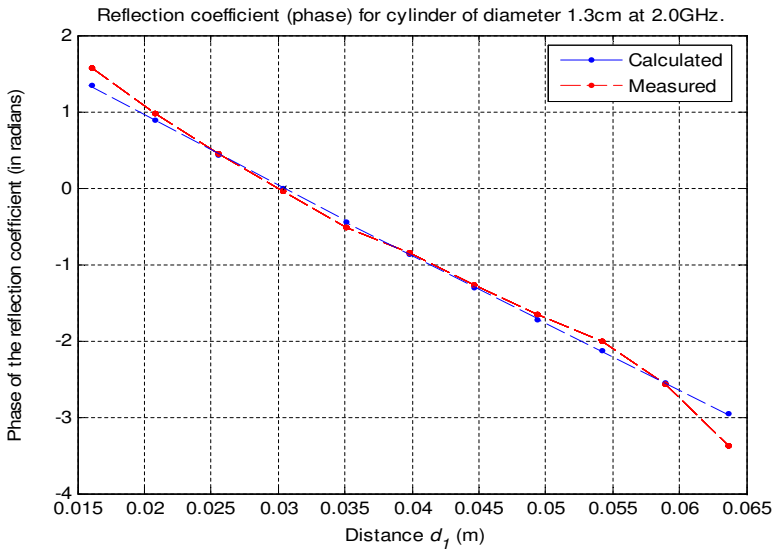


(ii)

Figure 7.3: The measured and calculated reflection coefficients at 2.0 GHz frequency as a function of the distance $d_1$ between the object and the antenna (i) Amplitude, (ii) Phase.

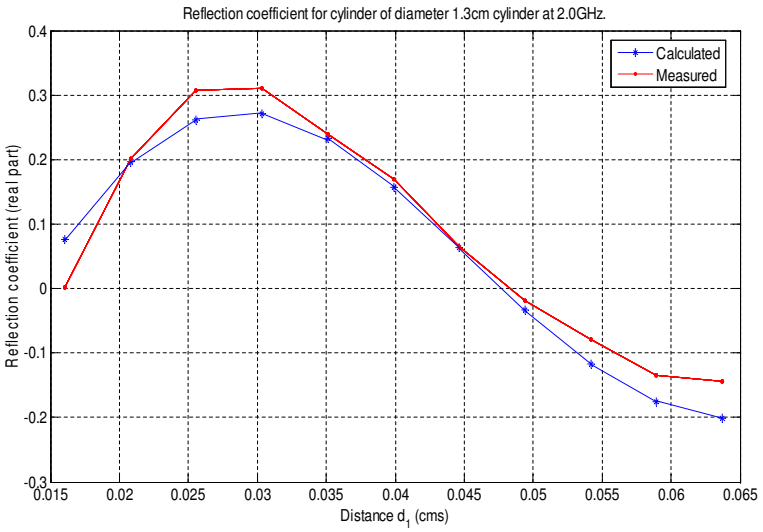


(i)

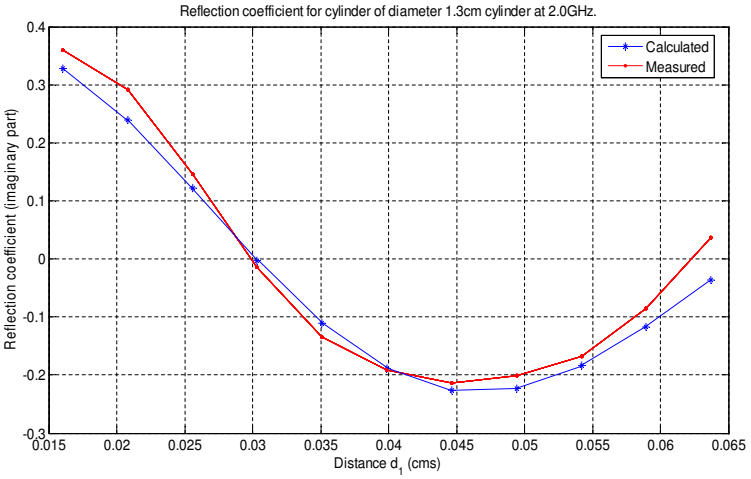


(ii)

Figure 7.4: The measured and calculated reflection coefficients at 2.0 GHz frequency as a function of the distance $d_1$ between the object and the antenna (i) Real part, (ii) Imaginary part.

1. The magnitude of the reflection coefficient plotted using the experimental results decreases as $d_1$ increases (see in Figure 7.3(i)) and this is very similar to the calculated results.

2. The phase plots are very similar to each other and in general the phase of the reflection coefficient shows a significant change with respect to the distance of the scattering object (Figure 7.3(ii)).

3. Real and Imaginary values of both sets of data have good agreement (Figure 7.4).

4. When the cylinder is close to the antenna, the theoretical result indicates that the magnitude of the reflection coefficient should continue to increase but, the magnitude of the reflection coefficient of the measured result does not exactly follow this. The field pattern very close to the antenna is rather complicated in practice [97, 107, 110]. Equation (7.9) associated with the normalised aperture plane would not be the best solution when the cylinder's reflection is being influenced by the antenna near field effect.

5. It is very important to keep the cylinder parallel with the aperture plane. Also, when changing the distance, the cylinder must be placed along the centre line of the antenna beam. Otherwise, these may cause errors. Apart from this, there would be effects from noise due to scattering from nearby objects and also from the signals received from internal and external sources around the measuring environment although we have attempted to avoid these.

## 7.3 Scattering from cylindrical waves

There are differences between the reflection of plane waves and cylindrical waves (we discussed this in section 3.4). In this section we consider scattering with cylindrical

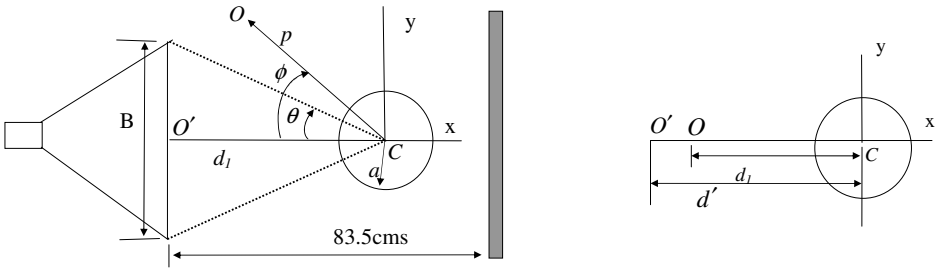


Figure 7.5: Scattering from cylindrical waves at the circular boundary of the conducting cylinder. (i) The coordinate system. (ii) When the field point and the source lie along the $x$ axis. Note $\phi$ is different to the case of plane wave scattering (Figure 7.1).

waves from the circular boundary of the conducting cylinder used in the experimental application.

### 7.3.1 Transmitted and received waves

The cylindrical coordinate system for the scattering problem with cylindrical waves is shown in Figure 7.5 (i). Consider a cylindrical wave incident upon the boundary of the cylinder. This wave is due to the wave excited from the antenna and we assume this wave is finite at point $C$, the centre of the cylinder. Consider two different points: a field point $O$ and a source point $O'$ as shown in the figure. Similar to the

solution we obtained for the forward problem in section 3.4.2, when $p < d'$, the field intensity of the scattered wave at the field point $O$ due to the source point $O'$ with respect to the centre of the cylinder can be written using equation (3.60) as

$$E_z^s(p,\phi;f_i) = E\sum_{n=-\infty}^{\infty} j^{-n}\left[-\frac{J_n(k_i a)}{H_n^{(2)}(k_i a)}H_n^{(2)}(k_i d')H_n^{(2)}(k_i p)\right]e^{jn\phi}, \tag{7.16}$$

where $\phi$ is the angle that $CO$ makes with the $x$ axis and $p$ and $d'$ are the distances between the points $C$ and $O$ and the points $C$ and $O'$, respectively and $E$ is a constant for the medium and is defined in equation (3.54). The subscript $i$ relates to the frequency $f_i$ of the signal used. Similarly to the procedure we followed to obtain equation (3.55), the transmitted wave at $O$ due to the source point $O'$ with respect to $C$ is

$$E_z^t(p,\phi;f_i) = E\,H_0^{(2)}\left(k_i\sqrt{d'^{\,2}+p^{\,2}-2d'p\cos(\phi)}\right). \tag{7.17}$$

### 7.3.2 Cylindrical waves normalised to the antenna aperture

In the previous section, equations (7.16) and (7.17) were obtained considering $O'$ as the source point which generates the cylindrical waves. In order to consider the situation that the whole aperture radiates the cylindrical waves towards the cylinder, we now normalise the scattered and incident fields over the area of the antenna aperture. This is similar to the case of plane wave scattering discussed in section 7.1.2.

In order to consider the situation where a single antenna is used for both transmission and receiving, it is necessary to find the received signal over the whole aperture area of the antenna. Therefore, the field point $O$ must be considered to be lying along B in the aperture plane such that the angle $\phi$ varies by between $+\theta$ and $-\theta$ with respect to the position of $O$ in the xy-plane (Figure 7.5). The total field at the antenna plane is the sum of all the field components along the line B,

the width of the antenna, which can be found as

$$E_z^s(f_i) = E\sum_{n=-\infty}^{\infty} j^{-n}\left[-\frac{J_n(k_i a)}{2\theta H_n^{(2)}(k_i a)}H_n^{(2)}(k_i d')\right]\int_{-\theta}^{+\theta} H_n^{(2)}(k_i p)e^{jn\phi}d\phi. \quad (7.18)$$

In order to obtain a reasonable solution to $E_z^s(f_i)$ in equation (7.18) with the length $p$ which varies with the angle $\phi$, we replaced the argument $k_i p$ in the Hankel function $H_n^{(2)}(k_i p)$ with $\frac{k_i d_1}{\cos(\theta/2)}$ by averaging the angle over the aperture ($d_1$ is the distance to the measuring point from the centre of the cylinder). Here, in order to meet the criteria of the addition theorem, we must have $d_1 < d'$ (Figure 7.5 (ii)). Then, following the same procedure in section 7.1.2, the average scattered field captured by the antenna aperture is

$$E_z^s(f_i) = \frac{2E}{\pi}\sum_{n=-\infty}^{\infty} j^{-n}[-\frac{J_n(k_i a)}{2\theta H_n^{(2)}(k_i a)}H_n^{(2)}(k_i d')H_n^{(2)}(\frac{k_i d_1}{\cos(\theta/2)})]\frac{2\sin(n\theta)}{n}. \quad (7.19)$$

Similarly, using equation (7.17), by averaging the angle $\phi$ over the aperture, an approximate solution for the transmitted wave at $O$ due to the source point with respect to $C$ can be obtained as

$$E_z^t(f_i) = EH_0^{(2)}\left(k_i\sqrt{{d'}^2 + {d_1}^2 - 2d'd_1}\right). \quad (7.20)$$

Then, using equation (7.19) and (7.20), an approximate solution for the reflection coefficient (normalized to the area of the antenna aperture for cylindrical waves) for frequency $f_i$ may be found as

$$\Gamma(f_i) = \frac{E_z^s(f_i)}{E_z^t(f_i)}. \quad (7.21)$$

Equation (7.21) was used to calculate the reflection coefficient of the cylinder for different values of $d_1$, which is the distance to the measuring point from the centre of the antenna aperture. In this equation, we can also change $d'$, the distance to the source from the centre of the cylinder (Figure 7.5 (ii)), and calculate the corresponding values of the reflection coefficient. When cylindrical waves are considered, the value of the reflection coefficient changes not only with the distance

to the measuring point from the centre of the cylinder, but also with the distance to the source point from the centre of the cylinder. This is illustrated in the next section.

## 7.4 Results comparison with cylindrical waves

In the experimental situation, when the scattering object is very close to the source, the wave incident upon the object is complicated and cannot be a pure plane wave. When the object is far from the source the scattering results are better approximated by being from plane waves rather than from cylindrical waves. Therefore, in this section, we investigate the scattering responses using the equation (7.21) obtained for cylindrical waves with respect to the distance between the source and the scattering object.

Equation (7.21) was used to calculate the reflection coefficients of the cylinder at different distances from the antenna aperture. The radius of the cylinder is 0.065 cm and the distance $d_1$ was changed from 1 cm to 6 cm in 0.5 cm steps for each set of simulations. We computed at least 40 terms until the series in equation (7.19) converges to a constant value. In this study, the reflection coefficients were calculated not only with $d_1$ but also with different values of $r$, where $r = d' - d_1$ is the distance between the source point and the field point (see Figure 7.5(ii)). The value of $r$ is fixed for each set of calculations with different values of $d_1$. The computed results are plotted against the distance $d_1$ in Figure 7.6 and the details of each plot are summarised as follows:

1. Plot (1) is for the cylindrical waves when the value of $r$ is 2 m.

2. Plot (2) is for the cylindrical waves with $r = 0.1$ m. This plot has a small difference from plot (1) in amplitude even though the $r$ values are very different (0.1 m and 2 m).

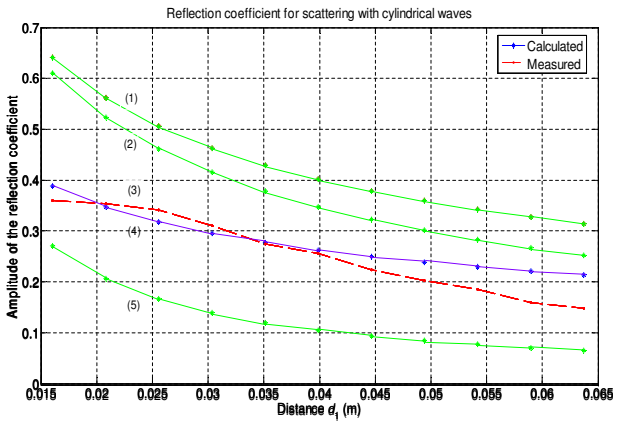


Figure 7.6: Calculated reflection coefficients (Magnitude) with cylindrical waves. The different labelled curves are described in the text.

3. Plot (3) is for the measured data of the reflection coefficient plotted against the distance $d_1$.

4. Plot (4) is for the calculated reflection coefficient using equation (7.15) which was obtained for the plane wave scattering.

5. Plot (5) is for the cylindrical waves with $r = 0.001$ m (when the source point $O'$ is very close to the field point $O$).

In addition to the above results, we have computed further the reflection coefficients with different values of $r$ and $d_1$. The following observations can be made:

(a) When the distance to the source point from the scattering object is less than the distance to the field point from the object, that is when $d' \leq d_1$, equation (7.21) does not give any solution (this equation is not valid). However, with a very small value of $r$ while $d' \geq d_1$ , we could use equation (7.21) to calculate the reflection

coefficient and the results are shown in plot (5).

(b) From the results we obtained by simulating with different values of $r$ (these results are not shown in Figure 7.6), we observed that, as $r$ becomes larger, the whole curve is shifted upward rapidly. However, a situation is reached where there is no further increase of the reflection coefficients (no further shifting of the curve upward) even if the value of $r$ is further increased. This can be seen in plot (2) and plot (1) and their corresponding $r$ values.

(c) The measured results in plot (3) closely agree with plot (4) which is for the plane waves normalised to the antenna aperture. Even with the use of the equation for cylindrical waves, a value of $r$ can be found so that the calculated reflection coefficients closely agree with the measured reflection coefficients (we found that the value of $r = 0.015$ m gives a good agreement of the calculated data with the measured results).

Overall, it can be understood that the variable $r$ in equation (7.21) determines the position of the curve of the reflection coefficient (magnitude) with respect to the distance of the scattering object. If $r$ is very small relative to $d_1$, the position of the curves are different. If $r$ is large relative to $d_1$ then the position of the curve moves upward.

## 7.5 Computation of unknowns using measurement results

In this experiment we have measured the reflection coefficients of the internal object using the forward and backward signals at the antenna point. Now we compute the object size and its distance from the measurement plane using the inverse method.

In the inverse problem the field at the receiver is known by measurement and $a$ and $d_1$ are the unknowns. Finding solutions to two unknowns is not possible unless

two equations are obtained by using two different frequencies. Use of this method for an over-determined system is also possible but it is important to use suitable frequencies [111]. At the antenna point the magnitude and phase measurements were recorded for a range of frequencies. Two equations for two different frequencies were used to find $a$ and $d_1$.

Now the general equation is formed using the measurement values and the forward equation as found from equation (7.15). The general equation has two constituent equations of the form

$$\Delta\Gamma_1 = \begin{bmatrix} \Delta\Gamma_{1,1} \\ \\ \Delta\Gamma_{1,2} \end{bmatrix} = \begin{bmatrix} \Gamma^M_{1,1} - \Gamma_1 \\ \\ \Gamma^M_{1,2} - \Gamma_2 \end{bmatrix} = \begin{bmatrix} 0 \\ \\ 0 \end{bmatrix}, \tag{7.22}$$

where we now use the subscripts 1,1 and 1,2 in $\Gamma$ to indicate two different frequencies. The terms $\Gamma^M_{1,1}$ and $\Gamma^M_{1,2}$ are the field measurements from the antenna $A_1$ for two different frequencies. The terms $\Gamma_1$ and $\Gamma_2$ are the theoretical solutions for the reflection coefficients applicable to the measurement system (as found in equation (7.15)) for frequency $f_1$ and frequency $f_2$, respectively.

The inverse algorithm was used to calculate the values of $a$ and $d_1$ using the measured data from the experiment. Figure 7.7 shows some examples of the computed results for the solution of equation (7.22) using two sets of guess values. The measurement results obtained with a 0.013 m diameter cylinder were used for this calculation. These plots illustrate two iteration processes and in each case show estimates of the two unknowns $a$ and $d_1$ converging towards some values closer to their exact values (the radius of the cylinder, $a = 0.0065$ m and the distance to the centre of the cylinder from the antenna, $d_1 = 0.0365$ m). Each set of guess values needs a different number of iterations. In general, more iteration is required when the guess values are further away from the exact values.

The method of computing unknowns using the inverse algorithm has been ex-

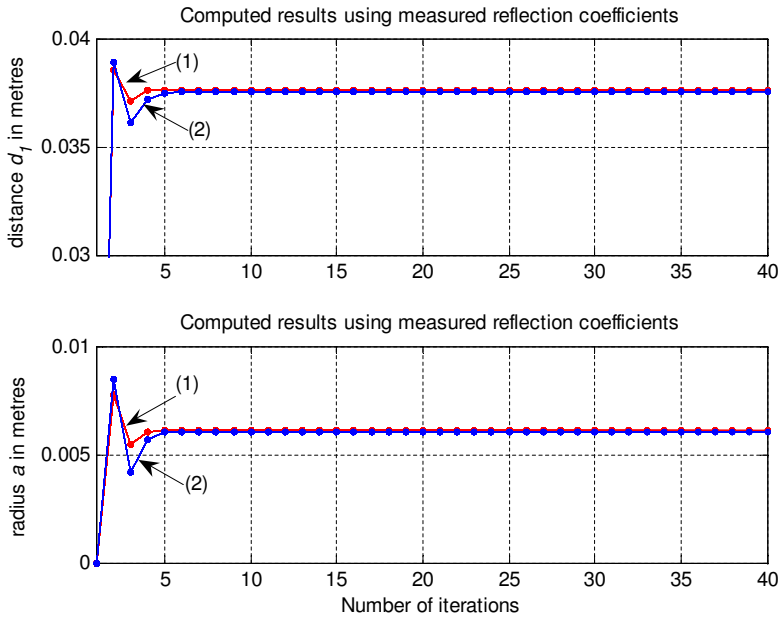


Figure 7.7: Plot of calculated values of $a$ and $d_1$ using the inverse method. Plot (1) with $d_1 = 0.0368$ m, $a = 0.0068$ m, (2) with $d_1 = 0.036$ m, $a = 0.0058$ m

plained in sections 2.4, 3.3.2 and 4.3 and also the calculated numerical results have been given in sections 2.5, 3.6 and 4.6 for 1, 2 and 3-dimensional studies, respectively. It is emphasised that although we used known values of $a$ and $d_1$ (two reasonable values) to calibrate the forward waves in the inverse method they are determined from the measurements by being unknown in both the forward and backward wave expansions. Thus we have a basis on which to assess the success of the method.

## 7.6 Inverse solutions in conjunction with the scanning method

In order to find the solutions for the radius of the unknown object and its position using the measured results, our method requires a series of tests. Here we use a

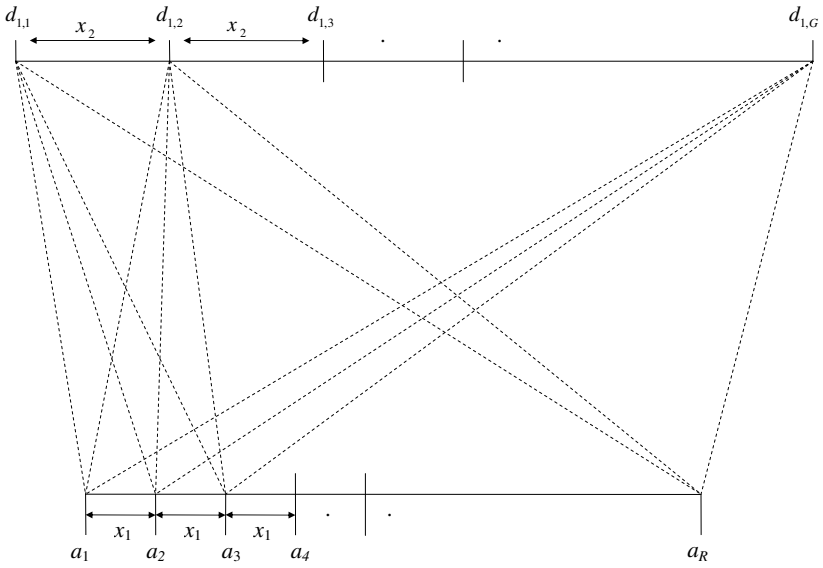


Figure 7.8: Test for unknowns within the required scanning range.

scanning method to test for possible solutions of the unknowns.

### 7.6.1 Test series

Equation (7.22) was used for a series of tests to calculate the unknowns using the measured data and the procedure is as follows. First, use a pair of known values of $a$ and $d_1$ to find the safe region. The safe region is the limit of the guess values of $a$ and $d_1$ where the general equation safely converges to a feasible value (real, positive and of the right magnitude). Using a number of guess values, $a_{1,g}, d_{1,g}$ the safe range for $a$ and $d_1$ are found such that within these ranges the system converges safely to the exact known values of $a$ and $d_1$. As described previously in section 5.5 and Senaratne *et. al.* [112, 113], using the values of $x_1$ and $x_2$, a complete test for finding the unknowns can be performed. This is described in the following paragraph and illustrated in Figure 7.8.

First, we take two suitable ranges, $a_1$ to $a_R$ and $d_{1,1}$ to $d_{1,G}$, within which the exact values of $a$ and $d_1$ can be expected. These are the full scanning ranges and, in this computation process, we used multiple ranges for $a_1$ and $d_1$ : $a_1$ from 0.5 cm to 2 cm and $d_1$ from 0.5 cm to 6 cm. The two increments from one pair of guess values to the subsequent pair of $a$ and $d_1$ are marked as $x_1$ and $x_2$, respectively, in Figure 7.8. The test starts with the initial pair of guess values, $d_{1,1}$ and $a_1$, and computes $a$, $d_1$ and $|\Delta\Gamma_{1,1}|, |\Delta\Gamma_{1,2}|$ using the inverse algorithm. We have a stopping criterion, that is the calculated values of $a$, $d_1$ are real and positive and $|\Delta\Gamma_{1,1}|, |\Delta\Gamma_{1,2}|$ must tend to zero. If the result does not meet this criterin, then the system takes the next pair of guess values $d_{1,1}$, $a_2$ and calculates $a$ and $d_1$ using the same process. Similarly, this will continue until $a_G$, the last guess value of $a$ in that row is used. Next, the calculation starts with the guess values $d_{1,2}$, $a_1$ and continues the same process until the pair $d_{1,2}$, $a_R$ is used. The tests continue until the last pair of guess values, $d_{1,G}$, $a_R$ are used. Figure 7.9 shows the magnitudes values of the residuals of the reflection coefficient (in figure these are shown as $|F_1|$ and $|F_2|$ for frequencies $f_1$ and $f_2$, respectively) calculated in the iteration process explained previously. The corresponding calculated values of $a$ and $d_1$ were shown in Figure 7.7.

### 7.6.2 Microwave scanning results

So far, we have explained the calculation process of $a$ and $d_1$ for only one set of measured data which was obtained with the cylinder of 0.0065 m diameter, kept at 0.0415 m away from the antenna aperture. In the experiment, we have measured data with the cylinder placed at different positions between the antenna and the wall. Using these results the above process was carried out to calculate the cylinder radius and its distance from the antenna aperture for all of these positions. Figure 7.10 shows the results of seven calculations. For comparison, both the estimated and actual $a$ and $d_1$ values are plotted in the figure. These results show that there

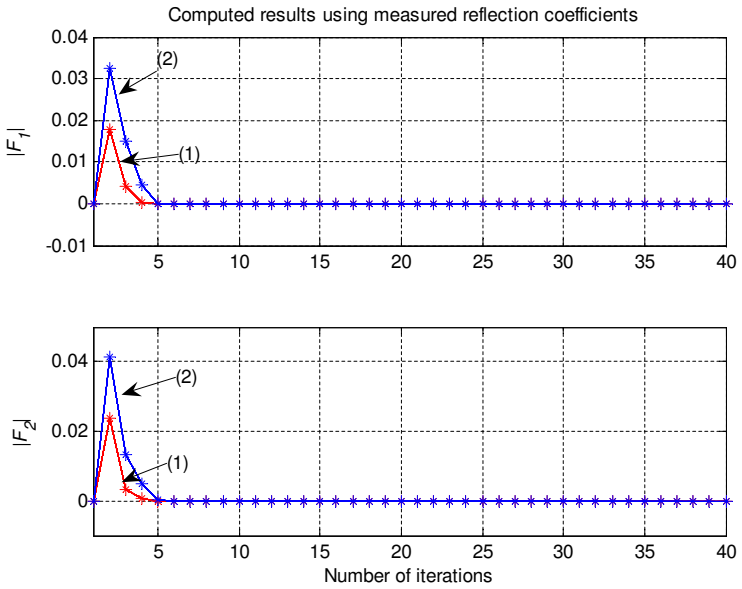


Figure 7.9: Plot of calculated values of $|F_1|$ and $|F_2|$ using the inverse method. Plot (1) with $d_1 = 0.0368$ m, $a = 0.0068$ m, (2) with $d_1 = 0.036$ m, $a = 0.0058$ m

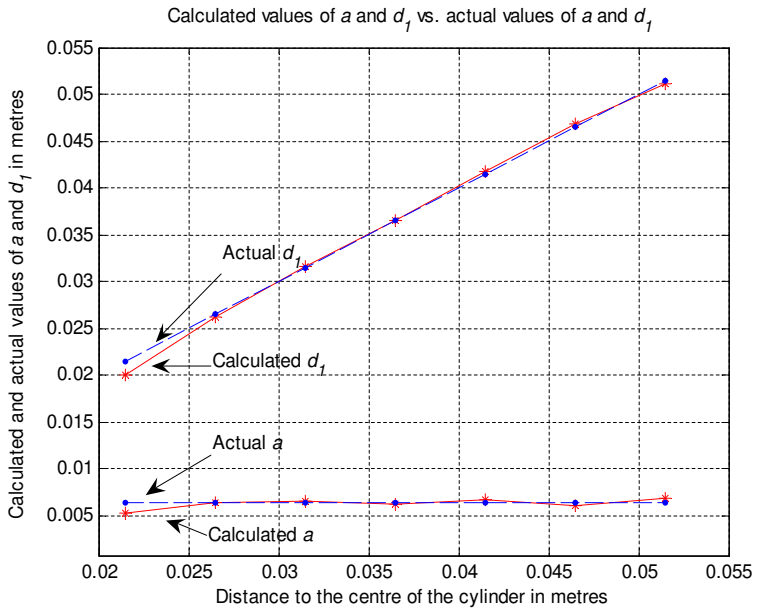


Figure 7.10: Calculated and measured results for the internal object using microwave measurements.

is a good agreement between the calculated and the actual values of $a$ and $d_1$.

The above results are for antenna position one in the experimental model. However, using the same procedure, it is possible to find the corresponding unknowns for other antennas. Once these calculated results are available the location of the object can be easily found using simple geometry.

In a practical application for the detection of a breast tumour, it would be important to measure the reflected wave using at least three antennas [114]. The complex reflection coefficient of the chest wall and the skin reflection can be estimated using a set of pre-recorded data or, at the time of obtaining measurements, by comparison with the measurements that can be obtained from normal tissue when the object or tumour is absent. We acknowledge that this may be difficult in practice but a clinical trial would provide a set of average values that would help for a reasonable estimation.

# Chapter 8

# Conclusions and future work

In previous chapters we obtained solutions to forward and inverse problems of microwave scattering associated with three different coordinate systems. These outcomes have a potential for detecting a foreign object inside a host material. This chapter presents the conclusions of this work and future directions for developing practical applications.

## 8.1 Discussion and conclusions

There are two major achievements in this research. One is obtaining solutions to the identified forward problems by expanding the classical theories found in electromagnetism. This work has been supported by mathematics. The other achievement is the development of the subsequent inverse algorithms to find the unknowns. Both of these cases were tested using simulations and experimental measurements.

### 8.1.1 Outcomes of the theoretical developments

The technical developments have begun with a plane wave reflection model. The microwave response at reflecting layers has been demonstrated using the electrical properties at both the sides of the boundaries of each layer. We have found that

the impedance in the front of each layer can be calculated from the measurements obtained from the surface of the host. These calculations have been made using the recursive equation (equation (2.30)) which was obtained using the plane wave reflection model. According to the simulation results, the front impedance which can be measured from the surface of the host contains information about the properties of the internal layers of the host. The test results have shown that there is a significant difference in the front-impedance when any two layers inside the host have differences in their dielectric properties. This result indicates that the detection of an internal object is possible using microwave surface measurements.

Next, using the solutions available in the literature, a microwave scattering problem of a cylindrically-shaped object has been obtained for a simple model using a cylindrical coordinate system. The plane wave incident upon the object boundary has been expressed in terms of cylindrical waves to obtain solutions for the field components of incident and scattered waves. The constructed solution at the field point was modified later so that the scattered field received at the source point can be found. This mathematical solution is useful for practical applications when taking microwave measurements using a single antenna for both transmitted and received signals.

In order to use this result for a more realistic application, we modified the forward model with a dielectric cylinder. Then, the new forward equation for the scattering problem of a dielectric cylinder was tested using simulations. According to this study we conclude that the dielectric property inside the scattering object makes a significant contribution to the backward wave which can be measured at the surface of the host. For a cylindrically-shaped object, we also obtained forward solutions for the case of microwave scattering from incident cylindrical waves and the result was tested using simulations. Again, we modified this solution for a non-conducting cylinder. This solution may be appropriate in practical applica-

tions when dealing with scattering problems associated with cylindrical waves. The inverse scattering problem associated with this cylindrical object has been solved using Newton's iterative method. Initially, this inverse algorithm was tested using the data generated analytically from the forward equation. Later we found that the algorithm is capable of finding unknowns using the data obtained from microwave measurements.

We have advanced our method for considering a scattering problem of a spherically-shaped object inside the host model. Using the available solutions in literature, a forward equation was obtained with the help of a spherical coordinate system. The incident and scattered wave fields have been expressed in terms of transverse electric and transverse magnetic modes. Then, by taking the wave functions as rectangular components of electric or magnetic vector potentials, the field components have been constructed. This approach has resulted in finding the solutions to the forward problem at an arbitrary field point in a radial direction from the centre of the sphere. Again, as in the cylindrical case, the solutions to the field components were obtained by rotating the field point into the source point. This solution facilitates the use of a single antenna for both transmission and receiving when this method is used in practical applications. The corresponding forward and inverse algorithms in the three-dimensional study were tested analytically using simulations. It has been found that these algorithms are capable of computing unknowns by applying microwave signals and analysing the backscattered waves received at the surface of the host material.

The convergence of the inverse algorithm has been studied by conducting a robustness analysis using a range of different guess values. The result of this analysis has revealed that the performance of the converging process depends upon the initial guess for the unknowns. The larger the difference between the guess value and the exact value the poorer the performance is. As a result of this study, a safe range

was found within which the algorithm can safely converge to the exact values. The results of this analysis have been used in the experimental study when finding the size of the scattering object and its distance from the antenna.

The accuracy of the calculated results using this inverse method depends upon the accuracy of the measurements. Therefore, we tested this algorithm in the presence of simulated measurement errors. According to the result of this test, this algorithm can calculate unknowns even with some errors in the measured data. However, when the errors in the measured data are large the corresponding errors in the calculated values of unknowns are also relatively large.

### 8.1.2 Experimental developments

In the experimental study we obtained measurements by illuminating cylindrically and spherically-shaped objects using microwave signals. The measured values of the reflection coefficient of the conducting cylinder in this experiment agree with the values predicted using the forward equations of the theoretical model. However, there are some disagreements between the predicted and measured results when the object is very close to the antenna (this could be a problem with the antenna near field effect and this problem may need to be treated separately).

From the measured data, we found that the scattered waves from the object have been seriously affected by the reflection from the wall behind the object. However, we could distinguish the response of the object by taking two sets of separate measurements: one set is with the wall and the object and the other is with the object itself. The difference between these data was analysed using the polar plots and by referring to the Smith chart. These plots have shown that there was an offset in the whole set of data (the phase and the magnitude of the reflection coefficient) in the polar plane. We found that this offset is approximately equal to the phase and magnitude values of the measured reflection coefficient of the wall.

The reflection coefficients measured from the experimental study have been used to compute the radius of the object and its distance from the antenna. The computed results are very close to their actual values. The inverse algorithm was used together with the scanning method to compute the values of the unknowns using the measured data. The simulation process has run within two specified ranges to search for the two unknowns. The selection of the guess values makes a significant contribution to the calculated results and this depends upon the safe range. When the distance between two consecutive guess values exceeds the safe range we do not obtain satisfactory results. Alternatively, when this distance is very small we need a large number of scanning steps to cover the selected range. Therefore, when using the scanning method, it is important to set suitable increments for the guess values within the selected ranges to search for the unknowns. The inverse algorithm and the associated scanning method have performed well even in a situation where there are some errors in the measured data.

## 8.2 Future work

The results of the mathematical and experimental study reveal that the detection of a foreign object is possible using measured reflection coefficients. This method has a potential for further development to use in medical applications such as detecting a breast tumour as a cost effective screening method. In order to develop this method for practical application, more work is needed in both experimental and practical applications. Some of the areas for future study are discussed in the following sections.

### 8.2.1 Short term goals

The main target of the inverse algorithm is to find the size and the location of the scattering object. The location can be found once the distances to the object are found from at least three surface points, which can be achieved using the measurements obtained by three different antennas. In order to calculate the two unknowns from each antenna, we need to use at least two frequencies. This method may be further improved by solving for an over-determined system using several frequencies.

In the theoretical study, the solutions to the microwave scattering problems were obtained for both conducting and non-conducting objects. The experimental study presented in this thesis was conducted only with a conducting cylinder and a conducting sphere. Therefore it is important to conduct similar experiments with dielectric objects. The algorithms developed so far will support this work. Such experiments should aim to mimic the properties of the object lodged in the host material as closely as possible. Once this test model is constructed the rest of the measuring and estimating procedure is similar to the method illustrated in this thesis.

The antenna near field effect is another problem to be solved before proceeding to develop practical applications. In practical applications, the microwave measurements are taken by the antenna placed on the surface of the host material. Because of the complicated field pattern closer to the antenna, this near field effect could prevent the discovery of an object close to the surface of the host. In such a situation, the algorithm can compute incorrect results and it is possible to miss the object in the scanning process. Lifting the antenna from the surface could be a solution but further work is necessary to solve this problem.

### 8.2.2 Long term goals

We recommend the rest of the experimental study be performed in a suitable microwave laboratory. If the measuring chamber is properly insulated to microwaves, it would reduce the effect of the noise and interference coming from outside of the chamber.

Once the rest of the work in the laboratory experiment is completed, this method will need to be tested in a practical situation. This may be possible using a prototype breast model in the initial stage. However, in order to use this method for breast cancer detection, a number of clinical tests would be required.

In order to build a prototype test model, it is necessary to have more accurate estimates of the properties of breast tumours as well as of the properties of the other biological tissues including the skin-fat of the breast. In such a situation, the data and the information available in the literature search in this thesis may be inadequate and therefore further investigations would be required. The construction of the prototype experimental breast model needs a careful selection of appropriate materials which have electrical properties similar to those of the breast and a breast tumour. Apart from this, the prototype breast model must consist of layers for the skin fat and the chest wall.

Although we have used a larger antenna for the experimental study, the antenna system for this practical experiment must be designed and built so that it is feasible to use it with this prototype breast model. Again, there may be a number of antennas but, the detection and the calculation of the size and the distance of the scatterer from each antenna can be performed using the algorithm and the associated scanning method developed in this thesis.

The problem associated with reflection from the chest wall, breast skin and other interference must be treated using the prototype breast model before proceeding to any clinical experimentation. The reflected waves which can be measured from the

surface of the breast will contain all these unwanted backscattered waves. Having a sufficient amount of data available from the measurements, a substantial amount of noise could be filtered out to obtain the microwave response of the breast tumour. It is acknowledged that there is more work necessary to minimise these effects. The theoretical developments, analytical simulations and the experimental studies of this thesis have given the directions to achieve this goal.

# Appendix A

# Field equations

The fundamental electromagnetic wave theory is well established [7, 8, 14, 15, 99]. In this appendix we illustrate a number of wave solutions which are commonly used in electromagnetic wave problems.

**Field equations**
For a perfect dielectric medium, the field equations for **E**, the complex electric intensity and **H**, the complex magnetic intensity are:

$$\begin{aligned} \nabla \times \mathbf{E} &= -j\omega\mu\mathbf{H}, \\ \nabla \times \mathbf{H} &= j\omega\varepsilon\mathbf{E} + \mathbf{J}, \end{aligned} \tag{A.1}$$

where **J** is a vector which represents the source or the electric impressed current. Equation (A.1) can be used for a lossy medium by replacing $\mu$ and $\epsilon$ with their complex quantities $\hat{\mu}$ and $\hat{\epsilon}$, respectively and $\hat{\mu}$ and $\hat{\epsilon}$ are the complex permeability and permittivity, respectively [8]. (See section 1.3 in Chapter 1 for more details.)

For a homogeneous medium the divergence of **H** in the first equation of (A.1) is $\nabla \cdot \mathbf{H} = 0$. Any divergence-free vector is the curl of some other vector. Therefore,

$$\mathbf{H} = \nabla \times \mathbf{A}, \tag{A.2}$$

where **A** is called the magnetic vector potential. Using (A.1) and (A.2) we obtain,

$$\nabla \times (\mathbf{E} + j\omega\mu\mathbf{A}) = \mathbf{0}. \tag{A.3}$$

Any curl free vector is a gradient of some scalar and therefore

$$\mathbf{E} + j\omega\mu\mathbf{A} = -\nabla\Phi^a, \tag{A.4}$$

where $\Phi^a$ represents the magnetic scalar potential. In order to obtain the equation for **A**, substitute (A.2) and (A.4) into second equation of (A.1):

$$\nabla \times (\nabla \times \mathbf{A}) = j\omega\varepsilon(-\nabla\Phi^a - j\omega\mu\mathrm{A}) + \mathbf{J}$$
$$= -j\omega\varepsilon\nabla\Phi^a + k^2\mathbf{A} + \mathbf{J},$$

where $k = \omega\sqrt{\mu\varepsilon}$ is the wave number of the medium. The above equation can be arranged as

$$\nabla \times (\nabla \times \mathbf{A}) - k^2\mathbf{A} = -j\omega\varepsilon\nabla\Phi^a + \mathbf{J}. \tag{A.5}$$

Using the vector identity $\nabla^2\mathbf{A} = \nabla(\nabla \cdot \mathbf{A}) - \nabla \times (\nabla \times \mathbf{A})$, equation (A.5) can be written as

$$\nabla(\nabla \cdot \mathbf{A}) - \nabla^2\mathbf{A} - k^2\mathbf{A} = -j\omega\varepsilon\nabla\Phi^a + \mathbf{J}. \tag{A.6}$$

If $\nabla \cdot \mathbf{A} = -j\omega\varepsilon\Phi^a$ , then equation (A.6) becomes

$$\nabla^2\mathbf{A} + k^2\mathbf{A} = -\mathbf{J}. \tag{A.7}$$

Equation (A.7) is the Helmholtz equation but with a non-zero right-hand-side. The solutions to this equation are given in terms of vector potentials. From equation (A.7), equation (A.6) can be written as $\nabla(\nabla \cdot \mathbf{A}) = -j\omega\varepsilon\nabla\Phi^a$ and, by substituting this in equation (A.4),

$$\mathbf{E} = -j\omega\mu\mathbf{A} + \frac{1}{j\omega\varepsilon}\nabla(\nabla \cdot \mathbf{A}). \tag{A.8}$$

Now consider the field equations for a perfect dielectric with $\mathbf{M}$ being the magnetic displacement current,

$$\begin{aligned} \nabla \times \mathbf{H} &= j\omega\varepsilon\mathbf{E}, \\ \nabla \times \mathbf{E} &= -j\omega\mu\mathbf{H} - \mathbf{M}. \end{aligned} \tag{A.9}$$

In homogeneous media, $\nabla \cdot \mathbf{E} = 0$ ($\mathbf{E}$ is a divergence-free vector) and therefore this can be the curl of some other vector as,

$$\mathbf{E} = \nabla \times \mathbf{F}, \tag{A.10}$$

where $\mathbf{F}$ is called the electric vector potential. Therefore, the first equation of (A.9) can be written as,

$$\nabla \times (\mathbf{H} - j\omega\varepsilon\mathbf{F}) = \mathbf{0}. \tag{A.11}$$

Any curl-free vector is a gradient of some scalar. Hence,

$$\mathbf{H} - j\omega\varepsilon\mathbf{F} = \nabla\Phi^f \tag{A.12}$$

where $\Phi^f$ is the electric scalar potential. By substituting (A.10) and (A.12) into the second equation of (A.9),

$$\nabla \times (\nabla \times \mathbf{F}) - k^2\mathbf{F} = -\mathbf{M} - j\omega\mu\nabla\Phi^f. \tag{A.13}$$

Again, using the vector identity for $\nabla \times (\nabla \times \mathbf{F})$, equation (A.13) can be written as

$$-\nabla^2 \mathbf{F} + \nabla (\nabla \cdot \mathbf{F}) - k^2 \mathbf{F} = -\mathbf{M} - j\omega\mu\nabla\Phi^f. \tag{A.14}$$

If $\nabla \cdot \mathbf{F} = -j\omega\mu\Phi^f$ then equation (A.14) becomes

$$\nabla^2 \mathbf{F} + k^2 \mathbf{F} = \mathbf{M}. \tag{A.15}$$

Again, equation (A.15) is the Helmholtz equation but with a non-zero right-hand-side.

In a homogeneous and source-free region, the fields satisfy the following equations.

$$\begin{aligned} -\nabla \times \mathbf{E} = \hat{z}\mathrm{H}, \quad \nabla \cdot \mathbf{H} = 0, \\ \nabla \times \mathbf{H} = \hat{y}\mathbf{E}, \quad \nabla \cdot \mathbf{E} = 0 \end{aligned} \tag{A.16}$$

Since the fields $\mathbf{E}$ and $\mathbf{H}$ are a divergence-free, we can express them in terms of $\mathbf{A}$ the magnetic vector potential or, in terms of $\mathbf{F}$ the electric vector potential, see (A.2) and (A.10). We can employ solutions with a combination of $\mathbf{A}$ and $\mathbf{F}$, but $\mathbf{A}$ and $\mathbf{F}$ (as the dual relationship) must be a solution to Helmholtz equation in (A.7) with $\mathbf{J} = \mathbf{0} = (0, 0, 0)$, and $\mathbf{F}$ must be a solution to dual equation in (A.15) with $\mathbf{M} = \mathbf{0} = (0, 0, 0)$. Thus, from equations (A.5) and (A.13), the general equations for the vector potentials $\mathbf{A}$ and $\mathbf{F}$ are

$$\begin{aligned} \nabla \times (\nabla \times \mathbf{A}) - k^2 \mathbf{A} = -\hat{y}\nabla\Phi^a, \\ \nabla \times (\nabla \times \mathbf{F}) - k^2 \mathbf{F} = -\hat{z}\nabla\Phi^f, \end{aligned} \tag{A.17}$$

where $\Phi^a$ and $\Phi^f$ are scalars and $\hat{y} = j\omega\hat{\varepsilon}$ and $\hat{z} = j\omega\hat{\mu}$ (see section 1.2).

The complete solution for $\mathbf{E}$ and $\mathbf{H}$ is the combination of two partial solutions to electric and magnetic sources. From the Maxwell's relationship, we have $\nabla \times \mathbf{H} = \hat{y}\mathbf{E} + \mathbf{J}$, and this can be arranged as

$$\mathbf{E} = (\nabla \times \mathbf{H} - \mathbf{J})\frac{1}{\hat{y}}. \tag{A.18}$$

Therefore, (with the combination of two partial solutions) the solution to field $\mathbf{E}$ can be found in terms of $\mathbf{A}$ and $\mathbf{F}$ using equations (A.2), (A.10) and (A.18) as

$$\mathbf{E} = \frac{1}{\hat{y}} (\nabla \times (\nabla \times \mathbf{A}) - \mathbf{J}) - \nabla \times \mathbf{F}. \tag{A.19}$$

Similarly the solution to $\mathbf{H}$ fields can be found from the dual relationship and it is

$$\mathbf{H} = \frac{1}{\hat{z}} (\nabla \times (\nabla \times \mathbf{F}) - \mathbf{M}) + \nabla \times \mathbf{A}. \tag{A.20}$$

Thus, the electromagnetic fields for $\mathbf{E}$ and $\mathbf{H}$ in terms of $\mathbf{A}$ and $\mathbf{F}$, with $\mathbf{J} = \mathbf{0}$ and $\mathbf{M} = \mathbf{0}$, are

$$\begin{aligned} \mathbf{E} = -\nabla \times \mathbf{F} + \tfrac{1}{\hat{y}}(\nabla \times (\nabla \times \mathbf{A})), \\ \mathbf{H} = \nabla \times \mathbf{A} + \tfrac{1}{\hat{z}}(\nabla \times (\nabla \times \mathbf{F})). \end{aligned} \tag{A.21}$$

These are the general equations for fields and potentials for a homogeneous and source free region.

From equations (A.7) and (A.15), with $\mathbf{J} = \mathbf{0}$ and $\mathbf{M} = \mathbf{0}$, we have $\nabla^2\mathbf{F} = -k^2\mathbf{F}$ and $\nabla^2\mathbf{A} = -k^2\mathbf{A}$ , respectively. Using these relationships with $k^2 = -\hat{y}\hat{z}$ and, by using the vector identity$\nabla^2\mathbf{A} = \nabla(\nabla\cdot\mathbf{A}) - \nabla\times(\nabla\times\mathbf{A})$ , equation (A.21) can be written as

$$\begin{aligned}\mathbf{E} &= -\nabla\times\mathbf{F} - \hat{z}\mathbf{A} + \tfrac{1}{\hat{y}}\nabla(\nabla\cdot\mathbf{A}),\\ \mathbf{H} &= \nabla\times\mathbf{A} - \hat{y}\mathbf{F} + \tfrac{1}{\hat{z}}\nabla(\nabla\cdot\mathbf{F}),\end{aligned} \tag{A.22}$$

Each equation in (A.22) has both $\mathbf{F}$ and $\mathbf{A}$ vector potentials. Therefore both of these equations can be expanded conveniently by choosing one vector potential at a time. When $\mathbf{F} = \mathbf{0}$ and $\mathbf{A} = \mathbf{u}_z\psi$($\mathbf{u}_z$ is a unit vector in z-direction), we can represent the fields in terms of $\mathbf{A}$ using equation (A.22) as

$$\mathbf{E} = -\hat{z}\mathbf{A} + \frac{1}{\hat{y}}\nabla(\nabla\cdot\mathbf{A}), \qquad \mathbf{H} = \nabla\times\mathbf{A}. \tag{A.23}$$

When the equation (A.23) is expanded in rectangular coordinates, we obtain

$$\begin{aligned} E_x &= \tfrac{1}{\hat{y}}\tfrac{\partial^2\psi}{\partial x\partial z}, & H_x &= \tfrac{\partial\psi}{\partial y},\\ E_y &= \tfrac{1}{\hat{y}}\tfrac{\partial^2\psi}{\partial y\partial z}, & H_y &= -\tfrac{\partial\psi}{\partial x},\\ E_z &= \tfrac{1}{\hat{y}}\left(\tfrac{\partial^2}{\partial z^2} + k^2\right)\psi, & H_z &= 0.\end{aligned} \tag{A.24}$$

In equation (A.24), we can see that the $H_z$ component is zero and therefore this type of field is called transverse magnetic (TM) to the z-direction. Similarly by choosing $\mathbf{A} = \mathbf{0}$ and $\mathbf{F} = \mathbf{u}_z\,\psi$ we can represent the fields in terms of $\mathbf{F}$ using equation (A.22) as

$$\mathbf{E} = -\nabla\times\mathbf{F} \qquad \mathbf{H} = -\hat{y}\mathbf{F} + \frac{1}{\hat{z}}\nabla(\nabla\cdot\mathbf{F}). \tag{A.25}$$

When the equation (A.25) is expanded in rectangular coordinates, we obtain

$$\begin{aligned} E_x &= -\tfrac{\partial\psi}{\partial y}, & H_x &= \tfrac{1}{\hat{z}}\tfrac{\partial^2\psi}{\partial x\partial z},\\ E_y &= \tfrac{\partial\psi}{\partial x}, & H_y &= \tfrac{1}{\hat{z}}\tfrac{\partial^2\psi}{\partial y\partial z},\\ E_z &= 0, & H_z &= \tfrac{1}{\hat{z}}\left(\tfrac{\partial^2}{\partial z^2} + k^2\right)\psi.\end{aligned} \tag{A.26}$$

In equation (A.26) we can see that the $E_z$ component is zero and therefore this type of field is transverse electric (TE) to the z-direction.

# Appendix B

# Bessel functions

Bessel's differential equation of order $v$ is

$$x^2\frac{d^2y}{dx^2} + x\frac{dy}{dx} + (x^2 - v^2)y = 0, \tag{B.1}$$

where $v$ is an arbitrary real or complex number. Since this is a second-order differential equation, there must be two linearly independent solutions [8, 97, 103]. However, when $v = n$ an integer, then there are no longer two independent solutions ($n$ is referred to as the order of the Bessel function).

The Bessel functions of the first kind, denoted as $J_n(x)$ , are solutions to Bessel's differential equation and these solutions are finite at the origin ($x = 0$) as $n$ is an integer. The following relationship is valid for $v = n$ an integer:

$$J_{-n}(x) = (-1)^n J_n(x). \tag{B.2}$$

The Bessel functions of the second kind, denoted by $Y_n(x)$ , are also solutions to the Bessel differential equation. The following relationship is valid for $v = n$ an integer:

$$Y_{-n}(x) = (-1)^n Y_n(x). \tag{B.3}$$

For the non-integer $v$,

$$Y_v(x) = \frac{J_v(x)\cos(v\pi) - J_{-v}(x)}{\sin(v\pi)} \tag{B.4}$$

and

$$Y_n(x) = \lim_{v\to n} Y_v(x). \tag{B.5}$$

The function $Y_v(x)$ are sometimes called Neumann functions and are denoted by $N_v(x)$. The Bessel functions of first kind and the Bessel functions of the second kind are shown in Figures B.1 and B.2, respectively. These are the lowest order functions ($n$=0, $n$=1 and $n$= 2) and have been plotted with respect to their argument $x$.

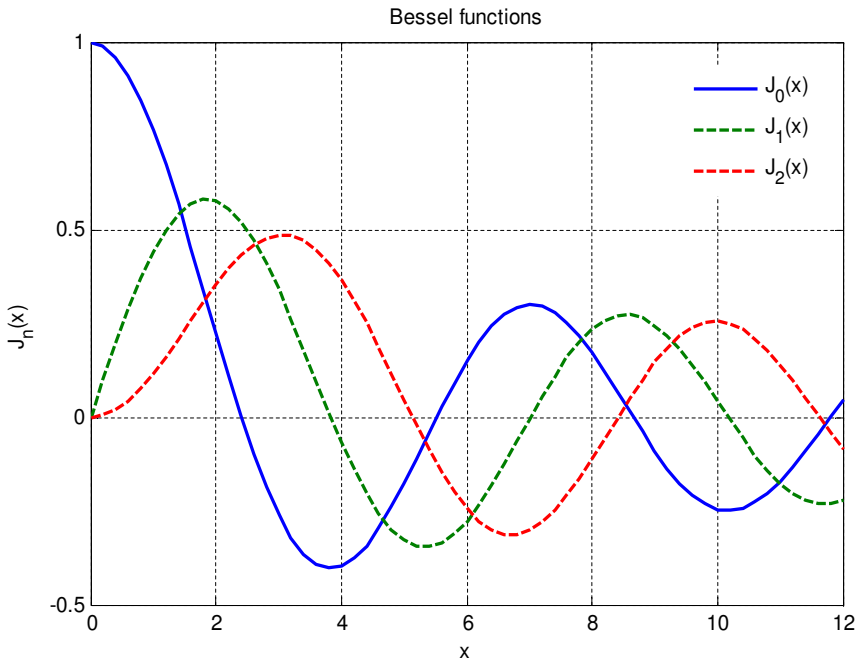


Figure B.1: The Bessel functions of first kind

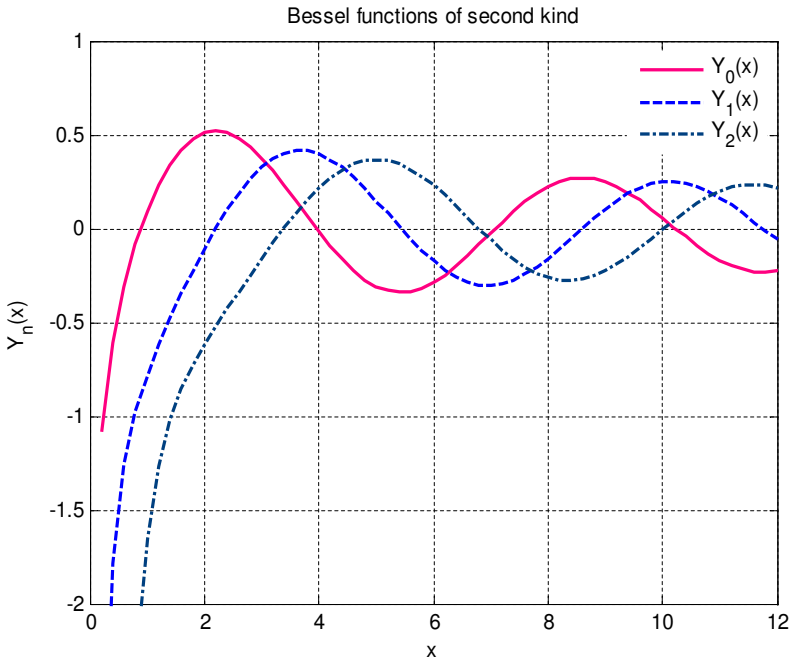


Figure B.2: The Bessel functions of second kind

Another pair of linearly independent solutions to Bessel's equation are the Hankel functions:

$$H_v^{(1)}(x) = J_v(x) + jY_v(x),$$
$$H_v^{(2)}(x) = J_v(x) - jY_v(x), \tag{B.6}$$

where $H_v^{(1)}(x)$ are the Hankel functions of first kind and $H_v^{(2)}(x)$ are the Hankel functions of second kind. These functions are used to express inward and outward propagating cylindrical waves, respectively.

The derivative formulae of the Bessel functions are

$$xJ_n'(x) + nJ_n(x) = xJ_{n-1}(x) \tag{B.7}$$

and

$$xJ_n'(x) - nJ_n(x) = -xJ_{n+1}(x). \tag{B.8}$$

From equations (B.7) and (B.8),

$$J_n'(x) = \frac{J_{n-1}(x) - J_{n+1}(x)}{2}. \tag{B.9}$$

Similarly,

$$xY_n'(x) + nY_n(x) = xY_{n-1}(x) \tag{B.10}$$

and

$$xY_n'(x) - nY_n(x) = -xY_{n+1}(x). \tag{B.11}$$

From equations (B.10) and(B.11),

$$Y_n'(x) = \frac{Y_{n-1}(x) - Y_{n+1}(x)}{2}. \tag{B.12}$$

From equations (B.9) and (B.12), the derivative of the Hankel function is given by

$$H_n^{(2)\prime}(x) = \frac{H_{n-1}^{(2)}(x) - H_{n+1}^{(2)}(x)}{2}. \tag{B.13}$$

The spherical Bessel functions are given by

$$j_n(x) = \sqrt{\frac{\pi}{2x}} J_{n+1/2}(x), \tag{B.14}$$

$$y_n(x) = \sqrt{\frac{\pi}{2x}} Y_{n+1/2}(x) = (-1)^{n+1}\sqrt{\frac{\pi}{2x}} J_{-n-1/2}(x). \tag{B.15}$$

Bessel functions of order $n+1/2$ are used in the solutions of the Helmholtz equation in spherical coordinates. The spherical Bessel functions are defined as

$$b_n(x) = \sqrt{\frac{\pi}{2x}} B_{n+1/2}(x), \tag{B.16}$$

where $B_n(x)$ denotes a solution to Bessel's equation ($J_n, Y_n$, $H_n^{(1)}$ and $H_n^{(2)}$ are the possibilities). Here, $j_n(x)$ is used to represent the spherical Bessel functions of the first kind and $h_n^{(2)}(x)$ is used to represent the spherical Hankel functions of the second kind.

# Appendix C

## C.1 Evaluation of the constant $u_n$

Here, we recall equation (3.11) to evaluate the constant $u_n$.

$$E_0 e^{-jk_1 p\cos\phi} = E_0 \sum_{n=-\infty}^{\infty} u_n J_n(k_1 p) e^{jn\phi}. \tag{C.1}$$

Multiply both the sides of equation (C.1) by $e^{-jm\phi}$ and integrate with respect to $\phi$ over the interval 0 to $2\pi$ to obtain

$$\int_0^{2\pi} e^{-jk_1 p\cos\phi} e^{-jm\phi} d\phi = \int_0^{2\pi} \sum_{n=-\infty}^{\infty} u_n J_n(k_1 p) e^{jn\phi} e^{-jm\phi} d\phi. \tag{C.2}$$

The right hand side of equation (C.2) can be simplified to

$$\int_0^{2\pi} \sum_{n=-\infty}^{\infty} u_n J_n(k_1 p) e^{jn\phi} e^{-jm\phi} d\phi = 2\pi u_m J_m(k_1 p). \tag{C.3}$$

The $m^{th}$ derivative of the left hand side of equation (C.2) with respect to $p$ is

$$\frac{d^m}{dp^m} \int_0^{2\pi} e^{-jk_1 p\cos\phi} e^{-jm\phi} d\phi = \int_0^{2\pi} k_1^m j^{-m} \cos^m(\phi)\, e^{-jk_1 p\cos\phi} e^{-jm\phi} d\phi. \tag{C.4}$$

When the right hand side of equation (C.4) is evaluated at $p = 0$ we obtain

$$k_1^m j^{-m} \int_0^{2\pi} \cos^m(\phi) e^{-jm\phi} d\phi = \frac{k_1^m 2\pi j^{-m}}{2^m}. \tag{C.5}$$

Similarly the $m^{th}$ derivative of the right hand side of equation (C.3) with respect to $p$ evaluated at $p = 0$ can be found as

$$\frac{k_1^m 2\pi u_m}{2^m}. \tag{C.6}$$

Then, with the results in equation(C.5), the constant $u_n$ is found as (putting $m = n$)

$$u_n = j^{-n}. \tag{C.7}$$

## C.2 Evaluation of the constant $g_n$

In order to evaluate $g_n$, multiply both sides of equation (4.14) by $P_q(\cos\theta)\sin\theta$ and integrate from 0 to $\pi$ on $\theta$. Then,

$$\int_0^\pi e^{-jkr\cos\theta}\, P_q(\cos\theta)\sin\theta\, d\theta = \int_0^\pi \sum_{n=0}^{\infty} g_n j_n(kr) P_n(\cos\theta) P_q(\cos\theta)\sin\theta\, d\theta. \tag{C.8}$$

When $n \neq q$, because of the orthogonality condition,

$$\int_0^\pi P_n(\cos\theta) P_q(\cos\theta)\sin\theta\, d\theta = 0. \tag{C.9}$$

When $n = q$, using the expression for the Legendre polynomials given in Rodrigues' formula [8], equation (C.9) is simplified to

$$\int_0^\pi \left(P_q(\cos\theta)\right)^2 \sin\theta\, d\theta = \frac{2}{2q+1}. \tag{C.10}$$

Therefore, the right hand side of equation (C.8) becomes

$$\int_0^\pi \sum_{n=0}^{\infty} g_n j_n(kr) P_n(\cos\theta) P_q(\cos\theta)\sin\theta\, d\theta = \frac{2g_q}{2q+1} j_q(kr). \tag{C.11}$$

The $q^{th}$ derivative of the left hand side of equation (C.8) with respect to $r$ evaluated at $r = 0$ is

$$j^{-q}k^q \int_0^\pi \cos^q\theta\, P_q(\cos\theta)\sin\theta\, d\theta = j^{-q}k^q \frac{2^{q+1}(q!)^2}{(2q+1)!}. \tag{C.12}$$

Similarly, the $q^{th}$ derivative [8] of the right hand side of equation (C.11) evaluated at $r = 0$ is

$$k^q \frac{2^{q+1}(q!)^2 g_q}{(2q+1)(2q+1)!}. \tag{C.13}$$

By comparing this result with left hand side equation in (C.12),

$$g_q = j^{-q}(2q+1). \tag{C.14}$$

By replacing $q$ by $n$,

$$g_n = j^{-q}(2n+1). \tag{C.15}$$

# Appendix D

# Legendre Functions

When solving the wave problems associated with spherical coordinates the Helmholtz equations are used in many cases. The $\theta$ equation in (4.4) is called Legendre's equation and its solutions are called the associated Legendre functions [8,97].

$$\frac{1}{\sin\theta}\frac{d}{d\theta}\left(\sin\theta\frac{dL}{d\theta}\right)+\left[v\,(v+1)-\frac{m^2}{\sin^2\theta}\right]L=0. \tag{D.1}$$

The solution to this, in general, is $L_n^m(\cos\theta)$ and, commonly used solutions are

$$P_n^m(\cos\theta),\ Q_n^m(\cos\theta). \tag{D.2}$$

The solutions $P_n^m(\cos\theta)$ are the associated Legendre functions of first kind and $Q_n^m(\cos\theta)$ are the associated Legendre functions of second kind.

Legendre's equation in (D.1) can be put into a common form using, $u$=$\cos\theta$, so that

$$(1-u^2)\frac{d^2L}{du^2}-2u\frac{dL}{du}+\left[v\,(v+1)-\frac{m^2}{1-u^2}\right]L=0. \tag{D.3}$$

Equation (D.3) is the associated Legendre equation and, if $m=0$, this equation reduces to the ordinary Legendre equation:

$$(1-u^2)\frac{d^2L}{du^2}-2u\frac{dL}{du}+v\,(v+1)\,L=0. \tag{D.4}$$

In spherical coordinates, the angle $\theta$ changes from 0 to $\pi$ and therefore the solutions must be expected over the range $-1\leq u\leq 1$. If $v$ is not an integer, $P_v(u)$ and $P_v(-u)$ are two independent solutions to the ordinary Legendre equation in (D.4). If $v=n$ is an integer, the Legendre function of the first kind becomes a finite series called the Legendre polynomial of degree $n$ . In this case, $P_n(-u)=(-1)^nP_n(u)$ [8]. The Legendre function of the second kind is defined as

$$Q_v(u)=\frac{\pi}{2}\,\frac{P_v(u)\cos\,v\pi-P_v(-u)}{\sin\,v\pi}. \tag{D.5}$$

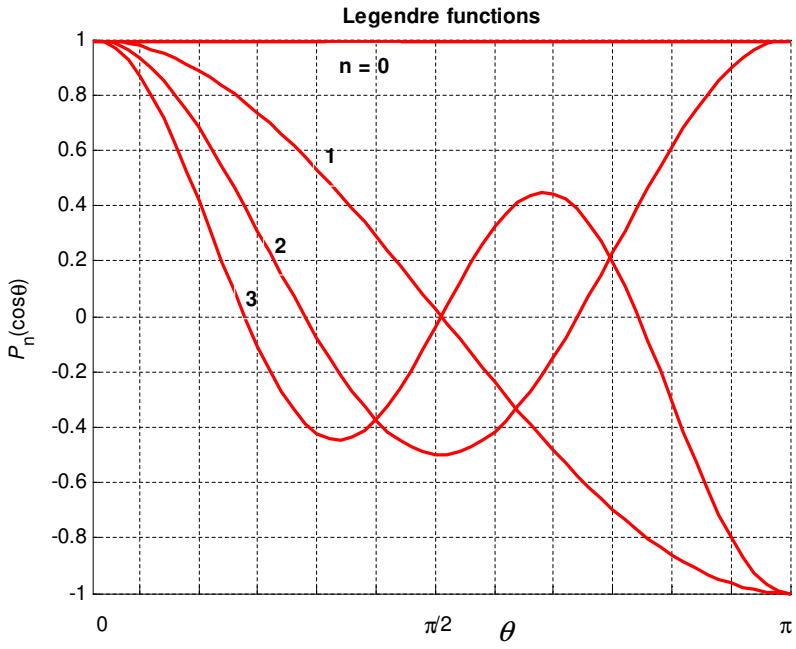


Figure D.1: Legendre functions of the first kind.

When $v = n$ is an integer,

$$Q_n(u) = \lim_{v \to n} Q_v(u) \tag{D.6}$$

and this is the second solution to Legendre's equation.

The Legendre polynomials are given by Rodrigues' formula,

$$P_n(u) = \frac{1}{2^n n!} \frac{d^n}{du^n}(u^2 - 1)^n. \tag{D.7}$$

Some of the lower order polynomials are

$$\begin{aligned} P_0(u) = 1 \qquad P_1(u) = u \qquad P_2(u) = \tfrac{1}{2}(3u^2 - 1) \\ P_3(u) = \tfrac{1}{2}(5u^3 - 3u) \qquad P_4(u) = \tfrac{1}{8}(35u^4 - 30u^2 + 3). \end{aligned} \tag{D.8}$$

The curves of the Legendre polynomials plotted against $\theta$ for $n = 0$, $n = 1$, $n = 2$ and $n = 3$ are shown in Figure D.1.

Now consider the associated Legendre equation in (D.3). For simplicity, take $m$ to be an integer. If equation (D.4) is differentiated $m$ times (we use $v = n$) the result is for $v = n$

$$\left[(1 - u^2)\frac{d}{du^2} - 2u\,(m + 1)\,\frac{d}{du} + (n - m)(n + m + 1)\right] \frac{d^m L}{du^m} = 0. \tag{D.9}$$

Now, letting $w = \left[(1-u)^{m/2}\right] \frac{d^m L}{du^m}$ in the above, equation (D.3) can be obtained with $L$ replaced by $w$. Hence the solutions to the associated Legendre equation are

$$P_n^m(u) = (-1)^m (1-u^2)^{m/2} \frac{d^m P_n(u)}{du^m}, \tag{D.10}$$

where $P_n(u)$ is the associated Legendre polynomial of degree $n$. All $P_n^m(u) = 0$ for $m > n$. Similarly for the second kind,

$$Q_n^m(u) = (-1)^m (1-u^2)^{m/2} \frac{d^m Q_n(u)}{du^m}. \tag{D.11}$$

Here, $Q_n(u)$ is the associated Legendre polynomial of degree $n$ of second kind. Some of these polynomials are

$$\begin{aligned}
&P_1^1(u) = -(1-u^2)^{1/2}, \quad P_2^1(u) = -3(1-u^2)^{1/2}u, \quad P_2^2(u) = 3(1-u^2) \\
&P_3^1(u) = -\tfrac{3}{2}(1-u^2)^{1/2}(1-5u^2), \quad P_3^2(u) = 15(1-u^2)u, \\
&P_3^3(u) = -15(1-u^2)^{3/2}.
\end{aligned} \tag{D.12}$$

For $P_n^m(u)$, when degree $n = 1$ there is only one solution, when $n = 2$ there are two solutions for first order and second order and, when $n = 3$ there are three solutions for first, second and third orders. When $m$ is not an integer, the situation becomes more complicated and the standard formulae can be found in [8].

# Appendix E

# The distance to the wave front from the cylinder

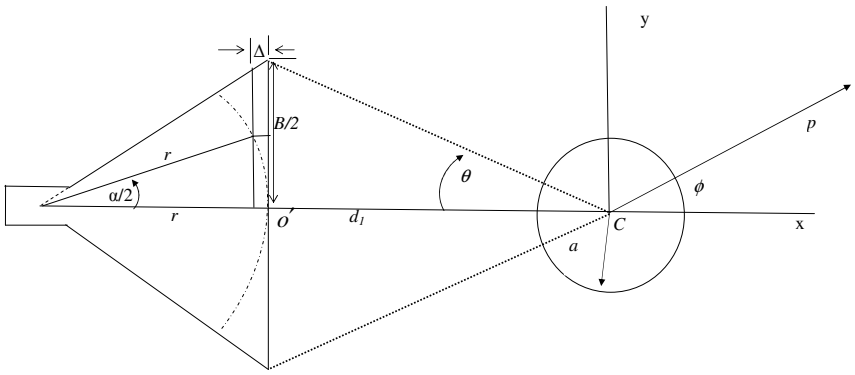


Figure E.1: Geometry of the antenna plane

Figure E.1 shows the geometry of the antenna in $xy$-plane. In the experiment the horn angle has been measured ($\alpha$=17.5 degrees). The arc drawn between two side

walls of the antenna represents the wave front which is presumed to be cylindrical in shape due to the mode of wave excitation from the antenna flange. From the geometry of the situation the small distance $\Delta$ between the arc and the aperture plane of the antenna at the mid-angle point between $O'$ and the edge of the antenna front face can be found as

$$\Delta = r(1 - \cos(\alpha/2)). \tag{E.1}$$

As the horn angle $\alpha$ is known by the measurements, the arc radius $r$ is found to be

$$r = \frac{B}{2}\cot(\alpha). \tag{E.2}$$

Therefore, using equations (E.1) and (E.2) the length $\Delta$ can be found as

$$\Delta = \frac{B}{2}\cot(\alpha)(1 - \cos(\alpha/2)). \tag{E.3}$$

Now, equation(E.3) can be used to find the distance to the wave front from the point $C$, the centre of the cylinder. Thus the approximate average distance to the wave-front from $C$ is $d_1^*$ where $d_1^* = d_1 + \Delta$. Using a similar mid-angle approximation for the scattered wave, again taking the half-angle point $\phi = \pi - \theta/2$, this average distance is $\frac{d_1^*}{cos(\frac{\theta}{2})}$ . In the application in Chapter 7, $\Delta = 0.006$ m.

# References


[1] Y. Yao, X. P. Zhao, J. Zhao and X. Zhou, *Microwave transmission behaviour of the single dissymmetrical hexagonal split-ring resonators,* Acta Physica Sinica, **55**, no. 12, 6435-40, (2006).

[2] K. L. Carr, P. Cevasco, P. Dunlea and J. Shaeffer, *Radiometric sensing: An adjuvant to mammography to determine breast biopsy*, IEEE MIT-S Digest, 929-32, (2000).

[3] F. Kuchar, R. Meisels, P. Oberhumer and R. Gajic, *Microwave studies of photonic crystals*, Advanced Engineering Materials, **8**, no. 11, 1156-61, (2006).

[4] S. Caorsi, A. Massa, M. Pastorino and A. Rosani, *Microwave medical imaging: Potentialities and limitations of a stochastic optimisation technique*, IEEE Trans. on Microwave Theory and Techniques, **52**, no. 8, 1909-16, (2004).

[5] N. J. Cronin, *Microwave and optical wave guides*, Bristol : Institute of Physics, (1995).

[6] A. Rosen, M. A. Stuchly, and A. V. Vorst, *Application of RF/microwaves in medicine*, IEEE Trans. on Microwave Theory and Techniques, **50**, no. 3, 963-974, (2002).

[7] D. M. Pozar, *Microwave engineering*, John Wiley  Sons, New York, 49-86, (2005).

[8] R. F. Harrington, *Time-harmonic electromagnetic fields*, McGraw-Hill, New York, (1961).

[9] S. O. Nelson, S. Trabelsi and A. W. Keaszewski, *RF sensing of grain and moisture content*, IEEE Sensors Journal, **1**, no. 2, 119-25, (2001).

[10] K. R. Demarest, *Engineering electromagnetics*, Prentice-Hall, 366-70, (1998).

[11] G. Bindu and K. T. Mathew, *Characterization of benign and malignant breast tissues using 2-D microwave tomographic imaging*, Microwave and Optical Technology Letters, **49**, no. 10, 2341-45, (2007).

[12] P. V. Parimi, W. T. Lu, P. Vodo, J. Sokoloff, J. S. Derov and S. Sridhar, *Negative refraction and left-handed electromagnetism in microwave photonic crystals*, Physical Review Letters, **92**, no. 12, 127401-04, (2004).

[13] Y. J. Feng, X. H. Teng, J. M. Zhao, Y. Chen and T. Jiang, *Anomalous reflection and refraction in anisotropic metamaterial realized by periodically loaded transmission line network*, Journal of Applied Physics, **100**, no. 11, 114901-07, (2006).

[14] S. N. Ghosh, *Electromagnetic theory and wave propagation*, Boca Raton, Florida: CRC Press; New Delhi: Narosa Publishing House, (2002).

[15] C. Someda, *Electromagnetic waves*, Boca Raton, Second Edn., CRC/Taylor Francis, (2006).

[16] G. N. Watson, *Theory of Bessel functions*, Cambridge, (1962).

[17] A. M. Maniatty and E. Park, *Finite element approach to inverse problems in dynamic elastography*, Proc. of 5th International Conference on Inverse Problems in Engineering: Theory and Practice, Cambridge, UK., **M01**, 1-8, (2005).

[18] T. Alarcon, H. M. Byrne and P. K. Maini, *Towards whole-organ modelling of tumour growth*, Progress in Biophysics Molecular Biology, **85**, no. 2-3, 451-72, (2004).

[19] J. W. Bandler, A. S. Mohamed, M. H. Baker, K. Madsen and J. Sondergaard, *EM-based optimisation exploiting partial space mapping and exact sensitivities*, IEEE Trans. on Microwave Theory and Techniques, **50**, no. 12, 2741-50, (2002).

[20] S. Caorsi, A. Massa, M. Pastorino and M. Donelli, *Improved microwave imaging procedure for non-destructive evaluations of two dimensional structures*, IEEE Trans. on Antennas and Propagation, **52**, no. 6, 1386-97, (2004).

[21] K. L. Carr, *Microwave radiometry: Its importance to the detection of cancer*, IEEE Trans. Microwave Theory and Techniques, **37**, 1862-69, (1989).

[22] P. M. Meaney, K. D. Paulsen and J. T. Chang, *Near-field microwave imaging of biologically based materials using a monopole transceiver system*, IEEE Trans. on Medical Imaging, **17**, 31-45, (1999).

[23] F. Comblet, A. Khenchaf, A. Baussard and F. Pellen, *Bistatic synthetic aperture radar imaging: Theory, simulations, and validations*, IEEE Trans. on Antennas and Propagation, **54**, no. 11, 3529-40, (2006).

[24] L. Curiel, R. Souchon, O. Rouviere, A. Gelet and J. Y. Chapelon, *Elastography for the follow-up of high-intensity focused ultrasound prostate cancer treatment: Initial comparison with MRI*, Ultrasound in Medicine and Biology, **31**, no. 11, 1461-68, (2005).

[25] A. Franchois and C. Pichot, *Microwave imaging-Complex permittivity reconstruction with a Levenberg-Marquardt method*, IEEE Trans. on Antennas and Propagation, **45**, no. 2, 203-215, (1997).

[26] J. R. Wang, P. E. Racette, J. R. E. Piepmeier, B. Monosmith and W. Manning, *Airborne cosmier observations between 50 and 183 GHz over snow-covered sierra mountains*, IEEE Trans. on Geoscience and Remote Sensing, **45**, no. 1, 55-61, (2007).

[27] A. Makkeasorn, N. B. Chang, M. Beaman, C. Wyatt and C. Slater, *Soil moisture estimation in a semiarid watershed using radarsat-1 satellite imagery and genetic programming*, Water Resources Research, **42** , no. 9, W09401, 1-15, (2006).

[28] G. Hong, G. Heygster, J. G. Miao and K. Kunzi, *Potential to estimate the canting angle of tilted structures in clouds from microwave radiances around 183 GHz*, IEEE Trans. Geoscience and Remote Sensing Letters, **2**, no. 1, 40-44, (2005).

[29] J. Morita, Y. N. Takayabu, S. Shige and Y. Kodama, *Analysis of rainfall characteristics of the madden-julian oscillation using TRMM satellite data*, Dynamics of Atmospheres and Oceans, **42**, no. 1-4, 107-26, (2006).

[30] G. Bindu, A. Lonappan, V. Thomas, C. K. Aanandan, K. T. Mathew and S. J. Abraham, *Active microwave imaging for breast cancer detection*, Progress in Electromagnetic Research, PIER, **58**, 149-69, (2006).

[31] I. Walterscheid, J. H. G. Ender, A. R. Brenner and O. Loffeld, *Bistatic SAR processing and experiments*, IEEE Trans. on Geoscience and Remote Sensing, **44**, no. 10, 2710-17, (2006).

[32] S. C. Mukhopadhyay, J.D.Woolley, G.Senaratne, G. Sengupta and S.Yamada, *Experimental observation of the effect of dielectric materials on the transfer impedance of planar electromagnetic sensors*, Proc. of ENDE, 21-23, (2003).

[33] Radiation research society, *Radiation research 137*, http://www.Jstor.Org/cgi-bin/jstor/viewitem/00337587/ap060480/06a00240/0?Frame=noframe dpi=3 backcontext=page, **137**, 417-18, (1994).

[34] V. M. D. Michael, *Matching clinical and biological needs with emerging imaging technologies*, C. I. P. National Cancer Institute, 1-16, (2005).

[35] World health organization, "Cancer", *Fact sheet No. 297*, http://www.who.int/mediacentre/factsheets/fs297/en/print.html, February (2006).

[36] UK. Cancer research, *UK breast cancer statistics*, http://info.Cancerresearchuk.Org/cancerstats/types/breast/, (2007).

[37] American Cancer Society, "*Breast cancer facts and figures 2005-2006*", (2006).

[38] —, "*Breast cancer facts and figures 2006-2007*", 1-28, (2007).

[39] World Health Organization, "Cancer", *facts sheet no. 297*, World Health Organization, (2006).

[40] Breast cancer: New Zealand facts, early detection, breast examination, http://www.littlies.co.nz/page.asp?id=147.

[41] B. C. Baguley, E. S. Marshall, G. C. Wake and D. J. N. Wall, *Modelling of cell population growth with application to cancer therapy in human tumour cell lines*, Progress in Biophysics Molecular Biology, **85**, 353-68, (2004).

[42] J. McCann, D. Stockton and S. Godward, *Impact of false-positive mammography on subsequent screening attendance and risk of cancer*, Breast Cancer Research, **4**, no. 5, 1-9, (2002).

[43] J. L. Xu, R. M. Fagerstrom, P. C. Prorok and B. S. Kramer, *Estimating the cumulative risk of a false-positive test in a repeated screening program*, Biometrics, **60**, no. 3, 651-60, (2004).

[44] J. G. Elmore, D. L. Miglioretti, L. M. Reisch, M. B. Barton, W. Kreuter, C. L. Christiansen and S. W. Fletcher, *Screening mammograms by community radiologist: Variability in false-positive rates*, Journal of the National Cancer Institute, **94**, no. 18, 1373-80, (2002).

[45] M. L. Brown, F. Houn, E. A. Sickles and L. G. Kessler, *Screening mammography in community practice - positive predictive value of abnormal findings and yield of follow-up diagnostic procedures*, American Journal of Roentgenology, **165**, no. 6, 1373-77, (1995).

[46] C. L. Christiansen, F. Wang, M. B. Barton, W. Kreuter, J. G. Elmore, A. E. Gelfand and S. W. Fletcher, *Predicting the cumulative risk of false-positive mammograms*, Journal of the National Cancer Institute, **92**, no. 20, 1657-1666, (2000).

[47] A. E. Gelfand and F. Wang, *Modelling the cumulative risk for a false positive under repeated screening events*, Stat. Med., **19**, 1865-79, (2000).

[48] Breastcancer.org, *Screening for breast cancer*, http://www.breastcancer.org/symptoms/new-research/, June, (2008).

[49] Peter Oehr, H. J. Biersack, R. E. Coleman, *PET and PET-CT in Oncology*, Published by Springer, ISBN 354043125X, 9783540431251, (2004).

[50] S. P. Poplack, K. D. Paulsen, A. Hartov, P. M. Meaney, B. W. Pogue, T. D. Tosteson, M. R. Grove, S. K. Soho and W. A. Wells, *Electromagnetic breast imaging: Average tissue property values in women with negative clinical findings*, Radiology, **231**, no. 2, 571-80, (2004).

[51] A. W. Preece, R. H. Johnson, J. L. Green and M. P. Robinson, *Dielectric imaging for localisation and detection of breast tumours*, IEEE MIT-S Digest, **GG-3**, 1145-47, (1993).

[52] D. W. Winters, E. J. Bond, B. D. Van Veen and S. C. Hagness, *Estimation of the frequency-dependent average dielectric properties of breast tissue using a time-domain inverse scattering technique*, IEEE Trans. on Antennas and Propagation, **54**, no. 11, 3517-28, (2006).

[53] J. S. Andrzej, S. S. Stanislaw, J. R. Barr and S. Arvind, *Dielectric properties of breast carcinoma and the surrounding tissues*, IEEE Trans. on Biomedical Engineering, **35**, no. 4, 257-63, (1988).

[54] S. S. Chau, R. K. Mishra, A. Swarup and J. M. Thomas, *Dielectric properties of normal and malignant human breast tissue at radio and microwave frequencies*, Indian J. Biochem and Biophysics, **21**, 76-79, (1984).

[55] T. Morimoto, Y. Kiinouchi, T. Iratani, S. Kumara, Y. Konishi, N. Mitsuyama, K. Komaki and Y. Monden, *Measurements of the electrical bio-impedance of breast tumours*, Eur. Surg. Res., **22**, 86-92, (1990).

[56] M. Lazebnik, L. McCartney, D. Popovic, C. B. Watkins, M. J. Lindstrom, J. Harter, S. Sewall, A. Magliocco, J. H. Booske, M. Okoniewski and S. C. Hagness, *A large-scale study of the ultrawideband microwave dielectric properties of normal breast tissue obtained from reduction surgeries*, Physics in Medicine and Biology, **52**, 2637-56, (2007).

[57] R. B. Keam, G. G. Senaratne, and R. Pochin, *One-dimensional propagation difference between tumour and healthy breast tissue at 2 GHz*, New Zealand National Conference on Non Destructive Testing, 21-25, (2004).

[58] E. C. Fear and M. A. Stuchly, *Microwave breast cancer detection*, IEEE MIT-S Digest, 1037-1040, (2000).

[59] T. C. Williams, E. C. Fear and D. T. Westwick, *Tissue sensing adaptive radar for breast cancer detection - investigations of an improved skin-sensing method*, IEEE Trans. on Microwave Theory and Techniques, **54**, no. 4, 1308-14, (2006).

[60] J. M. Sill and E. C. Fear, *Tissue sensing adaptive radar for breast cancer detection - experimental investigation of simple tumour models*, IEEE Trans. on Microwave Theory and Techniques, **53**, no. 11, 3312-19, (2005).

[61] E. C. Fear, *Microwave imaging of the breast*, Technology in Cancer Research Treatment, **4**, no. 1, 69-82, (2005).

[62] J. M. Sill and E. C. Fear, *Tissue sensing adaptive radar for breast cancer detection: Study of immersion liquids*, Electronics Letters, **41**, no. 3, 113-115, (2005).

[63] H. P. Schwan and K. Li, *Capacity and conductivity of body tissue at ultrahigh frequencies*, Proc. IRE, **41**, 1735-40, (1953).

[64] P. A. Bottomley and E. R. Andrew, *RF magnetic field penetration, phase shift and power dissipation in biological tissue: Implication for NMR imaging*, Phys. Med. Biol., **23**, 630-43, (1978).

[65] E. C. Fear, C. S. Hagness, P. M. Meaney, Okonieswski and M. A. Stuchly, *Enhancing breast tumour detection with near-field imaging*, IEEE Micro., **3**, no. 1, 48-56, (2002).

[66] K. D. Paulsen, M. J. Moskowitz and T. P, Ryan, *Temperature field estimation using electrical impedance profiling methods: I. Reconstruction algorithm and simulated results*, Int. J. Hyperthermia, **10**, 209-28, (1994).

[67] P. M. Meaney, K. D. Paulsen and T. P. Ryan, *Two-dimensional hybrid element image reconstruction for TM illumination*, IEEE Trans. Antennas and Propagation, **43**, 239-47, (1995).

[68] R. A. Kruger, K. K. Kopecky, A. M. Aisen, D. R. Reinecke, G. A. Kruger and W. L. Kiser, *Thermoacoustic CT with radio waves: A medical imaging paradigm*, Radiology, **211**, no. 1, 275-78, (1999).

[69] R. A. Kruger, K. D. Miller, H. E. Reynolds, W. L. Kiser, D. R. Reinecke and G. A. Kruger, *Breast cancer in vivo: Contrast enhancement with thermoacoustic CT at 434 MHz - feasibility study*, Radiology, **216**, no. 1, 279-83, (2000).

[70] R. A. Kruger, W. L. Kiser, D. R. Reinecke, G. A. Kruger and R. L. Eisenhart, Thermoacoustic CT with radio waves: A medical imaging paradigm, Microwave Symp. Dig., **2**, 591-94, (1999).

[71] L. H. V. Wang, X. M. Zhao, H. T. Sun and G. Ku, *Microwave-induced acoustic imaging of biological tissues*, Review of Scientific Instruments, **70**, no. 9, 3744-48, (1999).

[72] Q. H. Liu, Z. Q. Zhang, T. H. T. Wang, J. A. Bryan, G. A. Ybarra, L. W. Nolte and W. T. Joines, *Active microwave imaging 1-2-d forward and inverse scattering-methods*, IEEE Trans. on Microwave Theory and Techniques, **50**, no. 1, 123-33, (2002).

[73] G. P. Otto and W. C. Chew, *Microwave inverse scattering-local shape function imaging for improved resolution of strong scatters*, IEEE Trans. on Microwave Theory and Techniques, **42**, no. 1, 137-41, (1994).

[74] G. G. Cook, A. P. Panderson, A. J. T. Whitaker and J. C. Bennett, *High resolution three-dimensional microwave imaging of antennas*, IEEE Trans. Antennas and Propagation, **37**, no. 6, 768-77, (1989).

[75] Z. Zhao and N. H. Farhat, *Tomographic microwave diversity image-reconstruction employing unitary compression*, IEEE Trans. on Microwave Theory and Techniques, **40**, no. 2, 315-22, (1992).

[76] P. M. Meaney, M. W. Fanning, D. Li, S. P. Poplack and K. D. Paulsen, *A clinical prototype for active microwave imaging of the breast*, IEEE Trans. Microwave Theory and Techniques, **48**, 1841-53, (2000).

[77] Z. Q. Zhang, Q. H. Liu, C. J. Xiao, E. Ward, G. Ybarra and W. T. Joines, *Microwave breast imaging: 3-d forward scattering simulation*, IEEE Trans. on Biomedical Engineering, **50**, no. 10, 1180-89, (2003).

[78] A. E. Bulyshev, S. Y. Semenov, A. E. Souvorov, R. H. Svenson, A. G. Nazarov, Y. E. Sizov and G. P. Tatsis, *Computational modelling of three-dimensional microwave tomography of breast cancer*, IEEE Trans. on Biomedical Engineering, **48**, no. 9, 1053-56, (2001).

[79] S. C. Hagness, A. Taflove and J. E. Bridges, *Two-dimensional FDTD analysis of a pulsed microwave confocal system for breast cancer detection: Fixed-focus and antenna array sensors*, IEEE Trans. on Biomedical Engineering, **45**, no. 12, 1470-78, (1998).

[80] C. G. Hagness, A. Taflove and J. E. Bridges, *Three dimensional FDTD analysis of a pulsed microwave confocal system for breast cancer detection*, IEEE Trans. Antennas Propagation, **47**, 783-91, (1999).

[81] P. Kosmas, C. M. Rappaport and E. Bishop, *Modelling with the FDTD method for microwave breast cancer detection*, IEEE Trans. on Microwave Theory and Techniques, **52**, no. 8, 1890-97, (2004).

[82] E. C. Fear, X. Li, S. C. Hagness and M. A. Stuchly, *Confocal microwave imaging for breast cancer detection: Localization of tumours in three dimensions*, IEEE Trans. on Biomedical Engineering, **49**, no. 8, 812-22, (2002).

[83] A. Taflove and S. C. Hagness, *Computational electromagnetics: The finite difference time domain method*, second ed., Northwood, MA: Artech House, (2000).

[84] S. C. Hagness, A. Taflove and J. E. Bridges, *Wideband ultralow reverberation antenna for biological sensing*, Electronics Letters, **33**, no. 19, 1594-95, (1997).

[85] X. Li, E. J. Bond, B. D. Van Veen and S. G. Hagness, *An overview of ultra-wideband microwave imaging via space-time beamforming for early-stage breast-cancer detection*, IEEE Antennas and Propagation Magazine, **47**, no. 1, 19-34, (2005).

[86] Y. Xie, B. Guo, L. Z. Xu, J. Li and P. Stoica, *Multistatic adaptive microwave imaging for early breast cancer detection*, IEEE Trans. on Biomedical Engineering, **53**, no. 8, 1647-57, (2006).

[87] Y. Xie, B. Guo, J. Li and P. Stoica, *Novel multistatic adaptive microwave imaging methods for early breast cancer detection*, Eurasip Journal on Applied Signal Processing, Article ID 91961, 1-13, (2006).

[88] S. K. Davis, H. Tandradinata, S. C. Hagness and B. D. Van Veen, *Ultrawideband microwave breast cancer detection: A detection-theoretic approach using the generalized likelihood ratio test*, IEEE Trans. on Biomedical Engineering, **52**, no. 7, 1237-50, (2005).

[89] K. Siwiak, *Ultra-Wideband Radio Technology* / Kazimierz Siwiak and Debra McKeown, (2004).

[90] S. Trabelsi and S. O. Nelson, *Non-destructive sensing of physical properties of granular materials by microwave permittivity measurement*, IEEE Trans. on Instrumentation and Measurement, **55**, no. 3, 953-63, (2006).

[91] R. B. Keam and G. G. Senaratne, *Microwave moisture and salt measurement for the New Zealand dairy industry*, 5th ISEMA Conference on Wave Interaction with Water and Moisture Substances, 369-76, (2003).

[92] G. Senaratne and S.C. Mukhopadhyay, *Investigation of the interaction of planar electromagnetic sensor with dielectric materials at radio frequencies*, Fifth ISEMA Conference on Wave Interaction with Water and Moisture Substances, 95-99, (2003).

[93] J. R. Holdem, R. B. Keam and J. A. Schoonees, *Estimation of the number of frequencies and bandwidth for the surface measurements of soil moisture as a function of depth*, IEEE Trans. on Instrumentation and Measurements **49**, no. 5, 964-70, (2000).

[94] V. James and P. Christian, *Active microwave imaging: A model-based approach*, IEEE Trans. on Antennas and Propagation, **39**, no. 3, 285-90, (1991).

[95] R. Zoughi, *Microwave non-destructive testing and evaluation*, The Netherlands: Kluwer Academic, (2000).

[96] C. Salvatore, M. Andrea, P. Matteo and D. Massimo, *Improved microwave imaging procedure for non-destructive evaluation of two-dimensional structures*, IEEE Trans. on Antennas and Propagation, **52**, no. 6, 1386-95, (2004).

[97] S. A. Schelkunoff, *Electromagnetic waves*, Van Nostrand Company, Inc., Princeton, N.J., 51-52, (1943).

[98] K. Zhang, *Electromagnetic theory for microwaves and optoelectronics*, New York : Springer-Verlag, (1998).

[99] S. Ramo, J. R. Whinnery and T. V. Duzer, *Fields and waves in communication electronics*, New York : Wiley, (1994).

[100] R. B. Keam, J. R. Holdem and J. A. Schoonees, *Soil moisture estimation from surface measurements at multiple frequencies*, Aust. Journal of Soil Res., **37**, 1107-21, (1999).

[101] D. Kincaid and W. Cheney, *Numerical analysis: Mathematics of scientific computing*, Brooks/Cole, (2002).

[102] G. G. Evans, *Analytic methods for partial differential equations*, New York : Springer, (2000).

[103] K.F. Riley, *Mathematical methods for the physical science*, Cambridge University Press, (1974).

[104] E. J. Bond, X. Li, S. C. Hagness and B. D. V. Veen, *Microwave imaging via space-time beamforming for early detection of breast cancer*, IEEE Trans. on Antenna and Propagation, **51**, no. 8, 1690-705, (2003).

[105] M. N. Cinti, R. Pani, F. Garibaldi, R. Pellegrini, M. Betti, N. Lanconelli, A. Riccardi, R. Campanini, G. Zavattini, G. Di Domenico, A. Del Guerra, N. Belcari, W. Bencivelli, A. Motta, A. Vaiano and I. N. Weinberg, *Custom breast phantom for an accurate tumour SNR analysis*, IEEE Trans. on Nuclear Science, **51**, no. 1, 198-204, (2004).

[106] Agilent Technologies, *8714ES RF Network Analyzer, 300 kHz to 3 GHz*, User's Guide (downloaded on 20 August 2008): http://www.home.agilent.com/agilent/facet.jspx?kt=1cc=USlc=engk=8714ES.

[107] P. R. Karmel, G. D. Colef and R. L. Camisa, *Introduction to electromagnetic and microwave engineering*, New York: Wiley, (1997).

[108] P. L. Somlo and J.D. Hunter, *Microwave impedance measurements*, Peregrinus, UK, (1985).

[109] Test and Measurement World, *How does a Smith chart work?*, http://www.tmworld.com/article/CA187342.html (Editor), (2001).

[110] C. A. Coulson, *Waves: A mathematical approach to the common types of wave motion*, London; New York: Longman, (1977).

[111] G. G. Senaratne, R. B. Keam, W. L. Sweatman and G. C. Wake, *Solutions to the inverse problem in a two-dimensional model for microwave breast tumour detection*, International Journal of Intelligent System Technologies and Applications, IJISTA **03**, no. 1/2, 133-48, (2007).

[112] G. G. Senaratne, R. B. Keam, W. L. Sweatman and G. C. Wake, *Solutions to the two-dimensional boundary value problem for microwave breast tumour detection*, IEEE Microwave and Wireless Component Letters, **16**, no. 10, 525-27, (2006).

[113] G. G. Senaratne, R. B. Keam, W. L. Sweatman and G. C. Wake, *Solutions to the inverse problem with potential application for breast tumour detection using microwave measurements*, Computational and Mathematical Methods in Medicine, **8**, no. 4, 245-61, (2007).

[114] G. G. Senaratne, R. B. Keam, W. L. Sweatman, G. C. Wake and R. Simpkin, *An inverse method for detection of a foreign object using microwave measurements*, IET Science, Measurements and Technology (in press), (2008).